UNIVERSITY OF CALIFORNIA

Los Angeles

Multiscale Modeling and Control of Crystal Shape and Size Distributions: Accounting for Crystal Aggregation, Evaluation of Continuous Crystallization Systems and Run-to-Run Control

A dissertation submitted in partial satisfaction of the

requirements for the degree Doctor of Philosophy

in Chemical Engineering

by

Joseph Sangil Kwon

2015

ABSTRACT OF THE DISSERTATION

Multiscale Modeling and Control of Crystal Shape and Size Distributions: Accounting for Crystal Aggregation, Evaluation of Continuous Crystallization Systems and Run-to-Run Control

by

Joseph Sangil Kwon

Doctor of Philosophy in Chemical Engineering

University of California, Los Angeles, 2015

Professor Panagiotis D. Christofides, Chair

Crystallization plays a vital role in separation and purification methods for the production of therapeutic drugs. Considering the fact that crystal size and shape distributions have a significant influence on the bioavailability of drugs such as the dissolution rate, filterability, and stability as a carrier to the target site, the production of crystals with desired size and shape distributions is of particular interest to the pharmaceutical industry. Motivated by these considerations, this dissertation focuses on the development of a multiscale modeling and simulation framework for crystallization processes that elucidates the relationship between molecular-level processes like crystal nucleation, growth and aggregation and macroscopically-observable process behavior and allows computing optimal design

and operation conditions. Using protein crystallization as a model system, the multiscale framework encompasses: a) equilibrium Monte-Carlo modeling for computing solid-liquid phase diagrams and determining initial crystallization conditions that favor crystal nucleation, b) kinetic Monte-Carlo modeling for simulating crystal growth and aggregation and predicting the evolution of crystal shape distribution, and c) integrated multiscale computation linking molecular-level models and continuous-phase macroscopic equations, covering both batch and continuous crystallization systems. The multiscale model parameters and predictions are calibrated and tested with respect to available experimental data. Then, this dissertation addresses model predictive controller designs that utilize the insights and results from the multiscale modeling work and real-time measurements of solute concentration and temperature to manipulate crystallizer conditions that lead to the production of crystals with desired size and shape distributions. To enhance the ability of the predictive controller to deal with batch-to-batch parametric drifts, a common problem in industrial crystallization owing to changes, for example, in the pH level or impurity concentration in the feedstock container, a run-to-run-based model parameter estimation scheme will be presented that uses moving horizon estimation principles to update the predictive controller model parameters after each batch and leads to the consistent production of crystals of desired shape at the end of each batch.

The dissertation of Joseph Sangil Kwon is approved.

Tetsuya Iwasaki

Dante Simonetti

James F. Davis

Panagiotis D. Christofides, Committee Chair

University of California, Los Angeles

2015

Contents

List of Figures

ACKNOWLEDGEMENTS

I would first like to express my gratitude to my two co-advisors, Professor Panagiotis D. Christofides and Professor Gerassimos Orkoulas, for their endless support throughout my doctoral work. I still vividly remember the moment when I first contacted Professor Christofides in 2011 Spring. Throughout my doctoral study, he was always there to help me and guide me in the right direction. In particular, I highly appreciate his bottomless support when I was preparing for the on-site interview at TAMU. I received an offer from TAMU and I strongly believe it would not have been possible without Professor Christofides. I would like to thank my parents and Rev. Jong H. Kim and Mrs. Kim for their support and encouragement throughout my life.

I would like to thank Michael Nayhouse for being an impeccable partner on many of our projects on crystallization. I really enjoyed working with him as well as talking about Korean cultures. Furthermore, I would like to thank all of my labmates from my graduate career, in particular, Matt Ellis, Liangfeng Lao, Tueng-Sheng Tu, Larry Gao, Marquis Crose, Anh Tran, Helen Durand, and Anas Wael Alanqar, who were great labmates in addition to being good friends throughout my time at UCLA.

I was also fortunate to meet and get to know a number of people outside of my research group during my time at UCLA which made the experience much more enjoyable. I would like to thank Bonhye Koo, Soyon Kim, Sangjin Lee, Sangchul Lee, Woojin Ahn, Woosuk Kim, Jaehoon Lee, Yongwook Paik, with whom I had the pleasure of being good friends, in addition to playing sports with them.

Finally, I would like to thank Professor James F. Davis, Professor Tetsuya Iwasaki, and Professor Dante Simonetti for serving on my doctoral committee.

Financial support from the National Science Foundation (CBET-0967291) and the Extreme Science and Engineering Discovery Environment (TG-CCR120003) is gratefully acknowledged.

Chapter 2 is a version of: J. S. Kwon, M. Nayhouse, P. D. Christofides, and G. Orkoulas, "Protein crystal shape and size control in batch crystallization: comparing model predictive control with conventional operating policies," *Ind. & Eng. Chem. Res.*, 2014, **53**, 5002-5014.

Chapter 3 is a version of: J. S. Kwon, M. Nayhouse, P. D. Christofides, and G. Orkoulas, "Modeling and control of shape distribution of protein crystal aggregates," *Chem. Eng. Sci.*, 2014, **104**, 484-497.

Chapter 4 is a version of: J. S. Kwon, M. Nayhouse, P. D. Christofides, and G. Orkoulas, "Modeling and control of shape in continuous protein crystallization," *Chem. Eng. Sci.*, 2014, **107**, 47-57.

Chapter 5 is a version of: J. S. Kwon, M. Nayhouse, P. D. Christofides, and G. Orkoulas, "Protein crystal shape and size control using a plug flow crystallization configuration," *Chem. Eng. Sci.*, 2014, **119**, 30-39.

Chapter 6 is a version of: J. S. Kwon, M. Nayhouse, G. Orkoulas, D. Ni, and P. D. Christofides, "A method for handling batch-to-batch drift using moving horizon estimation: application to run-to-run MPC of batch crystallization," *Chem. Eng. Sci.*, 2015, **127**, 210-

219.

Chapter 7 is a version of: J. S. Kwon, M. Nayhouse, G. Orkoulas, D. Ni, and P. D. Christofides, "Run-to-run-based model predictive control of protein crystal shape in batch crystallization," *Ind. & Eng. Chem. Res.*, 2015, **54**, 4293-4302.

Chapter 8 is a version of: J. S. Kwon, M. Nayhouse, and P. D. Christofides, "Detection and isolation of batch-to-batch parametric drift and drift-tolerant model predictive control of batch crystallization process," *Ind. & Eng. Chem. Res.*, 2015, **54**, 5514-5526.

Chapter 9 is a version of: J. S. Kwon, M. Nayhouse, and P. D. Christofides, "Multi-scale, multidomain modeling and parallel computation: application to crystal shape evolution in crystallization," *Ind. & Eng. Chem. Res.*, 2015, submitted.

VITA

2006–2009 Bachelor of Science, Chemical Engineering, Chemistry, and Mathematics

Department of Chemical Engineering and Material Science

University of Minnesota Twin Cities

2009–2011 Master of Science, Electrical Engineering

Department of Electrical and Systems Engineering

University of Pennsylvania

PUBLICATIONS

1. J. S. Kwon, M. Nayhouse, and P. D. Christofides, "Multiscale, multidomain modeling and parallel computation: application to crystal shape evolution in crystallization," *Ind. & Eng. Chem. Res.*, 2015, submitted.

2. M. Nayhouse, A. Tran, J. S. Kwon, M. Crose, G. Orkoulas, and P. D. Christofides, "Modeling and control of ibuprofen crystal growth and size distribution," *Chem. Eng. Sci.*, 2015, **134**, 414-422.

3. M. Crose, J. S. Kwon, M. Nayhouse, D. Ni, and P. D. Christofides, "Multiscale modeling and operation of PECVD of thin film solar cells," *Chem. Eng. Sci.*, 2015, in press.

4. J. S. Kwon, M. Nayhouse, and P. D. Christofides, "Detection and isolation of batch-to-batch parametric drift and drift-tolerant model predictive control of batch crystallization process," *Ind. & Eng. Chem. Res.*, 2015, **54**, 5514-5526.

5. J. S. Kwon, M. Nayhouse, G. Orkoulas, D. Ni, and P. D. Christofides, "Run-to-run-based model predictive control of protein crystal shape in batch crystallization," *Ind. & Eng. Chem. Res.*, 2015, **54**, 4293-4302.

6. J. S. Kwon, M. Nayhouse, G. Orkoulas, D. Ni, and P. D. Christofides, "A method for handling batch-to-batch drift using moving horizon estimation: application to run-to-run MPC of batch crystallization," *Chem. Eng. Sci.*, 2015, **127**, 210-219.

7. J. S. Kwon, M. Nayhouse, G. Orkoulas, and P. D. Christofides, "Protein crystal shape and size control using a plug flow crystallization configuration," *Chem. Eng. Sci.*, 2014, **119**, 30-39.

8. J. S. Kwon, M. Nayhouse, G. Orkoulas, and P. D. Christofides, "Enhancing crystal production rate and reducing polydispersity in continuous protein crystallization," *Ind. & Eng. Chem. Res.*, 2014, **53**, 2561-2569.

9. J. S. Kwon, M. Nayhouse, P. D. Christofides, and G. Orkoulas, "Protein crystal shape and size control in batch crystallization: comparing model predictive control with conventional operating policies," *Ind. & Eng. Chem. Res.*, 2014, **53**, 5002-5014.

10. J. S. Kwon, M. Nayhouse, P. D. Christofides, and G. Orkoulas, "Modeling and control of crystal shape in continuous protein crystallization," *Chem. Eng. Sci.*, 2014, **107**, 47-57.

11. J. S. Kwon, M. Nayhouse, P. D. Christofides, and G. Orkoulas, "Modeling and control of shape distribution of protein crystal aggregates," *Chem. Eng. Sci.*, 2014, **104**,

484-497.

12. J. S. Kwon, M. Nayhouse, P. D. Christofides, and G. Orkoulas, "Modeling and control of protein crystal shape and size in batch crystallization," *AIChE J.*, 2013, **59**, 2317-2327.

13. M. Nayhouse, J. S. Kwon, V. R. Heng, A. M. Amlani, and G. Orkoulas, "Freezing transition studies through constrained cell model simulation," *Int. J. Thermophysics*, 2013, **53**, 5002-5014.

14. M. Nayhouse, J. S. Kwon, P. D. Christofides, and G. Orkoulas, "Crystal shape modeling and control in protein crystal growth," *Chem. Eng. Sci.*, 2013, **87**, 216-223.

15. M. Nayhouse, J. S. Kwon, and G. Orkoulas, "Phase transitions, criticality and three-phase coexistence in constrained cell models," *J. Chem. Phys.*, 2012, **136**, 201101.

Chapter 1

Introduction

The biopharmaceutical market is one of the fastest growing areas in the $1 trillion pharmaceutical industry. Within biopharmaceutical production, protein crystallization plays a crucial role. For example, more than 100 therapeutic proteins have been licensed and more proteins are currently under research or development. However, of the 100 therapeutic proteins with production licenses, only a few are being sold in crystalline form in the market due to significant technological challenges in their production. The main technological challenge in producing protein crystals lies in the complexity of protein crystallization and the presence of nonlinearities in many factors involved in the system. More specifically, the production of crystals with desired size and shape distributions from crystallization processes is a subject of great interest to the pharmaceutical industry, because crystal size and shape significantly influence the bioavailability of drugs such as the stability of a carrier to the target site, melting points, and dissolution rates [131].

1.1 Batch crystallization system with nucleation, crystal growth, and aggregation processes

Researchers recently have developed models for protein nucleation [40, 100] and crystal growth [31, 35, 38, 64], and consequently significant advances have been made in the field of modeling of crystallization processes describing the shape and size distributions of the produced protein crystals. To this end, kinetic Monte Carlo (kMC) simulation methods, which have been widely used to simulate molecular dynamic processes [10, 29, 30, 42, 43, 103, 104, 119, 44], have been successfully applied to compute the net crystal steady-state growth rate accounting for the dependence of migration and detachment rates on the local surface configuration. To implement the kMC methodology over the entire lattice, we extended the methodology of [25] to rate equations which were first developed by [32]. There have been a number of computational and theoretical studies to improve the understanding of the shape control of crystals in a variety of small-scale crystallization systems [78, 77, 126], however no significant advancement has been made associated with the shape control of crystal aggregates in a large batch crystallization system. Crystal aggregation is caused by shear-induced forces from a stirring process which is necessary for a large-scale batch crystallizer in order to maintain the particulate phase in suspension (i.e., to avoid crystal sinking) [112].

Within this context, the present work focuses on the modeling of aggregation of protein crystals along with crystal nucleation and growth to investigate the influence of stirring on

the size and morphology of crystal aggregates. It is assumed that the continuous phase is dilute enough to make only binary aggregation possible. Furthermore, the corresponding turbulent shear rate within the crystallizer is characterized by the average velocity gradient of the flow field. An appropriate aggregation kernel is used to compute the rate at which binary aggregation occurs, and this rate strongly depends on the crystal sizes and the crystallizer operating parameters [65, 109]. The aggregation of lysozyme crystals with a diameter approximately in the range of 1-50 micrometers is mainly induced by shear forces according to the Kolmogorov microscale analysis [65]. An aggregate will be formed as two crystals completely merge along with their internal coordinates resulting in a decrease in the total number of crystals and an increase in the average crystal size. For the purpose of simulation, it is assumed that the shape of the crystal resulting from aggregation is identical to that of the larger crystal participating in the aggregation event. Extensive simulation studies are carried out to evaluate the influence of aggregation on the shape and size distributions of the crystals at the end of the batch run.

1.2 Continuous crystallization system

Traditionally, batch crystallization processes have been widely used in the pharmaceutical industry. However, the batch process has a few well-known potential drawbacks such as batch-to-batch variability and the difficulty in the scale-up and the production of crystals with desired crystal size and/or shape distributions. Recently, continuous crystallization, which is able to consistently produce crystals with desired size and shape distributions

starting from fresh raw materials, is receiving growing attention in the pharmaceutical industry. Specifically, once a steady-state has been achieved in a continuous crystallizer, all crystals are produced under a uniform supersaturation level, which leads to greater reproducibility and controllability of major characteristics of crystals such as size and shape distributions. As a result, the number of downstream operations required to amend crystals with undesired size and shape distributions (e.g., granulation for the solid dosage forms) may be reduced. Consequently, using a continuous manufacturing process can stimulate the growth of the pharmaceutical industry as it may reduce the size of production facilities, operating costs, waste, energy consumption, and raw material usage considerably. Moreover, the reproducibility and controllability of the active pharmaceutical ingredients (APIs) in the final dosage form can be improved.

Motivated by this, a mixed suspension mixed product removal (MSMPR) crystallization process, which is analogous to the conventional continuously stirred tank crystallizer (CSTC), has received growing attention, and many efforts have been made to produce crystals from the MSMPR process with a higher production rate and desired product quality than those of batch crystallization processes [48, 3, 54]. Specifically, the presence of backmixing is modeled by employing the residence time mixing model in order to account for the fact that those crystals nucleated at a later stage during the crystallization process will reside a relatively short amount of time in the crystallizer and thus they will end up leaving the crystallizer with undesired size and shape distributions [68]. The modeling of a plug flow crystallizer (PFC) which is used to produce crystals with narrow size and shape

distributions has been performed as well [33, 123].

1.3 In-batch model predictive control and post-batch run-to-run control

A population balance equation (PBE) is widely used to describe the evolution of the crystal volume distribution for batch and continuous crystallization processes. In practice, however, the complexity of a population balance model usually leads to an implementation issue with the controller design [22]. Therefore, the method of moments is used to derive reduced-order ordinary differential equation (ODE) models in time, which are used to approximate the dominant dynamic behavior of the evolution of the crystal volume distribution in a continuous crystallizer [34, 59]. In order to obtain a closed form of the moment model, a normal distribution assumption is used to approximate the crystal volume distribution. In addition to a set of polynomials that describes the dependence of the crystal growth of each face on a supersaturation level, the mass and energy balance equations and the moment models are considered to design an in-batch model predictive control (MPC) system, which is used to produce crystals with a desired shape distribution. To improve the controller performance, an advanced real-time monitoring technique is necessary in practice, because the production of crystals which are off the desired specification at the outlet of the process is irreversible. Within this context, the measurements of crystals through the use of focused beam reflectance measurement (FBRM) and process vision and mea-

surement (PVM) [8, 63] are modeled using kMC simulations to account for the real-time physical crystallization process.

However, the conventional MPC technique is not designed to take advantage of the repetitive nature of batch processes and thus in most cases the control performance is not improved as batch runs are repeated. Furthermore, the control performance of the MPC is very sensitive to model uncertainties such as changes in the kinetic parameters, which tend to persist from run-to-run [91].

Motivated by the above considerations, we propose a Run-to-Run-based (R2R-based) MPC to enhance the controller performance by learning from the past batch runs. Furthermore, the idea of the parameter adaptive control (PAC) strategy that estimates controller model parameters and utilizes them for the computation of improved control inputs is borrowed and used along with the offset drift cancellation (ODC) scheme [107, 108, 88, 85, 17, 128]. The major benefit of the proposed R2R-based MPC scheme is its unique capability to deal with the uncertainties and drift in the process while simultaneously satisfying the constraints imposed on the state variables and inputs; this integrated approach will lead to the production of crystals with a desired shape distribution from batch-to-batch.

1.4 Outline of the dissertation

Chapter 2 focuses on the modeling of a batch crystallization process used to produce tetragonal hen egg white (HEW) lysozyme crystals via kinetic Monte Carlo (kMC) simulation.

The kMC simulation simulates the batch protein crystallization via adsorption, desorption, and migration mechanisms on the (110) and (101) faces. Then, in order to describe the nucleation occuring at different times in the batch simulations, the nucleation rate expression was extracted from experimental results by [41]. In addition, the dependence of the crystal growth on temperature and protein solute concentration is demonstrated in 3-D nonlinear models constructed from open-loop kMC simulations. The present work also develops mass and energy balances to account for the depletion in the protein solute concentration and the drop in the crystallizer temperature by crystallization. Finally, an MPC, which makes use of the mass and energy balances, is designed to produce crystals with a desired morphology by regulating the crystal growth conditions in the crystallizer through the manipulation of the jacket temperature which is in accordance with standard batch crystallization practice.

Chapter 3 focuses on the modeling of aggregation of protein crystals along with crystal nucleation and growth to investigate the influence of stirring on the size and morphology of crystal aggregates. First of all, it is assumed that the continuous phase is dilute enough to make only binary aggregation possible. Furthermore, the corresponding turbulent shear rate within the crystallizer is characterized by the average velocity gradient of the flow field. An appropriate aggregation kernel is used to compute the rate at which binary aggregation occurs, and this rate strongly depends on the crystal sizes and the crystallizer operating parameters [65, 109]. The aggregation for lysozyme crystals with diameters approximately in the range of 1-50 micrometers is mainly induced by shear forces according to the Kol-

mogorov microscale analysis [65]. An aggregate will be formed as two crystals completely merge along with their internal coordinates resulting in a decrease in the total number of crystals and an increase in the average crystal size. For the purpose of simulation, it is assumed that the shapes of the resulting bigger crystals are maintained for the aggregate after the aggregation process. Extensive simulation studies are carried out to evaluate the influence of aggregation on the shape and size distributions of the crystals at the end of the batch run. Additionally, this chapter focuses on the simulation and control of protein crystal aggregation along with crystallization. Initially, a population balance model is presented for the process which accounts for simultaneous nucleation, crystal growth, and shear-induced aggregation. The high-dimensionality of the population balance model, however, leads to complicated controller design, which cannot be readily implemented in practice [22]. To circumvent these problems, the method of moments is used to derive the moment model that describes the dynamic evolution of the three leading moments of the crystal volume distribution in a crystallizer [59]. The moment model is closed according to the fact that crystal volume can be properly approximated by a lognormal distribution. Along with nonlinear algebraic equations that describe the dependence of crystal growth rates on temperature and protein solute concentration, and the energy and mass balance models that describe the changes of the temperature in the crystallizer and the solute concentration in the continuous phase, the moment model is employed to design a model predictive controller (MPC). The proposed model predictive control scheme is used to regulate the average shape of crystal aggregates to a desired set-point value with a low polydispersity.

Chapter 4 focuses on the modeling of the nucleation and crystal growth in a continuous crystallization process with a fines trap through kinetic Monte Carlo (kMC) simulation. The simulation of a fines trap is performed using a classification function which uses a selection curve for fines dissolution in the continuous crystallizer. In addition to the solute depletion and the temperature change in the continuous phase by crystallization, the interplay of inflow/outflow in the continuous crystallizer is included in the mass and energy balance equations. To deal with a real-time implementation issue of a controller based on the population balance equation (PBE), moment models are developed to describe the dominant dynamic behavior of the continuous crystallization with a fines trap. Subsequently, the three leading moments are used along with the balance equations in order to design a model predictive controller.

Chapter 5 focuses on modeling and control of a continuous PFC used to produce tetragonal hen egg white (HEW) lysozyme crystals and proposes an optimization-based control scheme to produce crystals with desired size and shape distributions in the presence of feed disturbances. Initially, we model a continuous plug flow crystallizer with five segments for the production of lysozyme crystals through kMC simulation methods described in [66] using the rate equations originally developed by [32]. A seeding strategy is used to decouple the nucleation process from the crystal growth process [78, 33, 9, 36]. Furthermore, an upper bound on the supersaturation level is imposed as a constraint so that the system is forced to stay in the metastable regime where the degree of primary nucleation is negligible [116]. Then, a PBE is presented to describe the spatio-temporal evolution of the crystal

volume distribution, and by applying the method of moments to the PBE, a reduced-order moments model is derived because kMC models are not immediately available in a closed form [26]. Together with the mass and energy balance equations, the leading moments are used for the estimation of the spatio-temporal evolution of the crystal size and shape distributions in an optimization problem. Specifically, the crystallizer jacket temperatures at each segment and the superficial flow velocity are chosen as the decision variables in the optimization problem and the objective function is defined by the sum of the squared deviations of the average crystal size and shape from desired set-points throughout the PFC. Subsequently, the dynamic model developed in Section 5.2 is used for the design of a feedforward control (FFC) strategy for the production of crystals with desired size and shape distributions that suppresses the undesired effects caused by disturbances [45]. Lastly, the simulation results are presented, followed by discussion and conclusions.

Chapter 6 considers a batch process for the crystallization of lysozyme crystals with uncertainties in the crystal growth rates in the directions of the (110) and (101) faces as well as in the solubility. The kMC simulation originally developed in the previous work [67] is regarded as a representation of the batch crystallization process and is used for the simulation of tetragonal HEW lysozyme crystals. In order to produce crystals with a desired shape distribution, the optimal jacket temperature profile is computed from a conventional MPC using a nominal reduced-order moment model and is applied to the first batch. After the first run, the post-batch measurements (e.g., the crystal size and shape distributions and number of crystals) are used to solve a multivariable optimization prob-

lem (MOP) off-line for the identification of the process model parameters used in the MPC for the crystal growth rates and solubility. Additionally, the real-time measurements for the solute concentration and temperature in the crystallizer from the previous batch are used in the form of constraints in the MOP to ensure the physical relevance of the process model parameters computed from the MOP. Along with the adapted process model parameters, the exponentially-weighted-moving-average (EWMA) scheme is used to deal with the remaining offset in the crystal shape values and thereby to compute a set of new optimal jacket temperatures. As a result, the production of crystals with a desired shape distribution is achieved by suppressing the inherent variations and process drift in the crystal growth rates and solubility. Lastly, the control performance of the proposed R2R-based MPC is compared with those of the conventional MPC and EWMA-type constant supersaturation control (CSC).

Chapter 7 focuses on developing a run-to-run model parameter estimation scheme based on moving horizon estimation concepts in order to model the batch-to-batch dynamics of the process drift and compute improved estimates of process model parameters, utilizing post-batch measurements from multiple batch runs. The moving horizon estimation (MHE) approach is employed because it provides improved parameter estimation and greater robustness to poor guesses for initial states because of its ability to incorporate physical constraints into the optimization problem used for parameter estimation. Specifically, the key elements of the proposed R2R model parameter estimation scheme based on MHE concepts are: First, the variation of the process model parameters from batch-to-batch is estimated

by solving an R2R model parameter estimation scheme using the post-batch measurements from multiple batch runs. Second, the batch-to-batch parametric drift is modeled through the use of a nonlinear function (e.g., second, third, fourth order polynomial), and used to update the parameters of the model predictive controller (MPC) model (used for real-time feedback control within each batch) to suppress the undesired effects of the process drift in the next batch run.

Chapter 8 focuses on further refining the approach proposed in Chapter 7 by relaxing the requirement of the in-batch and post-batch process measurements over multiple batch runs and developing the use of the proposed parametric drift detection and isolation (PDDI) scheme for the detection and isolation of the parametric drift. Thus, it becomes easier to precisely calculate the magnitude of the process drift because we determine the parameter(s) in which the parametric drift is located. First, a PDDI scheme is proposed for the purpose of the detection and isolation of parametric drifts introduced to a batch crystallization process. Then, a parametric drift-tolerant control scheme (PDTC) is proposed that uses the PDDI scheme to improve the model of the in-batch model predictive controller (MPC) to achieve the production of crystals with a desired shape distribution.

Chapter 9 focuses on the development of a parallelized multiscale, multidomain modeling scheme that reduces computation time requirements without compromising the accuracy of established chemical models. Specifically, the parallelized multiscale modeling strategy is executed according to the following three steps to model a multiscale batch crystallization process. First, the nucleation and crystal growth processes in a batch crys-

tallization system are decomposed into a collection of tasks, where each task represents the crystal growth of a nucleated crystal. Second, the tasks are assigned according to a modulus function where the number of crystal modules is equal to the number of processors available. Third, the message passing interface (MPI) settings that use the information passing between the processors is used to link the macroscopic model to the microscopic models. A series of results demonstrating the computational efficiency of the approach using the batch crystallization process multiscale model are presented.

Finally, Chapter 10 summarizes the contributions of this dissertation.

Chapter 2

Protein crystal shape and size control in batch crystallization

2.1 Introduction

This chapter focuses on a batch protein crystallization process used to produce tetragonal hen egg white lysozyme crystals, and presents a comparative study of the performance of a model predictive control strategy formulated to account for crystal shape and size distribution with conventional operating strategies used in industry, namely, constant temperature control (CTC) and constant supersaturation control (CSC). Initially, a comprehensive batch crystallizer model is presented involving a kMC simulation model which describes the nucleation and crystal growth via adsorption, desorption, and migration mechanisms on

the (110) and (101) faces and mass and energy balances for the continuous phase, which are developed to estimate the depletion in the protein solute concentration and the variation in the crystallizer temperature. Existing experimental data are used to calibrate the crystal growth rate and to develop an empirical expression for the nucleation rate. Simulation results demonstrate that the proposed MPC, which adjusts the crystallizer jacket temperature, is able to drive the crystal shape to a desired set-point value with a low polydispersity for crystal size compared to CTC and CSC operating policies. The proposed MPC determines the optimal operating conditions needed to obtain protein crystals of a desired shape and size distribution as it helps avoid the small crystal fines at the end of the batch run.

2.2 Modeling and simulation

As noted previously, we will use kMC simulations in order to model protein crystal growth. We employ the solid-on-solid lattice model, and the resulting protein crystal becomes very compact by avoiding voids and overhangs. For this work we will focus on square lattice models of length and width $N = 50$ sites with periodic boundary conditions. Previous work [60] demonstrates that no finite size effects were found among systems of sizes $N = 30$, $N = 60$, and $N = 120$ sites. The rate equations for adsorption, desorption, and migration mechanisms, which are similar to those of Durbin and Feher [32], are introduced in the following section and they are normalized over all of the lattice sites. Then, by generating random numbers, each event of our kMC simulation is chosen and executed based on the nomalized rates of the three microscopic phenomena. For further details including deriva-

tion of the rate equations, update of each lattice height, and execution of events, you may refer to our earlier work [93, 66].

2.2.1 Surface kinetics

As noted in the previous work by [93, 66], the following rate expressions on the crystal surface follow those of [32], which were further developed by [60] for migration events. Every lattice site is considered for attachment where the attachment rate is independent of the surface micro-configuration and is defined as

$$r_a = K^+(\Delta\mu) = K_0^+ \exp\frac{\Delta\mu}{k_B T}, \tag{2.1}$$

where K_0^+ is the attachment coefficient, k_B is the Boltzmann constant, T is the temperature in Kelvin, and $\Delta\mu = k_B T \ln(c/s)$, where c is the protein solute concentration, s is the protein solubility, and $\Delta\mu$ is the crystallization driving force. The protein solubility is dependent on temperature (°C) and defined for pH $= 4.5$ and 4%(w/v) NaCl by [12, 13] with the following third-order polynomial:

$$s(T) = 2.88\times10^{-4}T^3 - 1.65\times10^{-3}T^2 + 4.619\times10^{-2}T + 6.008\times10^{-1}, \tag{2.2}$$

where the solubility computed by Eq. 2.2 has an error of 6.8% [13]. The migration rate is modeled by [60] by introducing an additional term in the desorption rate which causes migration to have a higher rate compared to the desorption rate. The desorption and migration rates are defined in the following way:

$$r_d(i) = K_0^+ \exp\left(\frac{\phi}{k_B T} - i\frac{E_{pb}}{k_B T}\right), \tag{2.3}$$

$$r_m(i) = K_0^+ \exp\left(\frac{\phi}{k_B T} - i\frac{E_{pb}}{k_B T} + \frac{E_{pb}}{2k_B T}\right), \tag{2.4}$$

where E_{pb} is the average binding energy per bond, $E_b = iE_{pb}$ is the total binding energy, and ϕ is the binding energy per molecule of a fully occupied lattice where the binding energies cannot be evaluated by experiments [32, 35]. A set of values of E_{pb} and ϕ for the (110) and (101) faces is determined through open-loop kMC simulations until the difference between the calculated and the experimental growth rates becomes negligible [32]. In contrast to the attachment events, the detachment and migration events are dependent on the surface micro-configuration because they take into consideration the total binding energy determined by the number of nearest neighbors as is shown in Eqs. 2.3 and 2.4. Therefore, the growth rate cannot be computed by simply subtracting the detachment from the attachment rates.

In summary, the nature of lysozyme crystals is that only half the molecules on the (101) face have points of attachment for incoming molecules, whereas every molecule on the (110) face has dangling bond [32], and this is reflected in the present study by accepting 50% of adsorption events on the (101) face, compared to 100% of those on the (110) face in the kMC simulation. On the other hand, desorption and migration events are always accepted as long as there exists at least one available site. Specifically, an available migration site implies an adjacent site which is lower in height than the current lattice site where a lysozyme molecule can migrate. If there exist mutiple sites available for the migrating molecule, a site is chosen randomly [44].

2.2.2 Mass balance

In [116], the authors modeled the 3-D crystal growth by multiplying a crystal shape factor to the third moment of the crystal size distribution. However, the crystal shape factor is dependent on the temperature and the solute concentration and is not constant. In the present work, the mass balance is evaluated by considering the geometry of lysozyme crystals, and thus we are able to model the shape evolution of lysozymes more precisely by considering the crystal growth in the (110) and (101) directions independently. We model a lysozyme as a rectangular prism, as shown in Fig. 2.1, whose bottom is a square with a side of h_{110} and a height of h_{101}. In [32], the growth rates for the (110) and (101) faces, G_{110} and G_{101}, are respectively related to h_{110} and h_{101} as follows:

$$G_{101} = 0.45\frac{dh_{101}}{dt} \cong 0.45\frac{\Delta h_{101}}{\Delta t} \Rightarrow \quad \Delta h_{101} = 2.22\Delta t G_{101}, \tag{2.5}$$

$$G_{110} = 0.5\frac{dh_{110}}{dt} \cong 0.5\frac{\Delta h_{110}}{\Delta t} \Rightarrow \quad \Delta h_{110} = 2\Delta t G_{110}, \tag{2.6}$$

where $\Delta t = 1$ second. From Eqs. 2.5 and 2.6, the crystal size at time $j\Delta t$ can be written as

$$h_{101}(j\Delta t) = \sum_{k=1}^{j} \Delta h_{101}(k) + h_{101}(0) \quad h_{110}(j\Delta t) = \sum_{k=1}^{j} \Delta h_{110}(k) + h_{110}(0), \tag{2.7}$$

where $\Delta h_{101}(k) = h_{101}(k\Delta t) - h_{101}((k-1)\Delta t)$ and $\Delta h_{110}(k) = h_{110}(k\Delta t) - h_{110}((k-1)\Delta t)$ for $k = 1, 2, \cdots, j$. Also, the volume of the crystal with a side $h_{110}(t)$ and a height $h_{101}(t)$ at time t, $V_c(t)$, follows as

$$V_c(t) = h_{110}^2(t) h_{101}(t), \tag{2.8}$$

and thus the volume change between time $t - \Delta t$ and t, $\Delta V_c(t)$, can be written as

$$\Delta V_c(t) = V_c(t) - V_c(t - \Delta t). \tag{2.9}$$

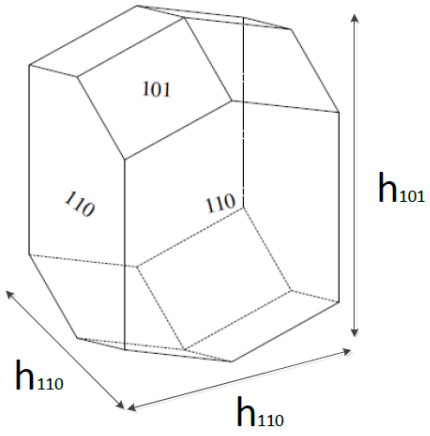

Figure 2.1: The geometry model for lysozyme crystals used in the present work.

The amount of the protein solute that is transported from the continuous phase to the crystal at time t can be calculated and takes the following form:

$$V\Delta c(t) = \Delta V_c(t)\rho_c N_c(t), \tag{2.10}$$

where V is the volume of the continuous phase (assuming the change in V is negligible), $N_c(t)$ is the number of crystals in batch at time t, ρ_c is the crystal density, and $\Delta c(t)$ is the change in the protein solute concentration between time $t-\Delta t$ and t where $\Delta c(t) = c(t) - c(t-\Delta t)$. We update the concentration after every $\Delta t(1.0 \text{ second})$. To integrate Eq. 2.10 into the controller, we estimate the total volume change of all the crystals (from i to $N_c(t)$) at time t as follows:

$$\sum_{i=1}^{N_c(t)} \Delta V_{c,i}(t) \approx N_c(t)\left\langle \Delta V_c(t)\right\rangle, \tag{2.11}$$

where the average change in volume over $N_c(t)$ crystals at time t, $\langle \Delta V_c(t)\rangle$, is approximated

by

$$\langle \Delta V_c(t) \rangle \approx \left[\langle h_{110}(t) \rangle^2 \langle h_{101}(t) \rangle - \langle h_{110}(t-\Delta t) \rangle^2 \langle h_{101}(t-\Delta t) \rangle \right]. \tag{2.12}$$

2.2.3 Energy balance

The energy balance of the batch crystallization process takes the following form [24]:

$$\frac{dT}{dt} = \frac{\rho_c \Delta H_c}{\rho C_p} \frac{d\varepsilon}{dt} - \frac{U_j A_j}{\rho C_p V} \left(T - T_j \right), \tag{2.13}$$

where $\varepsilon = \frac{V - V_c}{V} = 1 - \frac{V_c}{V}$ is the solids free volume fraction, T is the crystallizer temperature and T_j is the jacket temperature and the manipulated input. The process parameters used in the kMC simulations are given in Table 2.1. Taking the derivative of ε with respect to time and using Eq. 2.12, it follows that

$$\frac{dT}{dt} = -\frac{\rho_c \Delta H_c}{\rho C_p} \left(\frac{1}{V} \sum_{i=1}^{N_c(t)} \Delta V_{c,i}(t) \right) - \frac{U_j A_j}{\rho C_p V} \left(T - T_j \right), \tag{2.14}$$

since

$$\frac{d\varepsilon}{dt} = \frac{d}{dt} \left(1 - \frac{V_c}{V} \right) = -\frac{1}{V} \frac{dV_c}{dt} \cong -\frac{1}{V} \left(\sum_{i=1}^{N_c(t)} \Delta V_{c,i}(t) \right). \tag{2.15}$$

2.2.4 Simulation results with mass and energy balances

There are many simulation conditions that affect the crystal growth and the nucleation including temperature, pH, salt, and protein solute concentrations. Specifically, the supersaturation σ is defined as $\sigma = \ln(c/s)$ where c (mg/mL) is the protein solute concentration and s (mg/mL) is the solubility which is determined by Eq. 2.2 in terms of temperature (°C)

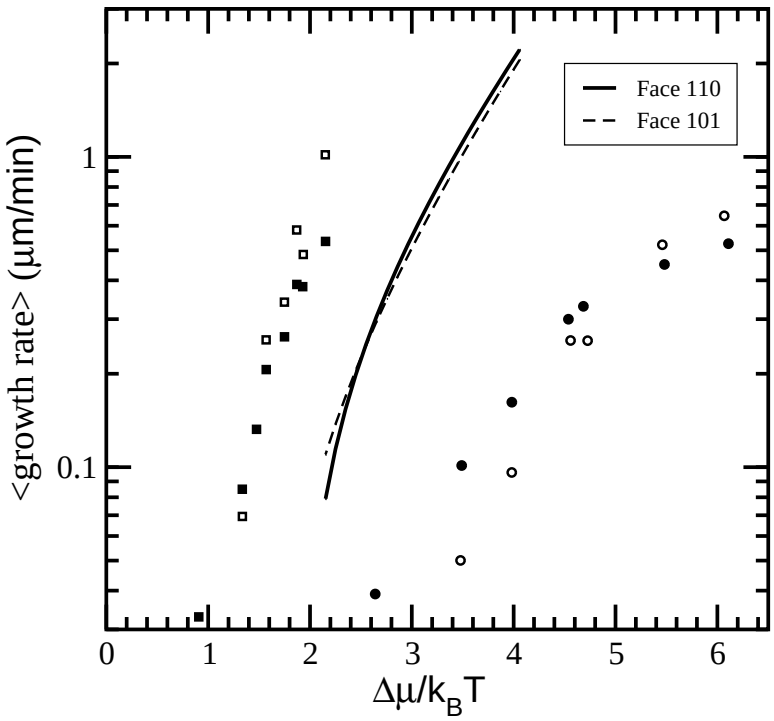

Figure 2.2: The expected growth rates versus the degree of supersaturation at $c = 45$ mg/mL and 4% NaCl are shown as the solid (110 face) and the dashed (101 face) lines. The (■) and (□) represent the measured experimental data for the 101 and 110 faces with 5% NaCl; (●)/(○) represent the measured experimental data with 3.5% NaCl; extracted from [31] at pH= 4.6.

ρ_c	crystal density	1400	mg/cm^3
ΔH_c	enthalpy of crystallization	44.5	kJ/kg
ρ	continuous phase solution density	1045	mg/cm^3
C_p	specific heat capacity	4.13	$kJ/K\ kg$
V	crystallizer volume	1	liter
A_j	surface area of heat transfer between crystallizer and jacket pipe	0.25	m^2
U_j	heat transfer coefficient between crystallizer and jacket pipe	1800	$kJ/m^2\ h\ K$

Table 2.1: Parameters for the batch crystallizer model of Eqs. 2.12 and 2.14

at pH = 4.5 and 4%(w/v) NaCl. In Fig. 2.2, crystals have been grown at supersaturation, $2.1 \leq \sigma \leq 3.95$, where $c = 45.0$ mg/mL. Through the trial and error procedure proposed in the previous work of our group [93, 66], our simulation results have been properly calibrated with the experimental result in Fig. 2.2 and a set of parameters was appropriately chosen to verify the crossover behavior of the growth rates of the (110) and (101) faces. The estimated simulation results at 4.0% NaCl are plotted against the experimental results at 3.5% and 5.0% NaCl from [40], in Fig. 2.2. The parameters for the kMC simulation in Figs. 2.2 to 2.9 are listed in Table 2.2.

In order to complete the kMC simulation model, mass and energy balances are developed in Sections 2.2.2 and 2.2.3 to estimate the depletion in the protein solute concentration and the drop in the crystallizer temperature due to the heat of fusion by crystallization. The evolution of the solute concentration, the supersaturation, and the temperature in the kMC

Face	E_{pb}/k_B	ϕ/k_B
(110)	1077.26 K	227.10 K
(101)	800.66 K	241.65 K

Table 2.2: Parameters for faces (110) and (101) at 45 mg/mL NaCl and pH= 4.5 at $T =$ 18°C. Additionally, $K_o^+ = 0.211$ seconds^{-1}.

simulation is shown in Fig. 2.3 for the initial solute concentration at 44 mg/mL and three different initial temperatures of 6, 10, and 18°C. It is observed that the solute concentration decreases more rapidly as the batch process proceeds further because, for an equivalent growth rate, larger crystals require more deposition compared to small crystals. The temperature of the crystallizer is also affected by the crystallization due to the heat of fusion in the crystallization process. It is verified from Fig. 2.3(a) that at a low initial temperature (i.e., low solubility and thus a high supersaturation level), crystals grow faster which results in a significant drop in the supersaturation level because of the loss in the protein solute for the continuous phase. We note that the drops in the temperature and the supersaturation depend on the length of batch process time and the size of the crystallizer.

For comparison purposes, kMC simulations are run under existing control strategies, a constant temperature control (CTC) and a constant supersaturation control (CSC). Under CTC, the decrease in the solute concentration throughout the entire batch process immediately leads to the drop in the supersaturation level since temperature is constant, and thus less nucleation and lower growth rates are observed. Under CSC, in order to main-

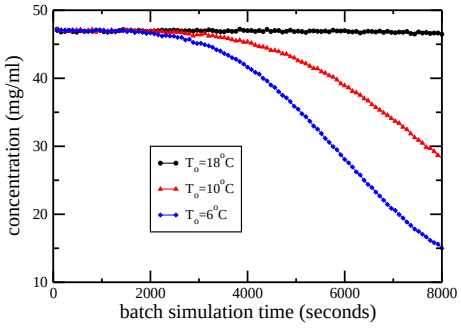

(a) concentration

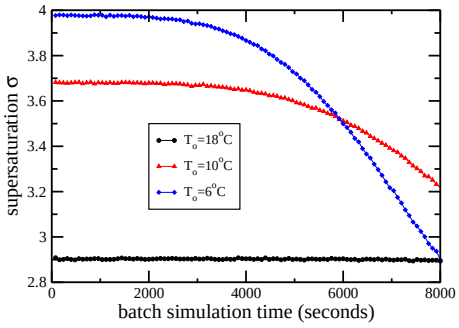

(b) supersaturation

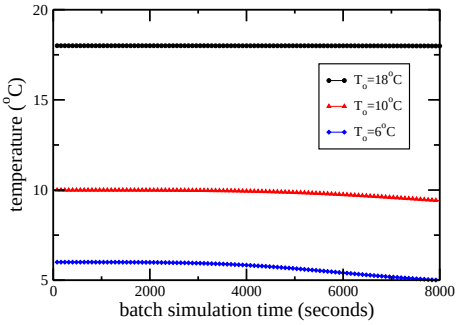

(c) temperature

Figure 2.3: Open-loop simulation results of solute concentration, supersaturation, and temperature for tetragonal lysozyme protein crystals at pH = 4.5. The data from the open-loop kMC simulations show the depletion in the protein solute concentration and the drop in the temperature due to the crystallization process. The initial protein concentration is 44 mg/mL and the different initial temperature values (6, 10 and 18°C) are used to verify the effect of the crystal growth.

tain a constant supersaturation level, the depletion in the solute concentration results in the decline in the temperature. Since there is a lower limit on the temperature, if the solute concentration drops too much, a method of simply lowering temperature cannot maintain the supersaturation level at a desired value (i.e., the controller is not robust). This problem steers us to design a new controller, which is presented in the next section in order to provide optimality as well as robustness in batch processes. Specifically, the crystal shape distribution of the final crystals can be driven to a desired range by the controller design described in the following section.

2.3 Model predictive control of crystal size and shape

In the kMC simulations, crystal nucleation and growth are considered along with mass and energy balances via molecular attachment, detachment, and migration events. Since the role of mass and energy balances becomes significant as crystal size increases, the balance equations have been considered in the controller design. The nucleation and the crystal growth rates have been manipulated by changing the temperature for a given concentration. In Table 2.2, parameters of crystal growth conditions (e.g., E_{pb}/k_B and ϕ/k_B) for kMC simulations are chosen to show the experimentally observed cross-over behavior in the crystal growth rates between the (110) and (101) faces [31, 32]. In addition to the nonlinear models described in Fig. 2.4, the mass and energy balances introduced play a key role in describing the behavior of the system dynamics such as the depletion in the solute concentration and the heat removal in the crystallizer due to the crystallization process. Then,

based on these equations, a model predictive controller is designed to produce crystals with the desired shape and size through the manipulation of the jacket temperature. MPC resolves the drawbacks of the classical control schemes such as proportional (P) control, as it explicitly takes into consideration the input/state constraints, optimality issues, the nature of the nonlinearity in the nonlinear growth rate, and the balance equations. A dynamic open-loop optimization method may be used. However, open-loop optimizations are not robust with respect to model imperfections and uncertainty in the protein concentration and the batch crystallizer.

2.3.1 The population balance equation for protein crystallization

A population balance equation (PBE) can describe the evolution of the particle growth in a batch protein crystallization with respect to its size and shape. To describe the behavior of the crystal size and shape distributions for the crystals nucleated at different times in a crystallization process, it is necessary to know the nucleation rate.

$$\frac{\partial n(h_{110},h_{101},t)}{\partial t}+G_{110}(T,c)\frac{\partial n(h_{110},h_{101},t)}{\partial h_{110}}+G_{101}(T,c)\frac{\partial n(h_{110},h_{101},t)}{\partial h_{101}}=B(T,c)\delta(h_{110},h_{101}). \tag{2.16}$$

In the kMC simulations, the characteristic crystal lengths are h_{110} and h_{101}, and $n(h_{110},h_{101},t)$ is the number of crystals of heights h_{110} and h_{101} for the (110) and (101) faces per unit volume, respectively, at time t. The nucleation rate is denoted as $B(T,c)\delta(h_{110},h_{101})$ and is a function of temperature, T, and protein solute concentration, c and the function $\delta(h_{110},h_{101})$ has a nonzero value only at $h_{110}=h_{101}=0$. Owing to the depen-

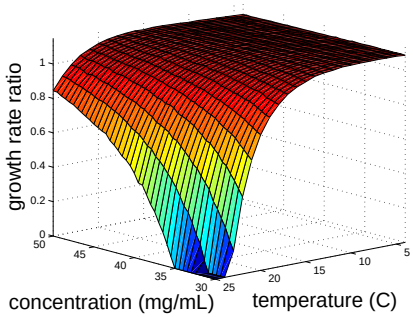

(a) Growth rate ratio

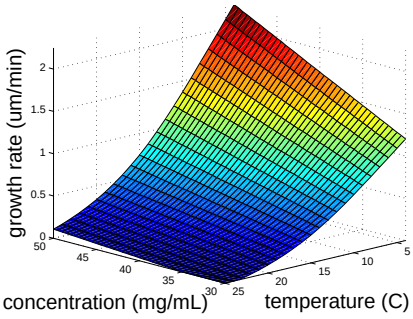

(b) Growth rate of the (110) face

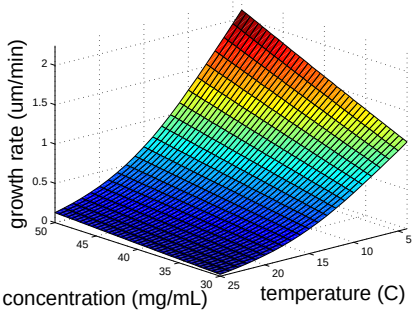

(c) Growth rate of the (101) face

Figure 2.4: Plots of the growth rate data obtained for the (110) face, the (101) face, and the growth rate ratio between the (110) and (101) faces for tetragonal lysozyme protein crystals at pH $= 4.5$. The data from the open-loop kMC simulations are plotted to demonstrate the effect of temperature and concentration variations on growth rates. Protein concentration and temperature range from 30 to 50 mg$/$mL and 4 to 25°C, respectively.

dence of detachment and migration rates on the surface configuration, [93] suggested kMC simulations to compute the net, steady-state growth rate as a function of temperature and protein concentration in the continuous phase. Therefore the growth rates for the (110) and (101) faces, $G_{110}(T,c)$ and $G_{101}(T,c)$, are expressed as functions of temperature, T, and protein solute concentration, c. Then we define a growth rate ratio, $\alpha(T,c) = h_{110}/h_{101} = G_{110}(T,c)/G_{101}(T,c)$, where the growth rate ratio is equal to the aspect size ratio at the steady-state and the growth rate ratio is obtained from kMC simulation. Then Eq. 2.16 can be written as follows,

$$\frac{\partial n(h_{110},h_{101},t)}{\partial t} + G_{110}(T,c)\frac{\partial n(h_{110},h_{101},t)}{\partial h_{110}} + G_{101}(T,c)\frac{\partial n(h_{110},h_{101},t)}{\partial h_{110}}\frac{\partial h_{110}}{\partial h_{101}} = B(T,c)\delta(h_{110},h_{101}), \tag{2.17}$$

where $\frac{\partial h_{110}}{\partial h_{101}} = \alpha(T,c)$ and substituting this into the above we obtain,

$$\frac{\partial n(h_{110},h_{101},t)}{\partial t} + \left(G_{110}(T,c) + \alpha(T,c)G_{101}(T,c)\right)\frac{\partial n(h_{110},h_{101},t)}{\partial h_{110}} = B(T,c)\delta(h_{110},h_{101}). \tag{2.18}$$

In the present work we assume that crystals are nucleated at negligibly small size (i.e., $h_{110} = h_{101} = 0$), and the number of nuclei newly formed at time t is denoted as $n(0,0,t)$. This assumption can be justified as follows. Initially, an HEW lysozyme nucleus is formed through the aggregation of three to four lysozyme molecules, and its size is relatively infinitesimal compared to the final crystal size which is on the order of several hundred micrometers [92]. Additionally, a nuclei cannot be detected until its size reaches the resolution limit, ~ 0.5 μm [120]. Because $B(T,c)\delta(h_{110},h_{101})$ acts only at $h_{110} = h_{101} = 0$, and the nucleus size in the (110) and (101) directions is uniformly negligible, for the simplicity of

calculations, we can assume that $B(T,c)\delta(h_{110},h_{101}) \cong B(T,C)\delta(h_{110})$. In other words, the crystal sizes in the directions of the (110) and (101) faces are on the same order of magnitude. As is pointed out by [83], Eq. 2.18 can be written replacing $B(T,c)\delta(h_{110},h_{101})$ with an appropriate boundary condition. Integrating Eq. 2.18 over h_{110} from 0^- to 0^+ gives,

$$(G_{110}(T,c)+\alpha(T,c)G_{101}(T,c))\int_{0^-}^{0^+}\frac{\partial n(h_{110},h_{101},t)}{\partial h_{110}}dh_{110}=B(T,c), \tag{2.19}$$

because,

$$\int_{0^-}^{0^+}B(T,c)\delta(h_{110})dh_{110}=B(T,c),$$

and,

$$\int_{0^-}^{0^+}\frac{\partial n(h_{110},h_{101},t)}{\partial t}dh_{110}=0.$$

It also follows that,

$$n(h_{110},h_{101},t)=0 \text{ at } h_{110}=h_{101}=0^- \qquad n(h_{110},h_{101},t)=n(0,0,t) \text{ at } h_{110}=h_{101}=0^+,$$

assuming all nuclei form with size $h_{110}=h_{101}=0$. Then Eq. 2.19 can be reduced to the following:

$$(G_{110}(T,c)+\alpha(T,c)G_{101}(T,c))\,n(0,0,t)=B(T,c). \tag{2.20}$$

Therefore the desired boundary condition is

$$n(0,0,t)=\frac{B(T,c)}{(G_{110}(T,c)+\alpha(T,c)G_{101}(T,c))} \qquad \text{at } h_{110}=h_{101}=0 \tag{2.21}$$

and with this boundary condition the resulting population balance of Eq. 2.16 has the

following form:

$$\begin{aligned}
&\frac{\partial n(h_{110},h_{101},t)}{\partial t} + G_{110}(T,c)\frac{\partial n(h_{110},h_{101},t)}{\partial h_{110}} + G_{101}(T,c)\frac{\partial n(h_{110},h_{101},t)}{\partial h_{101}} = 0 \\
&\alpha(T,c) = f_G(T,c) \\
&G_{110}(T,c) = f_{110}(T,c,t) \\
&G_{101}(T,c) = f_{101}(T,c,t) \\
&B(T,c) = f_{nucleation}(\sigma(t)) \\
&n(0,0,t) = \frac{B(T,c)}{(G_{110}(T,c) + \alpha(T,c)G_{101}(T,c))} \qquad \text{at } h_{110} = h_{101} = 0
\end{aligned} \tag{2.22}$$

where $G_{110}(T,C)$ and $G_{101}(T,C)$ are the growth rates for the (110) and (101) faces, and $\alpha(T,c) = \frac{G_{110}(T,C)}{G_{101}(T,C)}$ is the growth rate ratio. The nonlinear equations f_G, f_{110}, and f_{101} are written in terms of their dependencies on temperature, solute concentration and time. In this work, it is assumed that the nucleation rate on a surface is negligible. The number of crystals nucleated at time t is obtained from [41] and the nucleation rate, $f_{nucleation}(0,0,t)(\sigma)$, at time t (with units $[cm^{-3} \cdot \sec^{-1}]$), was obtained from [41] at pH = 4.5 and 4%(w/v) NaCl:

$$f_{nucleation}(0,0,t)(\sigma) = \begin{cases} 0.041\sigma + 0.063 & \text{for} \quad \sigma \geq 3.11 \\ 8.0 \times 10^{-8} \exp(4.725\sigma) & \text{for} \quad \sigma < 3.11 \end{cases} \tag{2.23}$$

We execute multiple kMC simulations for crystals nucleated at different times which is considered to be comparable to solving Eq. 2.22 directly. Theoretically speaking, it requires an infinite number of lattice sites in the kMC simulation to completely regenerate the deterministic PBE described by Eq. 2.22. From a practical standpoint, however, a kMC simulation with a finite number of lattice sites is used for the simulation of the crystallization process which may lead to a mismatch between the PBE and the kMC simulations.

Here we assume that the number of lattice sites being used in the kMC simulation is sufficient to make the mismatch negligible since, as described previously, no size effects were found in the systems with more lattice sites.

2.3.2 Model predictive control formulation

We consider the control of the shape and size of crystals nucleated at different times along with mass and energy balances as the batch crystallization process proceeds by using a Model Predictive Control (MPC) design. The control objective is to minimize the expected value of the growth rate ratio, $\langle\alpha\rangle$=$\langle G_{110}/G_{101}\rangle$. In order to prevent the formation of many small crystal fines at the end of the batch run, a desired minimum crystal size is considered in the cost function of the MPC formulation. Though various factors affect the evolution of the crystal morphology and the growth rate during the crystallization process [1, 90, 129, 86, 82], the jacket temperature is used as the manipulated input. The solute concentration is continuously measured, assuming all other parameters remain constant for the closed-loop simulations (e.g., pH, NaCl concentration, buffer concentration).

We note that the proposed modeling and control methods can be extended to the case of multiple manipulated variables. A number of practical considerations, including the mass and energy balances in Eqs. 2.12 and 2.14, and additional constraints are considered in the control problem. First, a constraint on the range of the jacket temperature $\left(4^{\circ}\text{C} \leq T_j \leq 25^{\circ}\text{C}\right)$ is imposed to ensure that the protein is not damaged. Second, there is a constraint of 2°C/min on the rate of change of the jacket temperature because of actuator

limitations. Another constraint limits the number of crystals nucleated during the second half of the batch run to avoid small crystal fines at the end of the batch run. The control action (jacket temperature) at time t is obtained by solving a finite-dimensional optimization problem in a receding horizon fashion. The cost function in the optimal control problem includes a penalty on the deviation of $\langle \alpha \rangle$ from its desired crystal shape. An additional penalty cost is included to account for the negative deviation of the crystal size when its size is less than the desired minimum. In the proposed MPC, crystal growth and nucleation are estimated by using the nonlinear equations, Fig. 2.4, and Eq. 2.23, respectively. The

proposed MPC formulation is presented as follows:

$$
\begin{aligned}
&\underset{T_{j,1},\ldots,T_{j,i},\ldots,T_{j,p}}{\textit{minimize}} \quad \sum_{i=1}^{p} F_{\langle\alpha\rangle,i} + F_{h_{110},i} + F_{h_{101},i} \\
&\text{subject to} \quad F_{\langle\alpha\rangle,i} = \left(\langle\alpha\rangle - \alpha_{\text{set}}\right)^2 \\
&\qquad F_{h_j,i} = \begin{cases} \frac{h_{j,min} - \langle h_j(t_i)\rangle}{h_{j,min}} & \text{for} \quad \langle h_j(t_i)\rangle < h_{j,min} \\ 0 & \text{for} \quad \langle h_j(t_i)\rangle \geq h_{j,min} \end{cases} \\
&\qquad G_i = f_r(T,C,t_i) \qquad G_j(t_i) = f_j(T,C,t_i) \\
&\qquad T_{\min} \leq T_{j,i} \leq T_{\max} \qquad \left|\frac{T_{j,i+1} - T_{j,i}}{\Delta}\right| \leq R_T \\
&\qquad \frac{dT}{dt} = -\frac{\rho_c \Delta H_c}{\rho C_p}\left(\frac{1}{V}\sum_{i=1}^{N_c(t)} \Delta V_{c,i}\right) - \frac{U_j A_j}{\rho C_p V}\left(T - T_{j,i}\right) \\
&\qquad \Delta c(t) = \frac{\rho_c}{V}\sum_{i=1}^{N_c(t)} \Delta V_{c,i} \\
&\qquad n(0,0,t) \leq n_{\text{limit}} \qquad \forall t \geq t_f/2 \\
&\qquad \langle h_j(t_i)\rangle = \frac{\langle h_j(t_{i-1})\rangle n(h_{110},h_{101},t_{i-1})}{n(h_{110},h_{101},t_i)} + R_j(t_{i-1})\Delta \\
&\qquad n(h_{110},h_{101},t_i) = n(h_{110},h_{101},t_{i-1}) + n(0,0,t_{i-1}) \qquad \forall i \\
&\qquad i = 1,2,\ldots,p \qquad j \in \{110,101\}
\end{aligned}
\tag{2.24}
$$

where t is the current time, t_i, $i = 1,2,\ldots,p$, is the time of the i^{th} prediction step ($t_i = t + i\Delta$), t_f is the total time of the batch simulation, $F_{\langle\alpha\rangle,i}$ is the cost function expressing the deviation of $\langle\alpha\rangle$ from its set-point, α_{set}, $F_{h_{110},i}$ and $F_{h_{101},i}$ are cost functions written as a penalty on the negative deviation of $\langle h_{110}\rangle$ and $\langle h_{101}\rangle$ from their desired values $h_{110,min}$ and $h_{101,min}$ at time t_i, p is the number of prediction steps, $p\Delta$ is the specified prediction horizon, $T_{j,i}, i = 1,2,\ldots,p$, is the jacket temperature at the i^{th} time step $\left(T_{j,i} = T_j(t + i\Delta)\right)$, $T_{\min}$ and $T_{\max}$ are

the lower and upper bounds on the jacket temperature, respectively, R_T is the limit on the rate of change of the jacket temperature, and n_{limit} limits the number of crystals nucleated during the latter half of the simulation time. The number of crystals, $n(h_{110}, h_{101}, t_i)$, and the average height of crystal face j, $\langle h_j(t_i) \rangle$, at time t_i are updated at every sampling time through the recursive equations (cf. Eq. 2.24). The set of optimal jacket temperatures, $(T_{j,1}, T_{j,2}, \ldots, T_{j,p})$, is obtained by solving the multi-variable optimization problem of Eq. 2.24, and only the first value of the optimal jacket temperature trajectory, $T_{j,1}$, is applied to the protein crystallization process until the next sampling time. Then, a new measurement of protein concentration in the continuous phase is received from the kMC simulation, and the MPC problem of Eq. 2.24 is re-solved for the computation of the next optimal input trajectory. In a previous work [116], empirical expressions were used to simulate the crystal growth and nucleation. In the present work, however, the kMC simulations are executed based on the rate equations described previously to simulate the crystallization process to a higher degree of accuracy. Furthermore, the uncertainty in the system and the model mismatch will be taken into account in the protein concentration variations. For further results including robust control of crystallization systems and model predictive control, readers may refer to [115, 23].

2.4 Batch crystallization under closed-loop operation

In this section, the proposed model predictive controller of Eq. 2.24 is solved via a local constrained minimization algorithm using the nonlinear algebraic models described previ-

ously (cf. Fig. 2.4) which show the solute concentration and temperature dependencies of the crystal growth rates and growth rate ratio, respectively. At each sampling time (1 second), the optimal jacket temperature, obtained by solving the optimization problem of Eq. 2.24, is applied to the closed-loop system until the next sampling time.

In this work, the solute concentration randomly fluctuates following the Gaussian distribution given by Eq. 2.25 below to simulate the uncertainty in the system at pH 4.5 and 4.0% NaCl, i.e.,

$$\langle C(t)\rangle = C_n, \qquad \langle C(t)C(t')\rangle = \sigma_n^2 C_n^2, \tag{2.25}$$

where C_n is the nominal concentration of the system and σ_n^2 shows how far a set of measured concentrations deviates from its nominal value. We also note that the concentration variation affects the attachment rate (cf. Eq. 2.1). For all closed-loop simulations, the nominal concentration is 44 mg/mL, and the deviation, σ_n, is equal to 1.5%. The maximum rate of change of the jacket temperature is 2°C/min. The volume of the crystallizer is 5.0 L. We note that we have taken into account the following heuristic: In the beginning, the crystallizer operates in the labile zone where the supersaturation level is so high that both nucleation and crystal growth occur. Then the crystallizer operates in the metastable region which is a relatively high supersaturation region where nucleation rarely occurs, but the crystal growth still occurs. This will help prevent the small crystal fines from appearing at the end of the batch run, and this heuristic is taken into consideration in this work as one of the constraints restricting the number of crystals nucleated during the latter half of the simulation time, $n_{\text{limit}} = 500$. Since the MPC formulation uses steady-state growth rates

(cf. Fig. 2.4(b) and 2.4(c)) which assumes that it is a slowly varying process, the number of prediction steps is set to be $p = 1$. The time interval between the two sampling times is 1 second. The prediction horizon of each step is fixed at $p\Delta = 1$ second. For the purpose of simulation, the solute concentration is set to be fluctuating every 1 second with the nominal value $C_n(t)$ at time t. The computation time that is required to solve the optimization problem with the current available computing power is negligible with respect to the sampling time interval. The closed-loop simulation duration is $t_f = 8000$ seconds.

In the closed-loop simulations, the control objective is to regulate the expected growth rate ratio to the desired set-point values, $\alpha_{\text{set}} = 0.85$ and $\alpha_{\text{set}} = 1.11$. We chose these two values to represent two different crystal morphologies available with lysozyme crystals. For the former set-point value, its protein crystal shape is slightly elongated along the (101) direction, while it is more equidimensional for the latter case. Thus, the cost function of this problem contains a penalty on the deviation of the expected growth rate ratio from the desired shape.

We compare the performance of the proposed MPC to that of two other conventional control strategies, constant temperature control (CTC) and constant supersaturation control (CSC). Compared to MPC, the crystal shape distribution as well as the solute concentration, the temperature, and the supersaturation propagate in very different manners under CTC and CSC. Under CTC, the crystallizer temperature is maintained constant which results in a constant solubility during the batch run, and thus the depletion in the solute concentration eventually leads to the decrease of supersaturation. Under CSC, however, the CSC scheme

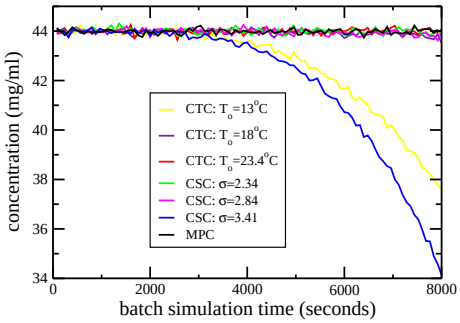

(a) concentration vs time

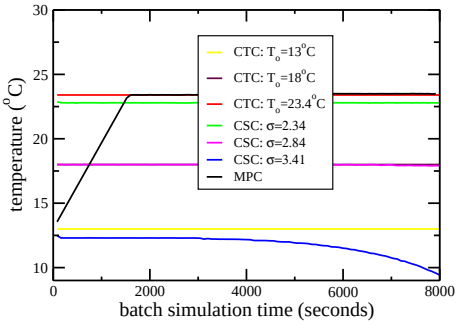

(b) temperature vs time

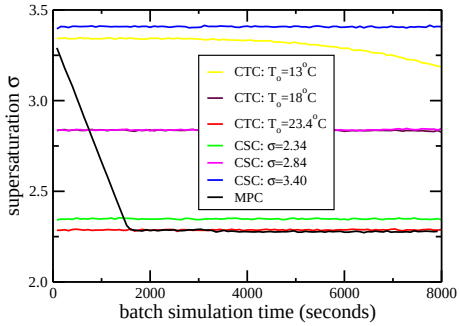

(c) supersaturation σ vs time

Figure 2.5: The propagation of temperature, concentration, and supersaturation with time during the batch run under closed-loop operation at different initial temperature values and supersaturation levels, including MPC aiming at growth rate ratio set-point value $\alpha_{\text{set}} = 0.85$.

tries to maintain a constant supersaturation throughout the batch run, and the jacket temperature is constantly decreased for the duration of the batch run to possibly maintain constant supersaturation despite the falling concentration levels. Under CSC, therefore, the growth rate, which only depends on the supersaturation itself, remains constant during the batch run. The nucleation rate also stays constant under CSC since it is only dependent on the supersaturation. In the cases of MPC and CTC, however, a biased nucleation occurs (e.g., 50% of crystals nucleate in the first 10% of the entire batch simulation time) throughout the batch run due to the change in the supersaturation because of the depletion in the solute concentration or the drop in the crystallizer temperature. We note that if the temperature reaches its optimal state relatively late in the batch run, the biased nucleation could result in a broader crystal shape distribution from a desired set-point value compared to that of the operation under CSC.

For the lower growth rate ratio set-point value, $\alpha_{\text{set}} = 0.85$, the results of the closed-loop simulations are shown in Figs. 2.5, 2.6, and 2.7 for the crystallizer temperature, the solute concentration, the supersaturation, the nucleation time distribution, and the crystal shape distribution at the end of the batch run. Specifically, Fig. 2.5 shows results for batch runs under three different control strategies (i.e., MPC, CTC at three different temperature values, and CSC at three different supersaturation values). Note that we chose three values for the initial temperature for the simulations under CTC at $T_o = 13^\circ$C, $T_o = 18^\circ$C, and $T_o = 23.4^\circ$C, which are two extremes and one in the middle of the temperature trajectory computed by the MPC executed at $c = 44$ mg/mL and $T_o = 13^\circ$C. The three values for

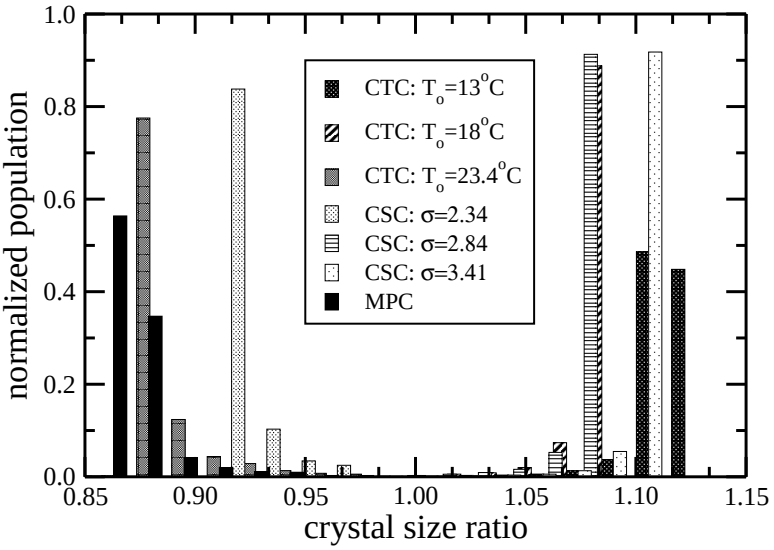

Figure 2.6: The final crystal shape distribution at the end of the batch simulation under different closed-loop operations under CTC and CSC at different initial temperature values and supersaturation levels for CTC and CSC, respectively, and MPC for the growth rate ratio set-point value, $\alpha_{\text{set}} = 0.85$. It is noted that the crystal shape distribution is a dimensionless variable and is normalized over the entire population so that summing over all histograms will add up to 1 for each control strategy.

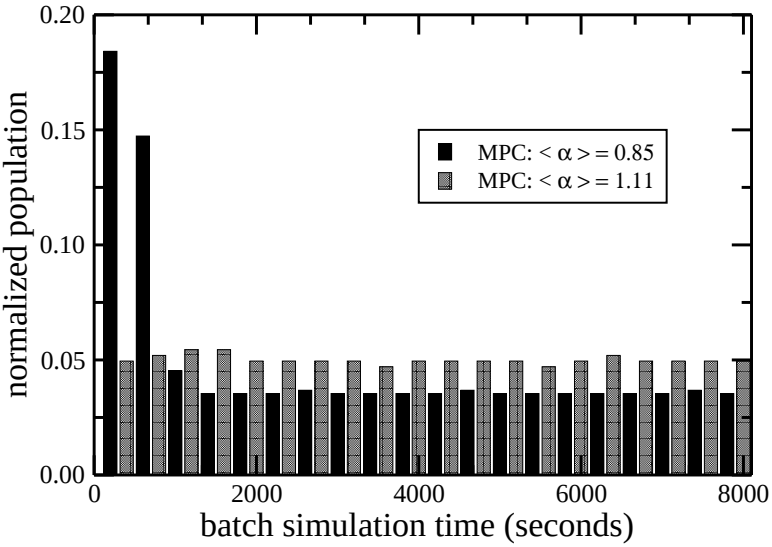

Figure 2.7: Profiles of nucleated crystals with time during the batch run under closed-loop operation using MPC aiming for different growth rate ratio set-point values, $\alpha_{\text{set}} = 0.85$ and $\alpha_{\text{set}} = 1.11$. It is noted that the nucleation time distribution is a dimensionless variable and is normalized over the entire crystal population so that summing over all histogram bars, for each different set of growth rate ratios, will add up to one.

the supersaturation were chosen in the same manner for the simulations under CSC at $\sigma = 2.34$, $\sigma = 2.84$, and $\sigma = 3.41$ respectively. As is pointed out in Figs. 2.2 and 2.4, two different sets of the solute concentration and the temperature may result in the same supersaturation σ, and supersaturation is the main driving force for the crystal growth and nucleation. Therefore the evolution of supersaturation can be used with the nucleation time distribution, Fig. 2.7, to explain the behavior of the crystal shape distribution under MPC for different set-point values.

It has been shown in our recent work [66] that the final crystal shape distribution is

very narrow when the initial temperature is close to the optimal temperature. Additionally, depending on the desired crystal morphology and the initial temperature of the crystallizer, it takes a different amount of time for the temperature to reach the desired set-point value. Specifically, in Fig. 2.6, for the lower desired crystal growth rate ratio, $\alpha_{\text{set}} = 0.85$, the initial temperature of the crystallizer was chosen to be $T_o = 13^\circ$C, although it is not very close to the optimal temperature $\sim$23.4°C. Therefore, starting from a high initial temperature is recommended, because the system reaches its optimal temperature faster which enables the crystals to uniformly nucleate along the batch and they experience the optimal temperature from the beginning. Note that the proposed MPC with a relatively low initial temperature still outperforms other conventional polices as is seen in Fig. 2.6, and the performance of the MPC can be further improved by using a higher initial temperature. Fig. 2.5(a) displays that the solute concentration has depleted significantly for the simulations under the CSC at $\sigma = 3.41$ and the CTC at $T_o = 13^\circ$C, which both result in the high supersaturation level and hence high growth and nucleation rates. On the other hand, the proposed MPC, CTC at the relatively high temperatures $T_o = 18^\circ$C and $T_o = 23.4^\circ$C, and the CSC at the low supersaturation levels $\sigma = 2.34$ and $\sigma = 2.84$ show no significant changes in their solute concentration because of a low growth rate resulting from a low supersaturation level. We note that in Fig. 2.5, the solute concentration, the supersaturation, and the temperature with time under CTC at $T_o = 18^\circ$C are very similar to those of CSC at $\sigma = 2.84$. The resulting crystal size and shape distributions are very similar as is shown in Fig. 2.6 and Table 2.3, which implies that CTC and CSC policies result in a similar performance when their

growth and nucleation rates are low and their initial conditions are identical. Due to the negligible depletion in the solute concentration, the black solid line in Fig. 2.5(b) shows that the MPC computes a jacket temperature first monotonically increasing to the optimal value and then staying constant. Usually for a low growth rate ratio, the optimal temperature is high and the system is usually very sensitive to the solute concentration changes as is shown in Fig. 2.4. Specifically, the growth rate ratio declines drastically at high temperature, where the desired low growth rate ratio is available, in response to a small variation in the concentration.

In Fig. 2.7, for $\alpha_{\text{set}} = 0.85$, the optimal temperature is $\sim$23.4°C and high initial supersaturation levels in the earlier stage result in the nucleation of 34% of the total crystals within the first 500 seconds of the batch run. In this case, owing to the favored nucleation in the beginning, the MPC results in a similar crystal shape distribution compared to that of CTC at $T_o = 23.4$°C where the constant optimal temperature is maintained for the crystallizer over the entire batch. However, the final crystal shape distribution for the MPC in Fig. 2.6 can be very narrow and even closer to the desired values by adjusting the initial temperature closer to the optimal temperature, from $T_o = 13$°C to $T_o = 23.4$°C. Evaluating the sensitivity of the controller design with respect to the initial temperature of crystallizer has been presented more rigorously in our recent work [66].

In Table 2.3, the characteristics of crystal size along the (110) direction of the final crystals at the end of the batch run are compared under different control strategies, including the expected crystal size along the (110) direction, $\langle h_{110} \rangle$, and r_{10}, r_{50}, r_{90}, which are the 10%,

Control strategy	$\langle h_{110} \rangle$	r_{10}	r_{50}	r_{90}	span
MPC	11.83	3.15	12.56	18.82	1.25
CTC: T=13°C	58.41	11.29	57.79	106.68	1.65
CTC: T=18°C	29.78	6.52	29.73	52.96	1.56
CTC: T=23.4°C	3.39	0.92	3.39	5.87	1.46
CSC: $\sigma = 2.34$	3.96	0.95	3.93	6.91	1.52
CSC: $\sigma = 2.84$	29.75	6.50	29.63	52.79	1.56
CSC: $\sigma = 3.41$	67.98	14.19	67.94	121.79	1.58

Table 2.3: Comparison between the simulation results for the crystal size in the (110) direction under five different control strategies for the desired growth rate ratio of $\alpha_{\text{set}} = 0.85$.

50%, and 90% population fractions of the crystal size distribution for h_{110}, respectively, representing the percentage of the population with a crystal size less than that value. Only the crystal size for the (110) direction, h_{110}, is included since h_{110} and h_{101} are on the same order of magnitude. This table also includes the span which is defined as $(r_{90} - r_{10})/r_{50}$, and it is a widely used characteristic in the pharmaceutical industry. Comparing the results of the five control strategies listed in Table 2.3, it is clear that the MPC is able to increase the crystal size and achieve a low polydispersity while it also drives the expected crystal shape, $\langle \alpha \rangle$, to the desired value as in Fig. 2.6. Although the CTC at $T_o = 23.4$°C results in a similar $\langle \alpha \rangle$ to that of MPC, it leads to much smaller crystal sizes with a high polydispersity, when neither of these attributes is desirable. The very low span value for the

MPC indicates a narrow crystal size distribution (a low polydispersity) which is obtained by properly dealing with the biased nucleation rate described previously. Again, the controller perfomance can be improved if we choose an initial temperature as close as possible to the optimal temperature.

In contrast to the results when the set-point is $\alpha_{\text{set}} = 0.85$, when the set-point is the higher desired crystal growth rate ratio, $\alpha_{\text{set}} = 1.11$, changes in the solute concentration are more significant because of the high growth and nucleation rates. Specifically, the solid black line in Fig. 2.8 shows that the crystallizer temperature manipulated by the proposed MPC results in the supersaturation first increasing due to a drastic drop in the crystallizer temperature, then decreasing almost to the lowest level, which is then followed by a series of rises and falls until the end of the batch run. Since the control objective is to obtain a very narrow final crystal shape distribution at a desired set-point value, the results can be understood as follows: after a drastic initial rise in the supersaturation (from σ=3.4 to σ=3.87), which does not significantly increase the number of crystals nucleated because a small increase in the supersaturation level does not result in a substantial increase in the nucleation rate for $\sigma > 3.11$ as is shown in Eq. 2.23, the supersaturation drops to a low level in order to minimize the nucleation rate as the growth condition is changing from the labile to the metastable zone. Thereafter, the following series of rises and falls is attributed to the optimal jacket temperature trajectory computed by the proposed MPC to bring the system to the vicinity of optimal growth conditions for a desired growth rate ratio while dealing with the solute concentration reduction from 44 to 35 mg/ml in Figs. 2.8(a)–2.8(c). Note

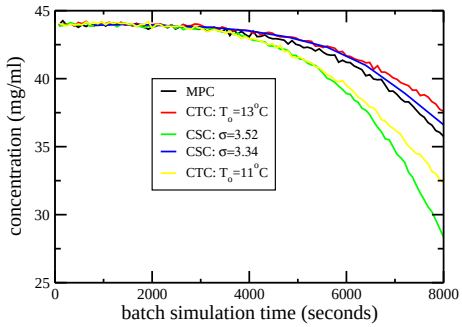

(a) concentration vs time

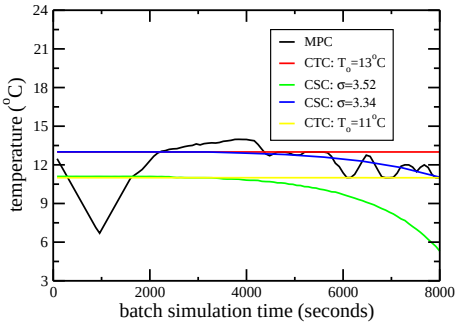

(b) temperature vs time

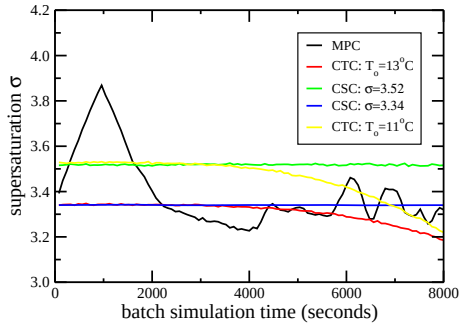

(c) supersaturation σ vs time

Figure 2.8: The propagation of temperature, concentration, and supersaturation with time during the batch run under closed-loop operation at different initial temperature values and supersaturation levels, including MPC aiming at growth rate ratio set-point value $\alpha_{\text{set}} = 1.11$.

that a high supersaturation level, which is necessary for the desired equidimensional shape, can result in a significant solute concentration drop due to a higher crystal nucleation rate as well as the fast crystal growth. The crystal growth rate ratio, however, is dependent on supersaturation which is the ratio between the solute concentration and the solubility. Thus, a desired supersaturation level can be maintained by appropriately decreasing the solubility, which is a function of the crystallizer temperature. In Fig. 2.8(b), the computed trajectory for the crystallizer temperature in the proposed MPC is similar to that of the standard CSC; however, it is different in the sense that the MPC deals with the nuclei formation in order to avoid the small crystal fines at the end of batch process. In Fig. 2.7, the crystallizer was run with a temperature which is relatively close to the optimal temperature $\sim 11^{\circ}$C and, as a result, crystals nucleate uniformly throughout the batch run. Due to the insensitivity of the system to variation in the temperature and solute concentration at a high desired crystal growth rate ratio, the crystal shape distribution under MPC is not as distinguished compared to that of the MPC at the low growth rate ratio, $\alpha_{\text{set}} = 0.85$, as is seen in Fig. 2.9.

The results in Table 2.4, compared to those in Table 2.3 for $\alpha_{\text{set}} = 0.85$, show that the MPC simulations result in a higher polydispersity but a narrower distribution around the desired crystal shape with a nearly uniform crystal nucleation rate when compared with the simulations under CTC and CSC. In addition, the MPC successfully deals with the significant concentration drop to maintain the desired crystal shape, $\alpha_{\text{set}} = 1.11$. Although the CTC and CSC result in similar shape distributions to that of MPC, their performances are not robust to a severe concentration drop. The relatively high span value for the MPC indi-

Control strategy	$\langle h_{110} \rangle$	r_{10}	r_{50}	r_{90}	span
MPC	22.76	4.54	22.29	42.57	1.71
CTC: T=11°C	25.14	4.45	24.58	46.82	1.72
CTC: T=13°C	21.03	4.08	20.79	38.38	1.65
CSC: $\sigma = 3.34$	22.39	4.71	22.37	40.07	1.58
CSC: $\sigma = 3.52$	28.23	5.84	28.21	50.63	1.59

Table 2.4: Comparison between the simulation results for the crystal size in the (110) direction under five different control strategies for the desired growth rate ratio of $\alpha_{\text{set}} = 1.11$.

cates a wide size distribution (high polydispersity) which results from the significant drop in the concentration at the end of the batch crystallization process described previously.

In summary, MPC successfully drives the final crystal shape distribution to a desired set-point value and is found to be robust with respect to both a fast nucleation rate in the earlier stage and a drastic drop in the solute concentration. Additionally, a low polydispersity can be achieved depending on the desired crystal morphology. For instance, for $\alpha_{\text{set}} = 1.11$, we are more likely to produce crystals with a narrow crystal shape distribution and with a high polydispersity because the crystallizer promptly responds to the depletion in the solute concentration which is reflected as a series of rises and falls in the crystallizer temperature in Fig. 2.8, and the high polydispersity results from uniformly nucleated crystals. For $\alpha_{\text{set}} = 0.85$, however, crystals with the desired shape and a low polydispersity can be achieved at a very high initial temperature in the crystallizer, because the system

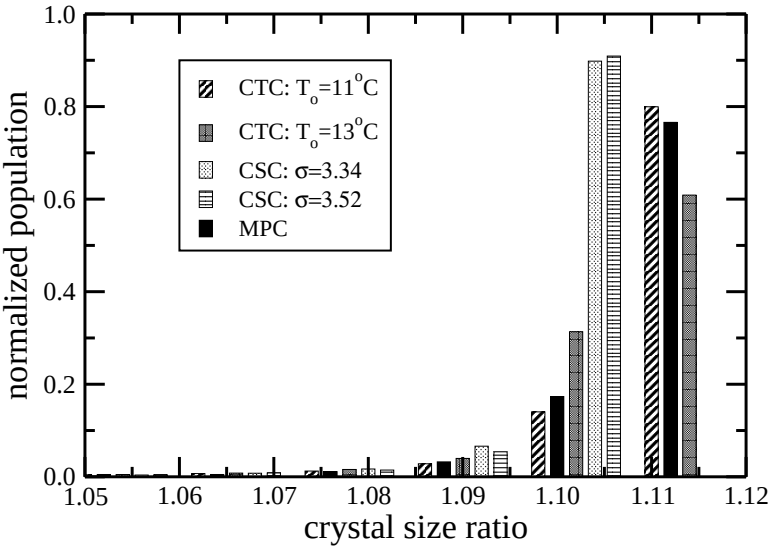

Figure 2.9: The final crystal shape distribution at the end of the batch simulation under different closed-loop operations using CTC and CSC at different initial temperature values and supersaturation levels for CTC and CSC, respectively, and MPC for the growth rate ratio set-point value $\alpha_{\text{set}} = 1.11$. It is noted that the crystal shape distribution is a dimensionless variable and is normalized over the entire population so that summing over all histograms will add up to one for each control strategy.

reaches its optimal temperature quickly which results in the crystals being uniformly nucleated throughout the batch.

2.5 Conclusions

The present work focused on comparing the performance of the proposed model predictive controller with that of CTC and CSC in regulating crystal shape and size distributions to desired values. In general, the CTC operating strategy drives the crystallizer conditions from the labile zone to the metastable zone, and the CSC policy maintains the crystallizer conditions in the metastable zone to maximize the size of protein crystals.

First, we focused on the modeling of a batch crystallization process used to produce tetragonal hen egg white lysozyme crystals via kinetic Monte Carlo (kMC) simulation. The kMC simulation simulated the batch protein crystallization via adsorption, desorption, and migration mechanisms on the (110) and (101) faces. Then, in order to describe the nucleation occurring at different times in the batch simulations, the nucleation rate expression was extracted from experimental results by [41]. In addition, the dependence of the crystal growth on temperature and protein solute concentration was demonstrated in 3-D nonlinear models constructed from open-loop kMC simulations. The present work also developed mass and energy balances to account for the depletion in the protein solute concentration and the drop in the crystallizer temperature by crystallization. Finally, an MPC was designed to produce crystals with a desired morphology by regulating the crystal

growth conditions in the crystallizer through the manipulation of the jacket temperature which was in accordance with standard batch crystallization practice.

Simulation results showed that the proposed MPC was able to regulate the crystal shape distribution to a desired set-point value while reducing the effects of an undesirable biased nucleation in the processing window and a drastic drop in the solute concentration. Comparing the simulation results of the MPC with those of other conventional operating strategies, crystals with a low polydispersity were produced depending on the desired crystal morphology. For instance, for $\alpha_{\text{set}} = 1.11$, the crystallizer under MPC resulted in a narrow crystal shape distribution with a high polydispersity, because the crystallizer immediately responded to the depletion in the solute concentration and produced a series of rises and falls in the jacket temperature computed from the proposed MPC in Fig. 2.8, and a high polydispersity resulted from uniformly nucleated crystals. For $\alpha_{\text{set}} = 0.85$, however, crystals with desired morphology and a lower polydispersity were obtained at a very high initial temperature in the crystallizer, because the system reached its optimal temperature quickly and it caused a uniform nucleation rate throughout throughout the batch. In this case, therefore, we reduced the batch time considerably, because the system reached its optimal state more quickly. Furthermore, only protein solute concentration and temperature measurements were needed to implement this operating policy in practice; no additional measurements such as crystal size and shape were required in the controller.

Chapter 3

Modeling and control of shape distribution of protein crystal aggregates

3.1 Introduction

This chapter focuses on the modeling and control of protein crystal aggregates in a large-scale batch crystallizer used to produce tetragonal HEW lysozyme crystals. Initially, a kinetic Monte Carlo (kMC) simulation is presented for the modeling of the crystal nucleation, growth, and shear-induced aggregation in an effort to control the evolution of the crystal shape distribution. Through experimental data, the crystal growth rate is calibrated and an empirical expression for the nucleation rate is also developed. Then the method of moments is applied to a comprehensive population balance model to derive a reduced-order moment model that describes the dynamic evolution of the three leading moments

of the crystal volume distribution. Along with mass and energy balances for the continuous phase, the moment model is used to design a model predictive control (MPC) strategy which drives the crystal shape distribution to a desired set-point value through the manipulation of the crystallizer jacket temperature. Compared to conventional operating strategies used in industry, it is demonstrated that the proposed MPC strategy is able to produce crystal aggregates with a desired shape distribution and a low polydispersity, effectively dealing with the undesired effects of biased nucleation, depletion in the solute concentration, and changes in the average crystal shape due to the aggregation process.

3.2 Crystallization process description and modeling

3.2.1 Crystal nucleation

In our previous work [69], we assume that a HEW lysozyme nucleus is a cube with infinitesimal size (i.e., $V = 0$) [92, 120]. The supersaturation σ is defined as $\sigma = \ln(c/s)$ where c (mg/mL) is the protein solute concentration and s (mg/mL) is the solubility. The protein solubility depends on temperature (°C) and is expressed by the following third-order polynomial at pH = 4.5 and 4%(w/v) NaCl [12, 13]:

$$s(T) = 2.88 \times 10^{-4} T^3 - 1.65 \times 10^{-3} T^2 + 4.62 \times 10^{-2} T + 6.01 \times 10^{-1}. \tag{3.1}$$

The nucleation rate, $B(T,c)$, at pH $= 4.5$ and 4%(w/v) NaCl is taken from [41]:

$$B(T,c) = \begin{cases} 0.041\sigma + 0.063 & \text{for} \quad \sigma \geq 3.11 \\ 8.0 \times 10^{-8} \exp(4.725\sigma) & \text{for} \quad \sigma < 3.11 \end{cases} \tag{3.2}$$

with units $[\text{cm}^{-3} \cdot \text{sec}^{-1}]$.

3.2.2 Crystal growth

We model the 3-D crystal growth with two representative faces (i.e., the (110) and (101) directions) via kMC simulations. Interested readers may refer to our earlier work [93, 66, 69] for further details regarding the kMC methodology. The following rate expressions adopted from [32] and [60] are used to simulate the kinetics of crystal growth.

Attachment rate:

$$r_a = K_0^+ \exp \frac{\Delta\mu}{k_B T}, \tag{3.3}$$

where K_0^+ is the attachment coefficient, k_B is the Boltzmann constant, T is the temperature (K), and $\Delta\mu = k_B T \sigma$.

Detachment rate:

$$r_d(i) = K_0^+ \exp\left(\frac{\phi}{k_B T} - i\frac{E_{pb}}{k_B T}\right), \tag{3.4}$$

Migration rate:

$$r_m(i) = K_0^+ \exp\left(\frac{\phi}{k_B T} - i\frac{E_{pb}}{k_B T} + \frac{E_{pb}}{2k_B T}\right), \tag{3.5}$$

where E_{pb} is the average binding energy per bond, ϕ is the total binding energy per molecule of a fully occupied lattice, and i is the number of nearest neighbors.

3.2.3 Crystal aggregation

General considerations

Aggregation processes result in a decrease in the total number of particles and an increase in the average particle size. The shear force induced by agitation, which is required in the scale-up of a particulate process, plays a key role in the aggregation maintaining the particulate phase in suspension. Aggregation has an important influence on the quality of particulate products, especially for dense particles such as protein crystals, and should be taken into consideration in the modeling of large-scale crystallization processes. This work is a comprehensive attempt to model the batch particulate process including nucleation, crystal growth, and aggregation in a stirred batch process, so that the design of the batch crystallizer and the subsequent scale-up process can be carried out in a more quantitative way because the effect of stirring is directly considered. In this context, it is necessary to find key kinetic expressions for aggregation that enable us to quantify the major factors including aggregation efficiency and frequency.

The aggregation process can be divided into two steps. First, particles must be transported into a very small neighborhood of one another. A simple idea is that an aggregate will be formed if an aggregate is sufficiently stable such that it can overcome repulsive forces such as hydrodynamic drag and the viscous fluid layer between those particles undergoing aggregation. More specifically, there are several aggregation types. Brownian motion is the prevailing mechanism for the induction of aggregation for submicrometer

particles. Particles whose sizes are in the range of 1-50 μm are under the influence of shear forces, and the aggregation process induced by the shear force dominates in particulate processes. Although it is not of particular interest in this work, crystals with a size larger than 50 μm are under the influence of differential sedimentation or inertia [21].

Maximum local energy dissipation rate ε_{max}

In [118] and [53], it is shown that crystallization experiments at higher stirrer speeds result in a reduced formation of crystal aggregates which is favorable in the subsequent separation process by filtration. Although higher stirrer speeds are preferred in order to achieve more crystals with uniform size and shape, it is apparent that there is a physical limitation on the stirrer speed that is achievable by a motor. Therefore it is important to identify a maximum local energy dissipation rate (ε_{max}), which measures the hydromechanical stress resulting from agitation and is related to the highest impeller speed for the batch crystallizer. This energy is usually converted into heat, but leads to a negligible temperature change. For a given input power level, P, we can calculate the corresponding mean power input, $\bar{\varepsilon}$, for a batch crystallizer as follows [118]:

$$\bar{\varepsilon} = \frac{P}{\rho V_{batch}} = \frac{\omega M_{torque}}{\rho V_{batch}} = \frac{2\pi n M_{torque}}{\rho V_{batch}} \tag{3.6}$$

where ρ is the density of the continuous phase in the stirred tank, and V_{batch} is the volume of the batch crystallizer. Additionally, the mean power input, $\bar{\varepsilon}$, by stirring in a tank is determined by measuring the torque, M_{torque}, at the agitator shaft at a specific stirrer speed, n. The ratio of the maximum local energy dissipation, ε_{max}, which depends on the geometrical

parameters of the reactor and stirrer types, and the impeller power, $\bar{\varepsilon}$, is determined from the following equation [52]:

$$\frac{\varepsilon_{max}}{\bar{\varepsilon}} \approx \frac{a}{(d/D)^2 (h/d)^{2/3} z^{0.6} (sin\theta)^{1.15} z_I^{2/3} (H/D)^{-2/3}} \tag{3.7}$$

The details of the geometry of the batch crystallizer and the stirrer type are taken from [118]: unbaffled vessel ($a = 16$); diameter of the impeller ($d = 0.06m$); inner tank diameter ($D = 0.12m$); height of the impeller blade ($h = 0.04m$); tank filling height ($H = 0.12m$); number of impeller blades ($z = 3$); blade inclination to the horizontal ($\theta = 40^o$); number of impellers ($z_I = 1$). Under these specifications, $\varepsilon_{max}/\bar{\varepsilon} = 72$.

Shear rate G_{shear}

In this work, the optimum mean power input of $\bar{\varepsilon} = 30$ mW/kg is considered, which corresponds to the maximum energy dissipation of $\varepsilon_{max} = 2.16$ W/kg according to Eq. 3.7. Furthermore, the range of stirrer speeds considered in this work is from 50 to 300 rpm, which is taken from the experimental work by [118] because the crystal growth condition is similar to that of our simulation. The turbulent shear rate within the stirred tank, G_{shear}, was characterized by the average velocity gradient of the flow field as is shown in the following expression from [16]:

$$G_{shear} = \left(\frac{\varepsilon}{\nu}\right)^{0.5} \tag{3.8}$$

where the kinematic viscosity is $\nu = 2.3 \times 10^{-6}$ cm^2/s, the initial solute concentration is $c = 47$ mg/mL, and the shear rate computed by Eq. 3.8 is $G_{shear} = 970/$s.

Kolmogorov microscale η

The Kolmogorov microscale, η, has been used to indicate the length scale of the smallest eddies in turbulent solid-liquid systems and is related to the local energy dissipation rate, ε, and kinematic viscosity, ν, as follows [65]:

$$\eta = \left(\frac{\nu^3}{\varepsilon}\right)^{1/4} \tag{3.9}$$

In this study, the Kolmogorov microscale is 48.7 μm when the optimum mean power input and the corresponding maximum energy dissipation are $\bar{\varepsilon} = 30$ mW/kg and $\varepsilon_{max} = 2.16$ W/kg, respectively.

Collision frequency β_{ij}

For particles and aggregates smaller than the Kolmogorov microscale, collisions induced by the shear force dominate those caused by viscous forces [65]. The aggregation kernel, $\beta(V_i, V_j)$, represents the rate at which particles with volumes V_i and V_j aggregate induced by the shear force and is as follows:

$$\beta_{ij} = \beta\left(V_i, V_j\right) = \psi G_{shear}\left(V_i^{1/3} + V_j^{1/3}\right)^3 \tag{3.10}$$

where ψ is a constant that depends on the type of flow. For example, ψ is 4/3 for laminar flow, and [109] derived $\psi = 1.29$ for turbulent flow. Additionally, [56] states that this expression for collision frequency can be used for particles with diameters of up to 5–10 times the Kolmogorov microscale.

Mass fractal dimension d_f

Assume for the moment that a crystal aggregate is a solid particle without any empty inner space and that its density is identical to that of protein crystals. For the purpose of simulation focusing on the shape evolution of crystals, we assume that there are only binary collisions and that the shape of a crystal aggregate after collision follows that of the bigger crystal when the binary aggregation occurs. Then, the mass $M(h_{110}, h_{101})$ of the aggregate enclosed within a small neighborhood from a suitably chosen center is given by:

$$M(h_{110}, h_{101}) = \frac{4}{3}\rho h_{110}^2 h_{101} \tag{3.11}$$

which is a function of a set of two internal coordinates in the (110) and (101) directions. More specifically, the characteristic crystal lengths are h_{110} and h_{101} as presented in Fig. 3.1. In general, if we were to account for the fact that the region enclosed within the sphere of radius R is not completely filled with particles but contains empty spaces, then the actual mass will be less than that given by Eq. 3.11. In fact, it turns out that in many cases, one can write

$$M(R) \propto k_a R^{d_f} \tag{3.12}$$

where d_f is the mass fractal dimension and it is usually less than three due to the porosity in aggregates, k_a is the shape factor (e.g., it is $\frac{4}{3}\rho\pi$ for a sphere), and R is the characteristic length. Interested readers may refer to [58] for further analysis on the mass and fractal dimension. In aggregation, it is assumed that the shape of the crystal resulting from aggregation is identical to that of the larger crystal participating in the aggregation event, but the

total number of crystals is reduced by one after each aggregation. Suppose there are two crystals where the volume of crystal 1 is greater than that of crystal 2, and we denote the dimension of each crystal for the (110) and (101) faces as $(h_{110,1}, h_{101,1})$ and $(h_{110,2}, h_{101,2})$, respectively. Therefore, we note that the volume of each crystal can be expressed in terms of a crystal shape factor, $\alpha_1 = h_{110,1}/h_{101,1}$ and $\alpha_2 = h_{110,2}/h_{101,2}$, as follows:

$$V_1 = h_{110,1}^2 h_{101,1} = \frac{h_{110,1}^3}{\alpha_1} \qquad\qquad V_2 = h_{110,2}^2 h_{101,2} = \frac{h_{110,2}^3}{\alpha_2}$$

As mentioned previously, the crystal shape after the aggregation, α_{agg}, remains identical to that of the bigger crystal (i.e., $\alpha_{agg} = \alpha_1$ since $V_1 > V_2$). Then the final crystal height in both faces after aggregation can be computed by the following balance equation based on the equation of total volumes before and after the aggregation:

$$h_{110,1}^2 h_{101,1} + h_{110,2}^2 h_{101,2} = \frac{h_{110,\text{agg}}^3}{\alpha_{agg}}$$

where $h_{110,\text{agg}}$ and $h_{101,\text{agg}}$ are the crystal heights of the new aggregate for the (110) and (101) faces, respectively. Therefore, we can eventually compute $h_{110,\text{agg}}$ and $h_{101,\text{agg}}$ in the following way:

$$h_{110,\text{agg}} = \alpha_{agg}^{1/3} \left(h_{110,1}^2 h_{101,1} + h_{110,2}^2 h_{101,2} \right)^{1/3}$$

and,

$$h_{101,\text{agg}} = \left(\frac{h_{110,1}^2 h_{101,1} + h_{110,2}^2 h_{101,2}}{\alpha_{agg}^2} \right)^{1/3}$$

The physical properties and other operating parameters of the particulate process are presented in Table 3.1.

ψ	a constant depending on the type of flow	1.29	·
G_{shear}	shear rate	970	$1/\mathrm{s}$
$\bar{\varepsilon}$	effective mean power input	0.03	$\mathrm{m}^2/\mathrm{s}^3$
ε_{max}	maximum local energy dissipation rate	2.16	$\mathrm{m}^2/\mathrm{s}^3$
ν	kinematic viscosity	2.3×10^{-6}	m^2/s
μ	dynamic viscosity	0.0024	kg/m s
A_H	Hamaker constant	10^{-19}	J

Table 3.1: Process parameters for aggregation.

Collision efficiency α_{ij}

In a stirred crystallizer, the aggregates of crystals are compact because they are subject to strong shear flow, and thus the collision efficiency corresponding to the impermeable aggregate is modeled by an equation in [122]. The collision efficiency α_{ij}, which is defined as the ratio of the number of collisions to the number of collisions that result in aggregation (i.e., the actual aggregation rate to the theoretical aggregation rate), is then computed by the following equation [127]:

$$\alpha_{ij} = 0.43 Fl^{-0.18} \qquad \text{where } 10 < Fl < 10^5 \tag{3.13}$$

where Fl is the flow number computed by [7] as follows:

$$Fl = \frac{6\pi\mu \left(V_i^{1/3} + V_j^{1/3}\right)^3 G_{shear}}{8A_H} \tag{3.14}$$

Fl can be understood as the ratio between the repulsive shear force and the attractive Van der Waals force. The coefficient 0.43 in Eq. 3.13 was obtained by [127]. The Hamaker constant A_H indicates the extent of Van der Waals interaction, and the value is approximately between 10^{-20} and 10^{-19} J for solid-liquid systems. In this study, the value of 10^{-19} J is chosen for A_H. Therefore, by Eqs. 3.10 and 3.13, we can conclude that increasing the shear rate increases the relative velocity (i.e., the average velocity gradient) of the particles, and hence the collision frequency is enhanced. However, the efficiency of collisions decreases to zero with further increases in the shear rate. This is because higher shear rates result in stronger hydrodynamic forces acting against the formation of aggregates and thus aggregates are not formed since they do not have sufficient time or energy to form bonds for aggregates. Since the aggregation rate is determined by the product of the collision frequency and the efficiency, shear rate has two conflicting effects on the aggregation. For the particular system considered in this work, we can compute the Kolmogorov time scale, $(\nu/\varepsilon)^{0.5}$, which indicates how much time is needed for the collision to be successful. With the system parameters described in Table 3.1, it is calculated that the Kolmogorov time scale is 10^{-4} s. This is sufficiently small such that the aggregation occurs successfully with the current mean power input, $\bar{\varepsilon} = 30$ mW/kg.

Total collision rate N_{ij}

Let N_{ij} be the total number of collisions occurring per unit time per unit volume between crystals with volumes V_i and V_j. The shape of lysozyme protein crystals is assumed to

be a rectangular prism, and aggregations are treated as binary hard sphere collisions. The number of aggregations occurring during sampling time Δ can be written in terms of the aggregation kernel $\beta\left(V_i, V_j\right)$, the batch reactor volume V_{batch}, the collision efficiency α_{ij}, and the concentrations of particles of volumes V_i and V_j as follows:

$$N_{ij} = \alpha_{ij}\beta\left(V_i, V_j\right) m_i m_j V_{batch}\Delta \qquad 1 \leq i, j \leq C_{total} \tag{3.15}$$

where m_i is the number concentration (i.e., the number of particles of class i per unit volume). The number C_{total} denotes the total number of crystal sizes. In the case of a discrete volume, the rate of formation of particles of size k from the collision of particles of volumes V_i and V_j is $\frac{1}{2}\sum_{V_i+V_j=V_k} N_{ij}$ where the notation $V_i + V_j = V_k$ indicates that the summation is over all the different combinations of collisions. A factor of $1/2$ is introduced because each collision is counted twice in the summation.

In order to execute an aggregation event between two lysozyme crystals in the simulation, the binary collision probability must first be calculated according to Eq. 3.15. For the purposes of the batch crystallization simulation, aggregation events are considered to occur every 0.5 seconds. By doing this we can multiply Eq. 3.15 by 0.5 seconds and the reactor volume to get the total number of collisions during the time period. This is the probability that aggregation occurs between the crystals of volumes V_i and V_j. Then, a random number in the interval $[0, 1)$ is generated, and the aggregation event is executed when the random number is less than the calculated probability. This process applies to all of the crystal sizes, and continues throughout the entire batch crystallization simulation.

3.2.4 Mass and energy balances for the continuous phase

Mass balance

The mass balance in the present work is modeled by assuming that the geometry of a lysozyme crystal is a rectangular prism as shown in Fig. 3.1, and that the shape of a lysozyme crystal is approximated by a ratio of crystal heights in the (110) and (101) directions. The amount of the protein solute removed from the continuous phase due to crystallization can be computed using the following equation:

$$\Delta c(t) = -\frac{\Delta V_c(t)\rho_c N_c(t)}{V_{batch}}, \tag{3.16}$$

where V_{batch} is the volume of the continuous phase (assuming the change in V_{batch} is negligible), $\Delta V_c(t)$ is the total volume change of the entire set of crystals, $N_c(t)$ is the number of crystals in batch at time t, ρ_c is the crystal density, and $\Delta c(t)$ is the change of the protein solute concentration in the continuous phase. For the derivation of Eq. 3.16, please refer to [69].

Energy balance

Similarly, the energy balance for the batch crystallization process is shown below:

$$\frac{dT}{dt} = -\frac{\rho_c \Delta H_c}{\rho C_p}\left(\frac{1}{V}\Delta V_c(t)\right) - \frac{U_j A_j}{\rho C_p V}\left(T - T_j\right) \tag{3.17}$$

where T is the crystallizer temperature, and T_j is the temperature of the jacket. For the derivation of Eq. 3.17, please refer to [69].

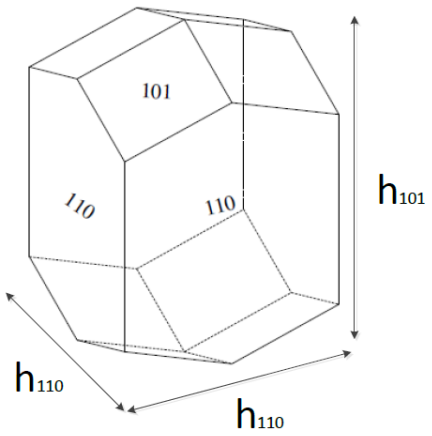

Figure 3.1: The geometry model for lysozyme crystals used in the present work.

Table 3.2: Parameters for the batch crystallizer

ρ_c	crystal density	1400	mg/cm^3
ΔH_c	enthalpy of crystallization	-4.5	kJ/kg
ρ	continuous phase solution density	1000 + c	mg/cm^3
C_p	specific heat capacity	4.13	$kJ/K\ kg$
V_{batch}	crystallizer volume	1	L
A_j	surface area of crystallizer wall	0.25	m^2
U_j	heat transfer coefficient of crystallizer wall	1800	$kJ/m^2\ h\ K$

3.3 Population balance modeling

3.3.1 Population balance model of crystal volume distributions

In this section, we present a population balance model (PBM) for the lysozyme crystallization process accounting for simultaneous nucleation, crystal growth, and aggregation. The evolution of the crystal volume distribution in the batch crystallizer can be obtained from the following partial integro-differential equation:

$$\frac{\partial n(V,t)}{\partial t} + G_{volume}\frac{\partial n(V,t)}{\partial V} = \underbrace{\delta(V-V_0)B(T,c)}_{Birth\ by\ nucleation} + \underbrace{\frac{1}{2}\int_0^V \alpha_{eff}\beta(V-\bar{V},\bar{V})n(V-\bar{V},t)n(\bar{V},t)d\bar{V}}_{Birth\ by\ aggregation}$$
$$\underbrace{-n(V,t)\int_0^\infty \alpha_{eff}\beta(V,\bar{V})n(\bar{V},t)d\bar{V}}_{Death\ by\ aggregation} \tag{3.18}$$

where V and $V-\bar{V}$ denote the crystal volumes of the two crystals participating in the aggregation event, t is the time, $n(V,t)$ denotes the lysozyme crystal distribution with volume V, α_{eff} is a constant aggregation efficiency, $\beta(V-\bar{V},\bar{V})$ is the aggregation rate between the crystals with volumes V and $V-\bar{V}$, $\delta(V)$ is the standard Dirac function, and $B(T,c)$ is the nucleation rate. As in [69], $\frac{dV}{dt}$, which will be denoted as G_{volume} for the remainder, is computed by measuring the solute concentration drop,

$$G_{volume} = \frac{dV}{dt} \approx -\frac{1}{\Delta t}\left(\frac{V_{batch}\Delta c(t)}{\rho_c N_c(t)}\right), \tag{3.19}$$

where the parameters on right hand side are as in Eq. 3.16.

Then, we can write Eq. 3.18, along with the boundary condition which is derived in

Section 3.8.1, as follows:

$$\frac{\partial n(V,t)}{\partial t} + G_{volume}\frac{\partial n(V,t)}{\partial V} = \frac{1}{2}\int_0^V \alpha_{eff}\beta\left(V-\bar{V},\bar{V}\right)n(V-\bar{V},t)n(\bar{V},t)d\bar{V} - n(V,t)\int_0^\infty \alpha_{eff}\beta\left(V,\bar{V}\right)n(\bar{V},t)d\bar{V} \tag{3.20}$$

$$n(0,t) = \frac{B(T,c)}{G_{volume}}$$

3.3.2 Lognormal volume distribution and moment model

Due to the complexity of the population balance model, it is not directly applicable for numerical computation of the size distribution in real-time, or for the design of model predictive controllers that can be readily implemented in practice. In order to circumvent these problems, the method of moments is applied to Eq. 3.18 for the construction of a low-order ordinary differential equation (ODE) model that accurately reproduces the dominant dynamics of the particulate process. More specifically, the constructed low-order ODEs are used to describe the evolution of the three leading moments of the crystal volume distribution in the turbulent shear regime in a 5 L batch crystallizer. Then, under the assumption that the changes in the collision efficiency are negligible, we construct a framework for the moment models that describes aggregation mechanisms over the entire batch. These moment models provide acceptable simplification of the population balance equation by modeling the key behavior of crystal growth, nucleation, and aggregation in the continuous phase. First of all, it is shown in Fig. 3.3 that the lysozyme crystal volume distribution obtained from kMC simulations can be appropriately characterized by the following log-

normal function:

$$n(V,t) = \frac{1}{3\sqrt{2\pi} ln\bar{\sigma}} \exp\left(-\frac{ln^2\left(\frac{V}{V_g}\right)}{18ln^2\bar{\sigma}}\right)\frac{1}{V} \tag{3.21}$$

where $V_g = \frac{M_1^2}{M_0^{3/2}M_2^{1/2}}$ is the average crystal volume, and $\bar{\sigma}$ is the standard deviation of the crystal volume distribution which is expressed as $ln^2\bar{\sigma} = \frac{1}{9}ln\left(\frac{M_0M_2}{M_1^2}\right)$. Then we apply the method of moments to Eq. 3.18 to compute the approximate models that describe the evolution of the three leading moments of the volume distribution. For this purpose, we define the j^{th} moment model of the crystal volume distribution as follows:

$$M_j = \int_o^\infty V^j n(V,t)dV \tag{3.22}$$

Furthermore, the moment models of the system can be closed according to the assumption above that the volume distribution follows that of a lognormal distribution, and thus an arbitrary moment, M_k, is computed as follows:

$$M_k = M_0 V_g^k \exp\left(\frac{9}{2}k^2 ln^2\bar{\sigma}\right)$$

For further details of the derivation of moment models, the reader may refer to Section 3.8.2. The equations given below describe the three leading moment models for $j = 0,1,2$.

Zeroth moment:

$$\frac{dM_0}{dt} = B(T,c) - \alpha_{eff}\left(M_0M_1 + 3M_{1/3}M_{2/3}\right) \tag{3.23}$$

where α_{eff} is the collision efficiency described in Eq. 3.13, and $B(T,c)$ is replaced by the boundary condition in Eq. 3.20.

First moment:

$$\frac{dM_1}{dt} = G_{volume} M_0 \tag{3.24}$$

Second moment:

$$\frac{dM_2}{dt} = 2G_{volume} M_1 + 2\alpha_{eff} \left(M_1 M_2 + 3M_{4/3} M_{5/3} \right) \tag{3.25}$$

In summary, we can complete the moment models as follows:

$$\begin{aligned}
G_{volume} &\approx -\frac{1}{\Delta t} \left(\frac{V_{batch} \Delta c(t)}{\rho_c M_0} \right) \\
\frac{dM_0}{dt} &= B(T,c) - \alpha_{eff} \left(M_0 M_1 + 3M_{1/3} M_{2/3} \right) \\
\frac{dM_1}{dt} &= G_{volume} M_0 \\
\frac{dM_2}{dt} &= 2G_{volume} M_1 + 2\alpha_{eff} \left(M_1 M_2 + 3M_{4/3} M_{5/3} \right) \\
\frac{dT}{dt} &= -\frac{\rho_c \Delta H_c}{\rho C_p V} \frac{dM_1}{dt} - \frac{U_j A_j}{\rho C_p V} \left(T - T_j \right) \\
\Delta c(t) &= -\frac{\rho_c}{V} \frac{dM_1}{dt} \\
M_k &= M_0 V_g^k \exp\left(\frac{9}{2} k^2 ln^2 \bar{\sigma} \right) \qquad \text{for } k = \left(\frac{1}{3}, \frac{2}{3}, \frac{4}{3}, \frac{5}{3} \right) \\
V_g &= \frac{M_1^2}{M_0^{3/2} M_2^{1/2}} \qquad ln^2 \bar{\sigma} = \frac{1}{9} ln \left(\frac{M_0 M_2}{M_1^2} \right)
\end{aligned} \tag{3.26}$$

Although an aggregation kernel with a constant collision efficiency was used to close the moment models, the model can be further improved by using a nonconstant collision efficiency.

3.3.3 Relation between crystal volume and shape distributions

In the moment model, we can accurately estimate M_0, which represents the number of crystals in the system, and it is highly coupled with other moments as is shown in Eqs. 3.24–3.25. Therefore, we should carefully connect M_0 to the shape distribution, $\alpha = h_{110}/h_{101}$. In the model predictive controller (please see Eq. 3.30 below), the average height of the (110) face, $\langle h_{110}(t)\rangle$, at time t is estimated at every sampling time through the following equation:

$$\langle h_{110}(t)\rangle = \frac{\langle h_{110}(t-\Delta)\rangle M_0(t-\Delta)}{M_0(t)} + G_{110}(t-\Delta)\Delta \tag{3.27}$$

where $G_{110}(t)$ is the growth rate for the (110) face, and in the same manner the average height of the crystal face (101), $\langle h_{101}(t)\rangle$, can be computed as follows,

$$\langle h_{101}(t)\rangle = \frac{\langle h_{101}(t-\Delta)\rangle M_0(t-\Delta)}{M_0(t)} + G_{101}(t-\Delta)\Delta \tag{3.28}$$

where $G_{101}(t)$ is the growth rate for the (101) face. By the above equations, we can approximate the average crystal shape in the following way:

$$\langle \alpha \rangle \approx \frac{\langle h_{110}(t)\rangle}{\langle h_{101}(t)\rangle} \tag{3.29}$$

3.4 Open-loop simulation results

Executing multiple kMC simulations with an infinite number of lattice sites can be considered to be similar to solving Eq. 3.18 directly [37, 87]. In this work, we assume that the number of lattice sites used in the kMC simulation is sufficiently large, and as a result, no

size effects are observed in the systems with more lattice sites [60].

In Fig. 3.2, crystal growth at pH = 4.5 and 4%(w/v) NaCl has been properly modeled through a procedure described in previous works [93, 66, 69], and plotted against the experimental results at 3.5% and 5.0% NaCl from [31]. In particular, $\left(\phi/k_B, E_{pb}/k_B\right)_{110} = (1077.26\ K, 227.10\ K)$ and $\left(\phi/k_B, E_{pb}/k_B\right)_{101} = (800.66\ K, 241.65\ K)$ provide a best fit between the simulation results and the experimental data for the (110) and (101) faces, respectively. Additionally, $K_o^+ = 0.211$ seconds^{-1}. Then, a set of 3-D plots (cf. Fig. 3.4) are made from the open-loop kMC simulation using the parameters presented above and they are used to describe the temperature and solute concentration dependencies of the steady-state crystal growth rates for the (110) and (101) faces and the crystal growth rate ratio.

One of the major contributions of this work is the development of the aggregation process along with nucleation and crystal growth in the kMC simulation. In addition to the growth conditions including temperature, protein solute concentration, pH, and salt concentration [1, 129, 86, 82], there are many other factors that affect the aggregation rate, as discussed in the previous sections and shown in Eqs. 3.6–3.15. Additionally, the evolution of aggregation along with nucleation and crystal growth is estimated by using the moment models described in Eq. 3.26. To verify the accuracy of the moment models, an open-loop simulation is run. Then, the evolution of the number of crystals (M_0), the average crystal shape, the temperature, the solute concentration, and the moment model in the kMC simulation are plotted together in Fig. 3.3. The concentration remains almost constant at 47

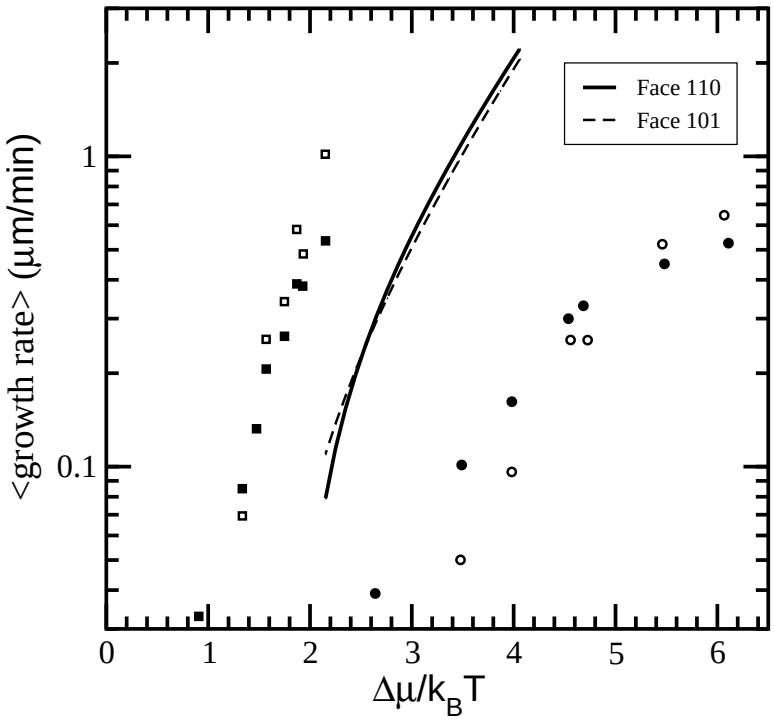

Figure 3.2: Growth rates versus the degree of supersaturation at $c = 45$ mg/mL and 4% NaCl. The solid and dashed lines show the growth rates for the kMC model on the (110) and (101) faces, respectively. Experimental data from [31] is also shown at pH$=$ 4.6 where the (■) and (□) represent the (101) and (110) faces with 5% NaCl and the (●)/(○) represent the (101) and (110) faces with 3.5% NaCl.

mg/mL. As is seen in Eq. 3.13, the collision efficiency decreases as the crystal sizes increase, because crystals are less likely to adhere to one another due to a short contact time which is unfavorable for aggregation.

In this work, however, a constant aggregation efficiency is used to deal with the closure issue in the moment models, and it results in a minor mismatch in M_0 between the moment models and the kMC simulations as is shown in Fig. 3.3. This happens because the constant aggregation efficiency is not able to capture the size-dependent nature of the aggregation. Regardless of the discrepancy in M_0 between the moment models and the kMC simulations, Eqs. 3.27–3.29 successfully estimate the average crystal shape distribution based on the growth rates for the (110) and (101) faces and the number of crystals in the crystallizer.

The moment models are used in the next section to design a new controller in order to provide optimality as well as robustness in regulating the batch process.

3.5 Model predictive control of size and shape of crystal aggregates

In the batch crystallization simulation, the role of aggregation events becomes significant in a scaled-up crystallizer as crystal size and the number of crystals increase. Then, the moment model is considered in the controller design in order to predict the system dynamics with a set of low-order ordinary differential equations. The rates of nucleation and crystal growth are determined by the crystallizer temperature and solute concentration. However,

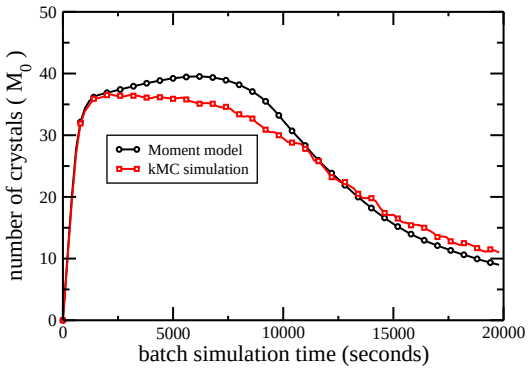

(a) number of crystals (M_0)

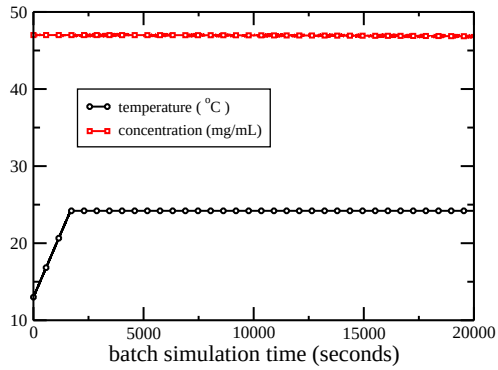

(b) temperature and concentration

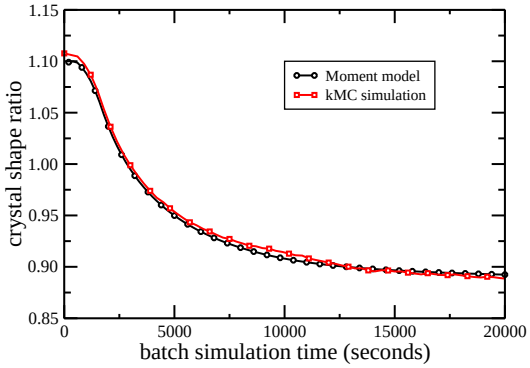

(c) crystal shape (α)

Figure 3.3: Profiles of the open-loop evolution of the number of crystals, temperature, protein solute concentration, and crystal shape for tetragonal lysozyme protein crystals at pH $= 4.5$. Please note that c and T profiles obtained from the moment models and the kMC simulations are identical.

the shear rate, which is determined by the stirrer speed (i.e., the only controllable variable in the aggregation rate), is fixed throughout the entire batch run.

In addition to the nonlinear models described in Fig. 3.4, and the mass and energy balances introduced in Eqs. 3.16 and 3.17, moment models, which account for the number of crystals (M_0) and the average volume (M_1) in the crystallizer, play a key role in estimating the evolution of the crystal volume and shape distributions (Eqs. 3.27–3.29). Conventional operating strategies may be used; however, there are some issues. For example, due to a lower limit on the temperature, the supersaturation level cannot be maintained at a set-point value when the depletion in the solute concentration is significant. Motivated by these considerations, a model predictive controller is designed using the manipulation of the jacket temperature to produce crystals with a desired shape and size.

3.5.1 Model predictive control formulation

In this work, we consider the control of crystals aggregates using the moment models and the balance equations in a model predictive control (MPC) design. The control objective is to minimize the deviation of the average crystal shape, $\langle \alpha \rangle$, from a set-point value. The jacket temperature is chosen as a manipulated input, and only the measurements of the solute concentration and the crystallizer temperature are required for the computation of the optimal jacket temperature, assuming other factors remain constant.

The mass and energy balance equations (Eqs. 3.16 and 3.17) and the moment model (Eq. 3.26) are considered along with other practical constraints in the control formulation.

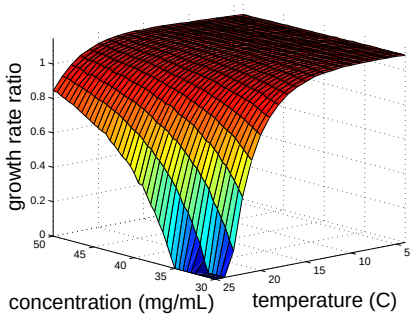

(a) Growth rate ratio

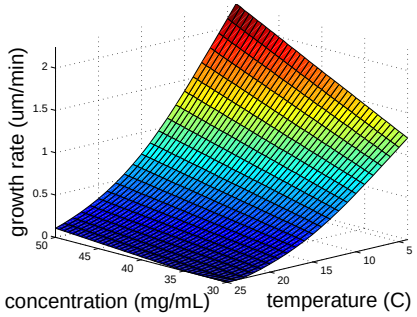

(b) Growth rate of the (110) face

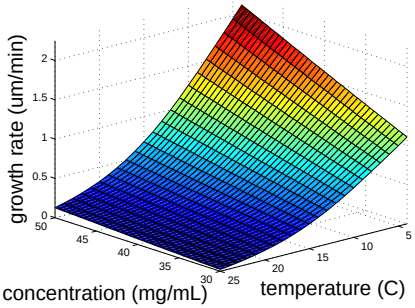

(c) Growth rate of the (101) face

Figure 3.4: Profiles for (a) the growth rate ratio between the (110) and (101) faces, and the growth rates for the (b) (110) and (c) (101) faces, over a protein concentration range from 30 to 50 mg/mL and a temperature range of 4 to 25°C. Each point on the three plots is generated by running the kMC simulation under open-loop conditions at pH= 4.5.

First, a constraint on the crystallizer temperature is imposed $\left(4^{\circ}\text{C} \leq T_j \leq 25^{\circ}\text{C}\right)$. Next, $R_T = 2.0^{\circ}$C/min is a constraint which restricts the maximum rate of change for the jacket temperature. The cost function penalizes the deviation of the average crystal shape, $\langle\alpha\rangle$, from a set-point value. The proposed MPC formulation is as follows:

$$
\begin{aligned}
&\underset{T_{j,1},\ldots,T_{j,i},\ldots,T_{j,p}}{\textit{minimize}} \quad \sum_{i=1}^{p} F_{\langle\alpha\rangle,i} \\
&\text{subject to} \quad F_{\langle\alpha\rangle,i} = \left(\langle\alpha\rangle - \alpha_{\text{set}}\right)^2 \\
&\qquad 4^{\circ}\text{C} \leq T_j \leq 25^{\circ}\text{C} \qquad \left|\frac{T_{j,i+1} - T_{j,i}}{\Delta}\right| \leq 2.0^{\circ}\text{C/min} \\
&\qquad \frac{dT}{dt} = -\frac{\rho_c \Delta H_c}{\rho C_p V}\frac{dM_1}{dt} - \frac{U_j A_j}{\rho C_p V}\left(T - T_{j,i}\right) \\
&\qquad \Delta c(t) = -\frac{\rho_c}{V}\frac{dM_1}{dt} \\
&\qquad \langle h_l(t_i)\rangle = \frac{\langle h_l(t_{i-1})\rangle M_0(t_{i-1})}{M_0(t_i)} + G_l(t_{i-1})\Delta \\
&\qquad \frac{dM_0}{dt} = B(T,c) - \alpha_{eff}\left(M_0 M_1 + 3M_{1/3}M_{2/3}\right) \\
&\qquad \frac{dM_1}{dt} = G_{volume} M_0 \\
&\qquad \frac{dM_2}{dt} = 2G_{volume} M_1 + 2\alpha_{eff}\left(M_1 M_2 + 3M_{4/3}M_{5/3}\right) \\
&\qquad M_k = M_0 V_g^k \exp\left(\frac{9}{2}k^2 ln^2\bar{\sigma}\right) \qquad \text{for } k = \left(\frac{1}{3},\frac{2}{3},\frac{4}{3},\frac{5}{3}\right) \\
&\qquad V_g = \frac{M_1^2}{M_0^{3/2}M_2^{1/2}} \qquad ln^2\bar{\sigma} = \frac{1}{9}ln\left(\frac{M_0 M_2}{M_1^2}\right) \\
&\qquad i = 1,2,\ldots,p \qquad \text{and} \qquad l \in \{110,101\}
\end{aligned}
\tag{3.30}
$$

where Δ is the sampling time, t is the current time, t_i, $i = 1,2,\ldots,p$, is the time of the i^{th} prediction step, $(t_i = t + i\Delta)$, t_f is the total simulation time, $F_{\langle\alpha\rangle,i}$ is the cost function penalizing the deviation of the average crystal shape $\langle\alpha\rangle$ from a desired crystal shape α_{set},

p is the number of prediction steps, $p\Delta$ is the prediction horizon, and $T_{j,i}$ is the jacket temperature at the i^{th} step, $\big(T_{j,i} = T_j(t+i\Delta)\big)$. The set of optimal manipulated input values along the prediction horizon, $(T_{j,1}, T_{j,2}, \ldots, T_{j,p})$, is obtained by solving the problem of Eq. 3.30. The controller is implemented in a receding horizon scheme where the first value of the optimal input trajectory, $T_{j,1}$, is applied to the process until the next sampling time. Then, a new protein concentration measurement is obtained from the kMC simulation, and the MPC problem of Eq. 3.30 is re-solved by rolling the horizon one step forward.

3.6 Closed-loop simulations of the batch crystallization process

The proposed model predictive controller solves a constrained minimization problem over a prediction horizon, and computes the optimal jacket temperature, which is then applied to the closed-loop system at each sampling time (Δ=1 second). Additionally, the uncertainty in the crystallizer is reflected through random fluctuations in the solute concentration with the Gaussian distribution presented in Eq. 3.31,

$$\langle C(t)\rangle = C_n, \qquad \langle C(t)C(t')\rangle = \sigma_n^2 C_n^2, \tag{3.31}$$

where C_n is the nominal concentration and $\sigma_n C_n$ is the standard deviation of the concentration measurements. For all closed-loop simulations, the nominal concentration is 47 mg/mL, and the standard deviation, $\sigma_n C_n$, is set to be 0.47 mg/mL at pH 4.5 and 4.0% NaCl. The volume of the crystallizer is 5 L. Since the MPC makes use of the steady-state

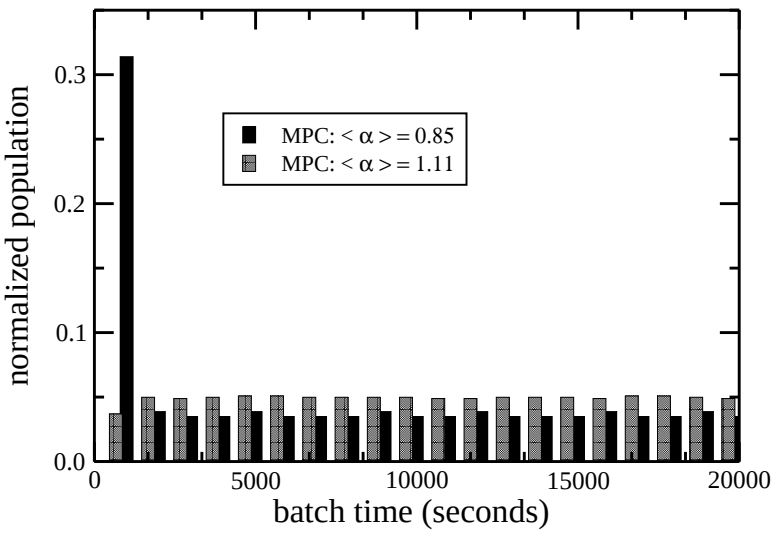

Figure 3.5: Normalized nucleation time distribution for the batch run under closed-loop MPC operation for $\alpha_{\text{set}} = 0.85$ and $\alpha_{\text{set}} = 1.11$.

growth rates (cf. Fig. 3.4(b) and 3.4(c)), the number of prediction steps is set to be $p = 1$. For the purpose of simulation, the solute concentration fluctuates every 1 second with the nominal value $C_n(t)$ at time t. The closed-loop simulation duration is $t_f = 20000$ seconds.

In the closed-loop simulations, two desired crystal morphologies, $\alpha_{\text{set}} = 1.11$ and $\alpha_{\text{set}} = 0.85$, are chosen where these two shapes represent the protein crystal with equidimensional and more elongated length in the (101) direction, respectively.

To verify the performance of the proposed MPC, its performance is compared with those of two other conventional control strategies, CTC and CSC. For further details regarding how CTC and CSC operate, readers may refer to [69]. Specifically in Fig. 3.5, for $\alpha_{\text{set}} = 0.85$, the optimal temperature is $\sim$24.2°C, and the nucleation of over 30% of the total crystals occurs within the first 5% of the entire batch run due to the high initial

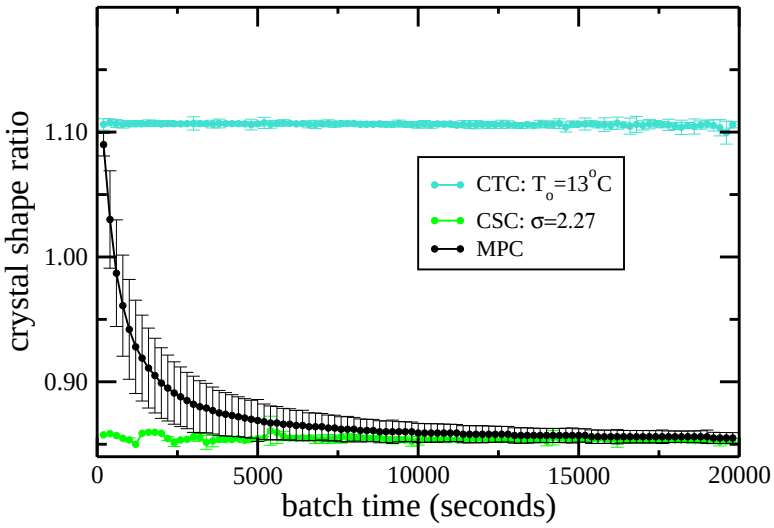

Figure 3.6: Profiles of the average crystal shape distribution with time under CTC and CSC. Additionally, MPC is shown with the set-point $\alpha_{\text{set}} = 0.85$.

supersaturation level maintained until the system reaches its optimal temperature. We note that the MPC in this case results in a broader crystal shape distribution compared to those of CTC and CSC from a desired set-point value owing to the biased nucleation in the beginning. In spite of this, the simulation under MPC shows a similar crystal shape distribution compared to that of CTC at $T_o = 24.2°\text{C}$ where the optimal temperature is maintained for the crystallizer over the entire batch.

The average crystal shape obtained at the end of the batch run for the MPC in Figs. 3.6 and 3.7 can be very narrow and even closer to the desired value when the initial temperature is much closer to the optimal temperature (for example, if T_o is changed from 13°C to 24.2°C). Furthermore, the controller performance can be further improved by adjusting R_T so that the system is able to change its temperature more quickly. For further analysis on

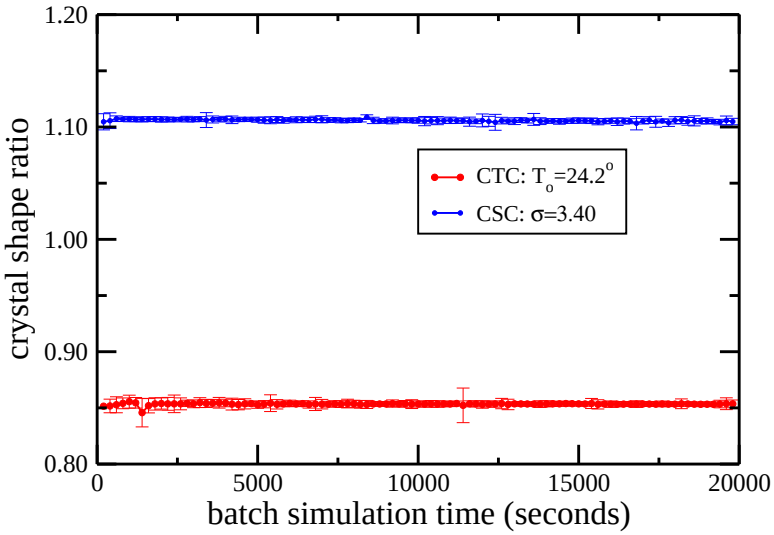

Figure 3.7: Profiles of the average crystal shape distribution with time under CTC and CSC.

this, readers may refer to [79].

For the closed-loop simulations at the lower set-point value, $\alpha_{\text{set}} = 0.85$, the simulation results are shown in Figs. 3.6, 3.7, and 3.8 for the evolution of the crystallizer temperature, the protein solute concentration, the supersaturation, and the average crystal shape throughout the batch operation. Additionally, the crystal shape distribution at four different times (5000, 10000, 15000, 20000 seconds) is presented in Fig. 3.13. In order to determine set-points for the CTC and CSC schemes, a simulation under MPC at $c = 47$ mg/mL and $T_o = 13°$C was run. For the temperature set-points of the simulations under CTC, two extremes of the temperature profile computed by the simulation under MPC are chosen as follows: $T_o = 13°$C and $T_o = 24.2°$C. Similarly, two extremes of the supersaturation profile computed by the simulation under MPC are chosen as follows: $\sigma = 2.27$ and $\sigma = 3.40$.

For the lower desired crystal growth rate ratio, $\alpha_{\text{set}} = 0.85$, it is recommended to start

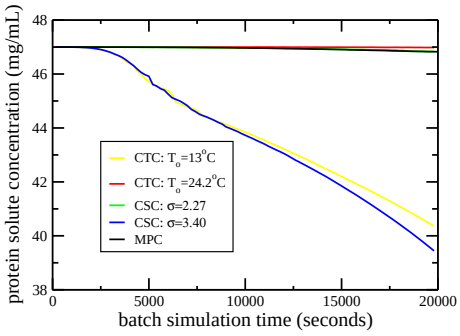

(a) protein solute concentration vs time

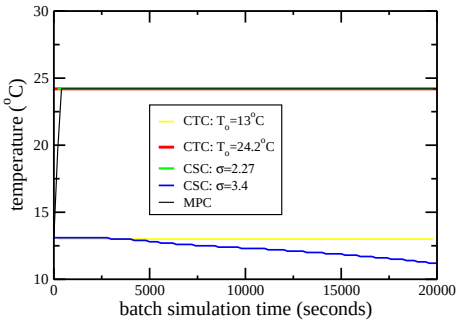

(b) crystallizer temperature vs time

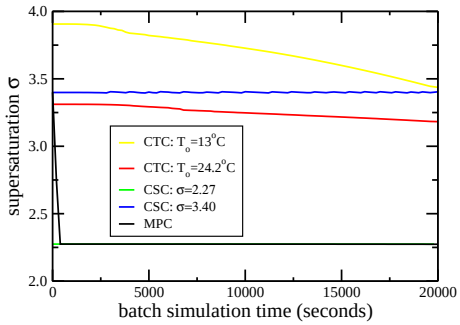

(c) supersaturation vs time

Figure 3.8: Profiles of protein solute concentration, crystallizer temperature, and supersaturation versus time under closed-loop MPC operation compared with closed-loop operations under CTC and CSC during the batch run. The growth rate ratio set-point value is set at $\alpha_{\text{set}} = 0.85$, and the data shown has different initial temperature values and supersaturation levels provided in the legend of each plot. For MPC, the starting temperature is 13°C.

the crystallizer with a higher initial temperature, allowing the system to achieve the optimal temperature earlier in the batch run which will result in a uniform crystal nucleation during the batch run, and the crystals will grow under optimal growth conditions from the beginning [66]. It is observed in Fig. 3.8(a) that the simulations under the CSC at $\sigma = 3.4$ and the CTC at $T_o = 13^{\circ}$C demonstrate significant depletion in the solute concentration because they both are at high supersaturation levels, and hence high nucleation and growth rates are expected. In contrast, in the proposed MPC, CTC at the high temperature $T_o = 24.2^{\circ}$C, and the CSC at the low supersaturation $\sigma = 2.27$, no significant solute concentration drop is observed as a result of the low nucleation and growth rates. On the other hand, in Figs. 3.6, 3.7, and 3.8, the solute concentration, the supersaturation, the temperature, and the average of the shape distribution with time under CTC at $T_o = 13^{\circ}$C are very similar to those of CSC at $\sigma = 3.40$. Therefore, we note that the CTC and CSC policies show similar controller performances when their supersaturation levels are nearly identical over most of the batch run. We also note that the proposed MPC with a relatively high initial temperature can outperform other conventional policies, and the performance of the MPC can be by far improved by adjusting the constraint on the rate of change for the jacket temperature.

In Fig. 3.8(b), the jacket temperature is increased early on in the batch run to the optimal value by the proposed MPC due to the fact that the solute concentration has minimal depletion for this T_o. The optimal temperature for the crystal growth at a low growth rate ratio is usually high when the system is especially sensitive to small changes in the solute concentration and the temperature as is shown in Fig. 3.4. The interested reader may refer

to our recent work [66] for further analysis on the sensitivity of the controller design in relation to the initial temperature of the crystallizer.

Control strategy	$\langle h_{110} \rangle$	r_{10}	r_{50}	r_{90}	span
MPC	26.04	3.13	23.72	48.71	1.91
CTC: T=13°C	41.27	0.52	3.43	20.94	5.96
CTC: T=24.2°C	20.11	0.70	18.04	39.20	2.13
CSC: $\sigma = 2.27$	46.06	8.02	41.82	78.73	1.69
CSC: $\sigma = 3.40$	45.33	0.60	2.89	19.25	6.44

Table 3.3: The simulation results for the crystal size in the (110) direction under MPC for $\alpha_{\text{set}} = 0.85$, as well as CTC and CSC. Units for the $\langle h_{110} \rangle$, r_{10}, r_{50}, and r_{90} are given in μm.

In Table 3.3, a comparison is shown under different control strategies for the average crystal size along the (110) direction, $\langle h_{110} \rangle$, and r_{10}, r_{50}, r_{90}, which are the 10%, 50%, and 90% population fractions. For instance, r_{10} for MPC is 3.13 μm, which means that 10% of crystals are smaller than 3.13 μm at the end of the batch run. The span, which is defined as $(r_{90} - r_{10})/r_{50}$, indicates the extent of crystal size distribution. In Table 3.3 and Figs. 3.6–3.7, it is demonstrated that the MPC is able to achieve a low polydispersity (a low span value) and a desired crystal shape distribution by appropriately dealing with the undesired effects such as the biased nucleation, disturbances, and the mismatch of moment models with the actual process. The controller performance can be further improved if we choose an initial temperature sufficiently close to the optimal temperature and use an actuator with

less restrictions on the jacket temperature change.

For $\alpha_{\text{set}} = 1.11$, a high supersaturation level is favored for crystal growth with equidimensional shape. As a result, the high nucleation and growth rates result in a significant drop in the solute concentration level. In Fig. 3.9, it is shown that the supersaturation level constantly fluctuates, which is attributed to the jacket temperature computed by the proposed MPC. Reflecting the heuristic that the system progresses from the metastable to the labile regime, the initial rise-and-fall in the supersaturation level can be understood as follows: Initially, the formation of small crystals occurs, and they grow spontaneously. Once a sufficient amount of nucleation occurs, the supersaturation level decreases to a minimum value and it eventually decreases the nucleation rate as well. In the end, the system proceeds to a regime where crystal growth dominates the crystal nucleation. The rise-and-fall in supersaturation, which results from the optimal temperature profile computed by the proposed MPC, extends to the end of the batch run as the solute concentration steadily decreases from 47 to 40 mg/mL as is shown in Figs. 3.9(a)–3.9(c). It is also demonstrated in Fig. 3.9(b) that the optimal temperature trajectory computed by the proposed MPC does not remain at a constant value, as the proposed MPC responds promptly to the solute concentration drop and disturbances in order to avoid the formation of small crystal fines at the end of the batch process. In Fig. 3.5, since the system reaches the optimal temperature quickly, the profile of nucleated crystals with time is uniform throughout the batch run. However, due to the insensitivity of the system to the changes in the supersaturation level in the high supersaturation region, the simulation results under other strategies are close to

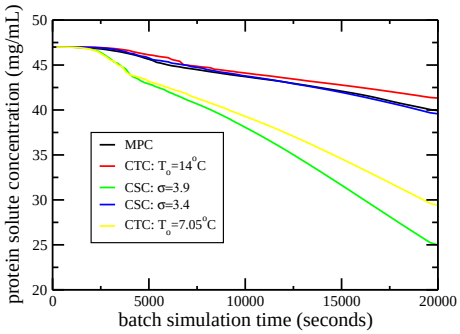

(a) protein solute concentration vs time

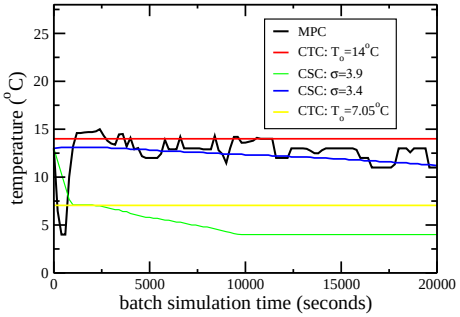

(b) crystallizer temperature vs time

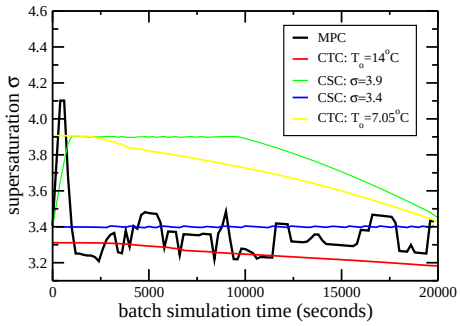

(c) supersaturation vs time

Figure 3.9: Profiles of protein solute concentration, crystallizer temperature, and supersaturation versus time under closed-loop MPC operation compared with closed-loop operation under CTC and CSC during the batch run. The growth rate ratio set-point value is set at $\alpha_{\text{set}} = 1.11$, and the data shown has different initial temperature values and supersaturation levels provided in the legend of each plot. For MPC, the starting temperature is 13°C.

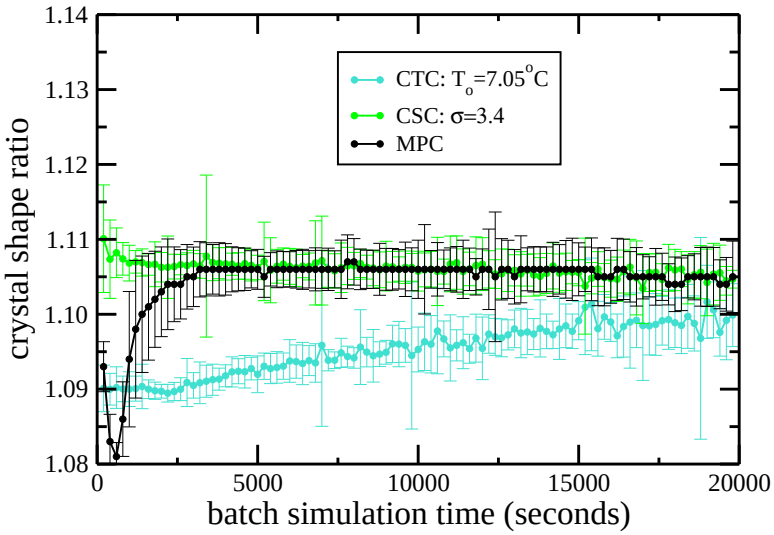

Figure 3.10: Profiles of the average crystal shape distribution with time under CTC and CSC. Additionally, MPC is shown using $\alpha_{\text{set}} = 1.11$.

those under MPC, as is seen in Figs. 3.10 and 3.11.

In Table 3.4, $\alpha_{\text{set}} = 1.11$ shows a high polydispersity because of the significant drop in the concentration, but a narrow crystal shape distribution is obtained by a nearly uniform crystal nucleation rate under MPC. The CTC at T=14°C and CSC with $\sigma = 3.4$ result in similar shape distributions to that of MPC, but they show high standard deviation in Figs. 3.10 and 3.11, and their spans are also high as is shown in Table 3.4, which implies that they are not robust when the depletion in the solute concentration is significant.

In Fig. 3.12, the more equidimensional crystal shape, $\alpha_{\text{set}} = 1.11$, can be achieved over a broad supersaturation range, and thus both the proposed MPC and other conventional strategies show good performances in regulating the crystal shape to a desired morphology. However, the conventional control strategies do not guarantee a low polydispersity, because

Control strategy	$\langle h_{110} \rangle$	r_{10}	r_{50}	r_{90}	span
MPC	31.30	0.49	5.24	14.5	2.67
CTC: T=7.05°C	73.61	0.45	1.97	3.84	1.72
CTC: T=14°C	23.10	0.74	4.30	17.35	3.87
CSC: $\sigma = 3.4$	33.98	0.93	4.84	20.88	4.12
CSC: $\sigma = 3.9$	88.17	0.41	1.45	3.55	2.16

Table 3.4: The simulation results for the crystal size in the (110) direction under MPC for $\alpha_{\text{set}} = 1.11$, as well as CTC and CSC. Units for $\langle h_{110} \rangle$, r_{10}, r_{50}, and r_{90} are given in μm.

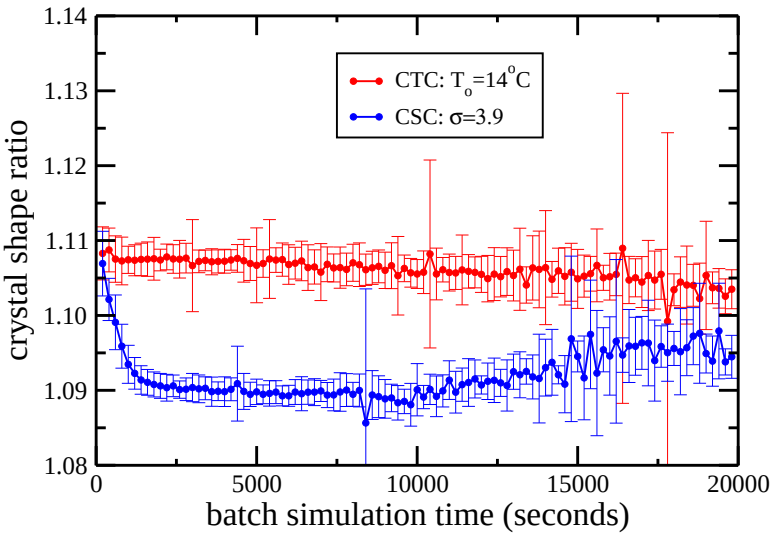

Figure 3.11: Profiles of the average crystal shape distribution with time under CTC and CSC.

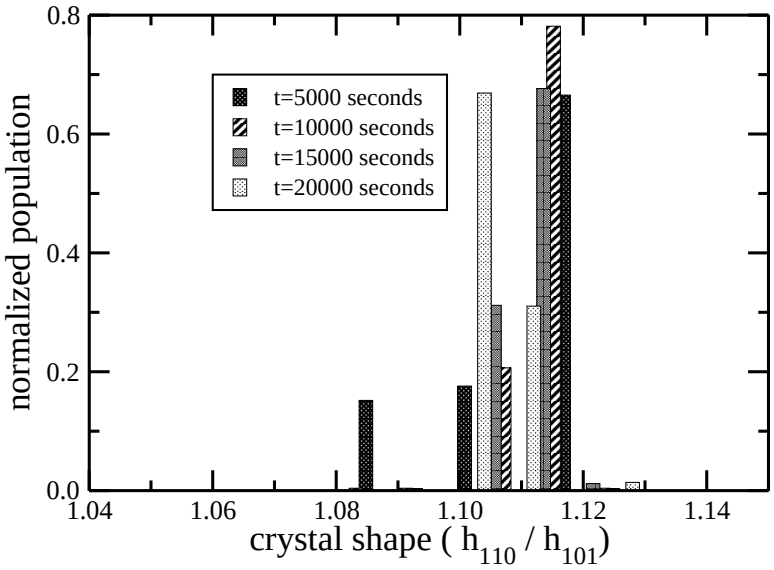

Figure 3.12: The normalized crystal shape distribution at four different times during the batch simulation under MPC for $\alpha_{\text{set}} = 1.11$.

polydispersity depends on the growth conditions as is shown in Table 3.4. In Fig. 3.13, it is apparent that the proposed MPC steadily drives the crystal shape distribution to a desired value, and eventually a narrow shape distribution is obtained at the end of the batch run.

In conclusion, MPC can successfully achieve the desired crystal shape distribution and is robust with respect to biased nucleation and a significant drop in the solute concentration, as has been demonstrated; however, whether a low polydispersity can be achieved is determined by the desired set-point value. For $\alpha_{\text{set}} = 0.85$, crystals with both the desired morphology and a low polydispersity can be achieved at a sufficiently high temperature in the crystallizer, which is typically close to an optimal temperature, because it takes less time for the system to reach its optimal state, causing uniform nucleation to occur through-

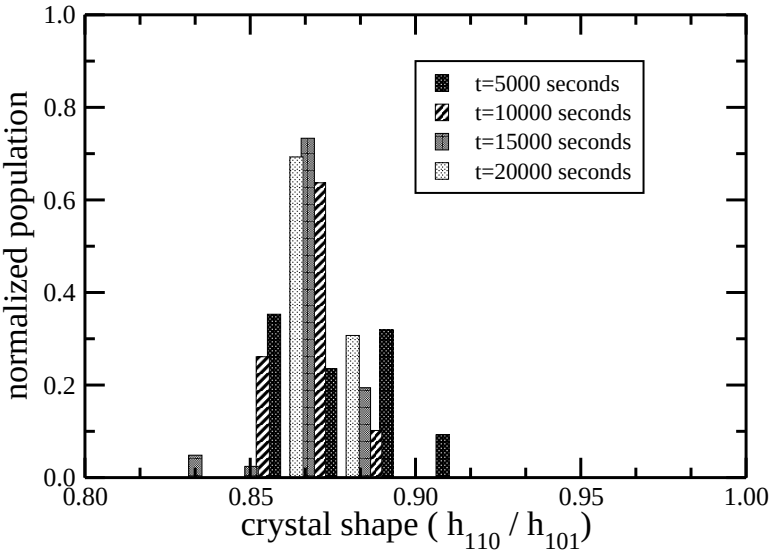

Figure 3.13: The normalized crystal shape distribution at four different times during the batch simulation under MPC for $\alpha_{\text{set}} = 0.85$.

out the batch run. For $\alpha_{\text{set}} = 1.11$, however, crystals with a narrow shape distribution and a high polydispersity can be obtained regardless of the initial temperature, because the crystallizer instantly responds to the depletion in the solute concentration, as is shown in Fig. 3.9. More details regarding robust control of crystallization systems and model predictive control can be found in [115, 23, 34].

On a final note, all the batch crystallization simulations executed in this work were done in parallel using Message Passing Interface (MPI) on the Hoffman2 cluster at UCLA. The Hoffman2 cluster is a shared resource comprised of 1032 nodes with a total of 9772 cores. The memory on each node, as well as the CPU speed, varies over the cluster. By using MPI we are able to divide the computational cost and memory requirements over multiple cores. The most computationally expensive part of these simulations is the crystal growth step.

Since the crystal growth step is executed independently for each crystal between controller calls, concentration fluctuations, and aggregation events, this step is easily parallelizable. It is also noted that the nucleation process does not affect the crystal growth stage since when a new crystal is born it directly enters the crystal growth process. Fig. 3.14 shows the amount of time necessary to run one batch crystallization simulation depending on the number of cores used. It can also be noticed that since the CPU speed varies, the error bars are quite large for the cases with less CPUs. Through our testing we found that using 20 cores was an appropriate tradeoff between time spent sending and receiving messages between cores while still reducing the time spent in the crystal growth process, as well as making sure the scheduler on the Hoffman2 cluster would accept our jobs in a reasonable amount of time. On average, the kMC simulations finished in 0.254 hours, spending 46% of the time in the crystal growth process for 20 cores. Due to the fact that all processors do not have the same speed, the process also spent 34% of the simulation time waiting for all cores to align in simulation time before controller calls, concentration fluctuations, and aggregation events. When looking at the single core case, 97% of the time was spent in the crystal growth process. It is noted that when using more cores, additional overhead is added when trying to balance the number of lysozyme crystals assigned to each core.

3.7 Conclusions

Initially, the present work focused on the modeling of protein crystal aggregation along with crystal nucleation and growth in a batch crystallization process via kinetic Monte

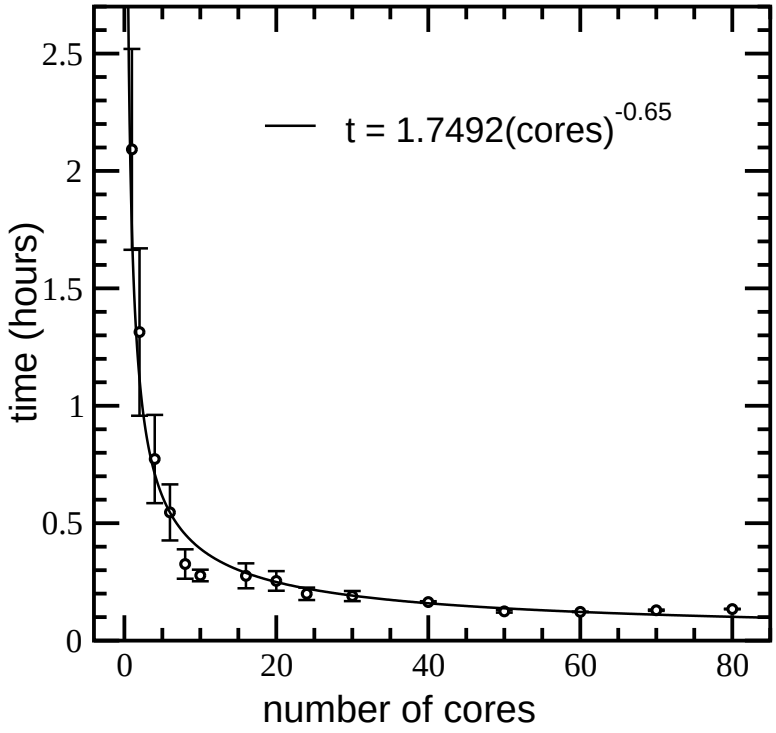

Figure 3.14: The amount of real time necessary to complete the batch crystallization simulations for varying numbers of cores. The standard error bars represent one standard deviation over 10 batch crystallization simulations for each point. The best fit line has equation: time $= 1.7492\,(\text{cores})^{-0.65}$ with an $R^2 = 0.9614$.

Carlo (kMC) simulation. More specifically, the kMC simulation modeled crystal growth via adsorption, desorption, and migration mechanisms on the (110) and (101) faces, and the nucleation rate from the experimental results by [41] was used in this work. Then the aggregation of protein crystals in the batch simulation was modeled through an aggregation kernel accounting for collision efficiency. Having considered the sizes of lysozyme crystals in this study, the aggregation was mainly induced by shear forces. Moreover, binary aggregation was assumed and thus an aggregate was formed as two crystals completely merged along their internal coordinates. Furthermore, we supposed the crystal shape of the aggregate followed that of the bigger crystal. Additionally, the high-dimensionality in the PBM could lead to a complicated controller design, which could not be immediately implemented in practice. To this end, moment models were derived to describe the dynamic evolution of the three leading moments of the crystal volume distribution. Finally, the moment model was used along with a nonlinear algebraic equation and energy and mass balances in order to design a novel model predictive controller (MPC). Under MPC, the shapes of crystal aggregates were regulated through the manipulation of the jacket temperature measuring the protein solute concentration and the crystallizer temperature, which was a common practice in batch crystallization.

Then the simulation results of the proposed MPC were compared with those of other strategies, CTC and CSC, where these strategies were not robust to a significant concentration drop and the uncertainties in the model. However, the proposed MPC was able to drive the crystal shape distribution to a desired set-point value by properly dealing with

the biased nucleation and a significant solute concentration drop. Moreover, the production of crystals with a low polydispersity was achieved depending on the desired crystal shape. For example, for $\alpha_{\text{set}} = 1.11$, crystals with a narrow shape distribution were obtained as the MPC promptly counteracted the depletion in the solute concentration. The ability to deal with this undesired effect was reflected as a fluctuation in the optimal crystallizer temperature computed by the proposed MPC as was shown in Fig. 3.9, and it led to an unsteady growth condition which produced crystals with a relatively high polydispersity. For $\alpha_{\text{set}} = 0.85$, however, crystals with a desired shape distribution and a narrow size distribution were achieved at a high initial temperature which was close to the optimal temperature, because the unwanted biased nucleation could be avoided. Additionally, allowing for a faster jacket temperature (manipulated input) change could be another choice reducing the amount of time needed to obtain crystals with desired properties, because the state of system could reach its optimal value faster.

3.8 Appendix

3.8.1 Derivation of the boundary condition for PBM

As is pointed out by [83], Eq. 3.18 can be rewritten by replacing the nucleation term with an appropriate boundary condition. Integrating Eq. 3.18 over V from 0^- to 0^+ gives,

$$G_{volume} \int_{0^-}^{0^+} \frac{\partial n(V,t)}{\partial V} dV = B(T,c),$$

since

$$\int_{0^-}^{0^+} B(T,c)\delta(V)dV = B(T,c),$$

and

$$\int_{0^-}^{0^+} \frac{\partial n(V,t)}{\partial t} dV = 0.$$

Additionally, when the average crystal volume is very small (i.e., $V \simeq 0$), aggregation rarely occurs and thus it is assumed that the aggregation terms are negligible,

$$\frac{1}{2}\int_{0^-}^{0^+}\int_0^V \beta(V-\bar{V},\bar{V})n(V-\bar{V})n(\bar{V})d\bar{V}dV = \int_{0^-}^{0^+} n(V)\int_0^\infty \beta(V,\bar{V})n(\bar{V})d\bar{V}dV = 0$$

and,

$$n(V,t) = 0 \text{ at } V = 0^- \qquad n(V,t) = n(0,t) \text{ at } V = 0^+,$$

assuming all nuclei form with size $V = 0$. Then Eq. 3.18 can be reduced to the following:

$$G_{volume}n(0,t) = B(T,c) \qquad \text{at } V = 0.$$

3.8.2 Derivation of the first moment model

We multiply the both sides of Eq. 3.18 by the j^{th} power of the crystal volume V^j, and integrate from $V = 0$ to $V = \infty$, to obtain:

$$\frac{dM_j}{dt} + G_{volume}\left(\left[V^j n(V,t)\right]_0^\infty - \int_o^\infty jV^{j-1}n(V,t)dV\right)$$
$$= \underbrace{\frac{1}{2}\int_0^\infty V^j \int_0^\infty \alpha_{eff}\beta(V-\bar{V},\bar{V})n(V-\bar{V})n(\bar{V})d\bar{V}dV - \int_0^\infty V^j n(V)\int_0^\infty \alpha_{eff}\beta(V,\bar{V})n(\bar{V})d\bar{V}dV}_{aggregation}$$

Suppose $n(V,t)$ is finite at $V = 0$ and $n(V,t) \to 0$ as $V \to \infty$. This implies that there are a finite number of nucleated crystals with infinitesimal volume but there are no crystals with

infinite size at time t. Since the total crystal volume is independent of the aggregation rate and depends only on the nucleation rate, the right hand side in the equation above, which is denoted as "aggregation," does not contribute to the first moment equation that describes the evolution of M_1 with time. As an example, the derivation of first moment model is presented with more details.

First moment: Making the substitution $V - \bar{V} = y$ and thus $dV = dy$ on the right hand side of the equation above, and using that $M_1 = \int_o^\infty V n(V,t) dV$, we obtain:

$$
\begin{aligned}
&\frac{dM_1}{dt} - G_{volume} M_0 \\
&= \frac{1}{2} \int_0^\infty V \left[\int_0^\infty \alpha_{eff} \beta\left(y, \bar{V}\right) n(\bar{V},t) d\bar{V} \right] n(y,t) dy - \int_0^\infty V \left[\int_0^\infty \alpha_{eff} \beta\left(V, \bar{V}\right) n(\bar{V},t) d\bar{V} \right] n(V,t) dV \\
&= \frac{1}{2} \int_0^\infty (\bar{V} + y) \left[\int_0^\infty \alpha_{eff} \left(\bar{V}^{1/3} + y^{1/3} \right)^3 n(\bar{V},t) d\bar{V} \right] n(y,t) dy \\
&- \int_0^\infty V \left[\int_0^\infty \alpha_{eff} \left(V^{1/3} + \bar{V}^{1/3} \right)^3 n(\bar{V},t) d\bar{V} \right] n(V,t) dV \\
&= \frac{\alpha_{eff}}{2} \left[8 M_1 M_3 + 6 M_2^2 + 2 M_0 M_4 \right] - \alpha_{eff} \left[M_0 M_4 + 4 M_1 M_3 + 3 M_2^2 \right] = 0
\end{aligned}
$$

Chapter 4

Modeling and control of crystal shape in continuous protein crystallization

4.1 Introduction

In this chapter, a continuous crystallization process with a fines trap is modeled in an effort to produce tetragonal hen egg white (HEW) lysozyme crystals with a desired shape distribution. The crystal shape of tetragonal lysozyme crystals is defined by the aspect ratio of the crystal heights in the directions of the (110) and (101) faces. A kinetic Monte Carlo (kMC) simulation is used to model the crystal nucleation, growth, and dissolution through a fines trap in a continuous crystallization process. Specifically, the crystal growth processes are simulated through adsorption, desorption, and migration mechanisms, and the crystal growth rates are calibrated through experimental data [31]. Additionally, a nucle-

ation rate expression is developed based on the results from an experimental work [41] to simulate the crystals nucleated at different times. Then, the method of moments is used to approximate the dominant behavior of a population balance equation (PBE) describing the evolution of the crystal volume distribution through the three leading moments. The moment model is used, along with solute mass and energy balance equations, to design a model predictive controller (MPC), which forces the crystallizer to produce crystals with a desired shape distribution. In the proposed MPC, the jacket temperature is manipulated to appropriately suppress the influence of undesired effects such as process disturbances and measurement noise, while handling significant changes in the set-point value. Furthermore, it is demonstrated that a continuous process with a fines trap can produce crystals with a low polydispersity.

4.2 Process descriptions

4.2.1 Continuous crystallizers

There are two types of continuous crystallizers that are widely used in the pharmaceutical industry: mixed suspension mixed product removals (MSMPR) and plug flow crystallizers (PFC). The choice of which to use is mainly determined by the characteristics of the process, as MSMPRs are generally preferred for low conversions and longer residence times, while PFCs are preferred for higher conversions with shorter residence times. In general, MSMPRs are preferred because they are fairly similar to the conventional batch processing

method traditionally used in the pharmaceutical industry [20].

The low conversion in MSMPRs can be improved by strategies such as the addition of a recycle stream or the addition of a fines trap. More specifically, an increase in yield was observed in [3, 130] through the implementation of recycle streams to MSMPR systems for the crystallization of cyclosporine. Additionally, it was demonstrated that the multistage MSMPR approach was simplified into a single-stage MSMPR by implementing a recycle stream and a fines trap [48].

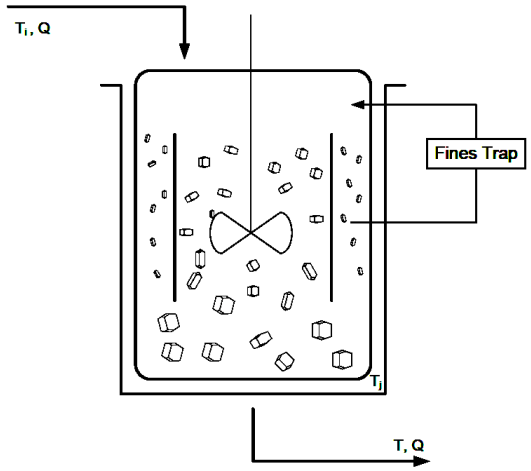

Figure 4.1: MSMPR crystallizer used in this work.

A fines trap is one of the most widely used product classification processes, and it can be established by shielding a part of a mixed crystallizer with a baffle as is shown in Fig. 4.1. As a result, the circulation of the continuous phase through the baffled region is typically slow, and larger crystals sink to the bottom of crystallizer while small crystal fines float on the top where a stream is drawn off and sent to the fines trap where small

crystals are dissolved and are recycled back to the crystallizer. By manipulating the stirrer speed in the baffled continuous crystallizer, we can control the maximum particle size $L_{\max}$ that will enter the fines trap stream. Specifically, while we can easily control the flow rate Q of a stream to the crystallizer, it is rather difficult to model and control the motion of particles which are under the influence of shear forces induced by agitation. In this work, we assume that the extent of aggregation is negligible because the residence time of a continuous process is typically one or two hours, and thus the average crystal size of the final products is not large enough to be influenced by the shear force due to significant stirring. Furthermore, a fines trap can considerably reduce the number of crystals, and thus it lowers the collision rates between crystals.

4.3 Description and modeling of continuous crystallization process

4.3.1 Crystal nucleation

In this work, only primary nucleation of HEW lysozymes is considered. Motivated by [92, 120, 67], we assume that crystals are nucleated with infinitesimal size (i.e., $V = 0$). Whether the nucleus grows or dissolves into the continuous phase is determined by the amount of free energy required for the formation of the crystal structure compared to the free energy required for the formation of the surface adjacent to the continuous phase. We

define the supersaturation $\sigma = \ln(C/S)$ as the difference in chemical potential between the current state, C (mg/mL), and the saturated state, S (mg/mL). The nucleation rate at pH = 4.5 and 4%(w/v) NaCl, $B(\sigma)$, is obtained from [41]:

$$B(\sigma) = \begin{cases} 0.041\sigma + 0.063 & \text{for} \quad \sigma \geq 3.11 \\ 8.0 \times 10^{-8} \exp(4.725\sigma) & \text{for} \quad \sigma < 3.11 \end{cases} \tag{4.1}$$

with units $[\text{cm}^{-3} \cdot \text{sec}^{-1}]$. Also, the solubility is an explicit function of temperature T (°C) and is computed using the following expression [12, 13]:

$$s(T) = 2.88 \times 10^{-4} T^3 - 1.65 \times 10^{-3} T^2 + 4.62 \times 10^{-2} T + 6.01 \times 10^{-1}. \tag{4.2}$$

4.3.2 Modeling of crystal growth and dissolution

In most crystallization processes, the solute molecules move from the bulk solution to the crystal surface and then they are converted into the crystalline form through surface reaction. The diffusion coefficient is usually high in crystallization systems, and thus the crystal growth is primarily controlled by the surface reaction (reaction-limited). As a result, the growth rate becomes size-independent, and it is usually assumed that the dissolution rate is also size-independent because the dissolution process is the reverse of the growth process [80].

For the purpose of comparison, the crystal is assumed to be equidimensional. As is given by [111], the time necessary to grow a lysozyme crystal from R_0=1 to R=10 μm,

assuming that the growth is reaction-limited, can be calculated as follows:

$$t_{rxn} = \frac{\rho_B}{k'' C_A M_B}(R - R_0)$$

Similarly, the time necessary to grow a lysozyme crystal from R_0 to R, assuming the growth is mass-transfer-limited, is:

$$t_{mt} = \frac{\rho_B}{2 D_A M_B C_A}(R^2 - R_0^2)$$

where k'' is the rate coefficient of surface reaction per unit area, M_B is the molecular weight of a lysozyme, C_A is the reactant concentration, ρ_B is the density of a lysozyme crystal, and D_A is the diffusion coefficient. The value of D_A is $10^5 - 10^6 \mathrm{cm}^2/\mathrm{sec}$ [62], and k'' can be considered the growth rate of the lysozyme crystal in this study, which is $0.1 - 1$ $\mu\mathrm{m}/\mathrm{min}$. Therefore, we can calculate t_{mt}/t_{rxn} from the preceding equations along with the approximated numbers for D_A and k'' as follows:

$$\frac{t_{mt}}{t_{rxn}} = \frac{k''}{2 D_A}(R + R_0) \tag{4.3}$$

where $t_{mt}/t_{rxn} \cong 10^{-11} - 10^{-13}$. Therefore, the crystal growth process is reaction-limited and thus is size-independent, as is the dissolution process.

4.3.3 Crystal growth

In kMC simulations, the protein crystals are very compact without voids and overhangs due to the solid-on-solid model which is assumed in this work. Additionally, along with a periodic boundary condition, we employ a square lattice model of length and width $N = 30$

sites because no finite size effects are observed [60]. Additionally, the rate equations are used to simulate the crystal growth mechanisms [32, 60].

Surface reaction	Rate equations
Adsorption r_a:	$K_0^+ \exp(\sigma)$
Desorption $r_d(i)$:	$K_0^+ \exp\left(\frac{\phi}{k_B T} - i\frac{E_{pb}}{k_B T}\right)$
Migration $r_m(i)$:	$K_0^+ \exp\left(\frac{\phi}{k_B T} - i\frac{E_{pb}}{k_B T} + \frac{E_{pb}}{2k_B T}\right)$

Table 4.1: Surface rate equations used to simulate the crystal growth process.

In Table 4.1, K_0^+ is the adsorption coefficient, i is the number of adjacent neighbors, E_{pb} is the average binding energy per bond, and ϕ is the total binding energy when a molecule is fully surrounded by neighbors (i.e., when i=4). Additionally, the fact that the migration rate is higher than the desorption rate is accounted for by multiplying an exponential factor into the desorption rate expression [60]. To evaluate a set of E_{pb} and ϕ values for the (110) and (101) faces, open-loop kMC simulations are executed by adjusting model parameters to make the difference between the growth rates in the simulations and the experiments from literature very small.

4.3.4 Mass and energy balances

Mass balance

A variety of shape descriptors are available such as roundedness, 2-D area, convexity, length/width, and aspect ratio. Therefore, the most appropriate shape descriptor to quantify

the crystal shape Fand use it in the controller design was carefully selected [51, 98]. A constant crystal shape factor has been widely used to model three-dimensional (3-D) crystal growth; however, this factor usually depends on the supersaturation level in practice. The mass balance is developed by modeling a representation of the crystal shape information as an aspect ratio of crystal heights in the (110) and (101) directions.

The inlet and outlet flows and the fines trap, which are key components in the continuous crystallizer, are considered in the mass balance for the protein solute in the continuous phase. Therefore, the amount of the protein solute, C, that remains in the continuous phase can be approximated through the following equation:

$$\frac{dC}{dt} = \underbrace{-\frac{\rho_c}{V_{MSMPR}}\frac{dV_{crystal}}{dt}}_{removed\ by\ crystals} + \underbrace{\frac{C_0}{\tau}}_{incoming\ flow} + \underbrace{\frac{\rho_c}{V_{MSMPR}}\frac{d\bar{V}_{fines}}{dt}}_{added\ by\ fines\ trap} - \underbrace{\frac{C}{\tau}}_{outgoing\ flow} \tag{4.4}$$

where V_{MSMPR} is the crystallizer volume, τ is the residence time of the crystallizer, and $V_{crystal}$ is the total volume of crystals removed from the continuous phase considering the geometry of the lysozyme crystals. In the kMC simulation, we have a constraint that the volume of crystals removed through the fines trap should not exceed 50% of the crystals leaving through the product stream. Initially, the residence time of a crystal is determined by the residence time distribution with a mean residence time of 1 hour. Then, the size of each crystal will be checked every second and, when its size is less than the cut-off size, it will be removed through the fines trap with a probability of 50% (i.e., accounting for the efficiency of the fines trap). However, in the controller, the moment models are solved in order to approximate the crystal volume distribution using the same residence time for both the product stream and the fines trap stream. We assume that the fines trap removes

crystals of volume $V_m (= 1\ \mu\text{m}^3)$ or smaller. To this end, $\bar{V}_{fines}$ is introduced to indicate the total volume of crystals passed through the fines trap and dissolved. In Eq. 4.4, the first term represents the depletion of the solute concentration in the continuous phase due to crystallization. Then, the second and third terms stand for the incoming flow of fresh solution to the crystallizer and the incoming flow of a particle-free solution from the fines trap, respectively. The last term indicates the outflow from the crystallizer.

Energy balance

The energy balance accounts for the temperature change due to the enthalpy of crystallization, the heat transfer by manipulating the jacket temperature, and the heat transported in/out in the inflow/outflow as follows:

$$\frac{dT}{dt} = -\frac{\rho_c \Delta H_c}{\rho C_p V_{MSMPR}} \frac{dV_{crystal}}{dt} - \frac{U_j A_j}{\rho C_p V_{MSMPR}} \left(T - T_j\right) + \frac{T_{in} - T}{\tau} \tag{4.5}$$

where T is the temperature inside the crystallizer, T_{in} is the inflow temperature, T_j is the jacket temperature, $\rho_c = 1400\ \text{mg/cm}^3$ is the crystal density, $\Delta H_c = -44.5\ \text{kJ/kg}$ is the enthalpy of crystallization, $\rho = (1000 + C)\ \text{mg/cm}^3$ is the continuous phase solution density, $C_p = 4.13\ \text{kJ/K} \cdot \text{kg}$ is the specific heat capacity, $V_{MSMPR} = 1\ \text{L}$ is the continuous crystallizer volume, $A_j = 0.25\ \text{m}^2$ is the surface area of crystallizer wall, and $U_j = 500$ $\text{kJ/m}^2 \cdot \text{h} \cdot \text{K}$, which is usually smaller than that of a batch process, is the heat transfer coefficient of the crystallizer wall. In practice, an appropriate cooling process is placed after the fines trap so that the changes in the crystallizer temperature caused by those streams are negligible.

In the kMC simulation, the residence time of a crystal is assumed to be distributed exponentially [76] as follows:

$$\exp(-T_r/\tau) = \mathrm{RN}$$

where T_r is the residence time of a crystal in the crystallizer, τ is the mean residence time, and RN is a random number generated between 0 and 1.

4.3.5 On-line imaging techniques for real-time measurement

As mentioned previously, crystal shape can significantly affect the bioavailability of pharmaceutical products. Nevertheless, the direct characterization of particle shape has been limited to off-line techniques. For example, the PharmaVision System 830 (PVS830) has been widely used for the characterization of chord length distribution (CLD) and crystal shape distribution (CSD). To perform the image analysis, a sample has to be collected using a pipette and quickly placed on a sample tray under a high-speed video camera. However, this imaging technique has a number of issues. Firstly, it cannot take images of particles as they actually exist in the crystallizer. Secondly, the sampling may alter the system condition and it leads to undesired dissolution, growth, and agglomeration of particles. Thirdly, in the course of sample preparation through dilution, cooling, or heating, the particles may be significantly damaged before they are measured.

Motivated by the above, new on-line in-process imaging techniques have been developed and released to the market such as the process vision measurement (PVM) developed by Lasentec, which has been widely used to capture the size and shape distributions of

crystals in crystallization processes. The PVM produces images of crystals which can be viewed through an external window. Through the PVM, measurements of both CLD and CSD are available by taking images of a number of crystals. Moreover, images taken using the PVM can be quickly verified through comparison with those from other analytical equipments such as focused beam reflectance measurement (FBRM) which is another widely used equipment using a focused beam of laser light to scan the size and shape of particles. As this light scans across those particles, passing in front of the probe window, light is scattered in all directions and the light scattered back to the probe is used to calculate CLD and the number of crystals every 30–40 seconds. Overall, the PVM, along with Lasentec FBRM, provides new insight into crystallization processes by quantifying CLD, CSD, and crystal count. To this end, a new software program has been developed to link PVM images with FBRM measurements [15, 14].

We note that the CLD and CSD are also influenced by system disturbances (i.e., particle orientation, noise in the system, and so on). Reflecting the presence of uncertainty in the kMC simulation, noise is introduced to the measurement of CLD and CSD in the simulations to account for the lack of knowledge of the direct measurements of actual particle distributions in practice. The noise is set to be 20% of its nominal value. In other words, when the measurements are sent to controller, they can be distorted up to 20% from their actual values.

4.4 Population balance modeling

4.4.1 PBE of crystal volume distributions

In this section, we describe the profile of the crystal volume distribution with time in a continuous crystallizer with a fines trap accounting for nucleation and crystal growth as follows:

$$\frac{\partial n(V,t)}{\partial t} + G_{vol}\frac{\partial n(V,t)}{\partial V} = -\underbrace{\frac{n(V,t)}{\tau}}_{outflow} - \underbrace{\bar{h}(V)\frac{n(V,t)}{\bar{\tau}}}_{fines\ trap} + \underbrace{\delta(V-V_0)B(\sigma)}_{nucleation} \tag{4.6}$$

where V denotes the crystal volume, t is the time, $\bar{\tau}$ is the residence time for the fines trap, $n(V,t)$ denotes the number of crystals with volume V at time t, $B(\sigma)$ is the nucleation rate, and dV/dt is the volumetric growth rate of crystals. The selection function for fines removal, $\bar{h}(V)$, is shown below:

$$\bar{h}(V) = \begin{cases} 1 & \text{for} \quad V \leq V_m \\ 0 & \text{for} \quad V > V_m \end{cases}$$

where V_m is the cut-off size of a fines trap. Approximating the total volume of the entire lysozyme crystal population as $V(t) \sim M_0(t)\langle h_{110}(t)\rangle^2\langle h_{101}(t)\rangle$, we can compute the volumetric growth rate G_{vol} by calculating the volumetric growth rate of crystals, dV/dt, using the following equation:

$$\begin{aligned} G_{vol} &= \frac{dV(t)}{dt} = \frac{dM_0(t)\langle h_{110}(t)\rangle^2\langle h_{101}(t)\rangle}{dt} \\ &= M_0(t)\left(2\frac{d\langle h_{110}\rangle}{dt}\langle h_{110}(t)\rangle\langle h_{101}(t)\rangle + \frac{d\langle h_{101}\rangle}{dt}\langle h_{110}(t)\rangle^2\right) + \frac{dM_0}{dt}\langle V(t)\rangle \end{aligned} \tag{4.7}$$

where the right hand side is readily available from measurements along with Eqs. 4.18-4.19, which will be discussed in Section 4.5.1. In the kMC simulation, which models an actual crystallizer, $dV_{crystal}/dt$ and $d\bar{V}_{fines}/dt$ are computed by summing the total volume of crystals grown and removed throughout a sampling time, respectively. Furthermore, $d\bar{V}_{fines}/dt$ is approximated by summing the number of crystals removed by the fines trap whose sizes are less than the cut-off size because the statistics (e.g., mean and standard deviation) of the crystal volume distribution are available from measurements along with Eqs. 4.13-4.14. Additionally, Eq. 4.6 can be rewritten with the addition of an appropriate boundary condition as is shown below:

$$\frac{\partial n(V,t)}{\partial t} + \frac{n(V,t)}{\tau} + \bar{h}(V)\frac{n(V,t)}{\bar{\tau}} + G_{vol}\frac{\partial n(V,t)}{\partial V} = 0 \tag{4.8}$$

$$n(0,t) = \frac{B(\sigma)}{G_{vol}}$$

Further details regarding the derivation of the boundary condition can be found in our previous work [67] .

4.4.2 Moment models

The numerical computation of the crystal volume distribution using Eq. 4.6 is computationally expensive and not readily accessible in general because of the complexity in the PBE. To deal with this issue, the method of moments is applied to Eq. 4.6 in order to derive moment models. Specifically, the j^{th} moment is defined as follows:

$$M_j = \int_o^\infty V^j n(V,t) dV \tag{4.9}$$

Along with the balance equations of Eqs. 4.4 and 4.5, the three leading moments are used to approximate the dominant behavior of the nucleation and crystal growth in a continuous crystallizer with a fines trap. For more details regarding the derivation of the following three moment models, the reader may refer to our earlier work [67].

Zeroth moment: The zeroth moment describes the rate of change of the total number of crystals with time and is the solution to the following differential equation given a suitable initial conditions:

$$\frac{dM_0}{dt} = B(\sigma) - \frac{M_0}{\tau} - \int_0^{V_m} \frac{n(V,t)}{\bar{\tau}} dV \tag{4.10}$$

where $B(\sigma)$ is replaced by the boundary condition of Eq. 4.8. On the right hand side, the term including an integral indicates the number of crystals below the cut-off size of the fines trap, and it can be evaluated from the measurement of the crystals when the statistics of size and shape distributions are available (e.g., mean, standard deviation).

First moment: The first moment describes the rate of change in the total crystal volume with time:

$$\frac{dM_1}{dt} = G_{vol} M_0 - \frac{M_1}{\tau} - \int_0^{V_m} V \frac{n(V,t)}{\bar{\tau}} dV \tag{4.11}$$

Second moment: The second moment describes the rate of change in the squared volume of the entire crystal population with time:

$$\frac{dM_2}{dt} = 2G_{vol} M_1 - \frac{M_2}{\tau} - \int_0^{V_m} V^2 \frac{n(V,t)}{\bar{\tau}} dV \tag{4.12}$$

When a fines trap is not used (i.e., $\bar{h}(V) = 0$), the first three moment equations and the mass and energy balance equations, Eqs. 4.4-4.5, constitute a closed set of differential

equations. However, the set of moment models above does not close owing to the classification function, $\bar{h}(V)$, for the fines trap. In order to close the set of moment equations and the balance equations, $n(V,t)$ is assumed to follow a normal distribution as follows:

$$n(V,t) = \frac{1}{\sigma_N\sqrt{2\pi}}\exp\left(-\frac{(V-\mu)^2}{2\sigma_N^2}\right) \tag{4.13}$$

where μ is the mean of crystal volume distribution, and σ_N is its standard deviation. They can be linked to the first three moments through the expressions below:

$$\mu = \frac{M_1}{M_0} \qquad\qquad \sigma_N = \sqrt{\frac{M_2}{M_0} - \mu^2} \tag{4.14}$$

The volume distribution of crystals obtained from the kMC simulations at $t = 1$ hour is presented in Fig. 4.2, verifying the normal distribution assumption. We should note that the volume distribution may show a biased bimodal behavior due to a burst of nucleation at a higher supersaturation level; however the assumption of a normal distribution is still acceptable as it does not affect the controller performance significantly in such a circumstance. Using Eqs. 4.13 and 4.14, we can numerically integrate the fines trap term in the moment models, Eqs. 4.10-4.12.

4.5 Open-loop simulation results

Analytically solving PBE for the profiles of the crystal shape and size distributions is equivalent to executing multiple kMC simulations over an infinite number of lattice sites. In this work, the kMC simulation is further developed from the previous work [67] to model

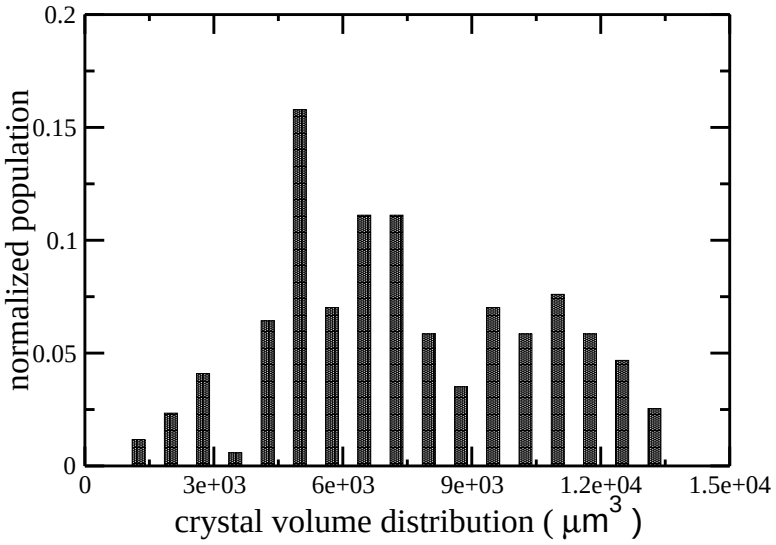

Figure 4.2: The normalized crystal volume distribution obtained from the kMC simulations at $t = 1$ hour.

continuous crystallization along with the dissolution of small crystal fines. In particular, $N = 30$ is used for the number of lattice sites, because no finite size effect is observed in the kMC simulations with lattice sites more than $N = 30$ as noted in [60].

In Fig. 4.3, the profiles of the number of crystals (M_0), the average crystal shape $\langle\alpha\rangle$, the crystallizer temperature, and the solute concentration obtained from the moment models (cf. Eqs. 4.10–4.12) are compared with those of the kMC simulation. The number of crystals decreases in the beginning until it reaches a steady-state because the simulation begins with a crystal-free solution. Afterward, the variables remain constant reflecting the steady-state operation of the continuous crystallizer. For example, the concentration and crystallizer temperature remain constant at 45 mg/mL and 23.7°C. Overall, the results obtained by the reduced moment models show a very good match with those of the kMC

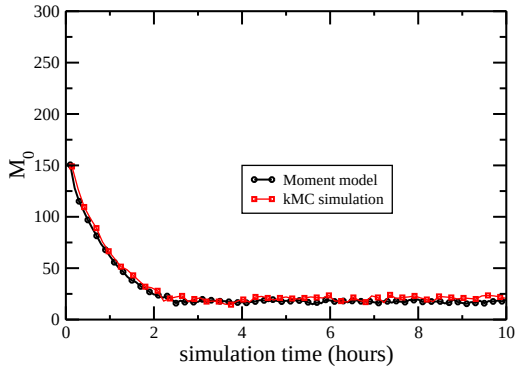

(a) number of crystals (M_0)

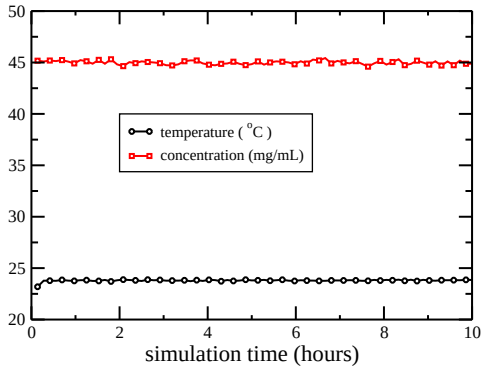

(b) temperature and concentration

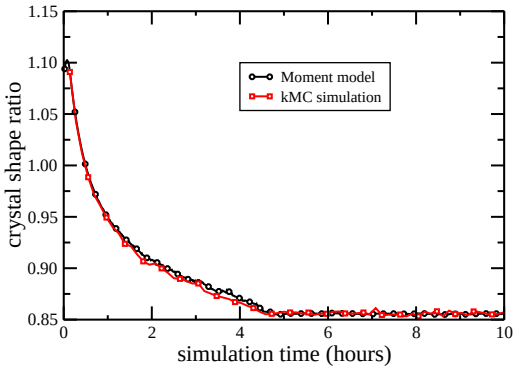

(c) crystal shape (α)

Figure 4.3: Profiles for open-loop simulations of the number of crystals, the crystallizer temperature, the protein solute concentration, and the average crystal shape ratio for the crystallization of tetragonal lysozyme protein at pH $= 4.5$.

simulation.

Sometimes, highly oscillatory behavior takes place in the crystallizer as a result of the interplay between nucleation and crystal growth. As is described in [22, 23], this is mainly caused by the nonlinearity in the nucleation rate (i.e., exponential dependence on supersaturation) as compared to that in the growth rate (i.e., linear dependence on supersaturation) which causes the following scenario: The number of fines progressively decreases as the supersaturation drops due to the consumption of protein solute by the crystal growth as well as the nucleation. As a consequence, the supersaturation level drops to a point where the nucleation rate begins to drop drastically, and thus no further nucleation occurs and the present small crystal fines grow into coarse crystals. Then, the supersaturation level starts to increase due to the absence of the nucleation until it reaches a point where a burst in the nucleation occurs with the production of a large number of fines. In this study, however, this oscillatory behavior of crystal size, number of crystals, supersaturation level, and so on, is not observed because the working range (e.g., the supersaturation level) is relatively high so that the nucleation rate shows a linear dependence on the supersaturation level (cf. the regime where $\sigma \geq 3.11$ in Eq. 4.1).

In Fig. 4.5, $\left(\phi/k_B, E_{pb}/k_B\right)$ values in the directions of the (110) and (101) faces are $(1077.26\ K, 227.10\ K)$ and $(800.66\ K, 241.65\ K)$, respectively, $K_o^+ = 0.211\ \mathrm{s}^{-1}$ is used for the open-loop simulation, and the crystal growth rates at 4%(w/v) NaCl and pH = 4.5 have been compared with the experimental results from [31] at 3.5% and 5.0% NaCl.

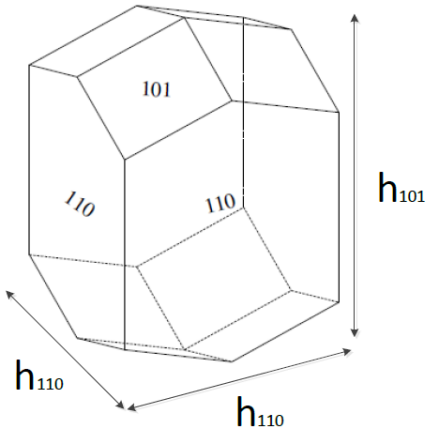

Figure 4.4: Geometry of tetragonal lysozyme crystal.

4.5.1 Modeling of crystal shape distribution from measurements

In kMC simulation, the 3-D crystal growth is modeled along the two representing characteristic lengths, h_{110} and h_{101}, which are shown in Fig. 4.4. Furthermore, the growth rates, $G_{110}(\sigma)$ and $G_{101}(\sigma)$, from Fig. 4.5 are approximated by the following polynomial expressions as functions of supersaturation:

$$\begin{aligned} G_{110}(\sigma) &= 0.1843 \times \sigma^3 - 1.1699 \times \sigma^2 + 2.8885 \times \sigma - 2.5616 \\ G_{101}(\sigma) &= 0.1893 \times \sigma^3 - 1.2264 \times \sigma^2 + 2.9887 \times \sigma - 2.5348 \end{aligned} \tag{4.15}$$

with units μm/min. These polynomials fit the experimental results very well with an R^2 value of nearly 1. Additionally, we note here that the growth rate ratio, $G_{110}(\sigma)/G_{101}(\sigma)$, is equal to the aspect ratio between the two heights at the steady-state.

The measurements of the mean of CLD, $\langle h \rangle$, and the mean of CSD, $\langle \alpha \rangle$, are available through the measurements of the crystals inside the crystallizer. By the definition of CLD

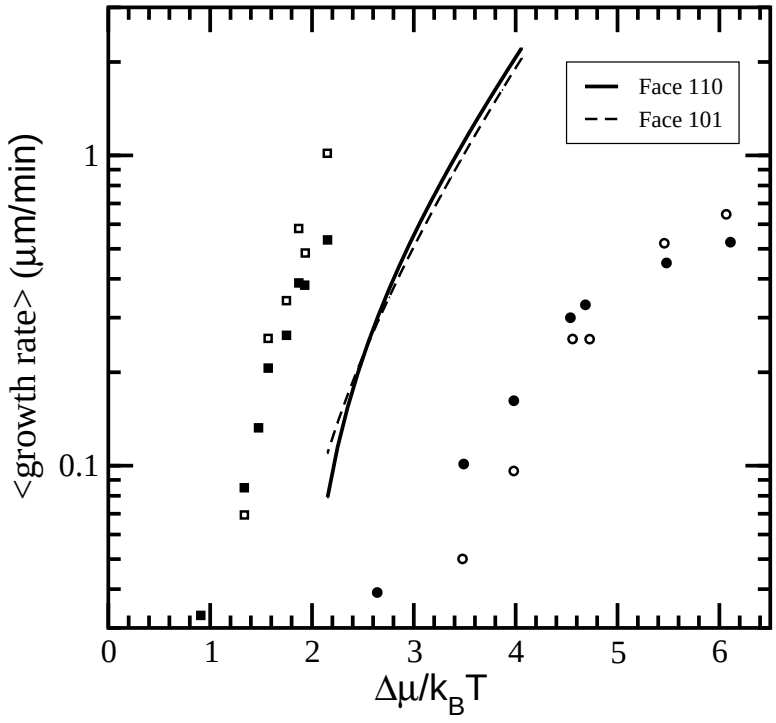

Figure 4.5: The solid and dashed lines show the growth rates for the kMC model on the (110) and (101) faces at $C = 45$ mg/mL and 4% NaCl. The (●)/(○) represent the growth rates for the (101) and (110) faces with 3.5% NaCl and the (■) and (□) represent the growth rates with 5% NaCl at pH= 4.6, which are both taken from [31] .

and CSD, we can link $\langle h \rangle$ and $\langle \alpha \rangle$ with $\langle h_{110} \rangle$ and $\langle h_{101} \rangle$ as follows:

$$\langle \alpha \rangle \approx \frac{\langle h_{110} \rangle}{\langle h_{101} \rangle} \qquad \langle h \rangle \approx \frac{\langle h_{110} \rangle + \langle h_{101} \rangle}{2} \tag{4.16}$$

In general, it is nearly impossible to obtain online measurements of the average crystal height in each direction, $\langle h_{110} \rangle$ and $\langle h_{101} \rangle$, during the processing. Instead, we will approximate the average heights on each face with the measurements of $\langle h \rangle$ and $\langle \alpha \rangle$, which are available through the PVM and FBRM:

$$\langle h_{101} \rangle = \frac{2\langle h \rangle}{\langle \alpha \rangle + 1} \qquad \langle h_{110} \rangle = \frac{2\langle h \rangle \langle \alpha \rangle}{\langle \alpha \rangle + 1} \tag{4.17}$$

We additionally note here that $M_0(t)$ is the number of crystals inside the crystallizer, which can also be measured using the FBRM. Then, we will make predictions of the average height of the (110) crystal face using the following ODE:

$$\frac{d\langle h_{110} \rangle}{dt} = G_{110} - \frac{BV_{MSMPR}\langle h_{110} \rangle}{M_0} \tag{4.18}$$

In the same manner, the average height of the (101) crystal face can be predicted as follows,

$$\frac{d\langle h_{101} \rangle}{dt} = G_{101} - \frac{BV_{MSMPR}\langle h_{101} \rangle}{M_0} \tag{4.19}$$

By combining the equations above, we can predict the average crystal shape in the following manner:

$$\langle \alpha \rangle \approx \frac{\langle h_{110}(t) \rangle}{\langle h_{101}(t) \rangle} \tag{4.20}$$

4.6 Model predictive control of crystal shape in continuous crystallization

4.6.1 Real-time feedback control of crystal shape

In order to control the crystal shape by manipulating the jacket temperature in the crystallizer, a control scheme inspired by our previous work [69, 67] is proposed in this work. The incoming stream to the crystallizer is a crystal-free solution with a protein solute concentration C=45 mg/mL at a flow rate of Q. At the same rate, crystals are removed from the crystallizer in the outgoing stream which has a solute concentration that is identical to that in the continuous phase in the crystallizer. In the simulation, it is assumed that CLD and CSD are measured in real time and that the measurements are used to estimate the average aspect ratio $\langle \alpha \rangle = \langle h_{110} \rangle / \langle h_{101} \rangle$ shown in Eq. 4.20. This can be achieved in practice using the aforementioned imaging techniques such as PVM and FBRM. Additionally, noise that fluctuates up to 20% from the nominal value is introduced to account for inaccuracies in currently available measurement techniques. Along with the noise, measurements are sent to a controller which computes the optimal jacket temperature to control the crystal shape $\langle \alpha \rangle$ to a desired value. Please note that the set-points $\alpha_{\text{set}} = 1.1$ and $\alpha_{\text{set}} = 0.85$ correspond to an equidimensional crystal and an elongated prism, respectively. For example, if a higher aspect ratio (elongated prism) is desired, the controller lowers the jacket temperature and thus the crystallizer temperature is lowered to a moderate value that favors the production of the desired shape.

4.6.2 Model predictive control formulation

A continuous crystallization process with a fines trap is modeled through a set of moment models along with the mass and energy balances in order to describe the evolution of the crystal size and shape distributions with time. Through the modeling of the crystallization process, we design a model predictive controller to regulate the shape and size distributions of crystals nucleated during the process. The controller minimizes the sum of the deviations of the average crystal aspect ratio and the growth rate ratio from the desired values while penalizing the control action. The jacket temperature is the manipulated input. However, in the continuous crystallizer, the proposed control design can be applied to the case of multiple inputs [1, 129, 86, 82] such as the solute concentration in the feed stream, the flow rates of the fines trap stream, and so on. Additionally, the measurements of the solute concentration, CLD and CSD, are assumed to be available at every sampling time (Δ=40 seconds). In particular, the uncertainty in the measurement of the solute concentration is reflected in the simulation by introducing the fluctuation of the concentration in the manner described in our earlier work [67].

In the control formulation, several process limitations are taken into account in the form of constraints along with the mass and energy balances (Eqs. 4.4 and 4.5). A limit on the range of the crystallizer temperature ($4^{\circ}\text{C} \leq T \leq 25^{\circ}\text{C}$), is imposed to prevent lysozyme proteins from being damaged. Additionally, there is a limit on the rate of the jacket temperature change of 2.0°C/min to account for actuator limitations. The cost function of the optimal control problem has penalties on the deviations of both $\langle \alpha \rangle$ and G_{110}/G_{101} from

the parameter α_{set} corresponding to the desired crystal shape, as well as a penalty on the control input. Furthermore, by adjusting the coefficients for the penalties on the off-spec production of the crystal shape and the control action, we can prevent unnecessarily aggressive control action. For example, when the penalty on the off-spec production of the crystal shape is more heavily weighted, the control actions will quickly force the crystals to reach a desired growth condition, subject to other constraints. On the other hand, when the penalty on the control actions is more heavily weighted, the controller will force the crystals to the desired growth condition more slowly. However, this is outside the scope of this work and will be further considered with details in the future. The MPC has the

following form:

$$
\begin{aligned}
\underset{T_{j,1},\ldots,T_{j,i},\ldots,T_{j,p}}{\text{minimize}} \quad & \sum_{i=1}^{p} w_1 \left(\frac{\langle \alpha(t_i) \rangle - \alpha_{\text{set}}}{\alpha_{\text{set}}} \right)^2 + w_2 \left(\frac{\frac{G_{110}(\sigma(t_i))}{G_{101}(\sigma(t_i))} - \alpha_{\text{set}}}{\alpha_{\text{set}}} \right)^2 + w_3 \left(\frac{T_{j,i+1} - T_{j,i}}{T_{j,i+1}} \right)^2 \\
\text{subject to} \quad & 4^\circ\text{C} \leq T_i \leq 25^\circ\text{C} \qquad \left| \frac{T_{j,i+1} - T_{j,i}}{\Delta} \right| \leq 2^\circ\text{C/min} \\
& G_{110}(\sigma) = 0.1843 \times \sigma^3 - 1.1699 \times \sigma^2 + 2.8885 \times \sigma - 2.5616 \\
& G_{101}(\sigma) = 0.1893 \times \sigma^3 - 1.2264 \times \sigma^2 + 2.9887 \times \sigma - 2.5348 \\
& \frac{dM_0}{dt} = B(\sigma) - \frac{M_0}{\tau} - \int_0^{V_m} \frac{n(V,t)}{\bar{\tau}} dV \\
& \frac{dM_1}{dt} = G_{vol} M_0 - \frac{M_1}{\tau} - \int_0^{V_m} V \frac{n(V,t)}{\bar{\tau}} dV \\
& \frac{dM_2}{dt} = 2G_{vol} M_1 - \frac{M_2}{\tau} - \int_0^{V_m} V^2 \frac{n(V,t)}{\bar{\tau}} dV \\
& \frac{dC}{dt} = -\frac{\rho_c}{V_{MSMPR}} \frac{dM_1}{dt} + \frac{C_0}{\tau} + \frac{\rho_c}{V_{MSMPR}} \frac{d}{dt} \left(\int_0^{V_m} V \frac{n(V,t)}{\bar{\tau}} dV \right) - \frac{C}{\tau} \\
& \frac{dT}{dt} = -\frac{\rho_c \Delta H_c}{\rho C_p V_{MSMPR}} \frac{dM_1}{dt} - \frac{U_j A_j}{\rho C_p V_{MSMPR}} \left(T - T_j \right) + \frac{T_{in} - T}{\tau} \\
& \frac{d\langle h_l \rangle}{dt} = G_l(\sigma) - \frac{B(\sigma) V_{MSMPR} \langle h_l(t) \rangle}{M_0(t)} \\
& \langle \alpha(t) \rangle \approx \frac{\langle h_{110}(t) \rangle}{\langle h_{101}(t) \rangle} \qquad \sigma = \ln(C/s) \\
& i = 1, 2, \ldots, p \qquad \text{and} \qquad l \in \{110, 101\}
\end{aligned}
\tag{4.21}
$$

where $p = 10$ is the number of prediction steps, w_1, w_2, w_3 are weighting coefficients, $t_i = t + i\Delta$ is the time of the i^{th} prediction step, and $T_{j,i}$ is the jacket temperature at the i^{th} prediction step. At every sampling time, the first three moments and the balance equations are updated along with the rate of change of the average height on each face l (cf. Eqs. 4.18–4.20). Then, the first value of the set of optimal jacket temperatures, $(T_{j,1}, T_{j,2}, \ldots, T_{j,p})$, is

applied to the system over the following sampling time. Then, a set of new measurements for CLD, CSD, protein solute concentration, and the number of crystals is collected from the kMC simulation, and a new set of optimal jacket temperatures is obtained by re-solving Eq. 4.21 based on the new measurements. In [116], empirical expressions are used to model the evolution of crystallization including both nucleation and crystal growth. However, in this work, the kMC simulations are used for more realistic modeling of a continuous crystallization process based on the rate equations described in Table 4.1. Additionally, readers who are interested in robust model predictive control of a crystallization process may refer to [115, 23].

4.7 Continuous crystallization under closed-loop operation

In Fig. 4.5, it is shown that the value of growth rate ratio $G_{110}(\sigma)/G_{101}(\sigma)$ ranges from 0.7 to 1.1. Two desired crystal morphologies, $\alpha_{\text{set}} = 1.1$ and $\alpha_{\text{set}} = 0.86$, are chosen as desired set-points in the closed-loop simulations.

Due to the dependence of the nucleation rate on the supersaturation level, an abrupt change in the crystallizer temperature in an effort to achieve a desired optimal temperature may result in biased nucleation. The biased nucleation is cumbersome, because the crystals nucleated in the earlier stage can go through undesired growth conditions, which leads to poor controller performance. In our earlier work [66], it was shown that, when the desired

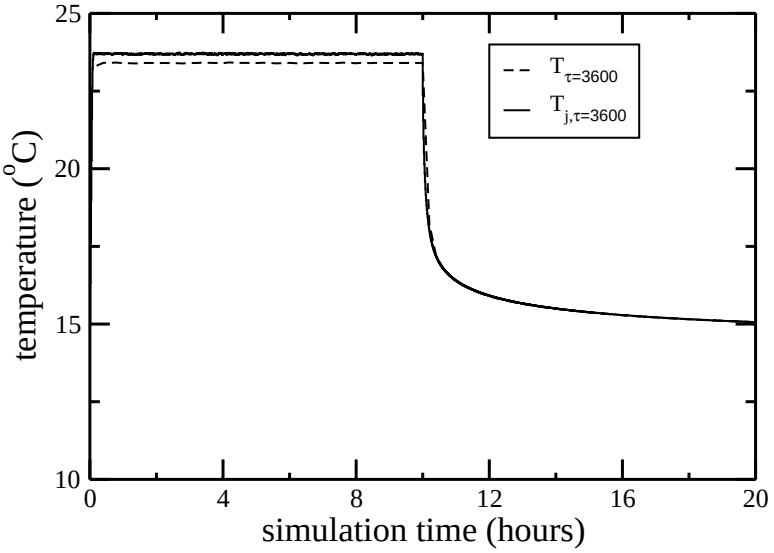

Figure 4.6: The profile of crystallizer temperature (T) and jacket temperature (T_j) at $\tau =$ 3600 seconds under MPC for the initial crystal shape set-point value, $\alpha_{\text{set}} = 0.86$. After $t = 10$ hours, the set-point is changed to $\alpha_{\text{set}} = 1.1$.

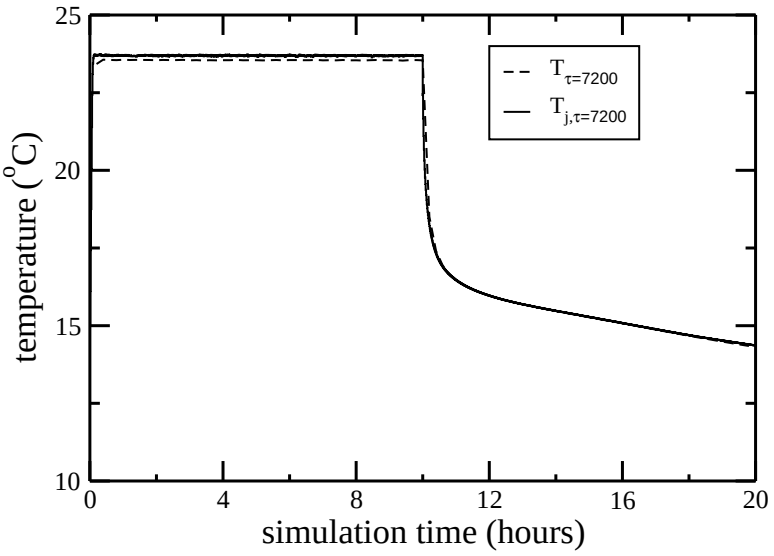

Figure 4.7: The profile of crystallizer temperature (T) and jacket temperature (T_j) at $\tau =$ 7200 seconds under MPC for the initial crystal shape set-point value, $\alpha_{\text{set}} = 0.86$. After $t = 10$ hours, the set-point is changed to $\alpha_{\text{set}} = 1.1$.

shape is $\alpha_{\text{set}} = 0.86$ and the initial temperature is $T_0 = 5°\text{C}$, the corresponding optimal temperature is $\sim$23.7°C and the nucleation of $\sim$34% of the entire crystal population occurs within the first $\sim$5% of the entire 4000-second batch process. In a continuous crystallizer, however, the issue with the biased nucleation can be avoided by simply operating a system at a steady-state, where the nucleation rate remains constant.

The steady-state crystallizer temperature is determined by the interplay among the inflow, crystallizer, and jacket temperatures as is shown in the energy balance equation (cf. Eq. 4.5). As in a batch process, the initial crystallizer temperature, which is equivalent to the inflow temperature, is important to the controller performance. For example, if the inflow temperature is too far from an optimal temperature, it results in a discrepancy between

the optimal temperature and the steady-state temperature due to the limited heat transfer rate. The difference can be more critical to the controller performance when the production of crystals with a lower set-point value is desired, because crystals with a low $\langle\alpha\rangle$ are usually produced at a high temperature where the crystal morphology is very sensitive to small changes in the supersaturation level [66]. In such cases, we can achieve better controller performance through the following: Firstly, adjusting the inflow temperature appropriately can enhance the performance of the proposed MPC by achieving a crystallizer temperature which is closer to an optimal temperature. Secondly, the heat transfer rate can be increased by using a material with a higher overall heat transfer coefficient, U_j, and thus the discrepancy can be reduced. Thirdly, the choice of an appropriate residence time is also important because the crystallizer temperature at steady-state is influenced by the residence time (cf. Eq. 4.5). For example, if the residence time is too small (e.g., less than an hour), crystals with desired shape and size distributions cannot be produced because crystals do not stay inside a crystallizer for a sufficient amount of time. On the other hand, if the residence time is too large, the dynamics of a continuous process become similar to those of a batch process in that crystals stay for a very long time inside a crystallizer, and thus a severe drop in the protein solute concentration is observed. Specifically, it is shown in Figs. 4.6, 4.7 and 4.8 that increasing the residence time will enable the system to reach a steady-state temperature which is much closer to a desired value, and thus will result in a narrow range of desired crystal shape distributions. Moreover, when $\tau \geq 2$ hours, a significant concentration drop was observed, and thus simply lowering temperature is not sufficient to maintain

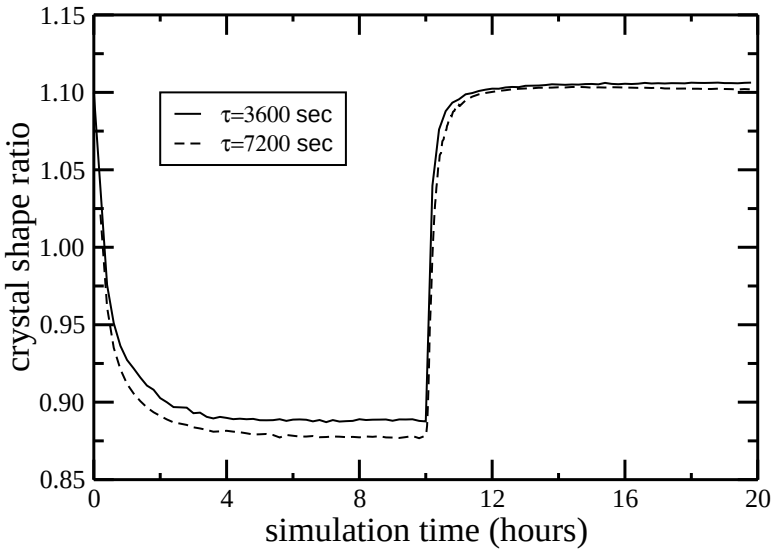

Figure 4.8: The profile of the average crystal shape $\langle\alpha\rangle$ under MPC for the initial crystal shape set-point value, $\alpha_{\text{set}} = 0.86$. After $t = 10$ hours, the set-point is changed to $\alpha_{\text{set}} = 1.1$.

the supersaturation level at an optimal value. It thus leads to poor controller performance, as is shown in Figs. 4.8 and 4.9.

In Figs. 4.6 to 4.11, the foregoing analysis is demonstrated through the profiles of the crystallizer temperature, the jacket temperature, the protein solute concentration, the average crystal volume, and the average crystal shape throughout the simulation at different residence times. In the beginning, the jacket temperature increases to the optimal value by the proposed MPC as is shown by Figs. 4.6 and 4.7, and the crystallizer temperature is driven by the jacket temperature accordingly. A burst of crystal nucleation, which is caused by a high supersaturation level, is appropriately suppressed through a fines trap where most of the small crystal fines are destroyed by adjusting the temperature, and thereby dissolution rates. As a result, large crystals grow larger and small crystal fines are dissolved back to the

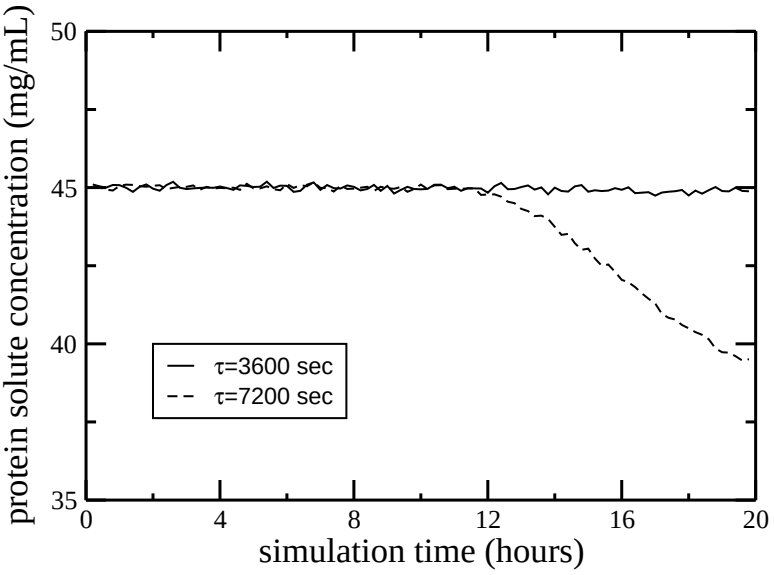

Figure 4.9: The profile of solute concentration (C) under MPC for the initial crystal shape set-point value, $\alpha_{\text{set}} = 0.86$. After $t = 10$ hours, the set-point is changed to $\alpha_{\text{set}} = 1.1$.

continuous phase. However, we note that no significant rise in the solute concentration is observed because typically the fraction of fines removed is $10^{-6} - 10^{-5}$ of the production rate on a mass basis.

In order to test the response time of the MPC to a change in the desired set-point, after 10 hours, the set-point is changed from $\alpha_{\text{set}} = 0.86$ to $\alpha_{\text{set}} = 1.1$ where a high supersaturation level is favored for the production of crystals with a shape more elongated in the (110) direction. As a result, the crystallizer temperature is decreased to $T = 15.0^{\circ}$C, owing to the jacket temperature computed by MPC, as is shown in Figs. 4.6 and 4.7. Specifically, for the closed-loop simulation of $\tau = 1$ hour, the crystallizer temperature remains constant once the system reaches a new steady-state for $\alpha_{\text{set}} = 1.1$. However, for $\tau = 2$ hours, the

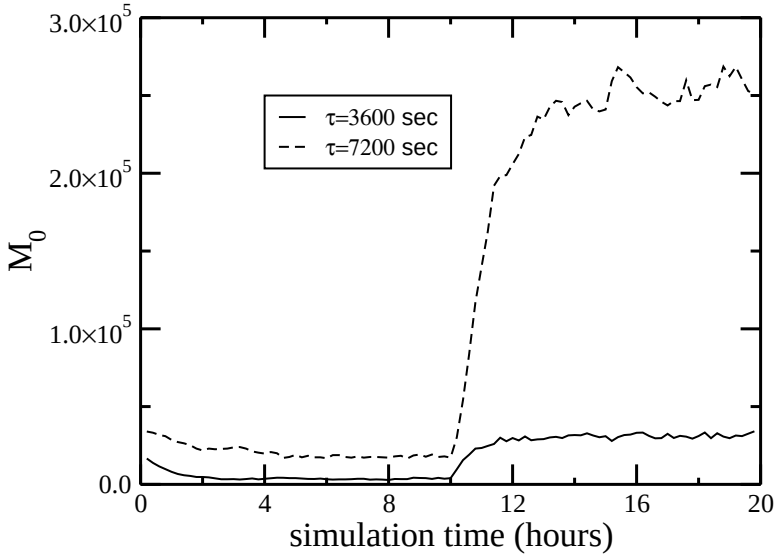

Figure 4.10: The profile of the average number of crystals (M_0) with time under MPC for the initial crystal shape set-point value, $\alpha_{\text{set}} = 0.86$. After $t = 10$ hours, the set-point is changed to $\alpha_{\text{set}} = 1.1$.

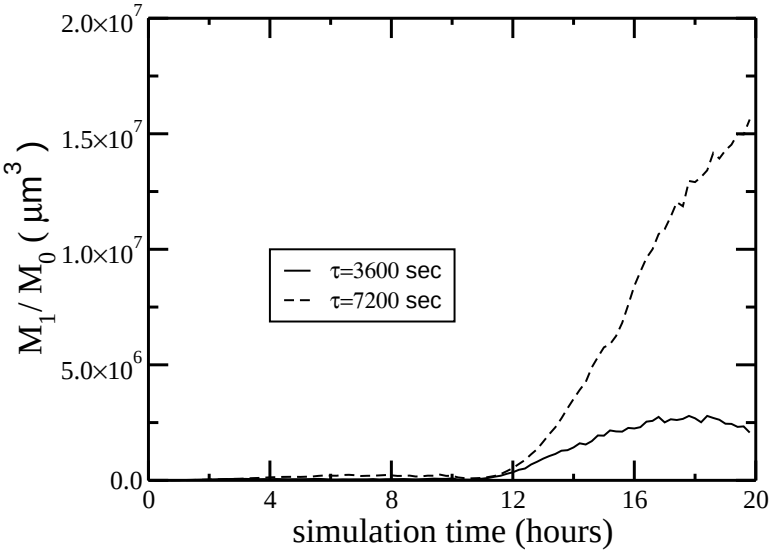

Figure 4.11: The profile of the average volume (M_1/M_0) of the crystal population in Fig. 4.10 with time under MPC for the initial shape set-point value, $\alpha_{\text{set}} = 0.86$. After $t = 10$ hours, the set-point is changed to $\alpha_{\text{set}} = 1.1$.

jacket temperature keeps decreasing to counteract the severe protein solute concentration drop and maintain a desired supersaturation level. In both cases above, the MPC is able to drive the crystal population to a desired value as is shown in Fig. 4.12. Additionally, as we change the set-point from $\alpha_{\text{set}} = 0.86$ to $\alpha_{\text{set}} = 1.1$, it is shown in Fig. 4.13 that it takes about 2 hours for the system to reach the new steady-state for $\tau = 2$ hour. Considering the fact that the mean residence time is 2 hours, a response time of about 2 hours is reasonable. Therefore, this verifies that the proposed MPC responds promptly to the change in the set-point, the severe concentration drop, and the system disturbances in an effort to produce crystals with a desired morphology. Furthermore, the system's response time to the set-point change can be even shorter when we use a shorter residence time, because the crystals with an undesired shape will exit the crystallizer more quickly. We can also use an actuator with less restrictions on the jacket temperature change, which will allow the system to reach the optimal jacket temperature value faster.

In conclusion, the MPC with a fines trap is able to drive the crystal population to a desired shape distribution by appropriately dealing with undesired effects such as biased nucleation, disturbances, and the mismatch of moment models from the actual process model as demonstrated by Figs. 4.8 and 4.12. It should be noted that the controller performance does not show further improvement although a longer prediction horizon is used, because the control action is restricted by a constraint on the rate of temperature change. Therefore, the controller performance can be further improved by adjusting the constraint on the rate of change of the manipulated input (i.e., jacket temperature) so that the system

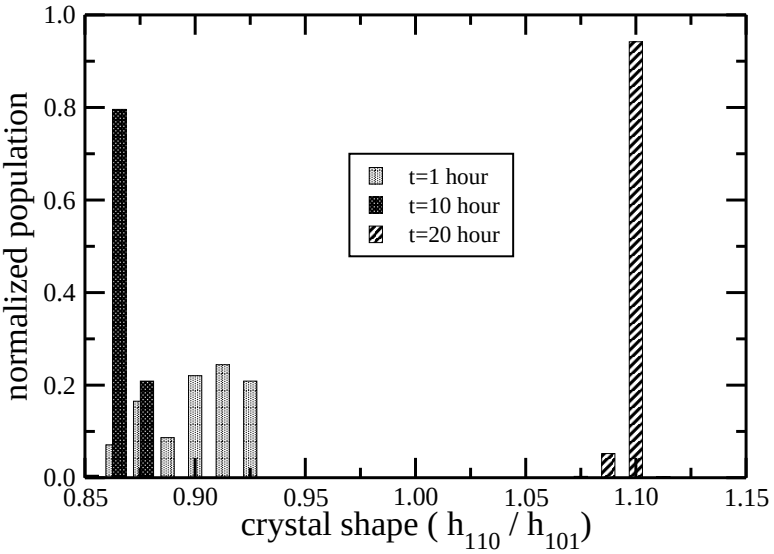

Figure 4.12: The normalized crystal shape distribution at three different times during the continuous simulation at $\tau = 7200$ seconds under MPC for the initial crystal shape set-point value, $\alpha_{\text{set}} = 0.86$. After $t = 10$ hours, the set-point is changed to $\alpha_{\text{set}} = 1.1$. The histograms are obtained by averaging 10 independent kMC simulations where the standard deviations for $t = 1$, $t = 10$, and $t = 20$ hours are 0.019, 0.003, and 0.002, respectively.

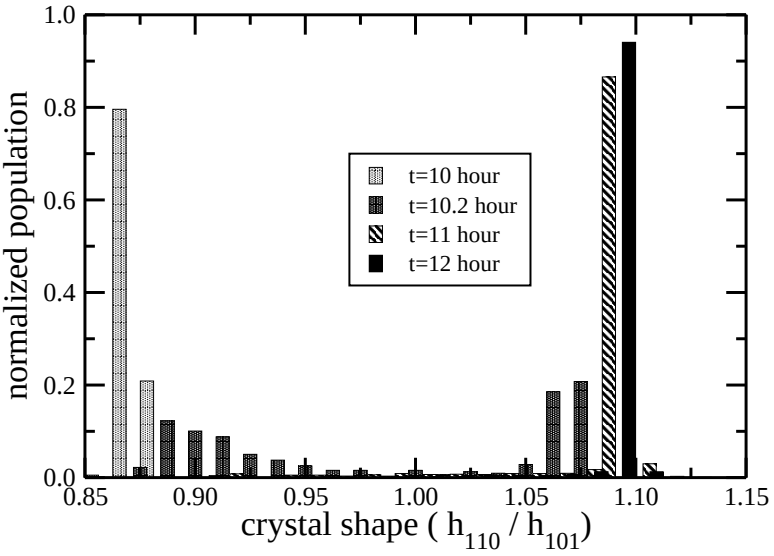

Figure 4.13: The normalized crystal shape distribution at four different times during the transition period ($t = 10 - 12$ hour) in the continuous simulation under MPC at $\tau = 7200$ for the crystal shape set-point change from $\alpha_{\text{set}} = 0.86$ to $\alpha_{\text{set}} = 1.1$. The histograms are obtained by averaging 10 independent kMC simulations where the standard deviations for $t = 10$, $t = 10.2$, $t = 11$, and $t = 12$ hours are 0.003, 0.008, 0.025, and 0.011, respectively.

takes more aggressive actions. Additionally, compared to a batch process, a continuous process can achieve a low polydispersity more easily for the following two reasons. Firstly, the fines trap removes most of the small crystal fines whose sizes are less than the pre-specified cut-off size, and this allows the remaining crystals to grow larger. Secondly, once the system reaches its steady-state during continuous crystallization, an optimal condition for the production of crystals with a desired shape can be maintained until the process is terminated.

4.8 Conclusions

Initially, we presented the modeling of the nucleation and crystal growth in a continuous crystallization process with a fines trap through kinetic Monte Carlo (kMC) simulation. The simulation of a fines trap was performed using a classification function which used a selection curve for fines dissolution in the continuous crystallizer. In addition to the solute depletion and the temperature change in the continuous phase during crystallization, the interplay of inflow/outflow in the continuous crystallizer was included in the mass and energy balance equations. To deal with a real-time implementation issue of a controller based on PBM, moment models were developed to describe the dominant dynamic behavior of the continuous crystallization along with a fines trap. Subsequently, the three leading moments were used along with the balance equations in order to design a model predictive controller.

The simulation results demonstrated that the crystal growth was successfully regulated at steady-state by properly adjusting the jacket temperature. The MPC also suppressed the influence of the biased nucleation, the disturbances in the measurements, and the sudden change in the desired operating environment (i.e., changes in the desired set-point value). Additionally, measurements of CSD and CLD through FBRM and PVM, respectively, were assumed to be available from the kMC simulation. Compared to a batch process, crystals with a lower polydispersity were produced due to the fines trap since it dissolved most of the fines whose volumes were less than 1 μm^3 in the crystallizer. We reduced the response time of the system toward the sudden set-point change by allowing a larger step change in

the jacket temperature.

Chapter 5

Crystal shape and size control using a plug flow crystallization configuration

5.1 Introduction

This chapter focuses on modeling and control of a continuous plug flow crystallizer (PFC) used to produce tetragonal hen-egg-white (HEW) lysozyme crystals and proposes an optimization-based control scheme to produce crystals with desired size and shape distributions in the presence of disturbances. Initially, a kinetic Monte Carlo (kMC) model is developed to simulate the crystal growth in a seeded PFC, which consists of five distinct segments. The crystal growth rate equations taken from [31] are used in the kMC simulations for the modeling of the crystal growth in the directions of the (110) and (101) faces. Then, a population balance equation (PBE) is presented to describe the spatio-temporal evolution of the

crystal volume distribution of the entire crystal population, and the method of moments is applied to derive a reduced-order moment model. Along with the mass and energy balance equations, the leading moments that describe the dominant dynamic behavior of the crystal volume distribution are used in the optimization-based controller to compute optimal jacket temperatures for each segment of the PFC and the optimal superficial velocity, in order to minimize the squared deviation of the average crystal size and shape from the set-points throughout the PFC. Furthermore, a feed-forward control (FFC) strategy is proposed to deal with feed flow disturbances that occur during the operation of the PFC. Using the proposed optimization and control schemes, crystals with desired size and shape distributions are produced in the presence of significant disturbances in the inflow solute concentration and size distribution of seed crystals.

5.2 Modeling of plug flow crystallizer

5.2.1 Process configuration

We consider a continuous plug flow crystallizer used to produce crystals with desired size and shape distributions through the manipulation of a set of jacket temperatures and of the superficial flow velocity which are computed by solving a multivariable optimization problem. The system parameters for the crystallizer considered in this work are taken from [2, 80] and are presented as follows: each segment of the PFC is 400 cm in length and 1.27 cm in inner diameter, and the PFC consists of 5 segments where the configuration of the

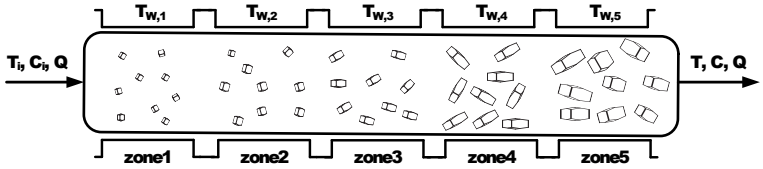

Figure 5.1: Plug flow crystallizer configuration. T is the crystallizer temperature, T_i is the inflow temperature, $T_{w,k}$ is the crystallizer jacket temperature at segment k, C_i is the inflow solute concentration, C is the solute concentration, and Q is the flow rate of the inflow stream.

PFC is presented in Fig. 5.1. It is assumed that the segments are connected without any gap. Additionally, we assume that the PFC is perfectly mixed in the radial direction and that there is no back-mixing in the axial direction.

In order to study the effect of manipulating a set of jacket temperatures on the shape and size distributions of crystals produced by the plug flow crystallizer, it is operated in the regime where primary nucleation is negligible. Therefore, a number of seed crystals with a height of 30 μm in the directions of both the (110) and (101) faces are fed through the entrance of the crystallizer. Specifically, the kMC simulations are used to simulate the crystal growth in the plug flow crystallizer described above. The crystal growth rates obtained from the kMC simulations are calibrated with literature data [31]. Additionally, the kMC simulations can be used to predict the crystal growth dynamics at the operating conditions where experimental data are not currently available. The details of the kMC simulations for the growth of the tetragonal lysozyme crystals, and the basic assumptions and the rate equations for the microscopic processes (adsorption, desorption and migration)

have been discussed extensively in previous work [66] and will not be repeated here.

During the PFC simulations, crystals are seeded at a rate of B_{seed} and continue along the PFC at the flow velocity until they exit the final segment. During this time the kMC simulations [66] are used to model the crystal growth depending on the local environment at the current location of the crystal. Each segment of the PFC has 80 sections where the solute phase properties are considered constant and an upwind finite difference method is used to update the solute concentration and temperature values every 0.333 seconds. It is noted that a variable number of the PFC sections were tested to ensure stability of the finite difference method.

5.2.2 Mass balance

The mass balance employed in this work to compute the spatio-temporal evolution of the solute concentration is as follows:

$$\frac{\partial C}{\partial t} = -v_z \frac{\partial C}{\partial z} - \rho_c \int_0^\infty G_{vol}(V,\sigma) n(V,z,t) dV \tag{5.1}$$

where $n(V,z,t)$ is the number distribution of lysozyme crystals and is a function of crystal volume V and of the position $z \in [0,L]$ in the axial direction at time t, L is the length of the reactor, v_z is the superficial flow velocity of the incoming flow in the axial direction, $C(z,t)$ is the protein solute concentration in the continuous phase, $\rho_c = 1400$ mg/cm^3 is the crystal density, and $\sigma = \ln(C/s)$ is the relative supersaturation where s (mg/mL) is the solubility. The solubility depends on the temperature T in Celsius, the pH of the solution, and the concentration of added electrolyte. At 4%(w/v) NaCl and pH=4.5, [13] represented

the experimental solubility data as a function of the temperature T in Celsius using the following third-order polynomial:

$$s(T) = 2.88 \times 10^{-4} T^3 - 1.65 \times 10^{-3} T^2 + 4.62 \times 10^{-2} T + 6.01 \times 10^{-1}. \tag{5.2}$$

Alternatively, since the saturated liquid solution is sufficiently dilute in protein, the experimental solubility data at 4%(w/v) NaCl and pH=4.5 can be fitted with the following van't Hoff type of formula:

$$\ln(s) = \frac{\Delta H_c}{R} \left(\frac{1}{T + 273.15} \right) + c. \tag{5.3}$$

Linear regression gives $c = 27.45$ and $\Delta H_c = -4.5$ kJ/kg for the enthalpy of crystallization, which is in good accord with experiments [110]. For modeling and control purposes, the polynomial representation, Eq. 5.2, that gives the same results as the van't Hoff equation in the operating range of interest, is used in this work. Additionally, $G_{vol}(V, \sigma)$ is the volumetric crystal growth rate, which can be calculated as follows:

$$G_{vol}(V, \sigma) = 2G_{110} \langle h_{101} \rangle + G_{101} \langle h_{110} \rangle^2 \tag{5.4}$$

where $\langle h_{110} \rangle$ and $\langle h_{101} \rangle$ are the average crystal heights in the directions of the (110) and (101) faces, respectively, and G_{110} and G_{101} are the crystal growth rates in the directions of the (110) and (101) faces, respectively, where the geometry of the HEW lysozyme crystals considered in this work is presented in Fig. 5.2. The kMC simulations produce dense grids of points of the growth rates for both the (110) and (101) faces as a function of σ and thus, for a given σ, the value of the growth rates for each are obtained from interpolation. Lastly, Eq. 5.1 is subject to an initial condition at $t = 0$ and a boundary condition at $z = 0$

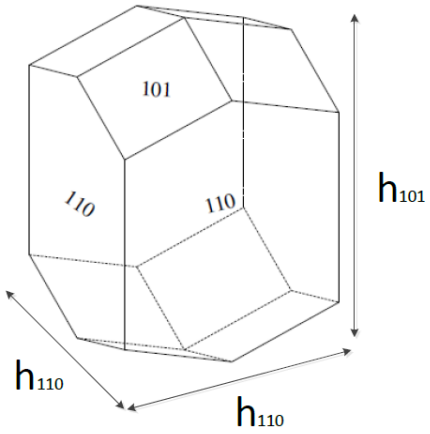

Figure 5.2: Geometry of HEW lysozyme crystal.

as follows:

$$C(z,0) = C_i$$
$$C(0,t) = C_i \tag{5.5}$$

where C_i is the inflow concentration and initial concentration of the PFC.

Remark 5.1 *In this work, the HEW lysozyme protein is chosen because it is one of the most widely studied proteins, and thus a significant amount of experimental data is available in the literature for the nucleation and crystal growth rates of HEW lysozyme protein crystals. The proposed control scheme can be applied to other plug flow crystallization systems provided that experimental data for the crystal nucleation and growth rates are available.*

5.2.3 Energy balance

The spatio-temporal evolution of the crystallizer temperature can be obtained by solving the following energy balance equation:

$$\frac{\partial T}{\partial t} = -v_z \frac{\partial T}{\partial z} - \frac{\rho_c \Delta H_c}{\rho C_p} \int_0^\infty G_{vol}(V,\sigma) n(V,z,t) dV - \frac{U_j A_j}{\rho C_p} \left(T - T_{w,k}\right) \tag{5.6}$$

where T is the crystallizer temperature, A_j is the heat transfer area per unit volume $(4/D)$ where D is the inner diameter of the plug flow crystallizer, $T_{w,k}$ is the crystallizer jacket temperature of the k^{th} segment, $\Delta H_c = -4.5$ kJ/kg is the enthalpy of crystallization [110], $\rho(z,t) = 1000 + C(z,t)$ mg/cm^3 is the suspension density, $C_p = 4.13$ kJ/K kg is the specific heat capacity, and $U_j = 500$ kJ/m^2 h K is the overall heat transfer coefficient of the crystallizer wall. Due to the small value of the enthalpy of crystallization, the term associated with latent heat effects in Eq. 5.6 makes negligible contribution to the rate of change of temperature. Furthermore, Eq. 5.6 is subject to an initial condition at $t = 0$ and a boundary condition at $z = 0$ as follows:

$$\begin{aligned} T(z,0) &= T_0 \\ T(0,t) &= T_0 \end{aligned} \tag{5.7}$$

where T_0 is the inflow temperature and initial temperature of the PFC.

5.2.4 Population balance equation

The population balance describing the spatio-temporal evolution of the crystal volume distribution for the PFC processes with seeding can be written in the form of the following

equation:

$$\frac{\partial n(V,z,t)}{\partial t} + v_z \frac{\partial n(V,z,t)}{\partial z} + \frac{\partial \left(G_{vol}(V,\sigma) n(V,z,t)\right)}{\partial V} = B_{seed}\delta(V - V_0, z - z_0) \tag{5.8}$$

where B_{seed} is the seeding rate, $\delta(\cdot)$ is the dirac delta function and V_0 is the size of the crystal seed. The term $v_z \partial n(V,z,t)/\partial z$ corresponds to the transport of crystals due to convection, and $\partial \left(G_{vol}(V,\sigma) n(V,z,t)\right)/\partial V$ corresponds to the crystal growth.

5.2.5 Method of moments

By applying the method of moments to Eq. 5.8, we derive moment models that allow us to compute the spatio-temporal evolution of the number of crystals (i.e., zeroth moment M_0) and the total volume (i.e., first moment M_1) of crystals in the PFC processes. The j^{th} moment equation has the following form:

$$\frac{\partial M_j}{\partial t} = -v_z \frac{\partial M_j}{\partial z} + j G_{vol} M_{j-1} \tag{5.9}$$

where we define the j^{th} moment as $M_j(z,t) = \int_0^\infty V^j n(V,z,t) dV$. For the derivation of the moment model, please refer to Section 5.8.1.

5.3 Steady-state model

Initially, we study the behavior of the PFC process at steady-state. The steady-state mass and energy balance equations, and the steady-state population balance equation, are obtained by setting the accumulation terms in Eqs. 5.1, 5.6, and 5.8 equal to zero. The

population balance equation at steady-state is a one-dimensional hyperbolic partial differential equation (PDE) and thus suggests the use of the method of characteristics for the computation of its solution, which will transform Eq. 5.8 into two ordinary differential equations (ODEs) of the crystal location, z, and of the crystal volume distribution, V, along the characteristic line (cf. Eq. 5.17). As a result, it is derived in Section 5.8.2 that a spatial profile of the average volume distribution is described as:

$$\frac{dV}{dz} = \frac{G_{vol}}{v_z}$$

5.3.1 Moment models

Specifically, the zeroth moment ($j = 0$) of the moment model, Eq. 5.9, at steady-state is as follows:

$$0 = -v_z \frac{dM_0}{dz} \tag{5.10}$$

Thus, it follows that $M_0(z)$ is an explicit function of z:

$$M_0(z) = M_0(0) \tag{5.11}$$

where $M_0(0)$ is the number of seed crystals fed to the plug flow crystallizer through the entrance at steady-state. This result is expected due to the lack of nucleation, aggregation, or breakage in the PFC process.

5.3.2 More profile equations at steady-state

The spatial profiles of both the solute concentration and the crystallizer temperature at steady-state are derived in Section 5.8.3. Specifically, the solute concentration $C(z)$ at steady-state is as follows:

$$C(z) = C_i - \frac{\rho_c G_{vol} M_0(0)}{v_z} z$$

Furthermore, the crystallizer temperature $T(z)$ at steady-state is obtained as follows:

$$T(z) = \left(T_{w,k} - \frac{A}{B} \right) \left(1 - \mathrm{e}^{-Bz} \right) + T_0 \mathrm{e}^{-Bz}$$

where $A = \frac{\rho_c \Delta H_c G_{vol} M_0(0)}{\rho C_p v_z}$ and $B = \frac{U_j a_j}{\rho C_p v_z}$

Remark 5.2 *The transient solution obtained from the dynamic model has been computed and has been found to converge to the steady-state profile obtained from the steady-state model for a sufficiently large time and for the same set of parameters.*

5.4 Multivariable optimization problem formulation

In this section, we propose a multivariable optimization problem (MOP), which will be solved in order to compute a set of optimal crystallizer jacket temperatures and an optimal superficial flow rate for the multi-segment PFC to produce crystals with desired size and shape distributions. To this end, an objective function is defined by the sum of the squared errors of the average crystal size and shape of the crystals throughout the PFC from the desired set-point values, $(\langle V(z,t) \rangle - V_{\text{set}})^2$ and $(\langle \alpha(z,t) \rangle - \alpha_{\text{set}})^2$, respectively. In particu-

lar, $\langle \alpha(z,t) \rangle$ is the average crystal shape which is defined as the ratio between the average crystal heights in the directions of the (110) and (101) faces throughout the PFC as follows: $\langle \alpha(z,t) \rangle \approx \frac{\langle h_{110}(z,t) \rangle}{\langle h_{101}(z,t) \rangle}$. The average crystal shape is approximated by this expression in order to make use of the measurements of $\langle h_{110} \rangle$ and $\langle h_{101} \rangle$ which are available on-line in real-time as is shown [68]. The decision variables are the jacket temperatures for each segment of the PFC, ($T_{w,1}$, $T_{w,2}$, $T_{w,3}$, $T_{w,4}$, $T_{w,5}$), and the superficial flow velocity, v_z. A constraint on the range of the crystallizer temperature is imposed ($4°\text{C} \leq T \leq 25°\text{C}$) to make sure the model protein remains in a proper condition for crystal growth. Please note that the growth rate expressions, G_{110} and G_{101}, used in the MOP below are calibrated in [66] with the experimental data of [31] for $2.1 \leq \sigma \leq 4.1$ and are presented in Fig. 5.3. We note that the constraint (cf. $\sigma(z,t) \leq 2.6$) in Eq. 5.12 is chosen in this range. Additionally, the inflow

temperature T_0 is set to be 18°C. The resulting optimization problem is as follows:

$$
\begin{aligned}
\underset{T_{w,1},T_{w,2},T_{w,3},T_{w,4},T_{w,5},v_z}{\text{Minimize}} \quad & \sum_{t=1}^{t_f}\sum_{z=1}^{L} w_1\left(\langle\alpha(z,t)\rangle-\alpha_{\text{set}}\right)^2+w_2\left(\langle V(z,t)\rangle-V_{set}\right)^2 \\
\text{subject to} \quad & G_{110}=0.1843\times\sigma^3-1.1699\times\sigma^2+2.8885\times\sigma-2.5616 \\
& G_{101}=0.1893\times\sigma^3-1.2264\times\sigma^2+2.9887\times\sigma-2.5348 \\
& 4^\circ\text{C}\le T\le 25^\circ\text{C} \qquad \sigma(z,t)\le 2.6 \\
& \frac{\partial M_0}{\partial t}=-v_z\frac{\partial M_0}{\partial z} \\
& \frac{\partial M_1}{\partial t}=-v_z\frac{\partial M_1}{\partial z}+G_{vol}M_0 \\
& \frac{\partial C}{\partial t}=-v_z\frac{\partial C}{\partial z}-\rho_c\frac{\partial M_1}{\partial t} \\
& \frac{\partial T}{\partial t}=-v_z\frac{\partial T}{\partial z}-\frac{\rho_c\Delta H_c}{\rho C_p}\frac{\partial M_1}{\partial t}-\frac{U_j a_j}{\rho C_p}\left(T-T_{w,k}\right) \\
& G_{vol}=2G_{110}\langle h_{101}\rangle\langle h_{110}\rangle+G_{101}\langle h_{110}\rangle^2 \quad k\in\{1,2,3,4,5\} \\
& \frac{d\langle h_i\rangle}{dz}=\frac{G_i}{v_z} \qquad i\in\{110,101\} \\
& \langle\alpha(z,t)\rangle\approx\frac{\langle h_{110}(z,t)\rangle}{\langle h_{101}(z,t)\rangle} \quad \langle V(z,t)\rangle=\langle h_{110}(z,t)\rangle^2\langle h_{101}(z,t)\rangle
\end{aligned}
\tag{5.12}
$$

where the weighting coefficients of the two objective functions, w_1 and w_2, are determined by trial and error until the optimal jacket temperatures and the superficial flow velocity drive both size and shape distributions of the crystal products to a set of desired values. Furthermore, the supersaturation level is defined as the logarithmic difference between the solute concentration and the solubility, $\sigma(z,t)=\ln(C(z,t)/s(z,t))$, and t_f is the total simulation time. An upper bound on the range of supersaturation level is provided as a constraint (cf. $\sigma(z,t)\le 2.6$) in Eq. 5.12 to prevent the primary nucleation of crystals during the process. The corresponding range of the average crystal shape is $\langle\alpha\rangle\le 1.05$. The polynomial

expressions for the growth rates, G_{110} and G_{101}, are obtained from open-loop simulations in [68]. The forward upwind (FU) discretization scheme, which guarantees the numerical stability of the system if the time and spatial discretization steps are relatively small [46], is applied to the moment models and the mass and energy balance equations in the MOP (cf. Eq. 5.12) to evaluate the spatio-temporal evolution of the system variables. Then, a set of optimal jacket temperatures and the superficial flow velocity, ($T_{w,1}$, $T_{w,2}$, $T_{w,3}$, $T_{w,4}$, $T_{w,5}$, v_z), are obtained by solving Eq. 5.12 off-line, and are applied to the crystallizer. We observed that the computation time needed to solve the optimization problem using the moments model is about 5-10 seconds. Therefore, if real-time measurements of the crystallizer outlet stream are available with a reasonable sampling time, the proposed method can be applied to an experimental plug flow crystallization system. In general, the computation time and the convergence of the solution computed from an optimization problem depend on the integration step size used to solve the moments model and thus should be chosen carefully to obtain an accurate solution meeting real-time computation requirements.

Remark 5.3 *The growth rates of the HEW lysozyme crystals in the directions of the (110) and (101) faces used in the simulations presented in the manuscript have been calibrated with available experimental results. However, no experimental results are currently available for the production of HEW lysozyme crystals through PFC. We note that the proposed optimization and control framework can be applied to other plug flow crystallization systems provided that the modeling, measurement, and computational requirements needed to implement the proposed approach in a practical setting are satisfied.*

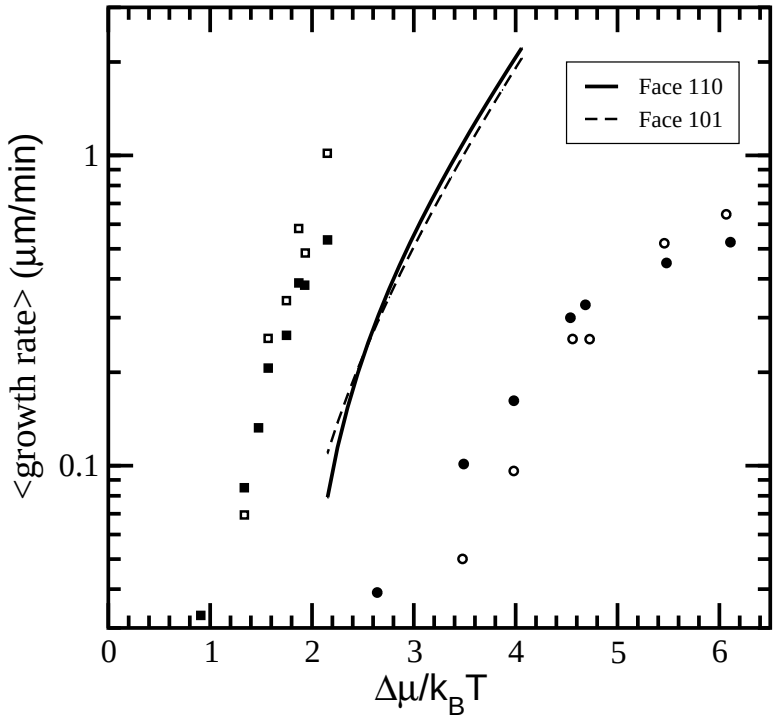

Figure 5.3: The solid and dashed lines show the growth rates for the kMC model on the (110) and (101) faces, respectively, at $C = 45$ mg/mL and 4% NaCl. The (•)/(○) represent the growth rates for the (101) and (110) faces with 3.5% NaCl and the (■) and (□) represent the growth rates with 5% NaCl at pH= 4.6, which are both taken from [31].

5.5 Feed-forward control

In continuous crystallization processes, disturbances (e.g., changes in the inflow solute concentration) influence the size and shape distributions of the crystal products during the steady-state operation of the PFC process [113]. Motivated by this, the following feed-forward control (FFC) strategy is proposed for the production of crystals with desired size and shape distributions to deal with a disturbance in the inflow solute concentration. We assume that the actuator limit on the rate of change of the jacket temperature is sufficiently high that the crystallizer temperature can be changed instantaneously. We note that if the jacket temperature change is not instantaneous, it will take additional time for the PFC temperature to reach a desired profile, and as a result the system may produce crystals with undesired size and shape distributions during the time required for the PFC temperature to reach the desired profile.

1. Initially, we compute a set of optimal jacket temperatures, ($T_{w,1}$, $T_{w,2}$, $T_{w,3}$, $T_{w,4}$, $T_{w,5}$), and an optimal superficial flow velocity, v_z, for the initial solute concentration, C_i. They are applied to the crystallizer until the change in the inflow solute concentration is measured (i.e., a disturbance is detected). In this step, the spatial temperature profile at the steady-state is similar to the one for $t = 4$ hours in Fig. 5.4.

2. When a change in the solute concentration is measured at the entrance of the PFC, a set of new optimal jacket temperatures, ($T_{w,1}^{\text{new}}$, $T_{w,2}^{\text{new}}$, $T_{w,3}^{\text{new}}$, $T_{w,4}^{\text{new}}$, $T_{w,5}^{\text{new}}$), is computed for the new inflow solute concentration, C_i^{new} while the superficial flow velocity re-

mains identical. Then, the old jacket temperature for zone 1 immediately replaced with the new jacket temperature and, for zone 2 to zone 5, the jacket temperatures remain identical because the inflow with the new solute concentration, C_i^{new}, has not reached zone 2 to zone 5 yet. Thus, the resulting set of jacket temperatures becomes ($T_{w,1}^{\text{new}}$, $T_{w,2}$, $T_{w,3}$, $T_{w,4}$, $T_{w,5}$).

3. When the inflow with the new solute concentration, C_i^{new}, has reached zone 2, the old jacket temperature, $T_{w,2}$, is replaced with the new jacket temperature, $T_{w,2}^{\text{new}}$. Thus, the resulting set of jacket temperatures becomes ($T_{w,1}^{\text{new}}$, $T_{w,2}^{\text{new}}$, $T_{w,3}$, $T_{w,4}$, $T_{w,5}$) and it is maintained until the inflow with the new solute concentration, C_i^{new}, reaches zone 3. In this step, the spatial temperature profile at the steady-state is similar to the one for $t = 10$ hours in Fig. 5.4.

4. This strategy continues until the inflow with a new solute concentration, C_i^{new}, reaches the entrance of zone 5, at which time the set of jacket temperatures becomes ($T_{w,1}^{\text{new}}$, $T_{w,2}^{\text{new}}$, $T_{w,3}^{\text{new}}$, $T_{w,4}^{\text{new}}$, $T_{w,5}^{\text{new}}$), which will be maintained for the rest of simulation. In this step, the spatial temperature profile at the steady-state is similar to the one for $t = 16$ hours in Fig. 5.4.

5. If a new disturbance in the inflow solute concentration is detected, Step 1 to Step 4 will be repeated.

For example, the set of the optimal jacket temperatures for the inflow solute concentration $C_i = 43$ mg/cm^3 is presented in Fig. 5.5, which is applied to the PFC until a change in

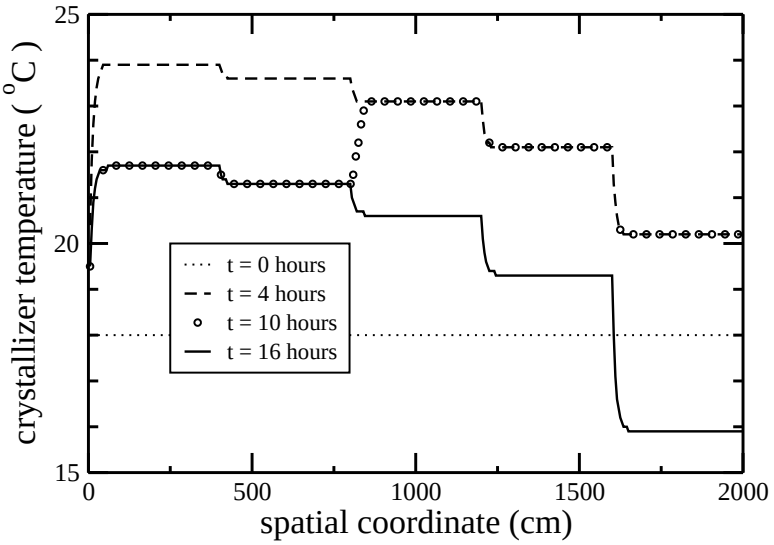

Figure 5.4: The spatial evolution of the crystallizer temperature (T) at different times under FFC. The desired set-point values are $h_{110} = 130$ μm and $\alpha_{\text{set}} = 0.85$ for the average crystal height in the direction of the (110) face and the crystal shape, respectively. The disturbance was introduced at $t = 8.33$ hours ($= 30\,000$ seconds) when the inflow solute concentration was changed from $C_i = 43$ to 34.4 mg/cm^3. It is noted that some of the data points for $t = 10$ hours have been excluded for clarity since they overlay the data points for $t = 4$ hours.

the inflow solute concentration is measured at $t = 8.33$ hours ($= 30\,000$ seconds). Specifically, this disturbance to the system is modeled by decreasing the inflow solute concentration, C_i, from 43 to 34.4 mg/cm^3 at $t = 30\,000$ seconds in the kMC simulations. Then, the set of new optimal jacket temperatures for the new inflow solute concentration $C_i^{\text{new}} = 34.4$ mg/cm^3 is computed and applied for $8.33 < t < 14.16$ hours according to the FFC strategy described above. For the production of crystals with desired size and shape distributions, the optimal superficial velocity $v_z = 0.0763$ cm/sec is computed for a given simulation time, $t_f = 20$ hours. In Table 5.1, a set of the jacket temperatures at different times is presented for clarity. For $t > 14.16$ hours, the inflow disturbance has reached zone 5 and as a result the set of old jacket temperatures has been completely replaced with the set of new jacket temperatures as is presented in Fig. 5.5. Owing to the FFC scheme, existing crystals that are in the middle or close to the outlet of the PFC can grow through the previous optimal jacket temperature profile, and as a result they are successfully produced with desired size and shape distributions. Furthermore, this FFC strategy only requires the measurement of the inflow solute concentration at the entrance of the PFC so it is robust to the inaccuracy of the on-line measurements. More results on the robust control of crystallization processes can be found in [23].

Remark 5.4 *The proposed optimization/control approach can be extended to account for crystal agglomeration and/or breakage events by constructing moment models that capture the dominant dynamic behavior of the agglomeration and breakage processes within the crystallization process.*

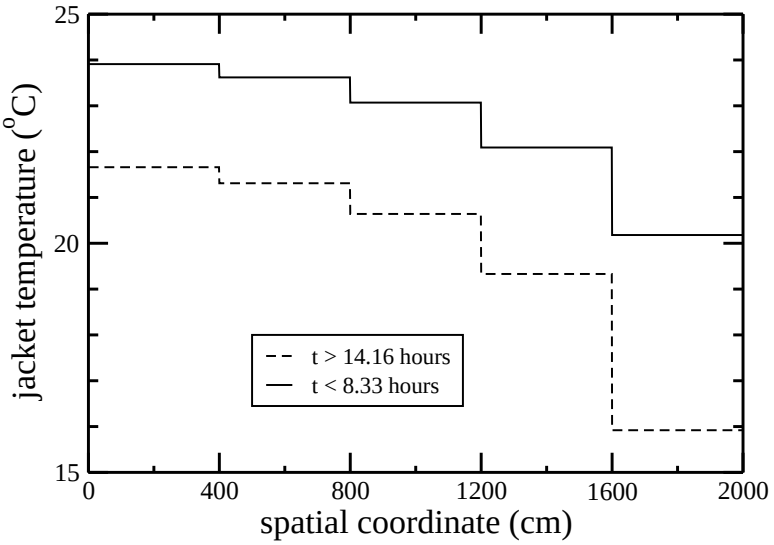

Figure 5.5: The spatial profile of the jacket temperature (T_w) computed by solving the MOP when the desired set-point values are $h_{110} = 130\ \mu$m and $\alpha_{\text{set}} = 0.85$ for the average crystal height in the direction of the (110) face and the crystal shape, respectively. To deal with the disturbance introduced in the inflow solute concentration, a set of new T_w values for $8.33 < t < 14.16$ hours is updated according to the FFC strategy.

		jacket temperature (°C)				
		$T_{w,1}$	$T_{w,2}$	$T_{w,3}$	$T_{w,4}$	$T_{w,5}$
time	$(0 \leq t < 8.33)$ hours	23.91	23.62	23.07	22.09	20.18
	$(8.33 \leq t < 9.79)$ hours	21.66	23.62	23.07	22.09	20.18
	$(9.79 \leq t < 11.24)$ hours	21.66	21.31	23.07	22.09	20.18
	$(11.24 \leq t < 12.70)$ hours	21.66	21.31	20.64	22.09	20.18
	$(12.70 \leq t < 14.16)$ hours	21.66	21.31	20.64	19.33	20.18
	$(14.16 \leq t < 20)$ hours	21.66	21.31	20.64	19.33	15.92

Table 5.1: The set of jacket temperatures at different times.

Remark 5.5 *As a complementary strategy to the proposed FFC scheme, a set of proportional-integral-derivative (PID) control schemes can be implemented for each zone to make slight adjustments to the optimal jacket temperatures (for a given crystallizer feed) and can be used to suppress the effect of unmodeled disturbances/modeling uncertainty through the use of real-time on-line measurements of the size and shape distributions of the crystals of the PFC outlet stream.*

5.6 Simulation results of continuous plug flow crystallizer

Continuous PFC processes have been traditionally operated at steady-states. However, a limitation of the steady-state model is that it cannot describe transient behavior of the system when there is a disturbance such as an abrupt change in the inflow solute concentration

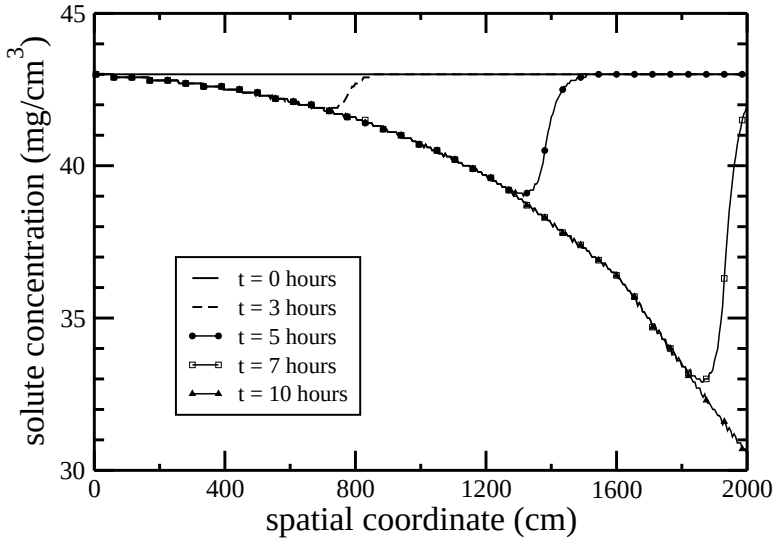

Figure 5.6: The spatial evolution of the protein solute concentration (C) at different times when there is no disturbance. The desired set-point values are $h_{110} = 130$ μm and $\alpha_{\text{set}} = 0.85$ for the average crystal height in the direction of the (110) face and the crystal shape, respectively.

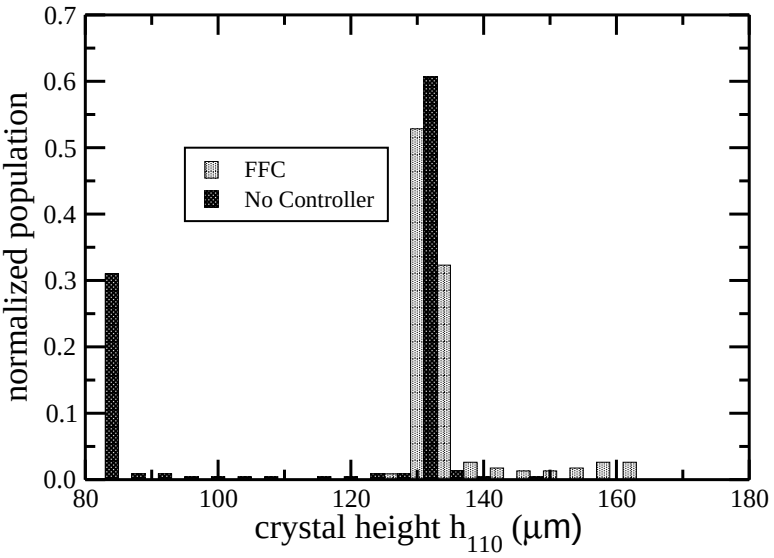

Figure 5.7: The normalized crystal size distribution obtained from the kMC simulations under the FFC scheme is compared with that under no control scheme. The jacket temperatures computed by solving the MOP are applied to the PFC, and the crystals are collected over a time period. The desired set-point values are $h_{110} = 130\ \mu$m and $\alpha_{\text{set}} = 0.85$ for the average crystal height in the direction of the (110) face and the crystal shape, respectively.

during the steady-state operation of the PFC. In light of this, we developed a dynamic model in Section 5.2 that describes the spatio-temporal evolution of system variables including the average crystal volume and shape, the number of crystals, and the solute concentration and crystallizer temperature. In this work, the PFC operates at 4%(w/v) NaCl and pH = 4.5. In Fig. 5.6, the transient solute concentration profiles obtained from the dynamic model employed in the kMC simulation are depicted at different times, and the concentration eventually reaches the steady state at $t \simeq 26\ 500$ seconds.

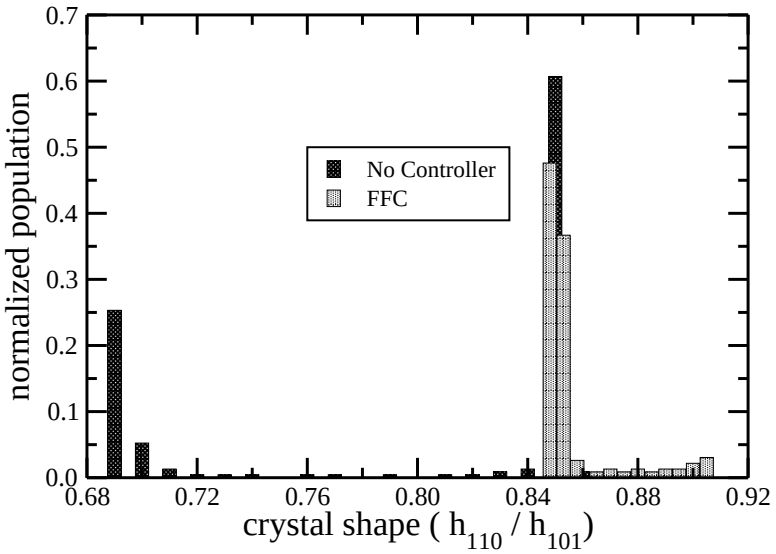

Figure 5.8: The normalized crystal shape distribution obtained from the kMC simulations under the FFC scheme is compared with that under no control scheme. The jacket temperatures computed by solving the MOP are applied to the PFC, and the crystals are collected over a time period. The desired set-point values are $h_{110} = 130$ μm and $\alpha_{\text{set}} = 0.85$ for the average crystal height in the direction of the (110) face and the crystal shape, respectively.

The constant supersaturation control (CSC) strategy is one of the most widely used operating strategies for the operation of crystallization processes in industry. Furthermore, the controller performance of a CSC strategy in batch processes can be close to that of model predictive control (MPC) if the desired supersaturation level is chosen appropriately. In a PFC, however, it is rather difficult to maintain a constant supersaturation level because the solute concentration drops along the spatial coordinate of the crystallizer. Thus, a PFC requires the design of a particular spatial temperature profile to compensate for the concentration drop, which is not possible without using a combination of steady-state and dynamic models. In addition, the size distribution of the crystals produced from the PFC depends on the total length of the PFC. Therefore, using the model-free CSC scheme does not guarantee the production of crystals with desired size and shape distributions.

In this work, however, the production of crystals with both desired size and shape distributions is achieved by applying the set of optimal jacket temperatures and the superficial flow velocity computed by solving the MOP (cf. Eq. 5.12) according to the proposed FFC strategy to deal with the change (i.e., disturbance) in the inflow solute concentration. All simulations are performed in parallel using Message Passing Interface (MPI) to make use of heightened computational and memory requirements for this continuous crystallization process. The desired set-point value, $\alpha_{\text{set}} = 0.85$, is chosen for the crystal shape because of the desire to work in a zone where the nucleation rate is negligible (i.e., the metastable regime). Also, the set-point $\langle h_{110} \rangle = 130\ \mu\text{m}$ is chosen for the crystal size in the direction of the (110) face. As presented in Figs. 5.7 and 5.8, the effect of the disturbance is suf-

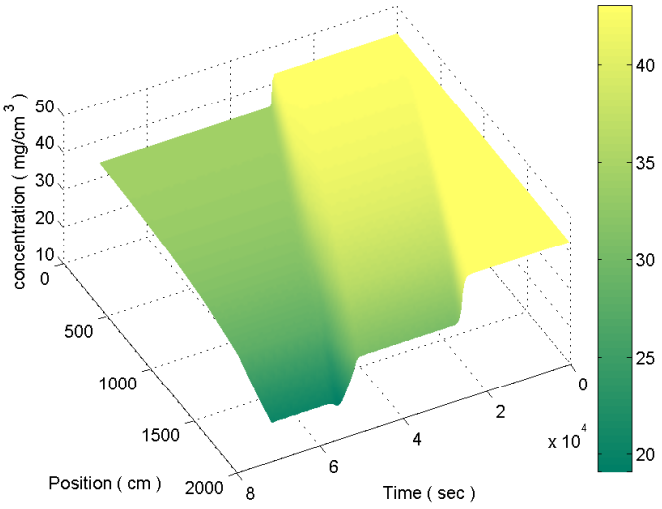

Figure 5.9: The spatio-temporal evolution of the protein solute concentration obtained from the kMC simulations in response to the disturbance introduced to the inflow solute concentration at $t = 8.33$ hours ($= 30\,000$ seconds) for which the inflow solute concentration is changed from $C_i = 43$ to 34.4 mg/cm^3. A set of optimal jacket temperatures is obtained for the desired set-point values, $h_{110} = 130$ μm and $\alpha_{\text{set}} = 0.85$, for the average crystal height in the direction of the (110) face and the crystal shape, respectively. Please note that the origin, $(z,t) = (0,0)$, is at the upper left of the position axis.

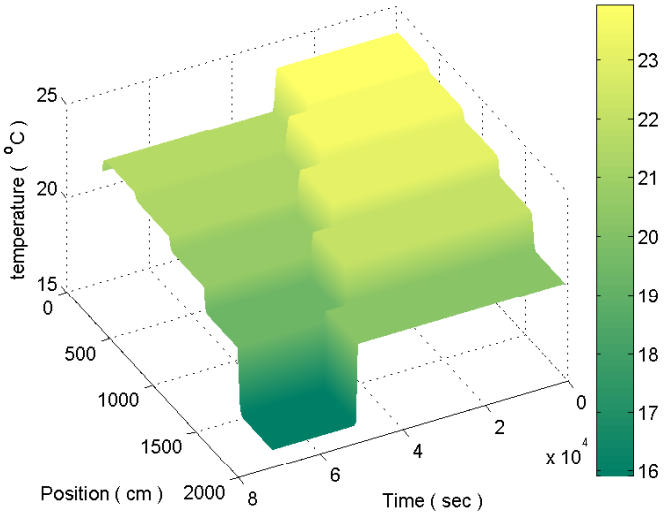

Figure 5.10: The spatio-temporal evolution of the crystallizer temperature obtained from the kMC simulations in response to the disturbance introduced to the inflow solute concentration at $t = 8.33$ hours ($= 30\,000$ seconds) for which the inflow solute concentration is changed from $C_i = 43$ to 34.4 mg/cm^3. The desired set-point values are $h_{110} = 130$ μm and $\alpha_{\text{set}} = 0.85$ for the average crystal height in the direction of the (110) face and the crystal shape, respectively. Please note that the origin, $(z,t) = (0,0)$, is at the upper left of the position axis.

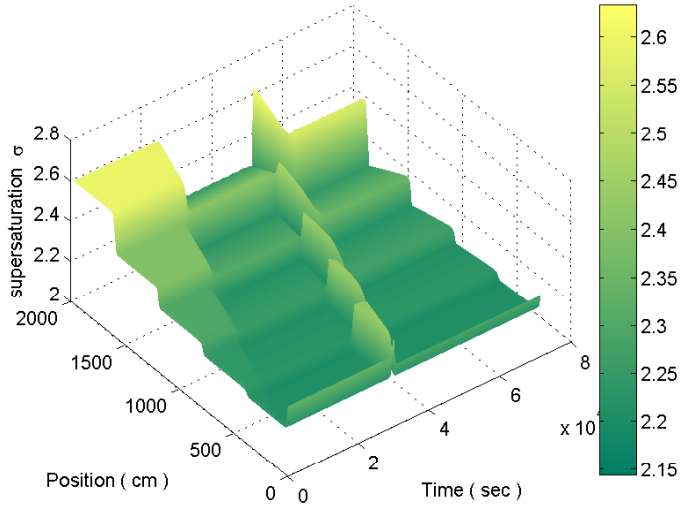

Figure 5.11: The spatio-temporal evolution of the supersaturation level obtained from the kMC simulations in response to the disturbance introduced to the inflow solute concentration at $t = 8.33$ hours ($= 30\,000$ seconds) when C_i is changed from 43 to 34.4 mg/cm^3. The desired set-point values are $h_{110} = 130$ μm and $\alpha_{\text{set}} = 0.85$ for the average crystal height in the direction of the (110) face and the crystal shape, respectively.

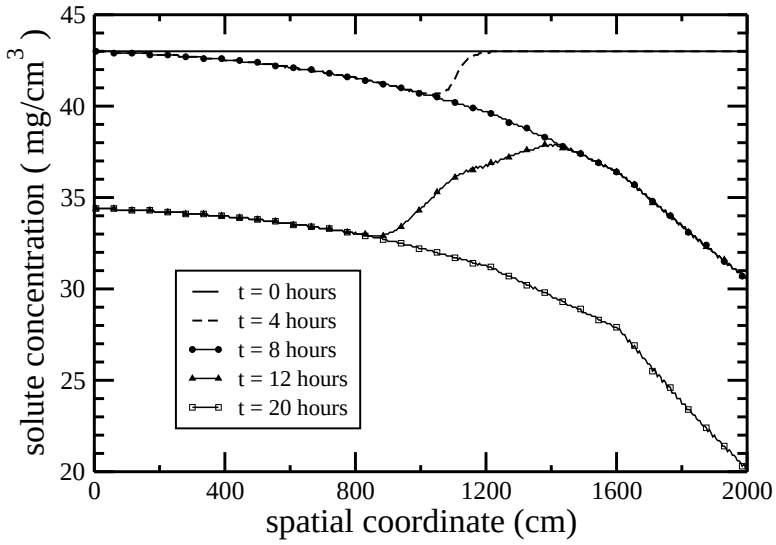

Figure 5.12: The spatial evolution of the protein solute concentration (C) at different times under FFC. The desired set-point values are $h_{110} = 130$ μm and $\alpha_{\text{set}} = 0.85$ for the average crystal height in the direction of the (110) face and the crystal shape, respectively. The disturbance was introduced at $t = 8.33$ hours (= 30 000 seconds) when the inflow solute concentration was changed from $C_i = 43$ to 34.4 mg/cm^3.

ficiently suppressed, and as a result, the average crystal size in the direction of the (110) face and the average crystal shape are successfully regulated to the desired values. Without the implementation of the proposed FFC scheme, as presented in Figs. 5.7 and 5.8, the effect of the disturbance cannot be sufficiently suppressed and as a result $\sim 30\%$ of the crystal products deviate from the desired set-point values. The optimal superficial flow velocity used in the kMC simulation is $v_z = 0.0763$ cm/sec, and the sets of the optimal jacket temperatures are (23.91, 23.62, 23.07, 22.09, 20.18) °C and (21.66, 21.31, 20.64, 19.33, 15.92) °C for $C_i = 43$ and $C_i = 34.4$ mg/cm^3, respectively.

The spatio-temporal profiles of the solute concentration, the crystallizer temperature, and the supersaturation level are presented in Figs. 5.9, 5.10, and 5.11, respectively. Because of the difference between the new jacket temperature profile computed for the new inflow solute concentration and the old jacket temperature profile, a set of discontinuous jumps is observed in Fig. 5.11. In Fig. 5.12, when the system is in a transient state at $t = 4$ hours, the spatial profile of the solute concentration is determined by the combination of the neighboring steady-state profiles at $t = 0$ and $t = 8$ hours, and a similar behavior is observed for another transient state at $t = 12$ hours. The benefit of using 5 different jacket temperatures is that we can avoid the unnecessary temperature change for those crystals which are quite far from the disturbance and there is no need to change the jacket temperature for those crystals. As a result, crystals with a desired size and shape distribution can be produced while the crystallizer is in a transient state.

The sensitivity of the size and shape of the crystals produced at the outlet of the PFC to the size of the initial seed crystals has been also investigated. Specifically, crystal size and shape distributions obtained from the kMC simulations for monodisperse seed crystals with different heights, (10, 20, 30, 40, 50, 60) μm, in the direction of the (110) face have been reported in Figs. 5.13 and 5.14. The weighting coefficients of the two objective functions used are $w_1 = 0.085$ and $w_2 = 1$. Fig. 5.13 shows that the average size of the crystals obtained by applying the jacket temperatures computed from the MOP becomes smaller than the desired set-point if the seed crystals are large while the small seed crystals can grow to a desired product size. In Fig. 5.14, the shape of the crystals produced from large

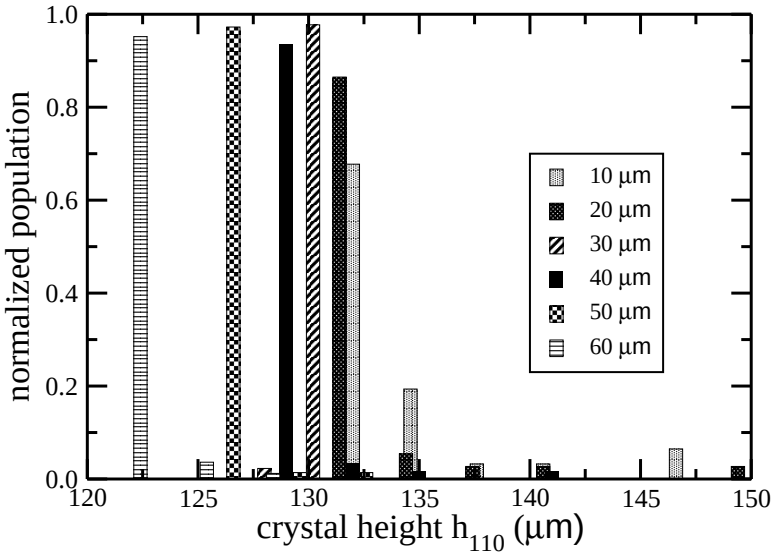

Figure 5.13: The normalized crystal size distribution obtained from the kMC simulations for seed crystals with different heights, (10, 20, 30, 40, 50, 60) μm, in the direction of the (110) face where the shapes of these crystal seeds are all cubical. For each run, the jacket temperatures computed by solving the MOP are applied to the PFC, and these crystals are collected throughout the PFC. The desired set-point values are $h_{110} = 130$ μm and $\alpha_{\text{set}} = 0.85$ for the average crystal height in the direction of the (110) face and the crystal shape, respectively.

crystal seeds deviates more from a desired set-point value than that of crystals produced from small crystal seeds. Larger crystal seeds grow slowly because they are already close to the desired crystal size, and as a result the crystal shape does not change significantly from the initial cubical shape. On the other hand, small crystals have to grow considerably to reach the desired size, and as a result the solute concentration is dropped to a regime where the production of crystals with a relatively low crystal aspect ratio is achieved. We want to note that for a different crystal seed size a set of appropriate weighting factors, w_1 and w_2, would need to be found to properly drive crystal shape and size to desired set-point values, respectively.

In conclusion, the proposed FFC scheme along with the optimal solution obtained by solving the MOP can successfully drive the average size and shape of the crystal population produced from the PFC to desired set-point values. Additionally, the effects of changes in the inflow concentration that occur during the steady-state operation are suppressed by the proposed FFC, and, owing to the absence of back-mixing in the PFC, the production of crystals with a very narrow size distribution (i.e., low polydispersity) is achieved. Lastly, the number of segments in the PFC can be easily extended if it is necessary for better performance of the proposed FFC scheme.

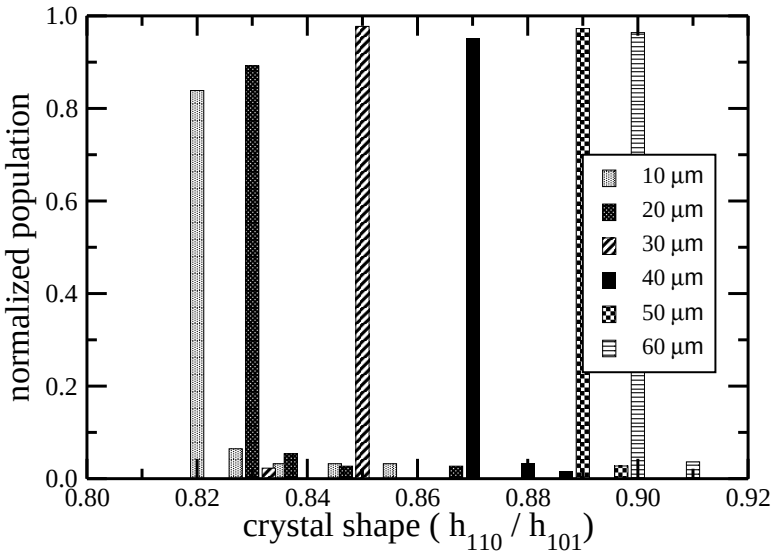

Figure 5.14: The normalized crystal shape distributions obtained from the kMC simulations for seed crystals with different heights, (10, 20, 30, 40, 50, 60) μm, in the direction of the (110) face where the shapes of these crystal seeds are all cubical. For each run, the jacket temperatures computed by solving the MOP are applied to the PFC, and these crystals are collected throughout the PFC. The desired set-point values are $h_{110} = 130$ μm and $\alpha_{\text{set}} = 0.85$ for the average crystal height in the direction of the (110) face and the crystal shape, respectively.

5.7 Conclusions

In this work, we first modeled the plug flow crystallization process where crystals grow from seeds through kMC simulations. In general, a continuous PFC is operated at a steady-state, and thus the steady-state model is typically used to describe the spatial profile of the important system variables; however, it cannot describe the transient behavior of the PFC. To this end, a dynamic model was developed to describe the spatio-temporal evolution of the number of crystals, the total crystal volume, the crystallizer temperature and the solute concentration, and the average crystal shape at a transient state as well as at a steady-state. Then, the method of moments was applied to the dynamic model to derive a reduced-order moments model which was used in the MOP to compute a set of optimal crystallizer jacket temperatures and a superficial flow velocity that minimize the sum of the squared deviations of the average crystal shape and size throughout the PFC from the desired set-point values.

In particular, when the disturbance was introduced, a set of new optimal jacket temperatures for each crystallizer segment was computed by solving the MOP for a new inflow solute concentration, and these were applied to the kMC simulation through the proposed FFC scheme. As a result, the production of crystals with desired size and shape distributions was achieved while $\sim 30\%$ of the crystal products were off the desired set-point values when the disturbance in the inflow solute concentration was not handled through the proposed FFC scheme.

5.8 Appendix

For the purpose of the derivation of the moment models (Section 5.8.1), the characteristic curve (Section 5.8.2), and the steady-state model (Section 5.8.3), the volumetric growth rate is assumed to be size-independent and is only a function of the supersaturation level, that is $G_{vol}(V,\sigma) \simeq G_{vol}(\sigma)$.

5.8.1 Derivation of the moment models

To begin with the derivation, we multiply Eq. 5.8 by V^j and integrate

$$\int_0^\infty V^j \frac{\partial n}{\partial t} + v_z \int_0^\infty \frac{\partial n}{\partial z} V^j dV + G_{vol} \int_0^\infty \frac{\partial n}{\partial V} V^j dV = \int_0^\infty B_{seed} \delta(V - V_0, z - z_0) V^j dV$$

By setting $M_j(z,t) = \int_0^\infty V^j n(V,z,t) dV$ and switching the order of the integral and derivative operators:

$$\frac{\partial M_j}{\partial t} + v_z \frac{\partial M_j}{\partial z} + G_{vol} \left[nV^j \Big|_{V=0}^{V=\infty} - j \int_0^\infty nV^{j-1} dV \right] = B_{seed} V_0^j \delta(z - z_0)$$

because $n(V,z,t)$ goes to 0 as V goes to ∞, and $n(V,z,t) = 0$ when $V = 0$ since there is no nucleation inside the crystallizer. Lastly, by rearranging the equation, we obtain:

$$\frac{\partial M_j}{\partial t} = -v_z \frac{\partial M_j}{\partial z} + jG_{vol}(\sigma) M_{j-1} + B_{seed} V_0^j \delta(z - z_0) \tag{5.13}$$

where the terms $\frac{\partial M_j}{\partial z}$ and $B_{seed} V_0^j \delta(z - z_0)$ are associated with crystal seeding, which acts only at $z = z_0$ (i.e., it acts like an impulse), and thus their orders of magnitude are much higher than those of $\frac{\partial M_j}{\partial t} dz$ and $jG_{vol}(\sigma) M_{j-1}$. Therefore, integrating Eq. 5.13 from z_0^- to

z_0^+ gives

$$0 = -v_z \int_{z_0^-}^{z_0^+} \frac{\partial M_j}{\partial z} dz + B_{seed} \int_{z_0^-}^{z_0^+} V_0^j \delta(z - z_0) dz$$

and as a result a boundary condition follows that

$$M_j(z,t)\Big|_{z=z_0} = \frac{B_{seed}}{v_z} V_0^j \tag{5.14}$$

Therefore, Eq. 5.13 can be written as follows:

$$\frac{\partial M_j}{\partial t} = -v_z \frac{\partial M_j}{\partial z} + jG_{vol}(\sigma) M_{j-1}$$

with the boundary condition of Eq. 5.14.

5.8.2 The method of characteristics

The two characteristic ODEs are derived as follows: First of all, taking the derivative of $n(V,z)$ with respect to an arbitrary characteristic s gives

$$\frac{dn}{ds} = \left(\frac{\partial n}{\partial V}\right) \frac{dV}{ds} + \left(\frac{\partial n}{\partial z}\right) \frac{dz}{ds} \tag{5.15}$$

But from Eq. 5.8, assuming that the growth rate is independent of size,

$$\frac{\partial n}{\partial t} = \left(\frac{\partial n}{\partial V}\right) G_{vol} + \left(\frac{\partial n}{\partial z}\right) v_z \tag{5.16}$$

Comparing the coefficients in Eqs. 5.15 and 5.16 gives the equations for the characteristic curve as follows:

$$\frac{dV}{ds} = G_{vol} \qquad \frac{dz}{ds} = v_z \tag{5.17}$$

and thus

$$\frac{dV}{dz} = \frac{G_{vol}}{v_z}$$

which defines the characteristic curve in the $V - z$ plane and allows calculation of the crystal volume distribution at any location z in the plug flow crystallizer. We note that the population distribution along a characteristic curve is constant letting $dn/ds = 0$ in Eqs. 5.15 and 5.16.

5.8.3 Balance equations at steady-state

The solute concentration $C(z)$ at steady-state can be computed by substituting Eq. 5.11 into Eq. 5.1, and it has the following form:

$$C(z) = C_i - \frac{\rho_c G_{vol} M_0(0)}{v_z} z$$

In a similar way, Eq. 5.11 can be substituted into Eq. 5.6 and, since $T_{w,j}$ is constant within each crystallizer segment, the crystallizer temperature $T(z)$ at steady-state can be obtained as follows:

$$\frac{dT}{dz} + BT(z) = -A + BT_{w,k} \tag{5.18}$$

where $A = \frac{\rho_c \Delta H_c G_{vol} M_0(0)}{\rho C_p v_z}$ and $B = \frac{U_j a_j}{\rho C_p v_z}$. Since this is a first-order ordinary differential equation, we can compute the solution $T(z)$ by multiplying Eq. 5.18 by an integrating factor e^{Bz} as follows:

$$\mathrm{e}^{Bz}\left(\frac{dT}{dz} + BT(z)\right) = \left(-A + BT_{w,k}\right)\mathrm{e}^{Bz}$$

and integrating yields

$$\int d\left(\mathrm{e}^{Bz}T(z)\right) = \left(-A + BT_{w,k}\right)\int \mathrm{e}^{Bz}dz$$

and applying the boundary condition for $T(z)$ at $z = 0$ gives

$$\mathrm{e}^{Bz}T(z) = \left(-A + BT_{w,k}\right)\frac{1}{B}\mathrm{e}^{Bz}\Big|_0^z + T_0$$

and it follows that

$$T(z) = \left(T_{w,k} - \frac{A}{B}\right)\left(1 - \mathrm{e}^{-Bz}\right) + T_0\mathrm{e}^{-Bz}$$

Chapter 6

Run-to-run-based model predictive control of protein crystal shape in batch crystallization

6.1 Introduction

In this chapter, a novel run-to-run-based model predictive controller (R2R-based MPC) is developed for a batch crystallization process with process drift and inherent variations in solubility and crystal growth rates. In order to achieve the production of crystals with desired product qualities, a conventional model predictive control (MPC) system with nominal process model parameters is initially applied to a batch protein crystallization process. However, the mismatch between the process model and the actual process dynamic behav-

ior, because of the process drift and variability, becomes severe as batch runs are repeated. To deal with this problem of batch-to-batch variability, after each batch run is completed, the post-batch crystal attribute measurements, including average crystal shape and size and the number of crystals, are used to estimate off-line the extent to which the process model (used in the MPC) parameters drifted from nominal values via a multivariable optimization problem. Along with the adapted controller model parameters, the exponentially-weighted-moving-average (EWMA) scheme is used to deal with the remaining offset in the crystal shape values and thereby to compute a set of optimal jacket temperatures. Furthermore, the crystal growth in the batch crystallization process is modeled through kinetic Monte Carlo (kMC) simulations which are then used to demonstrate the ability of the proposed R2R-based MPC scheme to suppress the inherent variations and process drift in solubility and crystal growth rates. It is demonstrated that crystals with a desired shape distribution are successfully produced after three batch runs through the use of the proposed R2R-based MPC, while it takes twenty-four batch runs for the system with the EWMA-type constant supersaturation control (CSC) to achieve the same objective.

6.2 Modeling of batch crystallization process

In this work, we focus on a batch protein crystallization process (cf. Fig. 6.1) for which the detailed geometrical parameters are taken from [118] and are presented as follows: a three-bladed propeller is used; both the inner diameter and the filling height of the crystallizer are 0.12 m; the clearance height (i.e., the height from the bottom of the crystallizer to the

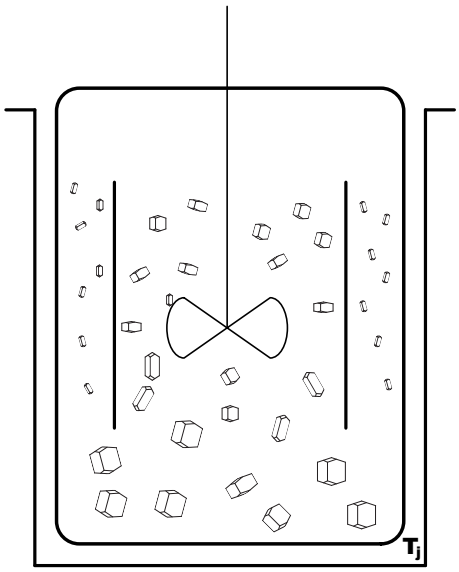

Figure 6.1: Batch crystallizer configuration.

impeller) is 0.04 m; the diameter of the impeller is 0.06 m.

6.2.1 Crystal nucleation and growth

The nucleation rate B of lysozyme crystals nucleated at 4%(w/v) NaCl and pH=4.5 is taken from [41] and is presented as follows:

$$B = \begin{cases} 0.041\sigma + 0.063 & \text{for} \quad \sigma \geq 3.11 \\ 8.0 \times 10^{-8} \exp(4.725\sigma) & \text{for} \quad \sigma < 3.11 \end{cases} \tag{6.1}$$

with units $[\text{cm}^{-3} \cdot \text{sec}^{-1}]$. For simulation and testing of the control performance of the proposed R2R-based MPC control scheme, the degree of secondary nucleation induced by the attrition process among crystals is disregarded. The supersaturation level σ is defined as the logarithmic ratio between the solute concentration C and the solubility s (mg/mL) as

Surface reaction	Rate equation
Adsorption r_a:	$K_0^+ \exp(\sigma)$
Desorption $r_d(i)$:	$K_0^+ \exp\left(\frac{\phi}{k_B T} - i\frac{E_{pb}}{k_B T}\right)$
Migration $r_m(i)$:	$K_0^+ \exp\left(\frac{\phi}{k_B T} - i\frac{E_{pb}}{k_B T} + \frac{E_{pb}}{2k_B T}\right)$

Table 6.1: Surface reaction rates

follows:

$$\sigma = \ln(C/s) \tag{6.2}$$

where the solubility s is calculated using the following second-order polynomial equation which has been calibrated with experimental data from [13] at 4%(w/v) NaCl and pH=4.5:

$$s = 0.0109T^2 - 0.1146T + 1.1773 \tag{6.3}$$

Please note that the temperature T in the crystallizer is in Celsius. The crystal growth is modeled through the kMC simulation using the rate equations presented in Table 6.1, which were originally developed by [32]

In order to capture the dependencies of the surface reactions (e.g., adsorption, desorption, and migration) on the surface micro-configuration, a number of modeling parameters are considered including the adsorption coefficient K_0^+, the number of nearest neighbors i, the average bonding energy per bond E_{pb}, and the total binding energy ϕ when a molecule is fully surrounded by neighbors (when i=4) [60]. In this work, extensive open-loop kMC simulations were executed in order to find a set of physically meaningful E_{pb} and ϕ values for the (110) and (101) faces such that the simulated growth rates are calibrated with

the experimental data in literature. Interested readers may find more detailed information regarding the development and execution of the kMC simulation for batch processes in [67]

6.2.2 Mass and energy balance equations

The mass balance equation for the amount of the protein solute C remaining in the continuous phase is the following ordinary differential equation (ODE):

$$\frac{dC}{dt} = -\frac{\rho_c}{V_{batch}} \frac{dV_{crystal}}{dt}, \qquad C(0) = C_0 \tag{6.4}$$

where $V_{crystal}$ is the total volume of crystals in the crystallizer, C_0 is the initial protein solute concentration, ρ_c is the crystal density, and V_{batch} is the volume of the batch crystallizer. Similarly, the evolution of the temperature T in the crystallizer is computed using the following ODE:

$$\frac{dT}{dt} = -\frac{\rho_c \Delta H_c}{\rho C_p V_{batch}} \frac{dV_{crystal}}{dt} - \frac{U_j A_j}{\rho C_p V_{batch}} \left(T - T_j\right), \qquad T(0) = T_0 \tag{6.5}$$

where T_j is the crystallizer jacket temperature, T_0 is the initial crystallizer temperature, ΔH_c is the enthalpy of crystallization, ρ is the density of the continuous phase, C_p is the specific heat capacity, A_j and U_j are the surface area and the overall heat transfer coefficient between the crystallizer wall and the jacket stream T_j, respectively, and the values for the process parameters are presented in Table 6.2.

ρ_c	1400	mg/cm^3
ΔH_c	-4.5	kJ/kg
$\rho(t)$	1000 + C(t)	mg/cm^3
C_p	4.13	$kJ/K \cdot kg$
V_{batch}	1	L
A_j	0.25	m^2
U_j	1800	$kJ/m^2 \cdot h \cdot K$
C_0	42	mg/cm^3
T_0	17	°C

Table 6.2: Parameters for the batch crystallizer model.

6.2.3 Population balance equation

The population balance equation (PBE) that describes the evolution of the crystal volume distribution for the batch crystallization process with crystal nucleation and growth is as follows:

$$\frac{\partial n(V,t)}{\partial t} + \frac{\partial \left(G_{vol}(V,\sigma)n(V,t)\right)}{\partial V} = B\delta(V) \tag{6.6}$$

where B is the nucleation rate, $\delta(\cdot)$ is the dirac delta function, and $G_{vol}(V,\sigma)$ is the volumetric crystal growth rate which will be precisely formulated in a following section. Additionally, we assume that at time $t = 0$ seconds there are no crystals inside the batch crystallizer. This PBE will be used for the design of a moment model in Section 6.2.5.

6.2.4 Moment models

In order to deal with the complexity of directly utilizing Eq. 6.6 for the numerical computation of a crystal volume distribution in real-time, the method of moments is applied to Eq. 6.6 and moment models that describe the dominant dynamics including the evolution of the number of crystals (i.e., zeroth moment M_0) and the total volume of crystals (i.e., first moment M_1) of crystals in the batch process are obtained. Then, this moment model can be used for the design of an MPC. The j^{th} moment is defined as $M_j(t) = \int_0^\infty V^j n(V,t)dV$. For the zeroth moment,

$$\frac{dM_0}{dt} = B, \tag{6.7}$$

and for $j \geq 1$, the j^{th} moment equation has the following form:

$$\frac{dM_j}{dt} = jG_{vol}M_{j-1} \tag{6.8}$$

6.2.5 Prediction of crystal shape

Based on the assumption that the geometry of the HEW lysozyme crystals is a rectangular prism [73], the volumetric crystal growth rate is formulated as follows:

$$G_{vol} = 2G_{110}\langle h_{110}\rangle\langle h_{101}\rangle + G_{101}\langle h_{110}\rangle^2 \tag{6.9}$$

where $\langle h_{110}\rangle$ and $\langle h_{101}\rangle$ are the average crystal heights in the directions of the (110) and (101) faces which can be computed from the following equations:

$$\begin{aligned} \frac{d\langle h_{110}\rangle}{dt} &= G_{110} - \frac{BV_{batch}\langle h_{110}\rangle}{M_0} \\ \frac{d\langle h_{101}\rangle}{dt} &= G_{101} - \frac{BV_{batch}\langle h_{101}\rangle}{M_0} \end{aligned} \tag{6.10}$$

where G_{110} and G_{101} are the crystal growth rates in the directions of the (110) and (101) faces. The following expressions are calibrated with the experimental data from [31] for $2.1 \leq \sigma \leq 4.1$ and are used in the MPC in order to predict the dynamic behavior of the crystal growth rates on each face:

$$\begin{aligned} G_{110} &= 0.1843\sigma^3 - 1.1699\sigma^2 + 2.8885\sigma - 2.5616 \\ G_{101} &= 0.1893\sigma^3 - 1.2264\sigma^2 + 2.9887\sigma - 2.5348 \end{aligned} \tag{6.11}$$

6.3 R2R-based model predictive control

6.3.1 Model predictive control formulation

In this section, we initially propose a model predictive controller (MPC) which will be used to compute a set of optimal jacket temperatures, and which will lead to the production of crystals with a desired shape distribution at the end of the batch. The moment models (cf. Eqs. 6.7 and 6.8) are derived from a population balance model and are used along with the mass and energy balance equations to describe the dominant dynamic behavior of the batch crystallization process. The growth rate equations are computed from open-loop kMC simulations. The design parameters for the proposed R2R-based MPC are chosen so that the proposed R2R-based MPC computes an optimal temperature profile which is required for the production of crystals with a desired shape distribution. The objective function (cf. Eq. 6.12a) is the sum of squared errors of the average crystal shape from a desired set-point value throughout the prediction horizon. The jacket temperature is used

as a manipulated input, and constraints on the temperature in the crystallizer and the rate of change of the jacket temperature are imposed (cf. Eq. 6.12b). The average crystal height on each face is updated according to Eq. 6.12g and the volumetric growth rate is computed through Eq. 6.12h. The resulting MPC formulation is given by the following optimization problem:

$$\min_{T_{j,1},\ldots,T_{j,i},\ldots,T_{j,p}} \quad \sum_{i=1}^{p} \left(\langle \alpha(t_i)\rangle - \alpha_{\text{set}}\right)^2 \tag{6.12a}$$

$$\text{s.t.} \quad 4^\circ\text{C} \le T \le 25^\circ\text{C} \qquad \left|\frac{T_{j,i+1}-T_{j,i}}{\Delta}\right| \le 2^\circ\text{C/min} \tag{6.12b}$$

$$G_{110} = 0.1843\sigma^3 - 1.1699\sigma^2 + 2.8885\sigma - 2.5616 \tag{6.12c}$$

$$G_{101} = 0.1893\sigma^3 - 1.2264\sigma^2 + 2.9887\sigma - 2.5348 \tag{6.12d}$$

$$s = 0.0109T^2 - 0.1146T + 1.1773 \tag{6.12e}$$

$$\frac{dM_0}{dt} = B, \qquad \frac{dM_1}{dt} = G_{vol}M_0 \tag{6.12f}$$

$$\frac{d\langle h_k\rangle}{dt} = G_k - \frac{BV_{batch}\langle h_k\rangle}{M_0}, \qquad k \in \{110, 101\} \tag{6.12g}$$

$$G_{vol} = 2G_{110}\langle h_{101}\rangle\langle h_{110}\rangle + G_{101}\langle h_{110}\rangle^2 \tag{6.12h}$$

$$\frac{dC}{dt} = -\frac{\rho_c}{V_{batch}}\frac{dM_1}{dt} \tag{6.12i}$$

$$\frac{dT}{dt} = -\frac{\rho_c \Delta H_c}{\rho C_p V_{batch}}\frac{dM_1}{dt} - \frac{U_j A_j}{\rho C_p V_{batch}}\left(T - T_{j,i}\right) \tag{6.12j}$$

$$\langle \alpha(t)\rangle \approx \frac{\langle h_{110}(t)\rangle}{\langle h_{101}(t)\rangle}, \qquad \langle V(t)\rangle = \frac{M_1(t)}{M_0(t)}, \qquad \sigma = \ln(C/s) \tag{6.12k}$$

where $p = 10$ is the number of prediction steps, Δ=40 seconds is the sampling time, $t_i = t + i\Delta$ is the time of the i^{th} prediction step, and $T_{j,i}$ is the jacket temperature of the i^{th} prediction step. At every sampling time, a set of optimal jacket temperatures, $(T_{j,1}, T_{j,2}, \ldots, T_{j,p})$,

is computed by solving Eq. 6.12 with new measurements (C and T) received from the crystallizer (i.e., kMC simulation) and the first value, $T_{j,1}$, is applied to the crystallizer until the next sampling time.

6.3.2 Batch-to-batch parameter estimation

The uncertainty associated with the solubility is modeled by multiplying correction factors $(\gamma_{s1},\ \gamma_{s2},\ \gamma_{s3})$ to the coefficients of the second-order polynomial equation (cf. Eq. 6.13c). Similarly, the uncertainty in the crystal growth rate is reflected by multiplying the nominal growth rate expressions by γ_{110}, γ_{101} (cf. Eq. 6.13d).

In this work, a multivariable optimization problem (MOP) is proposed in order to estimate the system parameters using the post-batch measurements. The correction factors, $\underline{\Gamma}$=[γ_{110} γ_{101} γ_{s1} γ_{s2} γ_{s3}], are chosen as the decision variables in the MOP. The objective function is the sum of squared errors of the predicted average values of the crystal size and shape at the end of the batch process from the measurements. Additionally, real-time measurements of (C, T) throughout the batch run are imposed as constraints in Eq. 6.13f to make sure that the predicted values are close to the measured ones, where ε_C and ε_T are tolerances. Another constraint is imposed in Eq. 6.13g for the feasibility of the computed decision variables in a practical sense. The post-batch measurements ($\langle\alpha\rangle$, $\langle V\rangle$, M_0) are used in Eqs. 6.13a and 6.13e. Please note that $\hat{X}_k$ is a predicted variable X for the k^{th} batch run and X_k represents a measured variable X after the k^{th} batch run. The resulting

optimization problem is as follows:

$$\min_{\underline{\Gamma}} \quad w_1 \left(\widehat{\langle \alpha(t_f) \rangle}_k - \langle \alpha(t_f) \rangle_k \right)^2 + w_2 \left(\widehat{\langle V(t_f) \rangle}_k - \langle V(t_f) \rangle_k \right)^2 \tag{6.13a}$$

$$\text{s.t.} \quad \text{Eqs. } 6.12c - 6.12k \tag{6.13b}$$

$$\hat{s} = 0.0109\gamma_{s1}T^2 - 0.1146\gamma_{s2}T + 1.1773\gamma_{s3} \tag{6.13c}$$

$$\hat{G}_{110} = \gamma_{110}G_{110}, \qquad \hat{G}_{101} = \gamma_{101}G_{101} \tag{6.13d}$$

$$\hat{M}_0(t_f) = M_0(t_f) \tag{6.13e}$$

$$|\hat{C}_k(t) - C(t)| \leq \varepsilon_C, \qquad |\hat{T}_k(t) - T(t)| \leq \varepsilon_T \tag{6.13f}$$

$$\underline{l}_\Gamma \preceq \underline{\Gamma}^T \preceq \underline{u}_\Gamma \tag{6.13g}$$

Remark 6.1 *It is important to note that although linearly-appearing parametric uncertainties are considered in the present work, certain classes of nonlinearly-appearing parametric uncertainties can be expressed as suitable definitions of the nonlinear terms in which the uncertain parameters appear with linear terms, and thus, they can be readily addressed within the proposed framework. In general, the handling of nonlinearly-appearing parametric uncertainties may lead to the need to solve constrained, nonlinear optimization problems, a task that can be handled with current optimization solvers, particularly given the off-line nature of the parameter estimation calculations.*

Remark 6.2 *Typically, the post-batch measurements are conducted off-line and thus the measurement noise is relatively small compared to that of real-time on-line measurements. Therefore, it is assumed that the accuracy of the post-batch measurements used in this work is acceptable.*

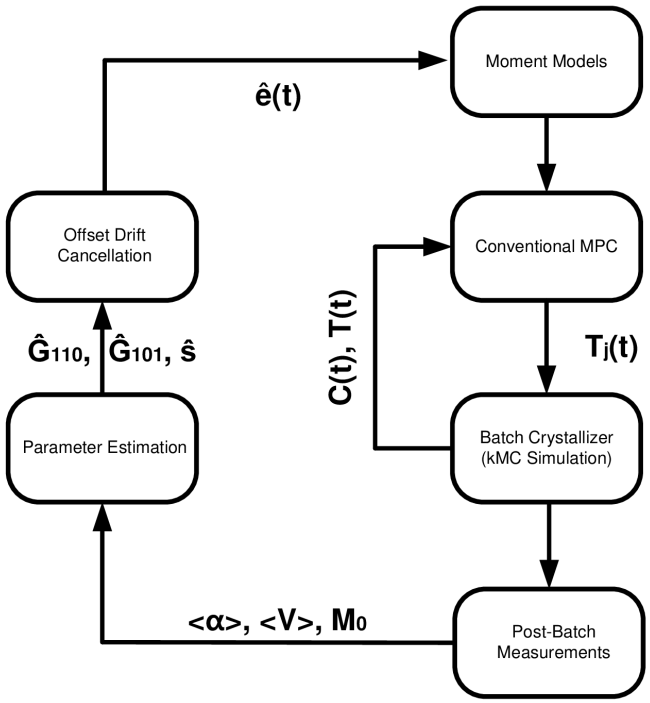

Figure 6.2: Closed-loop system under R2R-based MPC scheme.

6.3.3 Run-to-run control implementation algorithm

In general, there are many different ways that an R2R controller can be formulated, and the control performance is mainly determined by the design of the observer where a simple model may be an average of consecutive errors or may be as complicated as a Kalman filter.

For the batch crystallization process with changes in the process parameters, the parameter adaptive control (PAC) scheme can be used. However, if there are too many process parameters to estimate, a large number of measurements may be required for sufficient accuracy. Furthermore, by the time sufficient data has been obtained to estimate the pro-

cess model parameters, they may have drifted significantly [88]. In this situation, using PAC may further increase the offset. To deal with this issue, the following EWMA control scheme is proposed along with Eq. 6.13 for the computation of controlled inputs in the MPC as follows:

$$\widehat{\langle \alpha(t_f) \rangle}_{k+1} = f\left(\hat{\underline{\Gamma}}_{k+1}\right) + \hat{e}_{k+1} \tag{6.14}$$

where $\widehat{\langle \alpha(t_f) \rangle}_k$ is the predicted average crystal shape at the end of the k^{th} batch, $f\left(\hat{\underline{\Gamma}}_k\right)$ is a nonlinear equation that consists of Eqs. 6.12c-6.12k and depends on the system parameters $\hat{\underline{\Gamma}}_k$, and $\hat{e}_k$ is the estimated model prediction error. A schematic representation of the proposed R2R-based MPC structure is illustrated in Fig. 6.2.

1. During the k^{th} batch run, the real-time measurements of C_k and T_k are available from the batch crystallization process, and $\hat{\underline{\Gamma}}_k$ is used in the MPC to compute a set of optimal jacket temperatures T_j which will drive the temperature T in the crystallizer to a desired value.

2. At the end of the k^{th} batch run, the post-batch measurements of the product qualities such as average crystal size, shape, and number of crystals are measured and used to re-compute $\hat{\underline{\Gamma}}_{k+1}$ by solving the optimization problem, Eq. 6.13.

3. The model prediction error is updated recursively through a weighted average,

$$\hat{e}_{k+1} = (1-\lambda)\,\hat{e}_k + \lambda\left(\langle \alpha(t_f) \rangle_k - f\left(\hat{\underline{\Gamma}}_k\right)\right)$$

4. During the $k+1^{\text{th}}$ batch run, the predicted average crystal shape $\widehat{\langle \alpha(t_f) \rangle}_{k+1}$ is computed through Eq. 6.14 and used in the MPC to compute a set of optimal T_j values

and implement it in receding horizon fashion.

5. Increase k by 1 and repeat Step 1 to Step 5.

Remark 6.3 *In general, the learning factor λ can be understood as a process gain in the conventional P-controller in that a large λ would lead to fast convergence while a small λ is preferred for the stability of the controlled output. Therefore, the tradeoff between fast convergence and stability has to be evaluated by a trial and error procedure. Please note that the nominal system parameters are used a priori for $\hat{\underline{\Gamma}}_0$ and it is assumed that there is no parametric model mismatch in the beginning (i.e., $\hat{e}_0 = 0$).*

Remark 6.4 *The ideas of both an offset drift cancellation (ODC) scheme and of an adaptive parameter control (APC) scheme are used in the proposed R2R-based MPC to reduce the offset while simultaneously achieving fast convergence. Therefore, the proposed R2R-based MPC is able to deal with the parametric mismatch (i.e., inherent variation) of crystal nucleation and growth rates as well as the process drift by adapting the process model parameters through the parameter estimation algorithm described above (cf. Eq. 6.13), which cannot be done by a conventional MPC with a nominal process model (cf. Eq. 6.12). Because of the predictive ability of a model predictive controller, the proposed R2R-based MPC is also able to predict the evolution of crystal shape with good accuracy during the process when the measurements of the product qualities (e.g., size, shape, and number of crystals) are not available, which will lead to an improvement in the control performance and the production of crystals with a desired shape distribution.*

6.4 Simulation results

There are many factors, including the pH and the concentration of added electrolyte (e.g., NaCl), that affect the solubility of the protein solute in the system. A change in the solubility of the protein solute perturbs the crystallization process parameters from their nominal values, which may lead to poor controller performance unless appropriate adjustments are made to the nominal process model used in the MPC. In order to evaluate the control performance of the proposed R2R-based MPC in the presence of variations in the solubility of the protein solute, the pH value used in the kMC simulation (representing the batch crystallization process) is perturbed to 4.5 from the nominal value 4.4, while the NaCl concentration remains constant at 4%. This causes a drop of roughly 50% in the solubility of the protein solutes. Furthermore, the solubility drifts at a rate that causes it to change 5% from its nominal value by the end of fifty batch runs, which is consistent with the drift rate defined in [108] for a slowly drifting process.

Typically, an ODC controller is used to deal with the process drift and is robust with respect to the process drift because of less aggressive control actions. On the other hand, a PAC controller is preferred in order to achieve fast convergence if a correct process model is assumed, but the control performance can be degraded if there are many process model parameters to estimate compared to the number of measurements available. Therefore, the choice of the R2R controller type depends on the processing goal.

In this work, both the ODC and PAC controllers are integrated with a conventional MPC such that the MPC along with the PAC adapts the model parameters and at the same

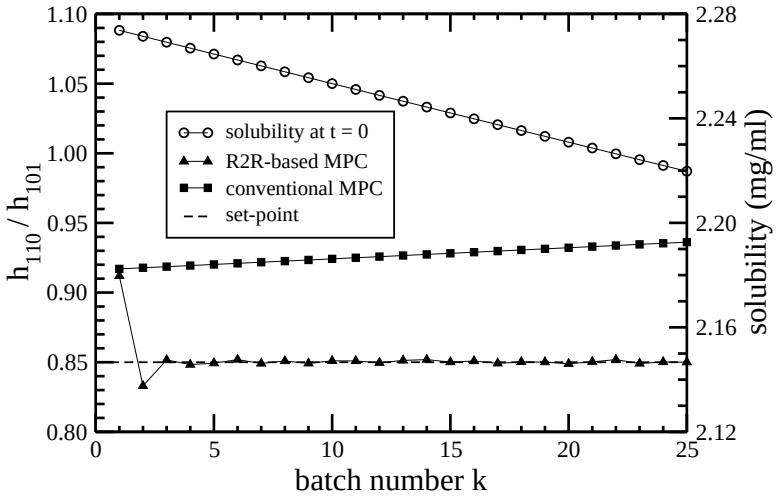

Figure 6.3: The evolution of the average crystal shape at $t = 20000$ seconds obtained from the kMC simulations from batch-to-batch under the conventional MPC and R2R-based MPC with the desired set-point $\langle \alpha_{\text{set}} \rangle = 0.85$. Additionally, the profile of solubility, which drifts from its nominal value, is plotted.

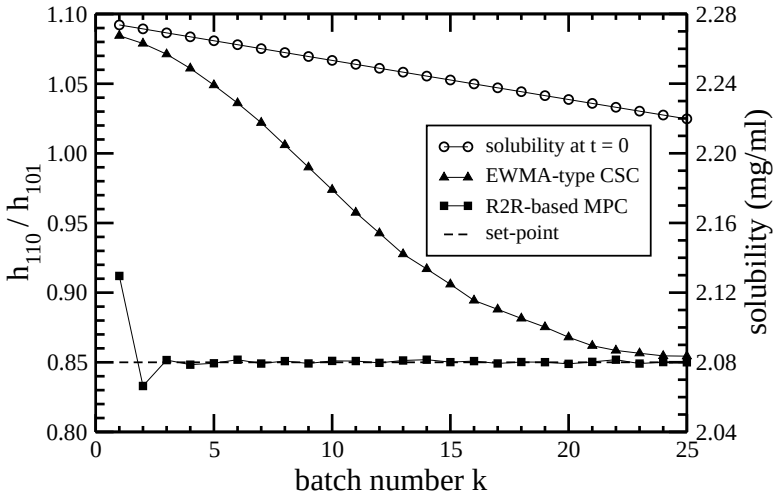

Figure 6.4: The evolution of the average crystal shapes at $t = 20000$ seconds in each batch run obtained from the kMC simulations from batch-to-batch under the EWMA-type CSC and R2R-based MPC. The desired set-point is $\langle \alpha_{\text{set}} \rangle = 0.85$. Additionally, the profile of solubility, which drifts from its nominal value, is plotted.

time handles the remaining offset through an EWMA-type control scheme. In Fig. 6.3, it is shown that the proposed R2R-based MPC with $\lambda = 0.3$ is able to achieve the production of crystals with a desired crystal shape distribution after three batch runs (i.e., fast convergence) while the control performance of a conventional MPC with nominal system parameters (cf. Eq. 6.12) becomes progressively worse as runs are repeated owing to process drift and variability.

For comparison purposes, the proposed R2R-based MPC scheme is compared with an EWMA-type constant supersaturation control (CSC) strategy where its desired set-point (i.e., supersaturation) for the k^{th} batch run is updated as is described below:

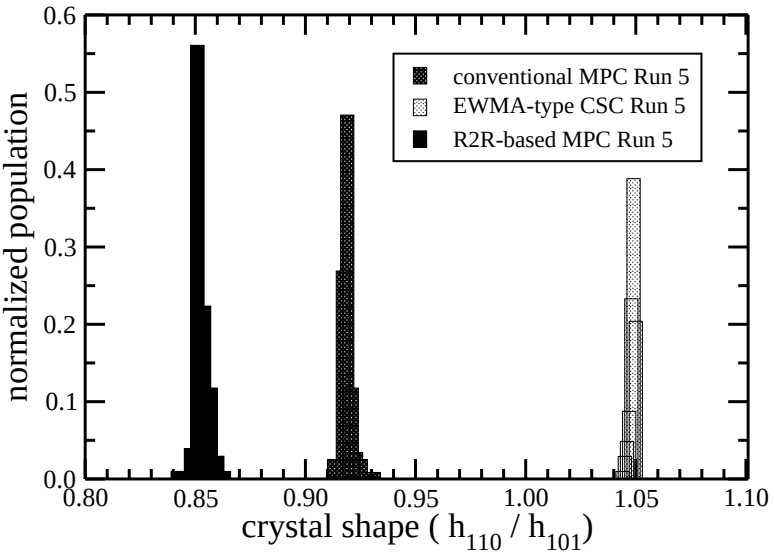

Figure 6.5: The normalized crystal shape distributions at $t = 20000$ seconds in each batch run obtained from the kMC simulations under the conventional MPC, EWMA-type CSC, and R2R-based MPC. The desired set-point is $\langle \alpha_{\text{set}} \rangle = 0.85$.

1. The desired supersaturation level $\sigma_{set,k}$, which will be applied to the k^{th} batch run, is computed as follows:

$$\sigma_{set,k} = \sigma_{set,k-1} + d_k$$

where the correction factor d_k has the following form:

$$d_k = d_{k-1} + \lambda \left(\langle \alpha(t_f) \rangle_{k-1} - \alpha_{\text{set}} \right).$$

2. At the end of the k^{th} batch run, the average crystal shape $\langle \alpha(t_f) \rangle_k$ is measured and is fed back to the proposed R2R-based MPC.

3. Increase k by 1 and repeat Step 1 to Step 3.

As is shown in Fig. 6.4, although both control schemes are able to produce crystals with a desired shape distribution after multiple runs, the convergence of the EWMA-type CSC is significantly slower than that of the proposed R2R-based MPC (twenty-four runs vs. three runs to achieve the same performance). Furthermore, the crystal shape distribution obtained by the proposed R2R-based MPC in Fig. 6.5 is closer to the desired set-point value, $\alpha_{\text{set}} = 0.85$, than that of the EWMA-type CSC. The superiority of the control performance of the proposed R2R-based MPC over the EWMA-type CSC and the conventional MPC without R2R model adaptation is the result of the parameter estimation step implemented in the proposed R2R-based MPC that effectively estimates the process model parameters by solving Eq. 6.13 with the post-batch measurements received from the previous run. As a result, the predicted solubility value approaches the actual solubility value as is shown in Fig. 6.6 with an offset of approximately 2% between the two profiles. This remaining offset caused by the process drift introduced to the current batch crystallization process is properly handled by an EWMA scheme (i.e., Steps 3 and 4 in the proposed R2R-based MPC), and thus in Fig. 6.7 the solubility at the end of each batch is successfully regulated to a constant value.

Furthermore, a comparison between a conventional MPC with an ODC scheme and with a PAC scheme is shown in Fig. 6.8. The conventional MPC with a PAC scheme converges quickly (after three batch runs) but with a persistent offset, while a conventional MPC with an ODC converges slowly but it eventually produces crystals with a desired shape. Therefore, both the ODC and PAC schemes are needed to reduce the offset while

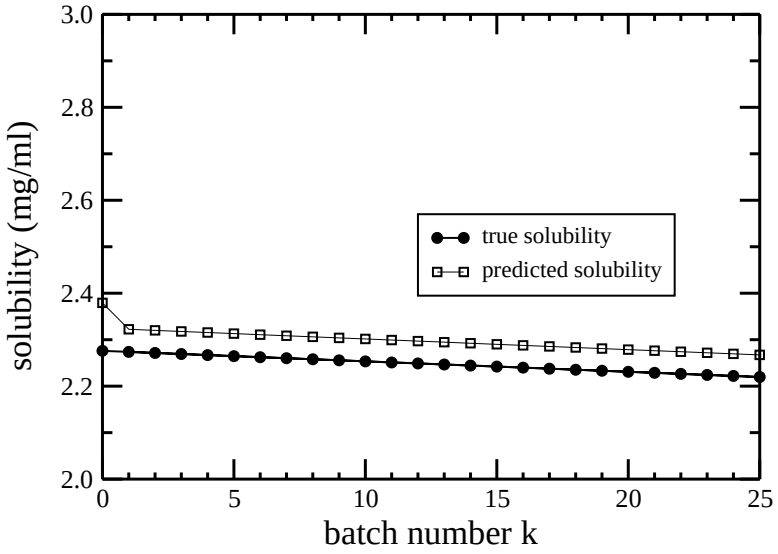

Figure 6.6: The evolution of the predicted and true solubilities in the beginning of batch runs from batch-to-batch under the R2R-based MPC. Please note that the discrepancy between the two

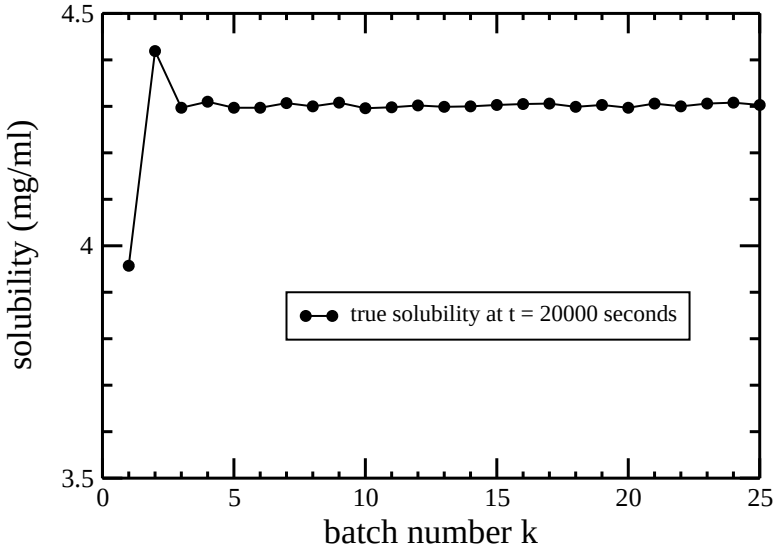

Figure 6.7: The evolution of the solubility at the end of batch runs from batch-to-batch under the R2R-based MPC.

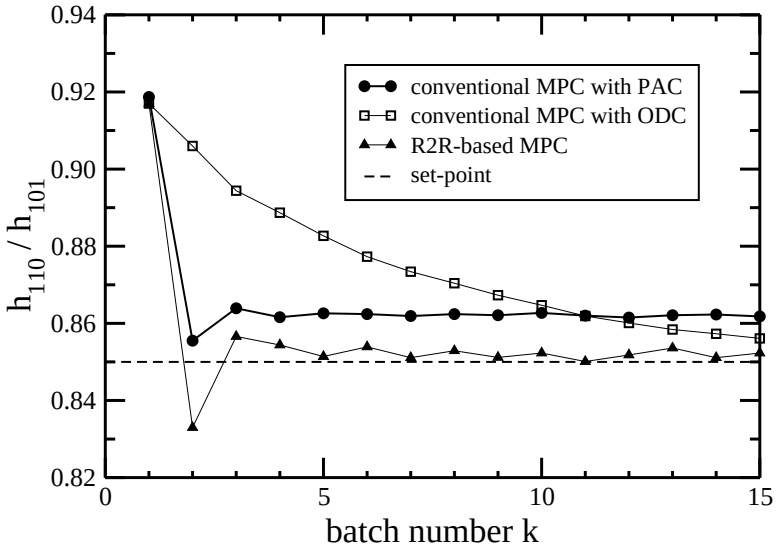

Figure 6.8: The evolution of the average crystal shape at $t = 20000$ seconds obtained from the kMC simulations from batch-to-batch under the conventional MPC with ODC and with PAC, and under the R2R-based MPC. The desired set-point is $\alpha_{\text{set}} = 0.85$.

simultaneously achieving fast convergence.

In Figs. 6.9 and 6.10, the jacket temperature profiles for the process under the EWMA-type CSC and the R2R-based MPC for different batch runs are presented. Please note that the jacket temperature profiles reach the optimal condition relatively quickly in the beginning and remain constant throughout the rest of the batch process. Moreover, the temperature profile over one entire batch run is added as an inset to each figure.

In addition to the constant process drift rate (i.e., 0.1% drop in solubility per batch) introduced in the simulations discussed above, a random process drift with an exponential distribution and a decaying process drift rate were also introduced in the solubility to

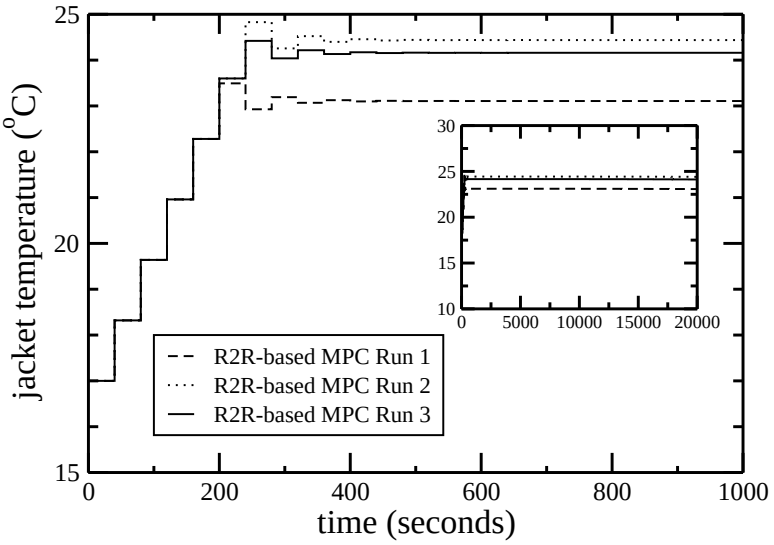

Figure 6.9: The evolution of the jacket temperature (T_j) computed by solving the R2R-based MPC with respect to time for $t < 1000$ seconds when the desired set-point is $\alpha_{\text{set}} = 0.85$. The inset shows the T_j profile from $t = 0$ to $t = 20000$ seconds.

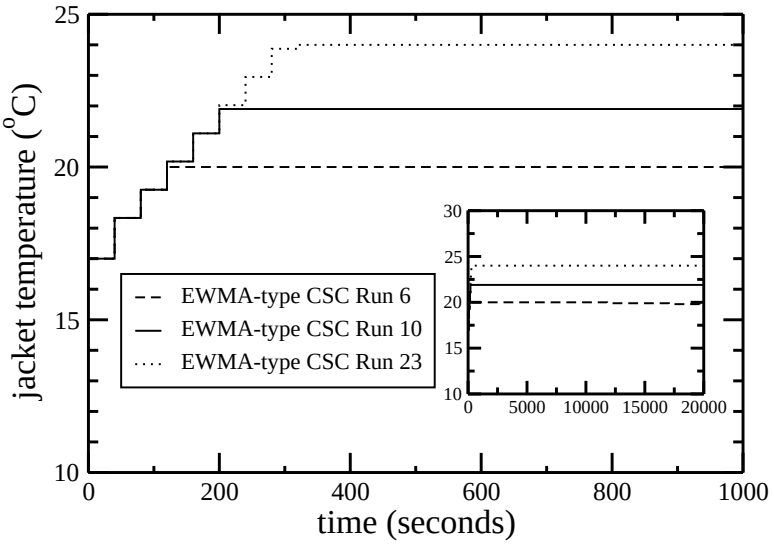

Figure 6.10: The evolution of the jacket temperature (T_j) with respect to time computed by solving the EWMA-type CSC with respect to time for $t < 1000$ seconds when the desired set-point is $\alpha_{\text{set}} = 0.85$. The inset shows the T_j profile from $t = 0$ to $t = 20000$ seconds.

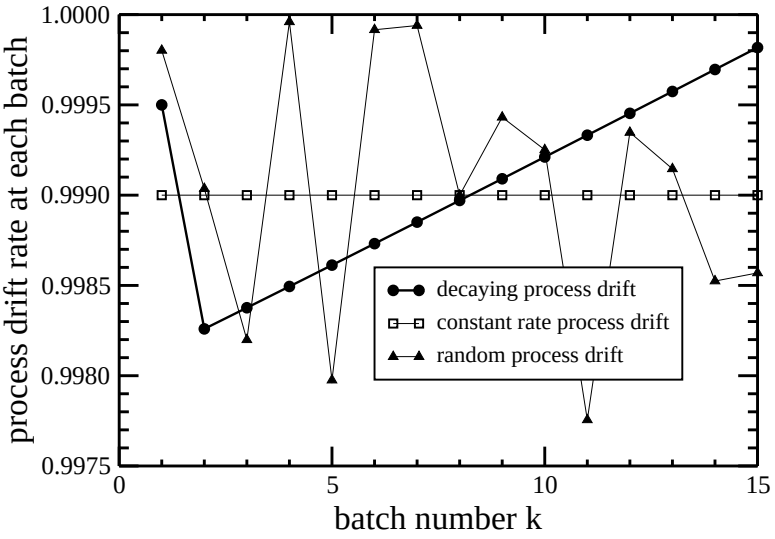

Figure 6.11: The evolution of the process drift rate from batch-to-batch. The type 1 process drift rate decays, the type 2 process drift rate is constant, and the type 3 process drift rate follows an exponential distribution.

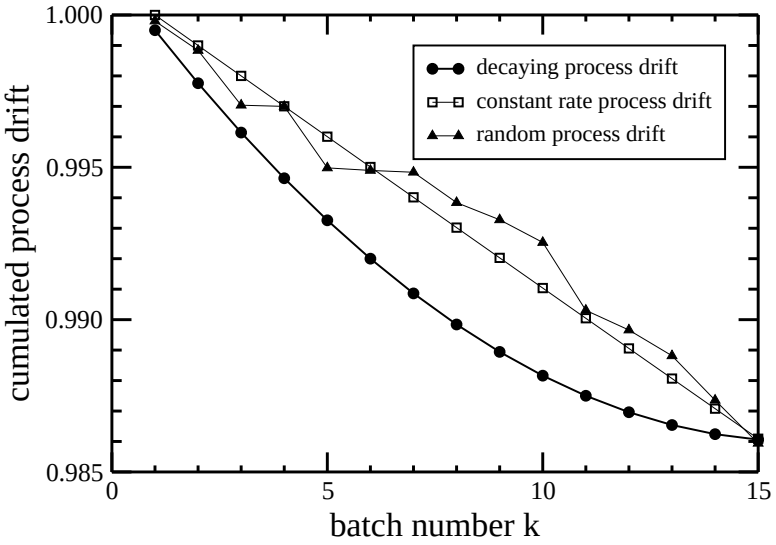

Figure 6.12: The evolution of the cumulative process drift from batch-to-batch, which indicates how much the real system has drifted from the initial nominal system. The type 1 process drift rate follows a decaying curve; the type 2 process drift rate is constant; and the type 3 process drift rate follows an exponential distribution.

evaluate the robustness of the proposed R2R-based MPC with respect to different types of process drift. As is presented in Figs. 6.11 and 6.12, the type 1 process drift rate is a decaying process drift rate for which the process drift rate decreases as runs are repeated, which is the most prevalent type of drift in the pharmaceutical/semiconductor industry [85]. The type 2 process drift rate is constant, and the type 3 process drift rate (i.e., variation from batch-to-batch) follows an exponential distribution. Please note that the means of the type 2 and type 3 process drifts are identical at a 0.1% drop in the solubility of the protein solute per batch and the y-axis in Fig. 6.12 indicates the degree of drift of the solubility variable from its nominal value by the end of each batch run. Thus, the value 1 on the y-axis corresponds to the nominal value, and the value decreases as the system drifts from its nominal value. Additionally, the cumulative process drifts are shown in Fig. 6.12, where the decaying characteristic of the type 1 process drift is more evident.

As in Fig. 6.7, the parametric mismatches in the solubility induced by the different types of process drifts are successfully handled by the proposed R2R-based MPC. It is apparent from Fig. 6.13 that the control performance of the proposed R2R-based MPC in response to the type 1 and type 3 process drifts is worse than its performance in response to the type 2 process drift. In particular, the control performance for the system with the type 3 process drift is worse than that for the system with the type 1 process drift because solubility under the type 3 process drift rate changes more drastically, and is thus more difficult to compensate quickly using the proposed R2R-based MPC. As presented in Fig. 6.14, for a high λ value, the proposed R2R-based MPC becomes vulnerable to the rapidly

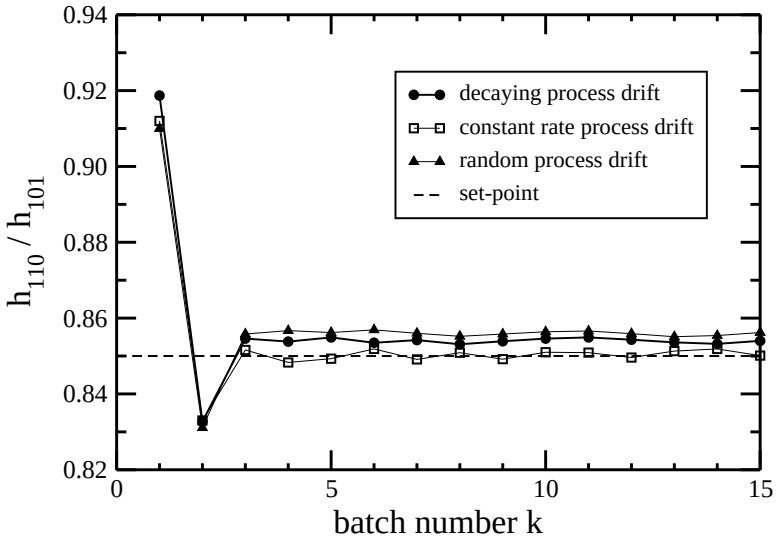

Figure 6.13: The evolution of the average crystal shape obtained from the kMC simulations from batch-to-batch under the R2R-based MPC with the three different process drift types described in Fig. 6.12. The type 1 process drift rate follows a decaying curve; the type 2 process drift rate is constant; and the type 3 process drift rate follows an exponential distribution.

changing process drift introduced to the system by the type 3 process drift, while this effect is relatively suppressed by using small λ values in the proposed R2R-based MPC. One potential solution to this problem is to adapt the learning factor λ after each batch to deal with the varying process drift rate.

Lastly, for the purpose of a test of the control performance when the controller does not account for uncertainty in the nucleation rate, the nucleation rate in the kMC simulation is dropped by 10% by multiplying Eq. 6.1 by 0.9. Since this uncertainty is not modeled in the controller process model, the other parameters $\underline{\Gamma}=[\gamma_{110}\ \gamma_{101}\ \gamma_{s1}\ \gamma_{s2}\ \gamma_{s3}]$ have to be

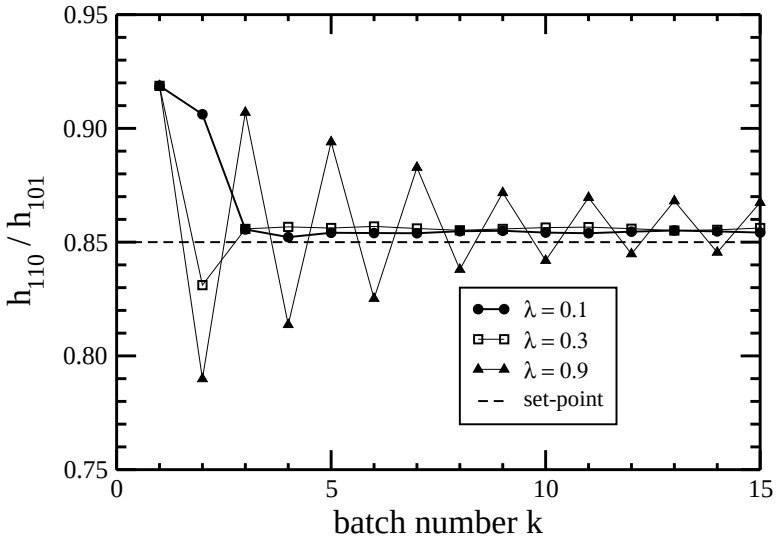

Figure 6.14: The evolution of the average crystal shape obtained from the kMC simulations from batch-to-batch under the R2R-based MPC for $\lambda = 0.1$, 0.3 and 0.9 with the type 3 process drift described in Fig. 6.12.

adjusted to compensate for the unmodeled uncertainty in the nucleation rate. Furthermore, the equality constraint (cf. Eq. 6.13e) forces the proposed R2R-based MPC to produce the same number of crystals as the previous batch run. As a result, it is shown in Fig. 6.15 that the controller model parameters are appropriately adjusted and thus the effect of the unmodeled uncertainty on the control performance is mitigated such that crystals are produced with a shape that is close to the desired set-point. However, the closed-loop performance under such an unmodeled uncertainty is slightly degraded, exhibiting an offset from the desired set-point. Such minor degradation is expected due to the nonlinear nature of the unmodeled uncertainty in the nucleation rate, while the ODC scheme used in the proposed R2R-based MPC is linear. To deal with this problem, a nonlinear ODC scheme could be adopted in order to improve the robustness of the proposed R2R-based MPC with respect to unmodeled uncertainties.

In this work, the closed-loop simulation results show that the average crystal shape distribution is driven close to a desired value after three batch runs under the proposed R2R-based MPC scheme, and hence varying the learning factor does not notably influence the control performance as is shown in Fig. 6.16. Therefore, the proposed R2R-based MPC is able to leverage smaller λ values (e.g., $\lambda = 0.1$) to reduce the effect of the measurement noise without significantly sacrificing the convergence speed.

Remark 6.5 *If the measurement noise is sufficiently high, an R2R controller may fail because the past measurements are not autocorrelated with those of the future runs [89, 57]. The best practice to deal with the measurement noise is to use a small learning factor λ in*

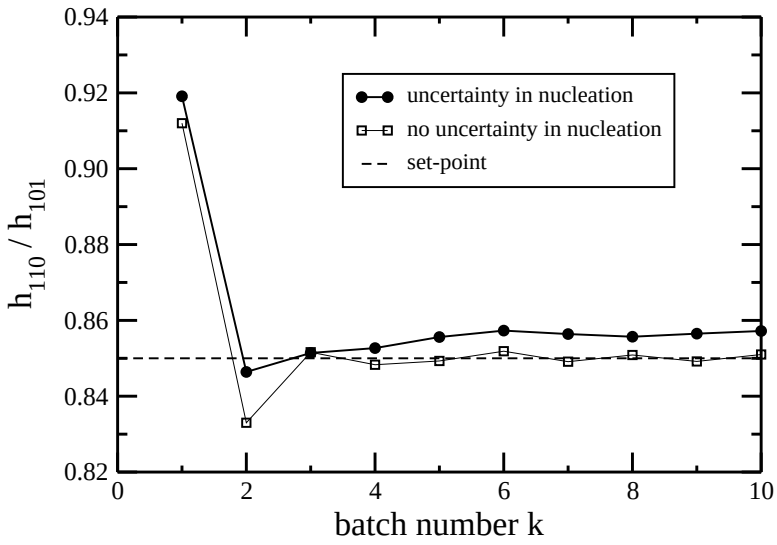

Figure 6.15: The evolution of the average crystal shape obtained from the kMC simulations from batch-to-batch under the R2R-based MPC when there is an unmodeled uncertainty in the nucleation rate and no uncertainty in the nucleation rate. The desired set-point is $\alpha_{\text{set}} = 0.85$.

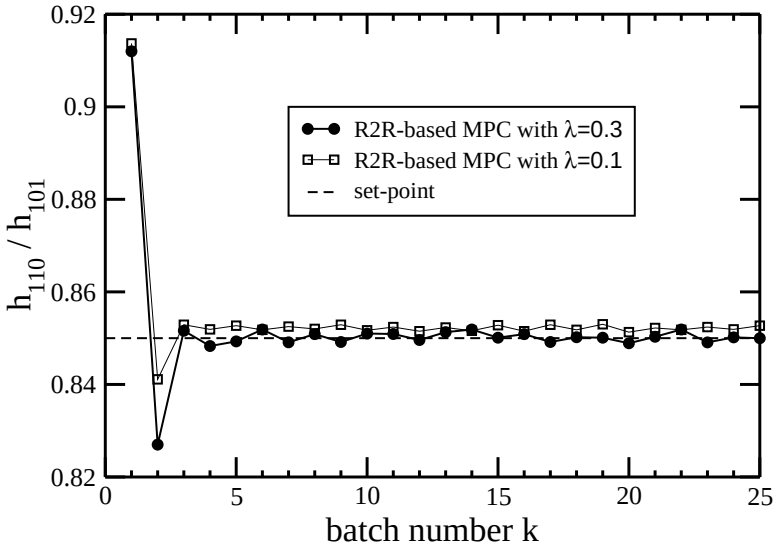

Figure 6.16: The evolution of the average crystal shape obtained from the kMC simulations from batch-to-batch under the R2R-based MPC with $\lambda = 0.1$ and $\lambda = 0.3$. The desired set-point is $\alpha_{\text{set}} = 0.85$.

an EWMA design at the cost of slower convergence. Additionally, a low-pass filter may be used to reduce the effects of noise of the measurements (both real-time and post-batch) on the operation of the batch crystallization process.

6.5 Conclusions

In this work, we considered the design of a novel R2R-based MPC for a batch crystallization process with significant process drift and inherent variations in solubility and crystal growth rates. In order to achieve the production of crystals with a desired crystal shape distribution, a conventional MPC with nominal process model parameters (cf. Eq. 6.12) was initially applied to the process. However, due to the process drift, the mismatch between the controller model and the process dynamic behavior became severe as batch runs were repeated. To deal with this problem, an R2R-based MPC was proposed that, after each batch run, received post-batch measurements, including measurements of the average crystal shape and size and the number of crystals, and used these to estimate off-line the process model parameters as they drifted from their nominal values via a multivariable optimization problem. Along with the adapted model parameters, an EWMA scheme was used to deal with the remaining offset in the model and thereby to compute via MPC a set of optimal jacket temperatures in real-time that drives the process to a desired condition. Furthermore, the crystal growth in the batch crystallization process was modeled through kMC simulations which were then used to demonstrate the ability of the proposed control scheme to suppress the inherent variation and process drift in solubility and crystal

growth rates. Through the proposed approach, the production of crystals with a desired shape distribution was successfully achieved after three batch runs through the use of R2R-based MPC while it took twenty-four batch runs for the system with the EWMA-type CSC strategy to produce crystals with the desired shape distribution.

Chapter 7

A method for handling batch-to-batch parametric drift using moving horizon estimation: application to run-to-run MPC of batch crystallization

7.1 Introduction

This chapter focuses on developing a run-to-run (R2R) model parameter estimation scheme based on moving horizon estimation (MHE) concepts for the modeling of batch-to-batch process model parameter variation using a polynomial regression scheme. Subsequently, the batch process model parameters computed via the proposed R2R model parameter es-

timation scheme are used in a model predictive controller (MPC) within each batch to compute a set of optimal jacket temperatures for the production of crystals with a desired shape distribution in a batch crystallization process. The ability of the proposed method to suppress the inherent variation in the solubility caused by batch-to-batch parametric drift and to handle the noise in post-batch measurements is demonstrated by applying the proposed parameter estimation and control method to a kinetic Monte Carlo (kMC) simulation model of a batch crystallization process used to produce hen egg white (HEW) lysozyme crystals. Furthermore, the performance of the proposed R2R model parameter estimation scheme is evaluated with respect to the different orders of polynomials and different moving horizon lengths in order to calculate the best parameter estimates. The average crystal shape distribution of crystals produced from the closed-loop simulation of the batch crystallizer under the MPC with the proposed R2R model parameter estimation scheme is much closer to a desired set-point value compared to that of the double exponentially-weighted-moving-average-based MPC (dEWMA-based MPC) and that of MPC based on the nominal process model.

7.2 Modeling of batch crystallization process

To present and evaluate the proposed technique for process model parameter estimation, we will focus on a batch crystallization process used to produce HEW lysozyme crystals.

7.2.1 Crystal nucleation

At 4%(w/v) NaCl and pH=4.5, the lysozyme crystals are nucleated according to the following rate expressions [41]:

$$B = \begin{cases} 0.041\sigma + 0.063 & \text{for} \quad \sigma \geq 3.11 \\ 8.0 \times 10^{-8} \exp(4.725\sigma) & \text{for} \quad \sigma < 3.11 \end{cases} \tag{7.1}$$

where B is the nucleation rate with units $[\text{cm}^{-3} \cdot \text{sec}^{-1}]$, and the supersaturation level σ is defined as follows:

$$\sigma = \ln(C/s) \tag{7.2}$$

where C is the solute concentration and s (mg/mL) is the solubility, which is calculated using the following third-order polynomial equation taken from [13]:

$$s(T) = 2.88 \times 10^{-4} T^3 - 1.65 \times 10^{-3} T^2 + 4.62 \times 10^{-2} T + 6.01 \times 10^{-1} \tag{7.3}$$

where the temperature in the crystallizer, T, is in degrees Celsius.

7.2.2 Crystal growth

The crystal growth is modeled through the kMC simulation using the following rate equations, which are adopted from [32]. The adsorption rate, r_a, is independent of each lattice site and is defined as follows:

$$r_a = K_0^+ \exp(\sigma) \tag{7.4}$$

where K_0^+ is the adsorption coefficient. On the other hand, the desorption and migration rates depend on the surface micro-configuration (i.e., the number of particles that surround

Face	E_{pb}/k_B	ϕ/k_B
(110)	1077.26 K	227.10 K
(101)	800.66 K	241.65 K

Table 7.1: Parameters for the (110) and (101) faces at 42 mg/mL NaCl and pH= 4.5 at $T = 18^{\circ}$C. Additionally, $K_o^+ = 0.211$ seconds^{-1}.

the particle of interest). Thus, the desorption rate for a lattice site with i nearest neighbors, $r_d(i)$, is given by:

$$r_d(i) = K_0^+ \exp\left(\frac{\phi}{k_B T} - i\frac{E_{pb}}{k_B T}\right) \tag{7.5}$$

where E_{pb} is the average bonding energy per bond and ϕ is the total binding energy when chemical bonds of a molecule are fully occupied by nearest neighbors (i.e., $i = 4$). In order to account for the fact that the migration rate is higher than the desorption rate, the migration rate, $r_m(i)$, is defined by multiplying Eq. 7.5 by an additional term and is shown below:

$$r_m(i) = K_0^+ \exp\left(\frac{\phi}{k_B T} - i\frac{E_{pb}}{k_B T} + \frac{E_{pb}}{2k_B T}\right) \tag{7.6}$$

The crystal growth rates obtained from the kMC simulations are calibrated with the experimental data from [32] by manipulating a set of E_{pb} and ϕ values for the (110) and (101) faces through extensive open-loop kMC simulations. The parameters for the kMC simulation are listed in Table 7.1.

7.2.3 Mass and energy balance equations

The mass and energy balance equations used to calculate the amount of the protein solute remaining in the continuous phase, C, and the temperature in the crystallizer, T, are given by the following ordinary differential equations:

$$\frac{dC}{dt} = -\frac{\rho_c}{V_{batch}} \frac{dV_{crystal}}{dt}, \qquad C(0) = C_0 \tag{7.7}$$

$$\frac{dT}{dt} = -\frac{\rho_c \Delta H_c}{\rho C_p V_{batch}} \frac{dV_{crystal}}{dt} - \frac{U_j A_j}{\rho C_p V_{batch}} \left(T - T_j\right), \qquad T(0) = T_0 \tag{7.8}$$

where $V_{crystal}$ is the total volume of crystals in the crystallizer, $C_0 = 42$ mg/cm^3 is the initial protein solute concentration, $\rho_c = 1400$ mg/cm^3 is the crystal density, $V_{batch} = 1$ L is the volume of the batch crystallizer, $T_0 = 17$ °C is the initial crystallizer temperature, $\Delta H_c = -4.5$ kJ/kg is the enthalpy of crystallization, $\rho(t) = 1000 + C(t)$ mg/cm^3 is the density of the continuous phase, $C_p = 4.13$ kJ/K kg is the specific heat capacity, and $A_j = 0.25$ m^2 is the surface area and $U_j = 1800$ kJ/m^2 h K is the overall heat transfer coefficients between the jacket stream T_j and the crystallizer wall.

7.2.4 Moment models

Due to the complexity of a population balance equation (PBE), it cannot be directly used for the computation of the crystal volume distribution in real-time. Motivated by this, a moments model is used to describe the evolution of the number and the total volume of crystals in the batch crystallization process in the process model and is used in the controller

with the form:

$$\frac{dM_0}{dt} = B \tag{7.9}$$

$$\frac{dM_1}{dt} = G_{vol} M_0 \tag{7.10}$$

where $M_j(t) = \int_0^\infty V^j n(V,t) dV$ is the j^{th} moment for $j = 0,\ 1$, $n(V,t)$ is the number of crystals with volume V at time t, and G_{vol} is the volumetric crystal growth rate, which is formulated as follows:

$$G_{vol} = 2G_{110}\langle h_{110}\rangle\langle h_{101}\rangle + G_{101}\langle h_{110}\rangle^2 \tag{7.11}$$

where the crystal growth rates in the directions of the (110) and (101) faces, G_{110} and G_{101}, can be obtained through the following expressions:

$$\begin{aligned} G_{110} &= 0.1843\sigma^3 - 1.1699\sigma^2 + 2.8885\sigma - 2.5616 \\ G_{101} &= 0.1893\sigma^3 - 1.2264\sigma^2 + 2.9887\sigma - 2.5348 \end{aligned} \tag{7.12}$$

which are calibrated with experimental data from [31]. Similarly, the average crystal heights, $\langle h_{110}\rangle$ and $\langle h_{101}\rangle$, are calculated by using the following ordinary differential equations:

$$\begin{aligned} \frac{d\langle h_{110}\rangle}{dt} &= G_{110} - \frac{BV_{batch}\langle h_{110}\rangle}{M_0} \\ \frac{d\langle h_{101}\rangle}{dt} &= G_{101} - \frac{BV_{batch}\langle h_{101}\rangle}{M_0} \end{aligned} \tag{7.13}$$

and thereby the average crystal shape, $\langle \alpha \rangle$, and size, $\langle V \rangle$, can be computed as follows:

$$\langle \alpha \rangle \approx \frac{\langle h_{110}\rangle}{\langle h_{101}\rangle} \qquad \langle V \rangle = \frac{M_1}{M_0} \tag{7.14}$$

A more detailed description regarding the derivation of the moment model that accounts for the dynamic evolution of the crystal volume distribution for the batch crystallization process can be found in [72].

7.3 MPC with R2R model parameter estimation

7.3.1 MPC formulation

In Section 7.3.1, a model predictive controller (MPC) is presented for in-batch control. Specifically, the dominant dynamic behavior of the evolution of the crystal shape distribution in the batch crystallization process is modeled through the process model (cf. Eqs. 7.1–7.3 and 7.7–7.14), which is used to compute a set of optimal jacket temperatures that minimizes the sum of the squared deviations of the average crystal shape from a set-point value over the entire prediction horizon. Constraints on the rate of change of the jacket temperature (i.e., manipulated input) and the temperature in the crystallizer are imposed. The resulting MPC formulation is given by the following optimization problem:

$$\min_{T_{j,1},\ldots,T_{j,i},\ldots,T_{j,p}} \quad \sum_{i=1}^{p} \left(\langle \alpha(t_i) \rangle - \alpha_{\text{set}}\right)^2 \tag{7.15a}$$

$$\text{s.t.} \quad \text{Eqs. } 7.1 - 7.3 \text{ and } 7.7 - 7.14 \tag{7.15b}$$

$$4^\circ\text{C} \leq T \leq 25^\circ\text{C} \qquad \left|\frac{T_{j,i+1} - T_{j,i}}{\Delta}\right| \leq 2^\circ\text{C/min} \tag{7.15c}$$

where $p = 10$ is the length of the prediction horizon, T is the crystallizer temperature, $\Delta = 40$ is the sampling time, α_{set} is the desired average crystal shape (i.e., set-point), $t_i = t + i\Delta$ is the time at the i^{th} prediction step, $T_{j,i}$ is the jacket temperature, and $\langle \alpha(t_i) \rangle$ is the average crystal shape at the i^{th} prediction step, respectively. At every sampling time, the real-time measurements for the solute concentration in the continuous phase and the temperature in the crystallizer are used to compute a set of optimal jacket temperatures,

$(T_{j,1}, T_{j,2}, \ldots, T_{j,p})$, by solving Eq. 7.15 where the first value, $T_{j,1}$, is applied to the crystallizer over the next sampling time.

7.3.2 MPC with R2R model parameter estimation scheme

For the batch crystallization process with changes in the process model parameters owing to process drift, an R2R model parameter estimation scheme based on MHE concepts is proposed and used along with post-batch measurements from multiple batch runs in a moving horizon fashion to estimate parameters of the batch crystallization model (cf. Eqs. 7.1–7.3 and 7.7–7.14). Then, the updated process model parameters are used in the MPC for the computation of control inputs applied to a batch crystallization process.

R2R model parameter estimation scheme based on MHE concepts

There are many different formulations for an R2R parameter estimation scheme and the design of the observer significantly affects the estimator performance. In this work, an optimization-based parameter estimation scheme is proposed in order to estimate the process model parameters using several sets of post-batch measurements. Specifically, the uncertainty in the solubility of the protein solute is accounted for by multiplying the nominal third-order polynomial equation for solubility, Eq. 7.3, by a correction factor γ_s. The uncertainty associated with the crystal growth rates in the directions of the (110) and (101) faces is taken into account by multiplying the nominal growth rate expressions for the (110) and (101) faces by the parameters γ_{110} and γ_{101}, respectively. Furthermore, to account for

the offset between the predicted and measured values for the average crystal shape and size, a set of correction factors (γ_α and γ_V), is introduced directly into the objective function.

Specifically, the optimization problem for the proposed R2R model parameter estimation scheme based on MHE concepts after the n^{th} batch run is formulated as follows:

$$\min_{\underline{Q}_1,\cdots,\underline{Q}_p} \quad \sum_{k=n-m+1}^{n} w_\alpha \left(\widehat{\langle \alpha(t_f) \rangle}_k + \gamma_\alpha(k) - \langle \alpha(t_f) \rangle_k \right)^2 + w_V \left(\widehat{\langle V(t_f) \rangle}_k + \gamma_V(k) - \langle V(t_f) \rangle_k \right)^2 \tag{7.16a}$$

$$\text{s.t.} \quad \text{Eqs. } 7.1 - 7.3 \text{ and } 7.7 - 7.14 \tag{7.16b}$$

$$\hat{s}(k) = \gamma_s(k) s(k) \tag{7.16c}$$

$$\hat{G}_{110}(k) = \gamma_{110}(k) G_{110}(k), \qquad \hat{G}_{101}(k) = \gamma_{101}(k) G_{101}(k) \tag{7.16d}$$

$$\gamma_x(k) = \sum_{r=1}^{p} q_{(x,r)} \left[\gamma_x(k-1) \right]^r \qquad \forall \ \gamma_x \in [\gamma_{110} \ \gamma_{101} \ \gamma_s \ \gamma_\alpha \ \gamma_V] \tag{7.16e}$$

where s is the solubility, and G_{110} and G_{101} are the crystal growth rates in the directions of the (110) and (101) faces. Please note that $\hat{X}_k$ is a predicted variable X for the k^{th} batch run and X_k represents a measured variable X after the k^{th} batch run. Furthermore, the correction factors are initially $\underline{\Gamma}(0)$ =[1 1 1 0 0], which are the nominal values for the batch crystallization process. More details about correction factors are presented below.

Referring to Eq. 7.16, we note that Eq. 7.16e is used in order to approximate the batch-to-batch parametric drift from the $k-m+1^{\text{th}}$ to k^{th} batch runs with a p^{th} order polynomial through the manipulation of the decision variables, $\underline{Q}_1 = [q_{(110,1)} \ q_{(101,1)} \ q_{(s,1)} \ q_{(\alpha,1)} \ q_{(V,1)}]$, $\cdots$, $\underline{Q}_p = [q_{(110,p)} \ q_{(101,p)} \ q_{(s,p)} \ q_{(\alpha,p)} \ q_{(V,p)}]$ in a moving horizon fashion. For example, the p^{th} order polynomial for the solubility correction factor $\gamma_s(k)$ can be written in the form

$\gamma_s(k) = \sum_{r=1}^{p} q_{(s,r)} [\gamma_s(k-1)]^r$. Then, the batch-to-batch dynamics of the process drift are estimated using Eq. 7.16e to predict a set of correction factors for the $k+1^{\text{th}}$ batch run, $\underline{\Gamma}(k+1) = [\gamma_{110}(k+1)\ \gamma_{101}(k+1)\ \gamma_s(k+1)\ \gamma_\alpha(k+1)\ \gamma_V(k+1)]$. The objective function (cf. Eq. 7.16a) consists of the sum of squared errors between the predicted average crystal size and shape, $\widehat{\langle \alpha(t_f) \rangle}$ and $\widehat{\langle V(t_f) \rangle}$, and the measured ones, $\langle \alpha(t_f) \rangle$ and $\langle V(t_f) \rangle$, which are obtained at the end of the batch crystallization process from the $k-m+1^{\text{th}}$ to k^{th} batch runs where m is the moving horizon length. In the beginning of the batch-to-batch estimation, the number of post-batch measurements is allowed to grow until it reaches the length of the horizon (i.e., until the batch number becomes equal to m).

We note that the sensitivity of the proposed R2R model parameter estimation scheme based on MHE concepts to the different orders of polynomials and different moving horizon lengths is further discussed in Section 7.4 below.

Remark 7.1 *While the sign and magnitude of the rate of the process drift change from batch-to-batch, if the overall batch-to-batch dynamics of the process drift can be described by a smooth function, Eq. 7.16e in the proposed R2R model parameter estimation scheme should be able to model such a drift, which should lead to good parameter estimates for the next batch run. Furthermore, the idea of the proposed R2R model parameter estimation scheme based on MHE concepts is related to that of least squares estimation in that the relationship between the independent variables and the dependent variables is modelled through a p^{th} order polynomial and is used to find the best fit polynomial of multiple data points. Other nonlinear functions besides polynomials can be also used if necessary.*

Remark 7.2 *A short horizon length allows the proposed model parameter estimation scheme to follow fast batch-to-batch dynamics of the process drift while a longer horizon length (i.e., post-batch measurements from multiple batch runs) is able to better deal with the noise in the process and post-batch measurements.*

MPC with R2R model parameter estimation scheme: implementation algorithm

An MPC with the proposed R2R model parameter estimation scheme is implemented for a batch crystallization process for the computation of the control inputs as follows:

1. At the end of the k^{th} batch run, the post-batch measurements of the product qualities such as the number of crystals and the average size and shape of the crystals are measured.

2. Then, the real-time measurements of the solute concentration in the continuous phase and the temperature in the crystallizer ($[C_{k-m+1}(t), T_{k-m+1}(t)], \ldots, [C_k(t), T_k(t)] \ \forall \ t \in [0, t_f]$) over the last m measurements (i.e., moving horizon length) are used to compute $\underline{Q}_1, \cdots, \underline{Q}_p$ that minimize the cost function, Eq. 7.16a. Please note that t_f is the final time for one batch run.

3. The one-step-ahead correction factors for the $k+1^{\text{th}}$ batch run, $\hat{\underline{\Gamma}}_{k+1}$, are predicted through the use of $\underline{Q}_1, \cdots, \underline{Q}_p$ obtained from Step 2. Then, the process model parameters are updated through $\hat{\underline{\Gamma}}_{k+1}$ and they are used in the model employed in the MPC to compute a set of optimal jacket temperatures T_j which will drive the temperature

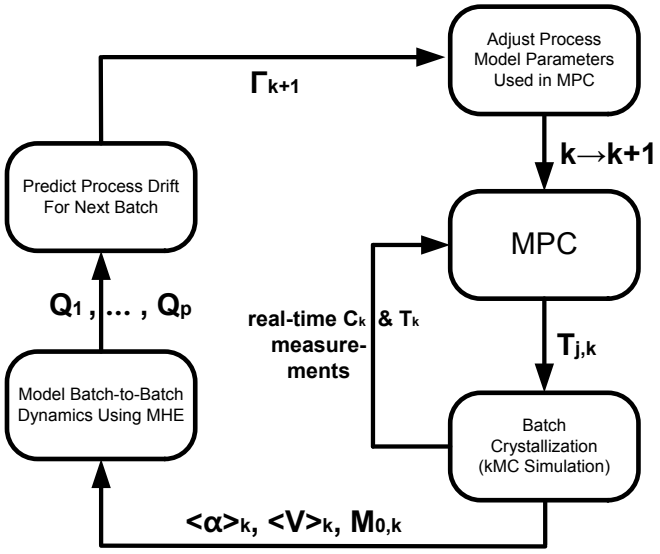

Figure 7.1: Model predictive control with R2R model parameter estimation.

T in the crystallizer to a desired value.

4. Increase k by 1 and repeat Step 1 to Step 4.

We note that the real-time measurements of the solute concentration and the temperature in the crystallizer are assumed to be available at each sampling time. A schematic representation of the MPC with the proposed R2R model parameter estimation scheme is shown in Fig. 7.1.

7.4 Application of MPC with R2R model parameter estimation to batch crystallization

One of the reasons that control of the size and shape distributions of crystals produced from a batch process may be difficult is because even minor contamination in the feedstock container (e.g., variations in the pH or elevated electrolyte concentration levels) may lead to a significant drift of key process parameters from batch-to-batch. Furthermore, minor contamination in the feedstock container cannot be identified immediately, and thus, its undesired effect on the product quality continues throughout succeeding batch runs until the feedstock container is replaced. To tackle this problem, we initially use the proposed R2R model parameter estimation scheme based on MHE concepts where a polynomial regression scheme is applied in a moving horizon fashion to approximate the batch-to-batch dynamics of the drift and adjust the MPC model parameters at the beginning of each batch. Then, the MPC with the updated process model parameters is used to compute the optimal jacket temperature by suppressing the effect of the process drift in the next batch. In the proposed estimation scheme, we note that only post-batch measurements are used for the parameter estimation scheme. Furthermore, process noise (approximately 2% of the nominal value) due to the stochastic nature of the crystal growth mechanisms and measurement noise (approximately 8% of the nominal value) are modeled through the kMC simulation. In order to simulate the operation of each batch run, a single kMC simulation is executed and used for the analysis per batch run.

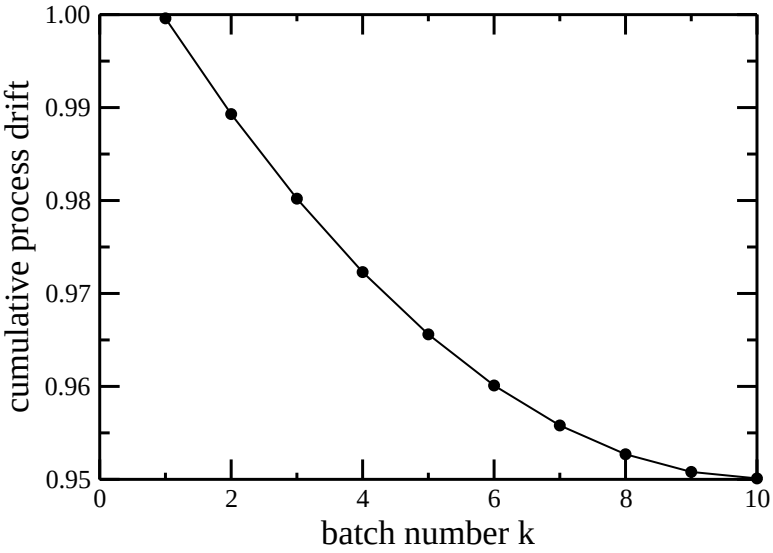

Figure 7.2: The evolution of the cumulative process drift with an exponentially decaying rate from batch-to-batch. Please note that the y-axis shows how much the batch system is perturbed from a nominal batch system (nominal batch system corresponds to a y-axis value equal to 1).

The controller performance of the MPC with the proposed R2R model parameter estimation scheme is initially evaluated in response to a process drift with an exponentially decaying process drift rate whose rate decays from 1 (i.e., nominal system) to 0.95 over ten batch runs (see, e.g., Fig. 7.2). Additionally, a more complicated process drift whose rate fluctuates is considered in order to evaluate the robustness of the MPC with the proposed R2R model parameter estimation scheme for a more realistic environment for the operation of the batch crystallization process (see, e.g., Fig. 7.3). For comparison purposes, the dEWMA-based MPC that captures the changes in the rate of the process drift and then adjusts the outputs to MPC, and the MPC that uses the nominal process model are also applied to the batch crystallization process model. To evaluate the controller performance, the mean squared error (MSE) of the offset ($\langle \alpha(t_f) \rangle_i - \alpha_{\text{set}}$) between the measured average crystal shape after the i^{th} batch run and the set-point value is introduced as follows:

$$\text{MSE} = \frac{\sum_{i=1}^{n} \left(\langle \alpha(t_f) \rangle_i - \alpha_{\text{set}} \right)^2}{n} \tag{7.17}$$

where n is the total number of batch runs.

7.4.1 dEWMA-based model predictive control

For the sake of comparison, a double-exponentially-weighted-moving-average (dEWMA) scheme, which is known for its ability to capture the batch-to-batch dynamics of the process drift [11, 117, 19, 125], is integrated with the MPC and its closed-loop performance is presented along with that of the MPC with the proposed R2R model parameter estimation

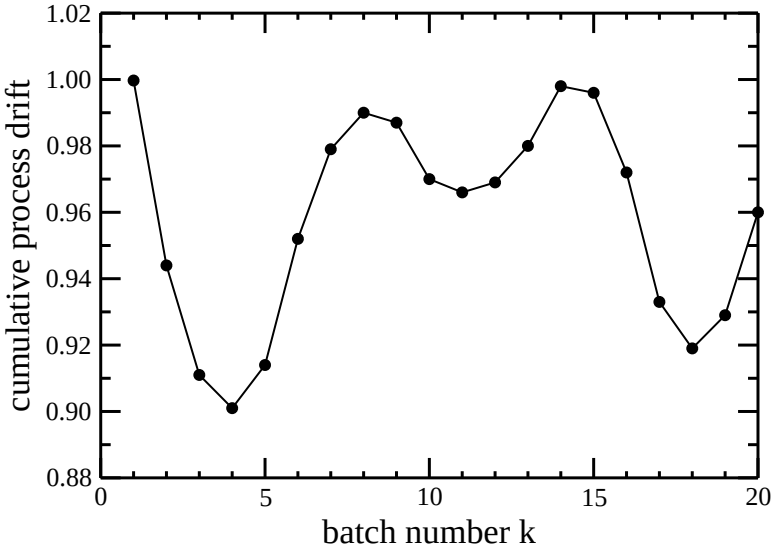

Figure 7.3: The evolution of the cumulative process drift where its rate changes from batch-to-batch. Please note that the y-axis shows how much the batch system is perturbed from a nominal batch system (nominal batch system corresponds to a y-axis value equal to 1).

scheme. In the dEWMA scheme, the predicted average crystal shape for the k^{th} batch run can be written as follows:

$$\widetilde{\langle \alpha(t_f) \rangle}_k = \widehat{\langle \alpha(t_f) \rangle}_k + \hat{e}_k + \Delta\hat{e}_k \tag{7.18}$$

where $\widetilde{\langle \alpha(t_f) \rangle}_k$ is the predicted average crystal shape at the end of the k^{th} batch, $\widehat{\langle \alpha(t_f) \rangle}_k$ is the predicted average crystal shape using only the nominal process model that consists of Eqs. 7.1–7.3 and 7.7–7.14, $\hat{e}_k$ is the estimated model prediction error, and $\Delta\hat{e}_k$ is used to compensate for the error in the parameter estimation caused by the change in the rate of the process drift. For a dEWMA-based MPC, the process model used in MPC (cf. Eqs. 7.1–7.3 and (7.7)–(7.14)) is not directly adjusted but its offset from the actual process model is approximated by $\hat{e}_k$+$\Delta\hat{e}_k$. The following control scheme is implemented for the computation of inputs in the proposed dEWMA-based MPC as follows:

1. At the end of the k^{th} batch run, post-batch measurements of the product variables such as the average crystal size and shape are obtained.

2. Then, the average crystal shape measured from Step 1, $\langle \alpha(t_f) \rangle_k$, is used to compute the estimated model prediction error, $\hat{e}_k$, and the estimated change in the rate of the process drift, $\Delta\hat{e}_k$, through the following equations:

$$\hat{e}_{k+1} = w_1 \left[\langle \alpha(t_f) \rangle_k - \widehat{\langle \alpha(t_f) \rangle}_k \right] + (1 - w_1)\hat{e}_k \tag{7.19a}$$

$$\Delta\hat{e}_{k+1} = w_2 \left[\langle \alpha(t_f) \rangle_k - \widehat{\langle \alpha(t_f) \rangle}_k - \hat{e}_k \right] + (1 - w_2)\Delta\hat{e}_k \tag{7.19b}$$

where $0 < w_1 \leq 1$ and $0 < w_2 \leq 1$ are the learning factors.

3. Then, the predicted average crystal shape for the $k+1^{\text{th}}$ batch run, $\widetilde{\langle \alpha(t_f) \rangle}_{k+1}$, that accounts for the change in the rate of the process drift is obtained from

$$\widetilde{\langle \alpha(t_f) \rangle}_{k+1} = \widehat{\langle \alpha(t_f) \rangle}_{k+1} + \hat{e}_{k+1} + \Delta\hat{e}_{k+1} \tag{7.20}$$

and is used in the process model employed in the MPC to compute a set of optimal jacket temperatures T_j which will drive the temperature T in the crystallizer to a desired value.

4. Increase k by 1 and repeat Step 1 to Step 5.

Please note that the first equation, Eq. 7.19a, is used to estimate the offset in the average crystal shape (i.e., output) and the second equation, Eq. 7.19b, is used to capture an additional offset in the average crystal shape due to the change in the rate of the process drift.

7.4.2 Exponentially decaying process drift

When the process drift decays with an exponential rate (Fig. 7.2), the closed-loop performance of the MPC with the nominal process model becomes progressively worse (Fig. 7.4) as runs are repeated due to the increasing mismatch between the process model and the actual batch crystallization process. In Fig. 7.4, it is also shown that the dEWMA-based MPC is able to produce crystals closer to the desired shape distribution compared to the MPC with the nominal process model, however, its convergence speed is so slow that there still remains an offset from the desired crystal shape. On the other hand, the

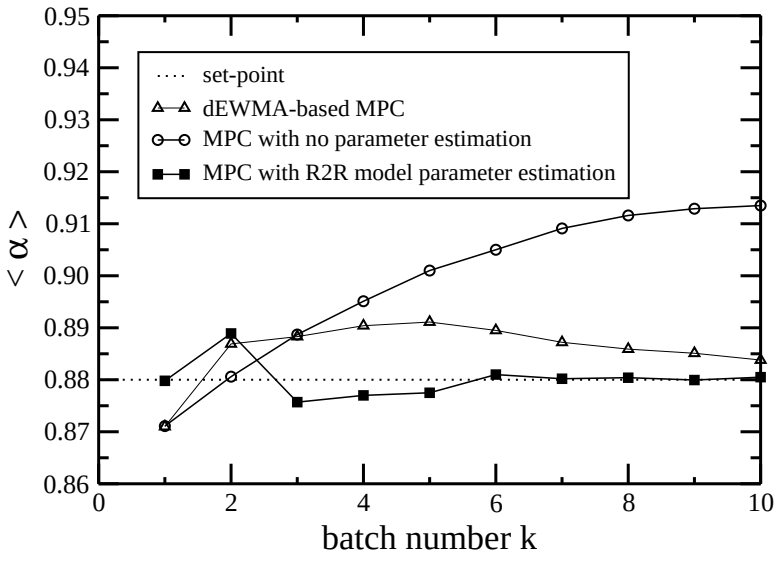

Figure 7.4: The evolution of the average crystal shape at $t = 20000$ seconds obtained from the kMC simulations from batch-to-batch under the MPC with the nominal process model, the dEWMA-based MPC with (w_1, w_2)=(0.5,0.5), and the proposed MPC with R2R model parameter estimation, with the desired set-point $\alpha_{\text{set}} = 0.88$.

Control Schemes	MSE
MPC with R2R model parameter estimation	1.14×10^{-5}
dEWMA-based MPC	8.17×10^{-5}
MPC with no parameter estimation	5.51×10^{-4}

Table 7.2: Comparison of the MSE values between the MPC with R2R model parameter estimation, the dEWMA-based MPC, and the MPC with no parameter estimation in response to the process drift with an exponentially decaying rate.

crystal shape distribution obtained by the MPC with the proposed R2R model parameter estimation scheme (Fig. 7.4) converges quickly (after five batch runs) and approaches the desired set-point value much more closely than those of the MPC with the nominal process model and the dEWMA-based MPC, because the exponentially decaying process drift can be better captured by the proposed R2R model parameter estimation scheme based on MHE. Specifically, the change in the solubility induced by the process drift introduced to the batch crystallization process is properly predicted by the proposed R2R model parameter estimation scheme as is shown in Fig. 7.5. Lastly, we summarize the performances of the MPC with the proposed R2R model parameter estimation, the dEWMA-based MPC, and the MPC with no parameter estimation in response to the process drift described in Fig. 7.2 by comparing their MSE values for the average crystal shape in Table 7.2.

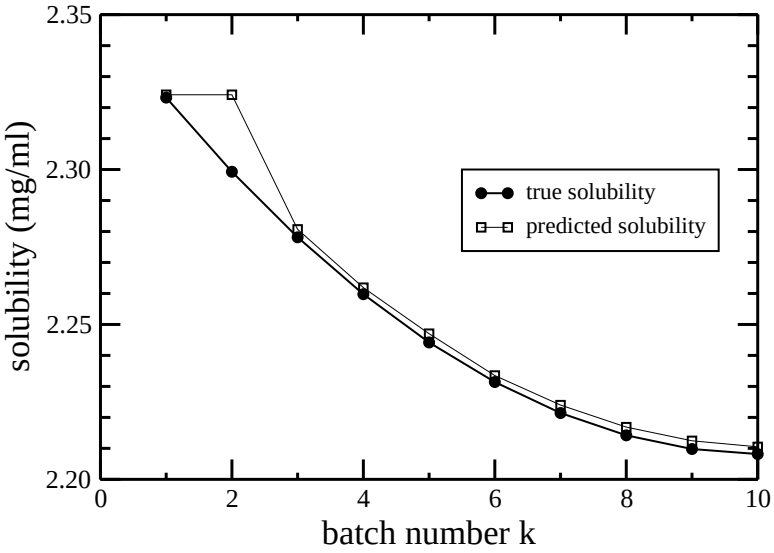

Figure 7.5: The evolution of the predicted and true solubilities at the beginning of batch runs. The predicted solubility is calculated using the proposed R2R model parameter estimation scheme. Please note that the average discrepancy between the two profiles from run 3 to run 10 (i.e., after the estimation scheme is applied to the batch system) is about 0.2%.

7.4.3 Sensitivity to different drift types and tuning parameters

In this section, we consider the more complicated drift from Fig. 7.3. As is shown in Fig. 7.3, the rate of this process drift changes more rapidly from batch-to-batch (e.g., the system drifts from 1 to 0.9 over the first four batch runs) compared to the process drift with an exponentially decaying rate (see, e.g., Fig. 7.2), and five inflection points (i.e., a point of a curve at which a change in the direction of the curvature occurs) are introduced in order to model a significant fluctuation in the rate of the process drift.

For a given polynomial order, although a longer horizon length provides better attenuation of random fluctuations, it may not be able to effectively capture fast batch-to-batch drift dynamics, therefore, an optimal horizon length should be chosen to balance the trade-off between noise handling and capturing fast drift dynamics. A comparative study using different moving horizon lengths for the proposed R2R model parameter estimation scheme is carried out. A 3^{rd} order polynomial is chosen for Eq. 7.16e for the comparison because it is the lowest order polynomial to effectively describe a curve with a pair of inflection points. Specifically, it is shown in Fig. 7.6 that the closed-loop performance initially improves as the horizon length is increased (from $m = 4$ to $m = 5$) due to the better handling of noise in the post-batch measurements, but then decreases with further increases of the horizon length (from $m = 5$ to $m = 7$) because the fast batch-to-batch dynamics of the process drift (e.g., drastic batch-to-batch fluctuations) are not captured with $m = 7$. Therefore, the closed-loop simulation under the MPC with the proposed R2R model parameter estimation scheme with $m = 7$ leads to the production of more off-spec crystals while crystals whose

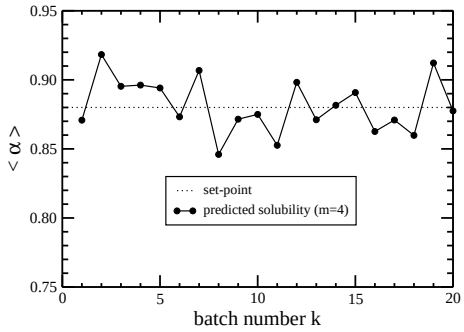

(a) moving horizon length m=4

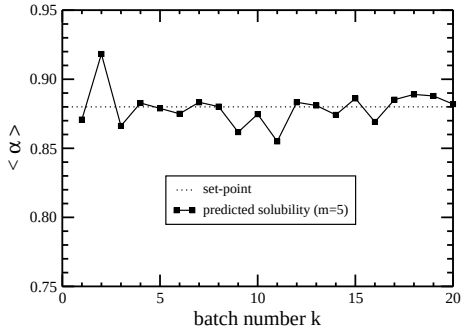

(b) moving horizon length m=5

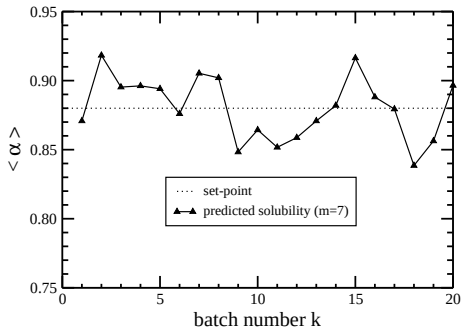

(c) moving horizon length m=7

Figure 7.6: The evolution of the average crystal shape obtained from the kMC simulations from batch-to-batch under the MPC with the proposed R2R model parameter estimation for the process drift described in Fig. 7.3. Different moving horizon lengths (m=4, 5, and 7) are used in order to estimate the batch-to-batch dynamics of the process drift.

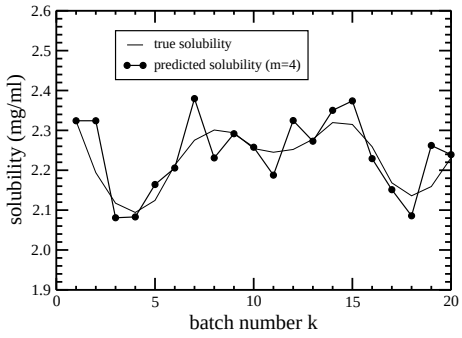

(a) moving horizon length m=4

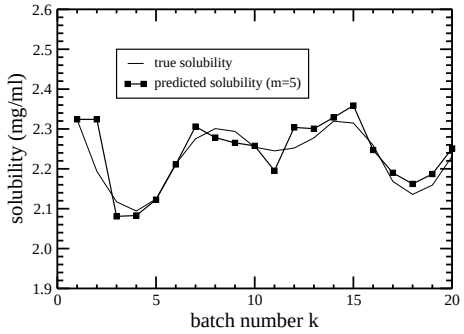

(b) moving horizon length m=5

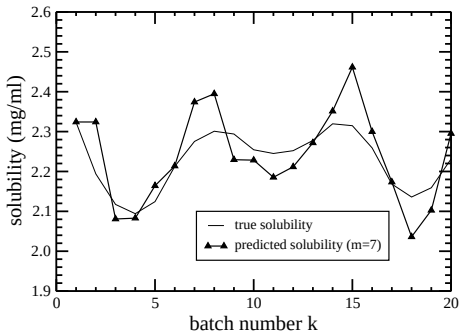

(c) moving horizon length m=7

Figure 7.7: The evolution of the predicted and true solubilities at the beginning of batch runs. The predicted solubility is calculated using the proposed R2R model parameter estimation scheme. Different moving horizon lengths (m=4, 5, and 7) are used in order to estimate the batch-to-batch dynamics of the process drift.

shapes are closer to a desired set-point value are produced under the MPC with $m = 5$. Additionally, it is presented in Fig. 7.7 that the solubility at the beginning of each batch predicted by the proposed R2R model parameter estimation scheme with a horizon length of 5 is much closer to the true value than those with the moving horizon lengths of 4 and 7 for the given 3rd order polynomial.

For a given horizon length, the performance of the parameter estimation increases as the order of the polynomials of Eq. 7.16e is increased due to additional degrees of freedom, but the performance then decreases as the order is further increased since a higher order polynomial overfits the process and measurement noise. For a horizon length of $m = 5$, which is found to be optimal from the previous analysis, the performance of the proposed R2R model parameter estimation scheme is tested with respect to different functions for Eq. 7.16e such as 2nd, 3rd, and 4th order polynomials. It is shown in Fig. 7.8 that the average crystal shape produced from a batch process under the MPC with the proposed R2R model parameter estimation scheme with a 3rd order polynomial is closer to a desired set-point value compared to those of the MPC's with 2nd and 4th order polynomials. Additionally, it is presented in Fig. 7.9 that for a given horizon length, the solubility predicted by the proposed R2R model parameter estimation scheme based on MHE concepts with a 3rd order polynomial is much closer to the true value than that predicted by the proposed method with 2nd and 4th order polynomials. Therefore, we can conclude that a horizon length of $m = 5$ and a 3rd order polynomial is optimal for this process. We note that the proposed R2R model parameter estimation scheme is not applied to the batch crystallization process

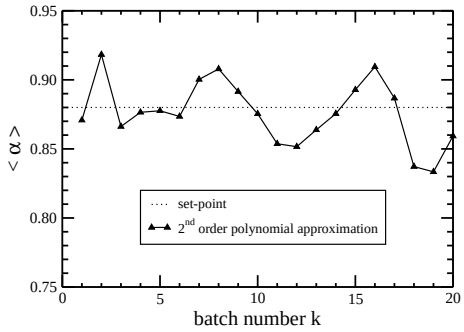

(a) 2nd order polynomial approximation

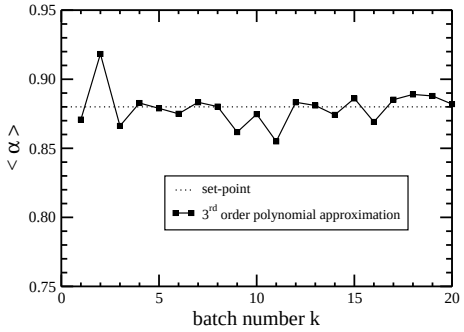

(b) 3nd order polynomial approximation

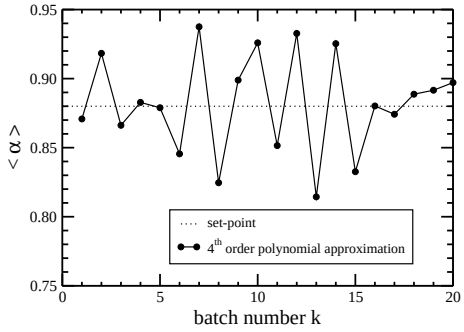

(c) 4th order polynomial approximation

Figure 7.8: The evolution of the average crystal shape obtained from the kMC simulations from batch-to-batch under the MPC with the proposed R2R model parameter estimation for the process drift described in Fig. 7.3. Different orders of polynomial expressions are used in order to estimate the batch-to-batch dynamics of the process drift.

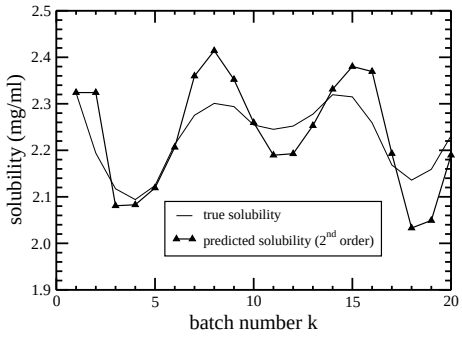

(a) 2nd order polynomial approximation

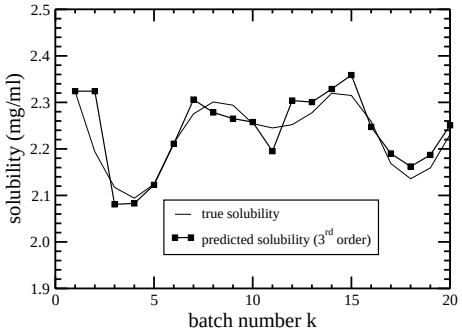

(b) 3nd order polynomial approximation

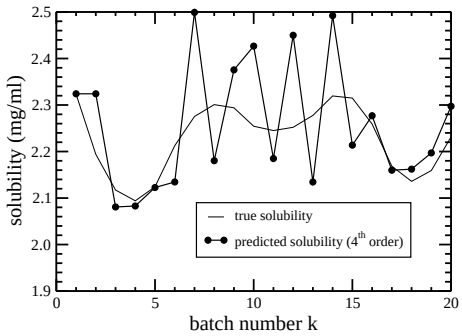

(c) 4th order polynomial approximation

Figure 7.9: The evolution of the predicted and true solubilities at the beginning of batch runs. The predicted solubility is calculated using the proposed R2R model parameter estimation scheme. Different orders of polynomial expressions are used to estimate the batch-to-batch dynamics of the process drift.

until the 2nd batch run because at least two post-batch measurements are required to apply the polynomial regression scheme for the prediction of the batch-to-batch dynamics of the process drift. Additionally, it is possible that, if the value of a parameter that is drifting in a particular batch is significantly off from the dominant trend in the batch-to-batch dynamics of a process drift, it cannot be easily modeled by a function. For example, the 11th batch run in Figs. 7.7 and 7.9 cannot be appropriately modeled by any polynomial, which results in poor controller performance by the MPC with the proposed R2R model parameter estimation scheme at that batch run as is shown in Fig. 7.10.

The controller performance of the MPC with the proposed R2R model parameter estimation scheme is also compared with those of the dEWMA-based MPC and the MPC with the nominal process model. In Fig. 7.10, it is evident that the MPC with the nominal process model is not able to handle the process drift described in Fig. 7.3, and as a result it may lead to the production of crystals with an undesired shape distribution. Furthermore, the production of crystals whose shapes are relatively closer to a desired set-point is achieved under the dEWMA-based MPC, which demonstrates that this scheme is more suitable than the MPC with the nominal process model for process drifts of a random nature. We compare the performances of the MPC with the proposed R2R model parameter estimation, of the dEWMA-based MPC, and of the MPC with the nominal process model in response to the process drift described in Fig. 7.3 using their MSE values of the average crystal shape in Table 7.3.

Since each batch has its own average crystal shape at the end of the process, there is

Control Schemes	MSE
MPC with R2R model parameter estimation	3.62×10^{-4}
dEWMA-based MPC	4.45×10^{-4}
MPC with no parameter estimation	1.25×10^{-3}

Table 7.3: Comparison of the MSE values between the MPC with R2R model parameter estimation, the dEWMA-based MPC, and the MPC with no parameter estimation in response to the process drift described in Fig. 7.3.

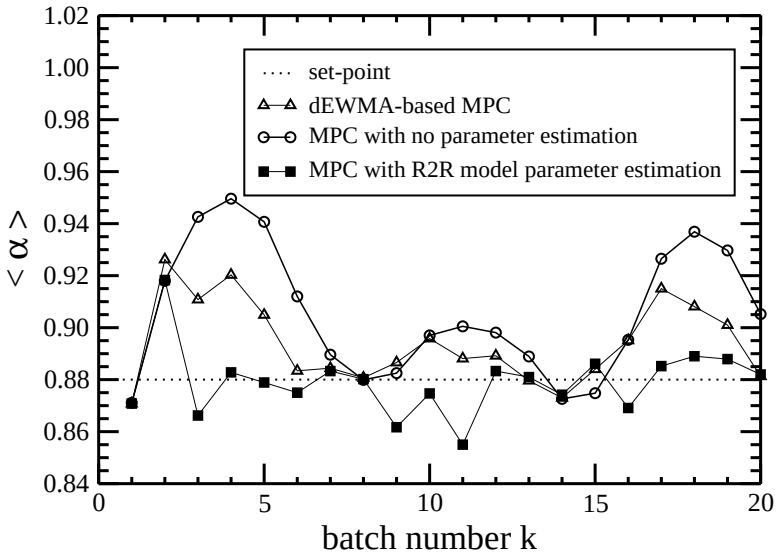

Figure 7.10: The evolution of the average crystal shape obtained from the kMC simulations from batch-to-batch under the MPC with the proposed R2R model parameter estimation scheme, the dEWMA-based MPC with (w_1, w_2)=(0.5,0.5), and the MPC with no parameter estimation, for the process drift described in Fig. 7.3.

a distribution for the average crystal shapes from all the batches (from 1st to 20th batch runs). In this work, we define this batch-wise crystal shape distribution as follows: a good batch-wise crystal shape distribution should have small batch-to-batch variations and its average should be close to the set-point value, while a poor batch-wise crystal shape distribution has large batch-to-batch variations and its average is offset from the set-point value. In order to compare the batch-wise crystal shape distributions obtained from the closed-loop simulations under different control schemes, a quantile plot is presented in Fig. 7.11 where the batch-wise crystal shape distribution obtained under the MPC with the proposed R2R model parameter estimation scheme is found to be better than those of the MPC with the nominal process model and the dEWMA-based MPC. Furthermore, the quantile plot indicates that the average of the points obtained under the proposed MPC with the R2R model parameter estimation scheme is very close to the desired set-point value, $\alpha_{\text{set}} = 0.88$. Therefore, the process drift described in Fig. 7.3 was properly modeled by the proposed R2R model parameter estimation scheme based on MHE concepts with a 3rd order polynomial for the moving horizon length of 5.

Remark 7.3 *The implementation of the proposed R2R model parameter estimation scheme based on MHE concepts can guarantee the better performance compared to the MPC with the nominal process model for a given moving horizon length when an appropriate function is chosen for the modeling of the batch-to-batch dynamics of the process drift. Once the batch-to-batch dynamics of the process drift are modeled well using a function, the proposed scheme becomes robust with respect to a rapidly changing process drift, while*

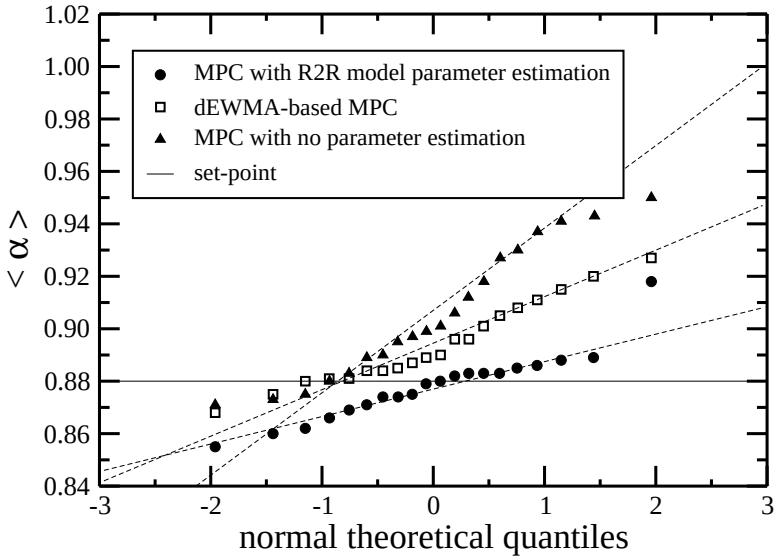

Figure 7.11: The quantile plot for the distributions of the average crystal shapes obtained from the kMC simulations from batch-to-batch under the MPC with the proposed R2R model parameter estimation scheme, the dEWMA-based MPC with (w_1, w_2)=(0.5,0.5), and the MPC with no parameter estimation, for the process drift described in Fig. 7.3. Please note that the dotted lines represent standard normal distributions for each data set and the x-axis indicates the standard deviations.

the dEWMA scheme may suffer from convergence issues given the difficulty in choosing the learning factors, w_1 and w_2.

7.5 Conclusions

In this work, we proposed an R2R model parameter estimation scheme based on a moving horizon approach in order to model batch-to-batch parametric drift using a polynomial regression scheme. Then, the batch process model parameters computed by the proposed parameter estimation scheme were used in an MPC within each batch to compute a set of optimal jacket temperatures for the production of crystals with a desired shape distribution. The ability of the proposed parameter estimation scheme to suppress the inherent variation in the solubility incurred by batch-to-batch drift and to deal with the noise in real-time and post-batch measurements was demonstrated by applying the MPC with the proposed estimation scheme to a kMC simulation of a batch crystallization process used to produce HEW lysozyme crystals. The performance of the proposed R2R model parameter estimation scheme was evaluated with respect to the use of different orders of polynomials and different moving horizon lengths. Lastly, the performance of the MPC with the proposed R2R model parameter estimation scheme was favorably compared with those of the MPC based on the nominal process model and the dEWMA-based MPC.

Chapter 8

Detection and isolation of batch-to-batch parametric drift in crystallization using in-batch and post-batch measurements

8.1 Introduction

This chapter focuses on the development of a parametric drift detection and isolation (PDDI) method for the handling of batch-to-batch parametric drift in a batch crystallization process used to produce HEW lysozyme crystals. The batch crystallization process is controlled by an in-batch model predictive control (MPC) system and is subject to batch-to-batch parametric drift in the solubility, growth rates, continuous-phase mass and energy balance parameters, and nucleation rate. The proposed PDDI scheme consists of two

parts: the preparatory stage before batch-to-batch operation and the post-batch stage during batch-to-batch operation. The goal of the preparatory stage is to compute the threshold values and signatures for individual parametric drift using simulations and batch process common cause variance described by noise. During batch-to-batch operation, the proposed PDDI system monitors closed-loop process residuals, which are computed by taking the difference between the time profiles of the states obtained through in-batch and post-batch measurements from the time profiles of the states obtained from the drift-free simulation with noise. While the measurements of the protein solute concentration and the temperature in the crystallizer are available in real-time, post-batch measurements are usually available for the quality of the crystal products (e.g., number of crystals, average crystal size and shape) and the PDDI method accounts for this key characteristic. Then, the residuals are compared with signatures obtained in the preparatory stage for each parametric drift for isolation of a parametric drift. The PDDI system estimates the magnitude of the parametric drift and updates the parameters of the batch process model used in the in-batch MPC system to compute a set of jacket temperatures for the production of crystals with a desired shape distribution in the next batch. The performance of the MPC with the proposed PDDI scheme is demonstrated by applying it to a multiscale simulation of a batch crystallization process with parametric drifts in the solubility and crystal growth rates. The closed-loop system simulations demonstrate that a parametric-drift handling scheme that integrates the in-batch MPC with the proposed PDDI system produces crystals with a crystal shape distribution which is closer, compared to that produced under the MPC with the nominal process

model, to a desired set-point value.

8.2 Batch crystallization model

We focus on a batch crystallization process used to produce HEW lysozyme crystals in order to demonstrate the proposed technique for parametric drift detection and isolation.

8.2.1 Crystal nucleation

The nucleation rate, $B(\sigma)$, of lysozyme crystals is given below [41]:

$$B(\sigma) = \begin{cases} 0.041\sigma + 0.063 & \text{for} \quad \sigma \geq 3.11 \\ 8.0 \times 10^{-8} \exp(4.725\sigma) & \text{for} \quad \sigma < 3.11 \end{cases} \tag{8.1}$$

with units $[\text{cm}^{-3} \cdot \text{sec}^{-1}]$, and the supersaturation level σ is computed through the logarithmic ratio between the solute concentration in the continuous phase C and the solubility s as follows:

$$\sigma = \ln(C/s) \tag{8.2}$$

where the solubility is calculated using the following equation [13]:

$$s(T) = 2.88 \times 10^{-4} T^3 - 1.65 \times 10^{-3} T^2 + 4.62 \times 10^{-2} T + 6.01 \times 10^{-1} \tag{8.3}$$

and T is the temperature in the crystallizer in degrees Celsius.

8.2.2 Crystal growth

The growth rate equations of Table 8.1 are adopted from [32] and used to model the crystal growth through the kMC simulation.

Surface reaction	Rate equation
Adsorption r_a:	$K_0^+ \exp(\sigma)$
Desorption $r_d(i)$:	$K_0^+ \exp\left(\frac{\phi}{k_B T} - i\frac{E_{pb}}{k_B T}\right)$
Migration $r_m(i)$:	$K_0^+ \exp\left(\frac{\phi}{k_B T} - i\frac{E_{pb}}{k_B T} + \frac{E_{pb}}{2k_B T}\right)$

Table 8.1: Surface reactions where K_0^+ is the adsorption coefficient, ϕ is the total binding energy of a fully occupied lattice, i is the number of nearest neighbors, and E_{pb} is the average bonding energy per bond.

Please note that the desorption and migration rates depend on the surface micro-configuration (i.e., they take into account the number of nearest neighbors i). The crystal growth rates obtained from the kMC simulations are calibrated with the experimental data from [31] by manipulating K_0^+ and the values of E_{pb} and ϕ for the (110) and (101) faces through extensive open-loop kMC simulations. The parameters used for the kMC simulation are listed in Table 8.2. The reader may refer to [93] for more details regarding the execution of the kMC simulation.

Face	E_{pb}/k_B	ϕ/k_B
(110)	1077.26 K	227.10 K
(101)	800.66 K	241.65 K

Table 8.2: Parameters for the (110) and (101) faces at 4%(w/v) NaCl and pH= 4.5 at $T = 18^{\circ}$C. Additionally, $K_o^+ = 0.211$ seconds^{-1}.

8.2.3 Mass and energy balance equations

The following mass and energy balance equations [101] are employed in this work to compute the evolution of the solute concentration and temperature in the crystallizer with time:

$$\frac{dC}{dt} = -\frac{\rho_c}{V_{batch}}\frac{dV_{crystal}}{dt}, \qquad C(0) = 48 \text{ mg/cm}^3 \tag{8.4}$$

$$\frac{dT}{dt} = -\frac{\rho_c \Delta H_c}{\rho C_p V_{batch}}\frac{dV_{crystal}}{dt} - \frac{U_j A_j}{\rho C_p V_{batch}}\left(T - T_j\right), \qquad T(0) = 17^{\circ}\text{C} \tag{8.5}$$

where $V_{crystal}$ is the total volume of crystals in the crystallizer and T_j is the jacket temperature (i.e., manipulated input). The process parameter values are shown in Table 8.3. The enthalpy of crystallization is taken from [110] and the specific heat capacity of the solution is assumed to be identical to that of water since the concentration of the protein solute in the solution is small in comparison to that of water.

8.2.4 Population balance equation

The evolution of the crystal volume distribution for the batch crystallization process with nucleation and crystal growth is described by the following population balance equation

ρ_c	crystal density	1400	mg/cm^3
ΔH_c	enthalpy of crystallization	-4.5	kJ/kg
$\rho(t)$	density of the continuous phase	1000 + C(t)	mg/cm^3
C_p	specific heat capacity	4.13	kJ/K kg
V_{batch}	volume of the crystallizer	1	L
A_j	contact area of the crystallizer wall and jacket	0.25	m^2
U_j	overall heat transfer coefficient	1800	kJ/m^2 h K

Table 8.3: Parameters for the batch crystallizer model.

(PBE) [55]:

$$\frac{\partial n(V,t)}{\partial t} + \frac{\partial \left(G_{vol}(V,\sigma)n(V,t)\right)}{\partial V} = B\delta(V) \tag{8.6}$$

where $n(V,t)$ is the number of crystals of volume V at time t, $\delta(\cdot)$ is the dirac delta function, and $G_{vol}(V,\sigma)$ is the volumetric crystal growth rate which will be formulated with greater detail in the following section. Eq. 8.6 accounts for the fact that crystals are nucleated with an infinitesimal size. The dirac function in the population balance equation captures the effect of nucleation rate, and will be used in the boundary condition and to simulate the nucleation process.

8.2.5 Moments model

By applying the method of moments to the PBE of Eq. 8.6, a moments model that describes the zeroth and first moments of the crystal volume distribution in the batch crystallizer can

be derived using standard techniques and has the following form [101]:

$$\frac{dM_0}{dt} = B \tag{8.7}$$

$$\frac{dM_1}{dt} = G_{vol} M_0 \tag{8.8}$$

where $M_j(t) = \int_0^\infty V^j n(V,t) dV$ is the j^{th} moment for $j = 0$, 1, and G_{vol} is formulated as follows:

$$G_{vol} = 2G_{110}\langle h_{110}\rangle\langle h_{101}\rangle + G_{101}\langle h_{110}\rangle^2 \tag{8.9}$$

where G_{110} and G_{101} are the crystal growth rates in the direction of the (110) and (101) faces, respectively. The following polynomial expressions for the growth rates G_{110} and G_{101} are obtained from open-loop simulations of the multiscale model used to model the batch crystallization process:

$$G_{110} = 0.1843\sigma^3 - 1.1699\sigma^2 + 2.8885\sigma - 2.5616 \tag{8.10}$$

and

$$G_{101} = 0.1893\sigma^3 - 1.2264\sigma^2 + 2.9887\sigma - 2.5348 \tag{8.11}$$

Lastly, the dynamic evolution of the average crystal heights, $\langle h_{110}\rangle$ and $\langle h_{101}\rangle$, is formulated as follows:

$$\begin{aligned} \frac{d\langle h_{110}\rangle}{dt} &= G_{110} - \frac{BV_{batch}\langle h_{110}\rangle}{M_0} \\ \frac{d\langle h_{101}\rangle}{dt} &= G_{101} - \frac{BV_{batch}\langle h_{101}\rangle}{M_0} \end{aligned} \tag{8.12}$$

Thus, the average crystal shape, $\langle \alpha \rangle$, and size, $\langle V \rangle$, can be computed as follows:

$$\langle \alpha \rangle \approx \frac{\langle h_{110}\rangle}{\langle h_{101}\rangle} \qquad \langle V \rangle = \frac{M_1}{M_0} \tag{8.13}$$

The reader may refer to [72] for a more detailed derivation of the moments model.

8.3 Parametric drift detection and isolation system design

8.3.1 In-batch MPC

We initially design an in-batch model predictive controller (MPC) for the drift-free batch crystallization process used for the production of HEW lysozyme crystals. First, the dominant dynamic behavior of the evolution of the crystal shape distribution in the batch crystallization process is modeled through the process model (cf. Eqs. 8.1–8.13), which is used to compute a set of optimal jacket temperatures that minimizes the squared deviation of the average crystal shape from a target value over the entire prediction horizon. There are constraints imposed on the rate of change of the jacket temperature and on the magnitude of the temperature in the crystallizer. The resulting optimization problem for the proposed in-batch MPC is formulated as follows:

$$\min_{T_{j,1},\ldots,T_{j,p}} \quad \sum_{i=1}^{p} \left(\langle \alpha(t_i) \rangle - \alpha_{\text{set}}\right)^2 \tag{8.14a}$$

$$\text{s.t.} \quad \text{Eqs. } 8.1 - 8.13 \tag{8.14b}$$

$$4^\circ\text{C} \leq T \leq 25^\circ\text{C} \qquad \left|\frac{T_{j,i+1} - T_{j,i}}{\Delta}\right| \leq 2^\circ\text{C/min} \tag{8.14c}$$

$$t_i = t + i\Delta \tag{8.14d}$$

where the length of the prediction horizon is $p = 10$, the sampling time is $\Delta = 40$ seconds, and $T_{j,i}$ is the jacket temperature at the i^{th} prediction step t_i. The in-situ measurements of C and T are available at every sampling instant. Then, the optimization problem of Eq. 8.14 is solved to compute a set of optimal jacket temperatures, $(T_{j,1},\ldots,T_{j,10})$, and

the first value, $T_{j,1}$, is applied to the crystallizer until the next sampling instant. Note that since we impose explicit constraints on the magnitude of the crystallizer temperature, there is no need to impose explicit constraints on the magnitude of the jacket temperature (i.e., manipulated input) as it is implicitly constrained by the crystallizer temperature constraint. The simulations were carried out on the Hoffman2 cluster at UCLA and the optimization problems were solved using the open source interior point optimizer, IPOPT.

8.3.2 Parametric drift detection and isolation

We consider batch-to-batch parametric drift in a batch crystallization process, particularly in the parameters of the mass and energy balance equations, the nucleation and crystal growth rate expressions, and the solubility expression. These batch-to-batch parametric drifts can be detected and isolated by observing the evolution of measured outputs of the closed-loop system through in-batch (e.g., C, T) and post-batch (e.g., $\langle\alpha\rangle$, M_0, $\langle h_{110}\rangle$, $\langle h_{101}\rangle$) measurement techniques. This consideration requires that each parametric drift is the one influencing a certain subset of the process outputs (i.e., each parametric drift has a unique parametric drift signature).

As described in Fig. 8.1, we first design and employ a PDDI scheme in order to detect a parametric drift in real-time over the course of a batch run via in-batch measurements and to further detect the drift at the end of a batch run via post-batch measurements. The information generated by the nominal batch crystallizer model initialized at the same state as the actual batch process, provides an estimate of the parametric drift-free batch process

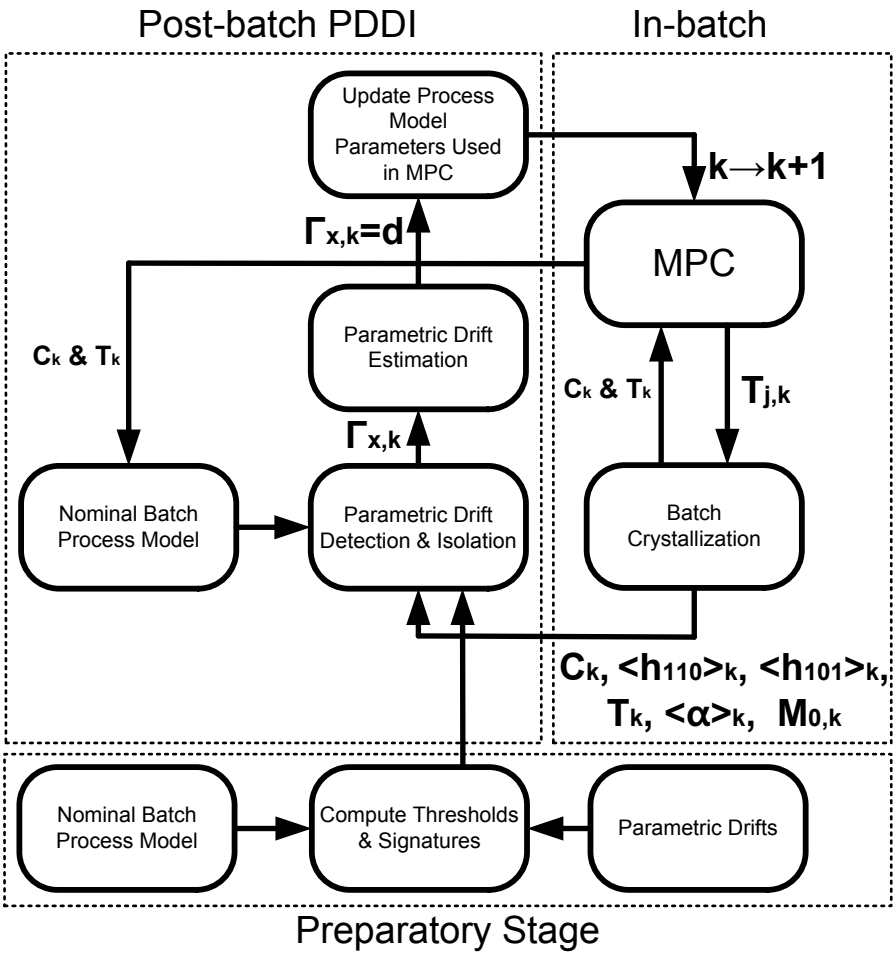

Figure 8.1: Structure integrating parametric-drift detection and isolation scheme with in-batch MPC.

variables and allows detection of the parametric drifts by comparing the nominal behavior with the actual process behavior (i.e., in-batch and post-batch process measurements). Specifically, the PDDI residual for each variable can be defined as:

$$\begin{aligned} r_x(t) &= |\bar{x}(t) - x(t)| \quad \text{for} \quad x \in \{C, T\} \\ r_x(t_f) &= |\bar{x}(t_f) - x(t_f)| \quad \text{for} \quad x \in \{\langle \alpha \rangle, M_0, \langle h_{110} \rangle, \langle h_{101} \rangle\} \end{aligned} \tag{8.15}$$

where $\bar{x}$ is the predicted evolution for the variable x, which is obtained from the nominal process model (cf. Eqs. 8.1–8.13) with noise for the same initial state and input trajectory that is applied to the actual batch process. The residuals r_T and r_C are calculated at every sampling instant using in-batch measurements while the residuals $r_{\langle \alpha \rangle}$, r_{M_0}, $r_{\langle h_{110} \rangle}$, and $r_{\langle h_{101} \rangle}$ are evaluated once using the above procedure at the end of the batch run because only post-batch measurements are available for those variables.

When there is a parametric drift in one of the process parameters from batch-to-batch, process residuals affected directly by the parametric drift will deviate from zero. Furthermore, it is assumed that the parametric drifts of interest will be sufficiently large so that their effects will not be masked by process or measurement noise. Therefore, the thresholds with respect to which the residuals will be compared should account for the effects of process and measurement noise. If no parametric drift occurs, the measurements are close to the nominal behavior (depending on the process and measurement noise levels) obtained via post-batch closed-loop kMC simulations using the input profile applied to the process at the last batch run. However, due to process and sensor measurement noise, the residuals $r_x(t)$ will be nonzero. This necessitates the use of parametric drift detection thresholds so

that a parametric drift in the variable x is declared only when a residual exceeds a specific threshold value, $r_{x,\max}$ that accounts explicitly for the effect of process and measurement noise. Below, we describe the PDDI scheme in detail.

Specifically, the proposed PDDI scheme consists of two parts: the preparatory stage before batch-to-batch operation and the post-batch stage during batch-to-batch operation. The goal of the preparatory stage is to compute the threshold values and signatures for each parametric drift as follows:

1. In the preparatory stage, we simulate batch runs under MPC with the nominal process model. The noise (common cause variance) which is obtained from historical data and sensor information is added to the process model used to simulate the batch crystallization process but not added to the batch process model used in the MPC. Then, these runs are used along with the same type of simulations for batch runs under MPC but without noise to compute residuals and calculate the threshold value for each variable x, $r_{x,\max}$, based on the maximum deviation (absolute value) of the time profiles of the residuals with and without noise from zero (difference between the time profiles of the variables from these two distinct sets of simulations).

2. We also calculate signatures for each drift in the preparatory stage. We simulate batch runs under MPC with the nominal process model. Again, the noise is added to the process model used to simulate batch crystallization but not added to the process model used in the MPC. Furthermore, we add a parametric drift to each of the five variables separately (i.e, therefore we need at least as many separate simulations as

the number of drifts considered). Then, we compute the residuals for each variable by calculating the difference between the time profiles of the states obtained using this simulation with parametric drifts and the time profiles of the variables obtained from the simulation with noise but no drift in the process model. The residual of C or of T that exceeds its threshold first is recorded, and the signature of this specific drift is calculated.

Note that if two or more parametric drifts are defined by the same signature, they cannot be isolated on the basis of the parametric drift signature. This problem will be addressed via another set of simulations discussed below. The post-batch stage of the proposed PDDI scheme during batch-to-batch operation is described as follows:

1. At the end of each batch run, we compute the residuals by calculating the differences between the time profiles of the states obtained through in-batch and post-batch measurements from the time profiles of the states obtained from the drift-free simulation with noise using the input trajectory applied to the process during the last batch. Then, we compare the residuals (calculated post-batch) with signatures obtained in the preparatory stage for each parametric drift.

2. After we narrow down the overall set of drift candidates to a few parametric drift candidates, we run optimization problems with the remaining drift candidates to match simulated drift behavior with the in-batch experimental output post-batch measurements in order to isolate the parametric drift and to estimate the magnitude of the parametric drift. Details of this step are give in Section 8.3.3 below.

3. Then, the parameters of the batch process model used in the MPC for the next batch are updated to account for the presence of drift.

Isolation of the parametric drift as can be accomplished using the proposed PDDI scheme allows for the design of a model predictive controller that can handle the parametric drift in its formulation by updating its model before each batch, and as a result, the PDDI scheme can enhance the controller performance by minimizing the production of crystals with undesired characteristics attributed to the parametric drift.

Also, it is important to point out the difference between the proposed PDDI scheme and the MHE formulation employed in [71] for computing parameter updates for the model used in the MPC in the next batch run. If the detection and isolation of the parametric drift is possible, then the only model parameters that are updated are those which are directly affected by the drift, and as a result, the accuracy of the model used in the MPC in the next batch is superior to the one of the model that uses a generic update for all of its parameters.

8.3.3 Parametric drift estimation

After a parametric drift has been detected and isolated, the PDDI system will estimate the magnitude of the parametric drift (i.e., how much the batch process is perturbed from nominal batch behavior). If two or more parametric drifts are defined by the same signature, isolation between them is not possible on the basis of the parametric drift signature and thus we have to find one drift that better matches the in-batch and the post-batch measurements by running the following optimization problem with candidates which have been selected

from the set of all possible drift candidates.

Specifically, a least squares optimization problem is solved to estimate the magnitude of the particular parametric drift (one at a time) utilizing the in-batch and post-batch measurements (e.g., C, T, $\langle\alpha\rangle$, M_0, $\langle h_{110}\rangle$, $\langle h_{101}\rangle$) and the control inputs (e.g., T_j) applied in the last batch run. In the optimization problem of Eq. 8.16 below, parametric drifts associated with the nucleation rate, the crystal growth rates in the directions of the (110) and (101) faces, the parameters of the solubility equation, and the parameters of the mass and energy balance equations are taken into account by multiplying the nominal expressions by the correction parameters γ_{nu}, γ_{110}, γ_{101}, γ_s, γ_C and γ_T, respectively. Furthermore, the objective function (cf. Eq. 8.16a) consists of a sum of squared errors between the predicted average crystal size and shape, $\widehat{\langle\alpha(t_f)\rangle}$ and $\widehat{\langle V(t_f)\rangle}$, and the measured ones, $\langle\alpha\rangle_{\text{measured}}$ and $\langle V\rangle_{\text{measured}}$. The resulting optimization problem is formulated as follows:

$$\min_{\Gamma} \quad w_\alpha \left(\widehat{\langle\alpha(t_f)\rangle} - \langle\alpha\rangle_{\text{measured}}\right)^2 + w_V \left(\widehat{\langle V(t_f)\rangle} - \langle V\rangle_{\text{measured}}\right)^2 \tag{8.16a}$$

$$\text{s.t.} \quad \text{Eqs. } 8.1 - 8.14 \tag{8.16b}$$

$$\hat{s}(t) = \gamma_s s(t), \qquad \hat{B}(\sigma) = \gamma_{\text{nu}} B(\sigma) \tag{8.16c}$$

$$\hat{G}_{110}(t) = \gamma_{110} G_{110}(t), \qquad \hat{G}_{101}(t) = \gamma_{101} G_{101}(t) \tag{8.16d}$$

$$\hat{T}(t) = \gamma_T T(t), \qquad \hat{C}(t) = \gamma_C C(t) \tag{8.16e}$$

$$\Gamma = [\gamma_{110},\ \gamma_{101},\ \gamma_T,\ \gamma_C,\ \gamma_{\text{nu}},\ \gamma_s] \tag{8.16f}$$

Assuming that we have already isolated a parametric drift, we can use only one correction factor (cf. PDDI with γ_x) and set the other correction factors equal to one. For example,

if a parametric drift in the solubility equation has been isolated, the correction parameters in Γ become $\gamma_{110} = \gamma_{101} = \gamma_T = \gamma_C = \gamma_{\text{nu}} = 1$ and $\gamma_s = d$ where d is the magnitude of the parametric drift for the solubility equation. Therefore, solving the optimization problem of Eq. 8.16 is reduced to finding the value of the magnitude d. If two or more parametric drifts are defined by the same signature, we have to run them one by one as described above until we find one that best matches the in-batch and post-batch measurements. Once the parametric drift is isolated and its magnitude d is estimated, the PDDI system will send the parametric drift information to the in-batch MPC to update its model, which will be used for the computation of the optimal jacket temperature in the next batch run. This control scheme is essentially a parametric drift tolerant control (PDTC) systems. A schematic representation of the PDTC scheme is shown in Fig. 8.1.

Using the PDTC scheme, the parameters in the process model used in the MPC in the next batch are updated based on the parametric drift detection and isolation via the proposed PDDI scheme. The proposed scheme can be applied to handle parametric drifts in the other parameters as well. However, the performance of the proposed PDDI scheme is dependent on the specific crystallization system, and in some cases, the parametric drift may be such that it is not possible to achieve good parametric drift detection and isolation.

While the number of decision variables in the optimization problems of Eq. 8.14 (MPC) and Eq. 8.16 (post-batch parameter estimation) are finite owing to the sample-and-hold implementation of the control actions (jacket temperature) to the crystallizer and the estimation of a finite number of parameter values, respectively, the crystallizer dynamics are

continuous, and therefore, they are modeled by differential equations. Of course, these differential equations are integrated numerically with a much smaller integration time step than the sampling time during the solution of the MPC optimization problem at each sampling time that leads to the calculation of the control actions.

More specifically, the optimization problem of Eq. 8.14 was solved to local optimality using the open-source interior point optimizer IPOPT, and the optimization problem of Eq. 8.16 was also solved to local optimality using the MATLAB function *fmincon* at the end of the batch process. While it takes negligible time for the former problem to be solved (much less than the sampling time period), it takes about 5-10 seconds for the latter.

8.4 Application of MPC with PDDI to batch protein crystallization

8.4.1 Process and measurement noise

Measurement and process noise is added to the process model used to simulate the batch crystallization process. Specifically, the measurement noise is introduced to the $C(t)$ and $T(t)$ measurements as follows:

$$C(t) = \bar{C}(t) + w_C(t), \quad T(t) = \bar{T}(t) + w_T(t) \tag{8.17}$$

where $\bar{C}(t)$ and $\bar{T}(t)$ are the average solute concentration in the continuous phase and the crystallizer temperature, and $w_C(t)$ and $w_T(t)$ are both Gaussian white noise with zero mean

and standard deviations of 2% of $\bar{C}(t)$ and $\bar{T}(t)$, respectively. Furthermore, the process noise is introduced to the nucleation rate and the growth rates in the directions of the (110) and (101) faces as follows:

$$B(\sigma) = \bar{B}(\sigma) + w_B(\sigma), \quad G_{110}(t) = \bar{G}_{110}(t) + w_{G_{110}}(t), \quad G_{101}(t) = \bar{G}_{110}(t) + w_{G_{110}}(t) \tag{8.18}$$

where $\bar{B}(\sigma)$, $\bar{G}_{110}(t)$, and $\bar{G}_{101}(t)$ are the nominal nucleation rate and the growth rates in the directions of the (110) and (101) faces, and $w_B(\sigma)$, $w_{G_{110}}(t)$, and $w_{G_{101}}(t)$ are also Gaussian white noise variables with zero mean and standard deviations of 2% of $\bar{B}(\sigma)$, $\bar{G}_{110}(t)$, and $\bar{G}_{101}(t)$, respectively.

8.4.2 Drift-free operation and parametric drifts

In Section 8.3.1, an in-batch MPC is designed for the drift-free batch crystallization process. The performance of the in-batch MPC is demonstrated by applying it to a drift-free closed-loop simulation with noise under nominal (i.e., no drifting) operation conditions where Fig. 8.2 shows the trajectory of the real-time in-batch measurements of $T(t)$ and $C(t)$ and Table 8.4 shows the post-batch measurements of $\langle \alpha(t) \rangle$, $M_0(t)$, $\langle h_{110}(t) \rangle$, and $\langle h_{101}(t) \rangle$ at $t = 18$ hours.

Note that under drift-free operating conditions, the production of crystals with a shape distribution which is very close to a desired set-point value, $\alpha_{\text{set}} = 0.89$, is achieved. The parametric drifts considered in this work and their magnitudes are given in Table 8.5. Specifically, the expressions for B, G_{110}, G_{101}, and S are multiplied by the values cor-

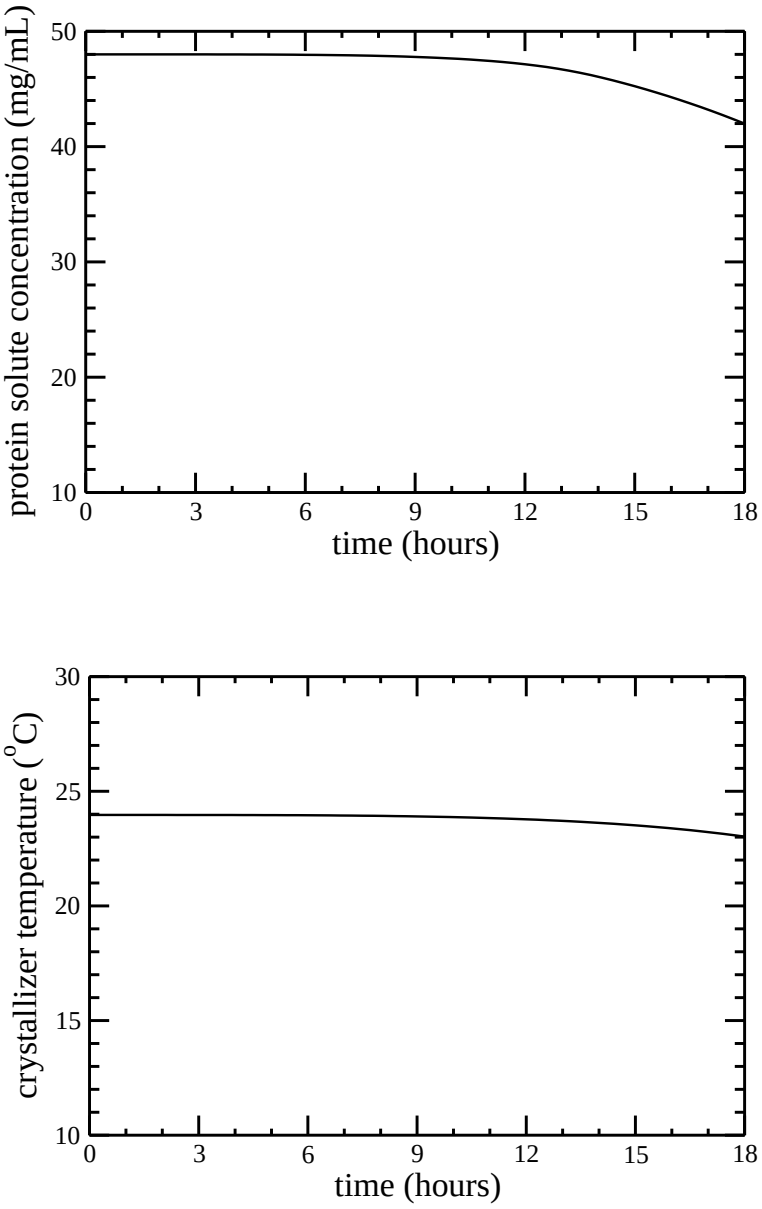

Figure 8.2: Profiles of the protein solute concentration and of the crystallizer temperature with time during batch crystallization under nominal (drift-free) operating conditions, for the growth rate ratio set-point values $\alpha_{\text{set}} = 0.89$.

$\langle\alpha\rangle$	M_0	$\langle h_{110}\rangle$	$\langle h_{101}\rangle$
0.895	384000	174 μm	185 μm

Table 8.4: Post-batch measurements for the batch crystallization process under drift-free closed-loop operation at $t = 18$ hours.

Types	% change from nominal value
ρ_c in mass balance, Eq. 8.4	-10%
U_j in energy balance, Eq. 8.5	-10%
G_{110} rate, Eq. 8.10	-30%
G_{101} rate, Eq. 8.11	-23%
Nucleation rate, Eq. 8.1	$+40\%$
Solubility, Eq. 8.3	$+10\%$

Table 8.5: Magnitude of parametric drift for each variable

responding to the % change presented in Table 8.5 (e.g., multiply Eq. 8.10 by 0.7 in order to model the parametric drift described in Table 8.5 for G_{110}).

8.4.3 Preparatory stage of PDDI

In the preparatory stage, we simulate batch runs using the process model with noise under the MPC with the nominal process model. Then, these runs are used along with the same type of simulations for batch runs but without noise to get the threshold values which are mainly attributed to the effect of the noise in the process model. Specifically, the maximum

value of each variable throughout the batch run is chosen as the threshold value for each variable, $r_{x,\max}$, and they are presented as follows:

$$\begin{aligned} r_{C,\max} &= 1.4 \text{ mg/cm}^3 \\ r_{T,\max} &= 1.1 \ ^\circ\text{C} \\ r_{\langle\alpha\rangle,\max} &= 0.021 \\ r_{M_0,\max} &= 64000 \\ r_{\langle h_{110}\rangle,\max} &= r_{\langle h_{101}\rangle,\max} = 10 \ \mu\text{m} \end{aligned} \tag{8.19}$$

Signatures for each parametric drift are also determined based on these threshold values. First, in-batch measurements are used for detection and isolation of parametric drifts at the end of a batch run. Specifically, a parametric drift is detected if $r_x(t_x) > r_{x,\max}$ for $x \in \{C,T\}$ where t_x is the first time r_x of the variable x exceeds the threshold value $r_{x,\max}$. Depending on whether the residual for C or T exceeds its threshold first, the process signature for a parametric drift in the variable x, $W^{x,\text{in}} = [W_C; W_T]$, is built as follows:

$$t_C > t_T \quad \rightarrow \quad [W_C; W_T] = [1;0] \tag{8.20a}$$

$$t_C < t_T \quad \rightarrow \quad [W_C; W_T] = [0;1] \tag{8.20b}$$

As a result, the possible candidates for parametric drifts can be divided into two subgroups based on their in-batch process signatures, $W^{x,\text{in}}$, as follows:

$$\begin{aligned} W^{C,\text{in}} &= W^{S,\text{in}} = W^{Nu,\text{in}} = [1;0] \\ W^{T,\text{in}} &= W^{G_{110},\text{in}} = W^{G_{101},\text{in}} = [0;1] \end{aligned} \tag{8.21}$$

If $t_C = t_T$, the in-batch measurements are not able to be used for the isolation of parametric drifts. Then, the post-batch measurements (e.g., $\langle\alpha\rangle$, M_0, $\langle h_{110}\rangle$, $\langle h_{101}\rangle$) are used

to compute the post-batch signature for a parametric drift in the variable x, $W^{x,\text{post}} = [W_{\langle\alpha\rangle}, W_{M_0}, W_{\langle h_{110}\rangle}, W_{\langle h_{101}\rangle}]$, as described below:

$$r_x > r_{x,\max} \quad \rightarrow \quad W_x = 1 \tag{8.22a}$$

$$r_x \leq r_{x,\max} \quad \rightarrow \quad W_x = 0 \tag{8.22b}$$

for $x \in \{\langle\alpha\rangle, M_0, \langle h_{110}\rangle, \langle h_{101}\rangle\}$. Note that it does not matter which residual exceeds its threshold value first because all residuals exceed their thresholds at $t = 18$ hours. For example, if we simulate a batch run with a parametric drift in the solubility curve and observe that $r_x > r_{x,\max}$ for $\langle\alpha\rangle$, $\langle h_{110}\rangle$, and $\langle h_{101}\rangle$ only, we obtain the post-batch process signature for the parametric drift in the solubility curve, $W^{S,\text{post}} = [1;0;1;1]$. In this work, however, all residuals exceed their thresholds and thus all signatures are identical as follows:

$$W^{C,\text{post}} = W^{S,\text{post}} = W^{Nu,\text{post}} = W^{T,\text{post}} = W^{G_{110},\text{post}} = W^{G_{101},\text{post}} = [1;1;1;1] \tag{8.23}$$

Therefore, it is not possible to further isolate parametric drifts based on the post-batch measurements (i.e., the post-batch measurements do not provide any information for isolation of parametric drifts). Instead, once we have selected two subgroups using the in-batch measurements (cf. Eq. 8.21), we will run simulations for the remaining drift candidates one by one to find the one that best matches the in-batch and post-batch measurements.

8.4.4 Post-batch stage of PDDI

In the post-batch stage of the proposed PDDI, we compute the residuals by calculating the difference between the time profiles of the states obtained through in-batch and post-batch

measurements from the time profiles of the states obtained from the drift-free simulation with noise used in the preparatory stage above. Then, we compare the residuals with signatures obtained in the preparatory stage for each parametric drift, and an optimization problem is solved to isolate the parametric drift and to estimate the magnitude of the parametric drift. Next, the batch process model used in the MPC for the next batch is updated.

Parametric drift in solubility

In the first scenario considered in this work, there is a parametric drift in the solubility equation, which results in crystals that do not meet the desired product quality. Specifically, a parametric drift, such as a change in the pH level of a feedstock container, is introduced at the beginning of the batch run such that the solubility is increased by 10% for a given temperature level. As a result, the set of optimal jacket temperatures computed by the in-batch MPC using the nominal process model will not drive the temperature in the crystallizer to a desired value because of the mismatch between the actual batch process and the solubility model used in the in-batch MPC.

Types	$r_{\langle\alpha\rangle}$	r_{M_0}	$r_{\langle h_{110}\rangle}$	$r_{\langle h_{101}\rangle}$
no PDTC	0.17	128000	40.1 μm	34.8 μm

Table 8.6: Residuals based on the post-batch measurements obtained at $t = 18$ hours for the batch crystallization process with a parametric drift in the solubility equation.

We now look at how the PDDI system responds to the same parametric drift in the solu-

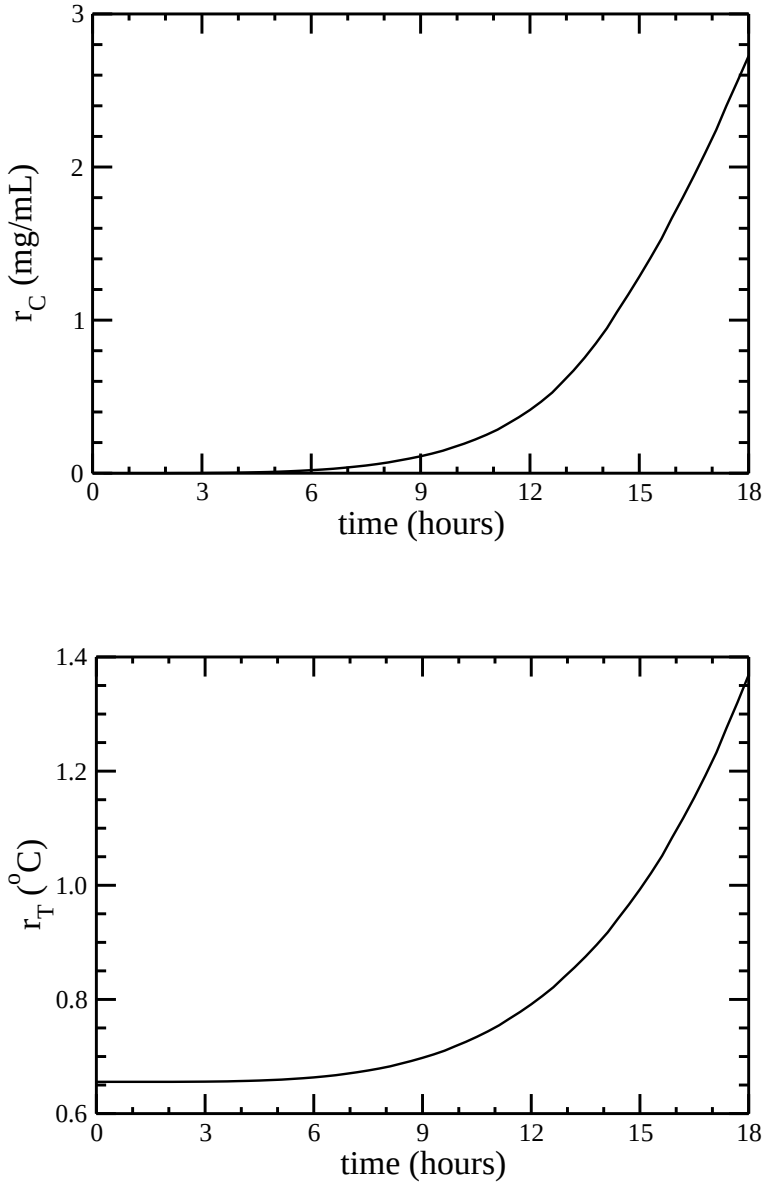

Figure 8.3: Residual profiles of the protein solute concentration, r_c, and of the crystallizer temperature, r_T, with time during batch crystallization in response to a parametric drift in the solubility equation, Eq. 8.3, under the MPC scheme with the nominal process model, for the growth rate ratio set-point value $\alpha_{\text{set}} = 0.89$.

bility equation. During batch-to-batch operations, the PDDI system performs two actions. First, it computes the residuals r_C and r_T at the end of each batch using in-batch measurements of those variables. If the residuals exceed their thresholds, a parametric drift is detected and isolated by comparing its in-batch process signature with the parametric drift signatures presented in Eq. 8.21. Specifically, the detection of a parametric drift is most evident in Fig. 8.3 and Table 8.6 where the residuals $r_c(t)$ and $r_T(t)$ exceed their thresholds at $t = 15.2$ and $t = 16$ hours while $r_{\langle\alpha\rangle}(t)$, $r_{M_0}(t)$, $r_{\langle h_{110}\rangle}(t)$, and $r_{\langle h_{101}\rangle}(t)$ exceed their threshold values at $t = 18$ hours. The resulting in-batch process signature, $[1;0]$, coincides with the signatures for parametric drifts in the solubility curve, mass balance parameters, and nucleation rate (cf. Eq. 8.21). Since in this work the post-batch measurements do not provide any information for isolation of the parametric drift, the second action of the PDDI scheme is to find the one that best matches the in-batch and post-batch measurements. Assuming only one parametric drift occurs in a single batch run, the magnitude of each parametric drift is computed by solving Eq. 8.16 for γ_s, γ_C, and γ_{nu} separately. As a result, the correction parameter for the solubility equation is successfully computed providing the best match with the prespecified parametric drift, which is $\gamma_s = +10\%$. This information is used to update the model of the MPC system to deal with the persistent parametric drift in the solubility that would have an effect on the product quality in the next batch run. The performance of the successful model parameter updating at the next batch run can be seen in Fig. 8.4 and Table 8.7 where the residuals obtained by the multiscale simulations under the PDTC scheme remain far below their threshold values.

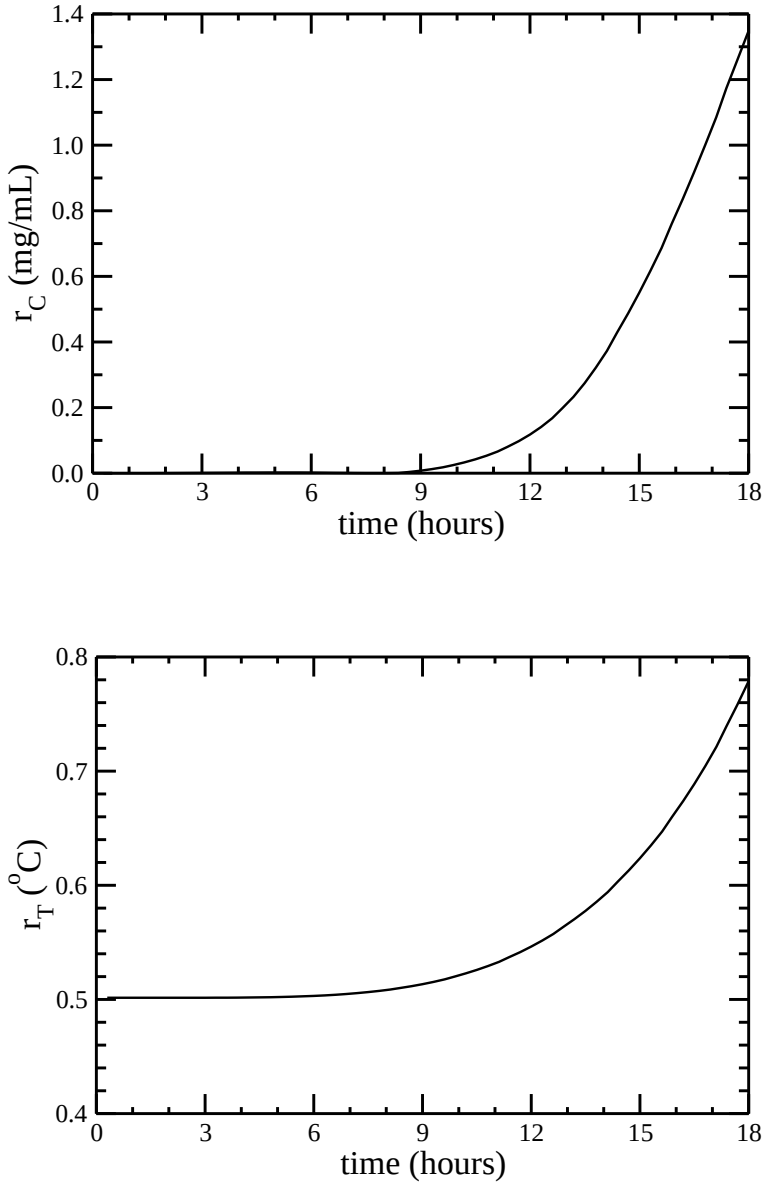

Figure 8.4: Residual profiles of the protein solute concentration, r_c, and of the crystallizer temperature, r_T, with time during batch crystallization in response to a parametric drift in the solubility equation, Eq. 8.3, under the PDTC scheme with γ_s, for the growth rate ratio set-point value $\alpha_{\text{set}} = 0.89$.

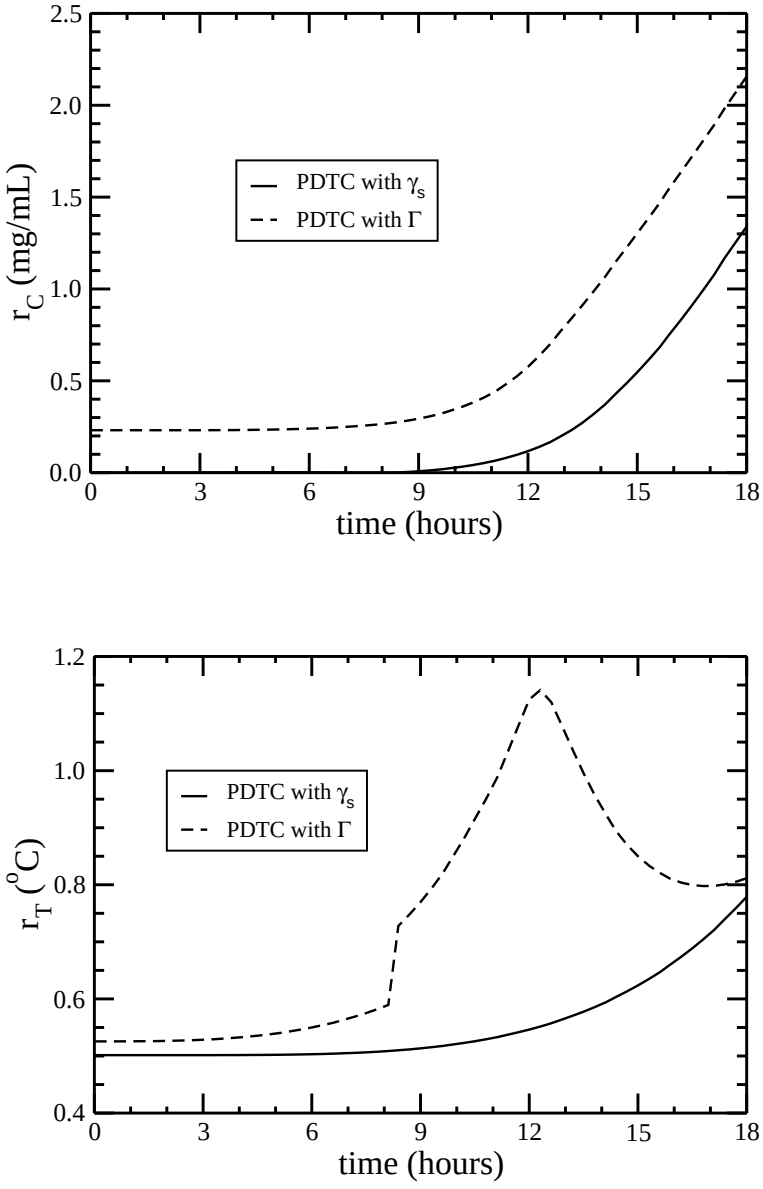

Figure 8.5: Comparison of the residual profiles of the protein solute concentration, r_c, and of the crystallizer temperature, r_T, with time during batch crystallization in response to a parametric drift in the solubility equation, Eq. 8.3, under the PDTC scheme with γ_s and the PDTC scheme with Γ (i.e., $\Gamma = [\gamma_{110},\ \gamma_{101},\ \gamma_T,\ \gamma_C,\ \gamma_{\text{nu}},\ \gamma_s]$), for the growth rate ratio set-point value $\alpha_{\text{set}} = 0.89$.

Types	$r_{\langle\alpha\rangle}$	r_{M_0}	$r_{\langle h_{110}\rangle}$	$r_{\langle h_{101}\rangle}$
PDTC with γ_s	0.0047	32000	1.95 μm	1.72 μm
PDTC with Γ	0.019	92000	12.1 μm	8.51 μm

Table 8.7: Comparison of the residuals based on the post-batch measurements for the batch crystallization process with a parametric drift in the solubility equation under PDTC scheme with γ_s and PDTC scheme with Γ at $t = 18$ hours.

For the purpose of testing the closed-loop performance if additional correction factors are used, the control performance of the PDTC with γ_s is compared with that of the PDTC with Γ where all six correction factors are used to compensate for the parametric drift in the solubility equation. In Fig. 8.5 and Table 8.7, the residuals obtained under the PDTC with γ_s are smaller than those under the PDTC with Γ indicating that the former scheme estimates the effect of the process drift in the solubility better than the latter scheme. It is also apparent in Fig. 8.6 that the crystal shape distribution obtained at $t = 18$ hours under the PDTC with γ_s is more narrow and closer to the set-point value than that under the PDTC with Γ.

Parametric drifts in G_{110} and G_{101} growth rates

In this scenario, we look at simultaneous parametric drifts in the growth rates in the directions of the (110) and (101) faces by multiplying the expressions for G_{110} and G_{101} (cf. Eqs. 8.10 and 8.11) by 0.7 and 0.77, respectively. This is a very typical parametric drift in the crystallization process because the presence of impurities will drop the overall crystal

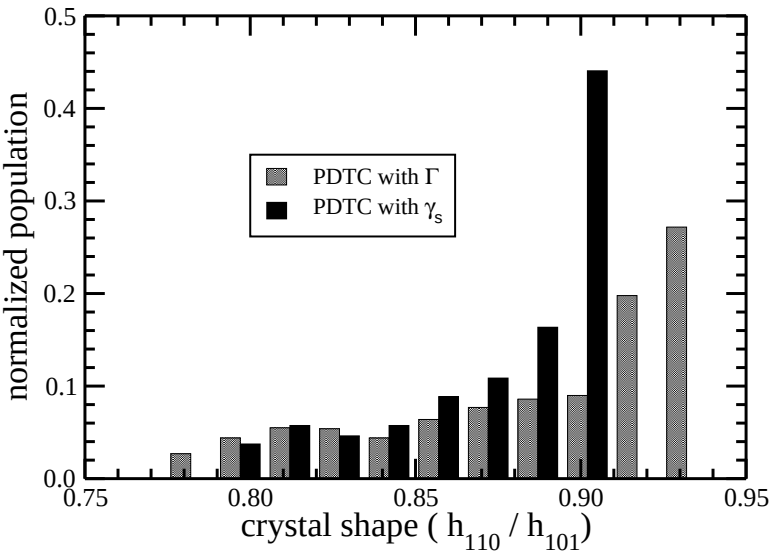

Figure 8.6: The normalized crystal shape distribution obtained from the kMC simulations under the PDTC scheme with γ_s is compared with that of the PDTC scheme with Γ (i.e., $\Gamma = [\gamma_{110},\ \gamma_{101},\ \gamma_T,\ \gamma_C,\ \gamma_{\text{nu}},\ \gamma_s]$) for the batch crystallization process with a parametric drift in the solubility equation, Eq. 8.3. The desired set-point value for the average crystal shape is $\alpha_{\text{set}} = 0.89$.

growth rates inhibiting the attachment of molecules of interest to the crystal surface. Furthermore, an impurity may favor one face over another which could cause the growth rate of one face to drop more than the growth rate of the other face. When there is no PDTC implemented, we see in Fig. 8.7 that the values of the $r_C(t)$ and $r_T(t)$ increase progressively because of the parametric drifts in the G_{110} and G_{101} equations and eventually they exceed their thresholds at $t = 17.7$ and $t = 15.2$ hours, respectively. As a result, the in-batch process signature of $[0;1]$ is obtained, indicating that there is a chance of a parametric drift in the mass balance parameters and growth rates in the directions of the (110) and (101) faces. The presence of a parametric drift is also apparent in Table 8.8 because the residuals $r_{\langle\alpha\rangle}(t)$, $r_{\langle h_{110}\rangle}(t)$, and $r_{\langle h_{101}\rangle}(t)$ have exceeded their thresholds at $t = 18$ hours.

Types	$r_{\langle\alpha\rangle}$	r_{M_0}	$r_{\langle h_{110}\rangle}$	$r_{\langle h_{101}\rangle}$
no PDTC	0.088	96000	21.1 μm	16.6 μm

Table 8.8: Residuals based on the post-batch measurements obtained at $t = 18$ hours for the batch crystallization process with parametric drifts in the growth rates in the direction of the (110) and (101) faces.

Then, we solve Eq. 8.16 to determine which of the remaining three candidates best matches the in-batch and post-batch measurements and its magnitude. Specifically, we used both γ_{110} and γ_{101} at the same time because it is very common in practice that growth rates in the directions of more than one face are affected by, for example, impurities. Then, the proposed PDTC scheme is applied to the next batch run to deal with the persistent parametric drifts in the G_{110} and G_{101} equations. The control performance is shown in Fig. 8.8

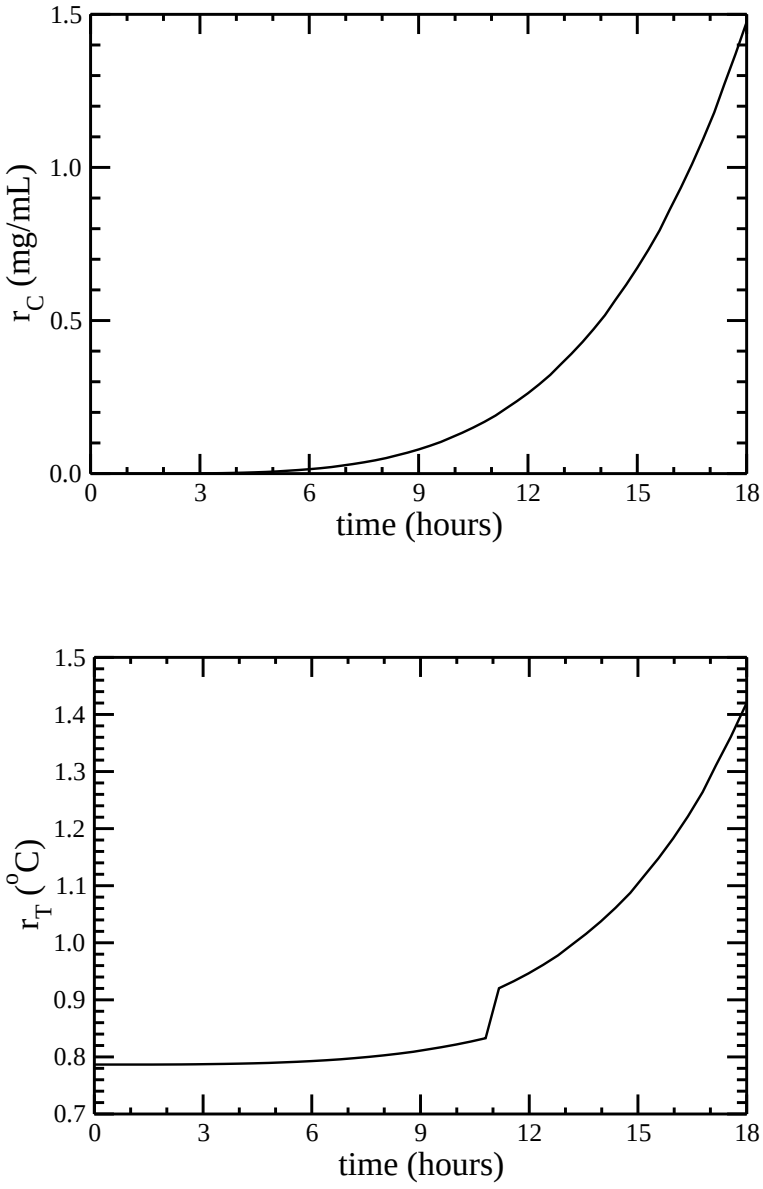

Figure 8.7: Residual profiles of the protein solute concentration, r_c, and of the crystallizer temperature, r_T, with time during batch crystallization in response to parametric drifts in the crystal growth rates in the directionss of the (110) and (101) faces, Eqs. 8.10 and 8.11, under the MPC scheme with the nominal process model, for the growth rate ratio set-point value $\alpha_{\text{set}} = 0.89$.

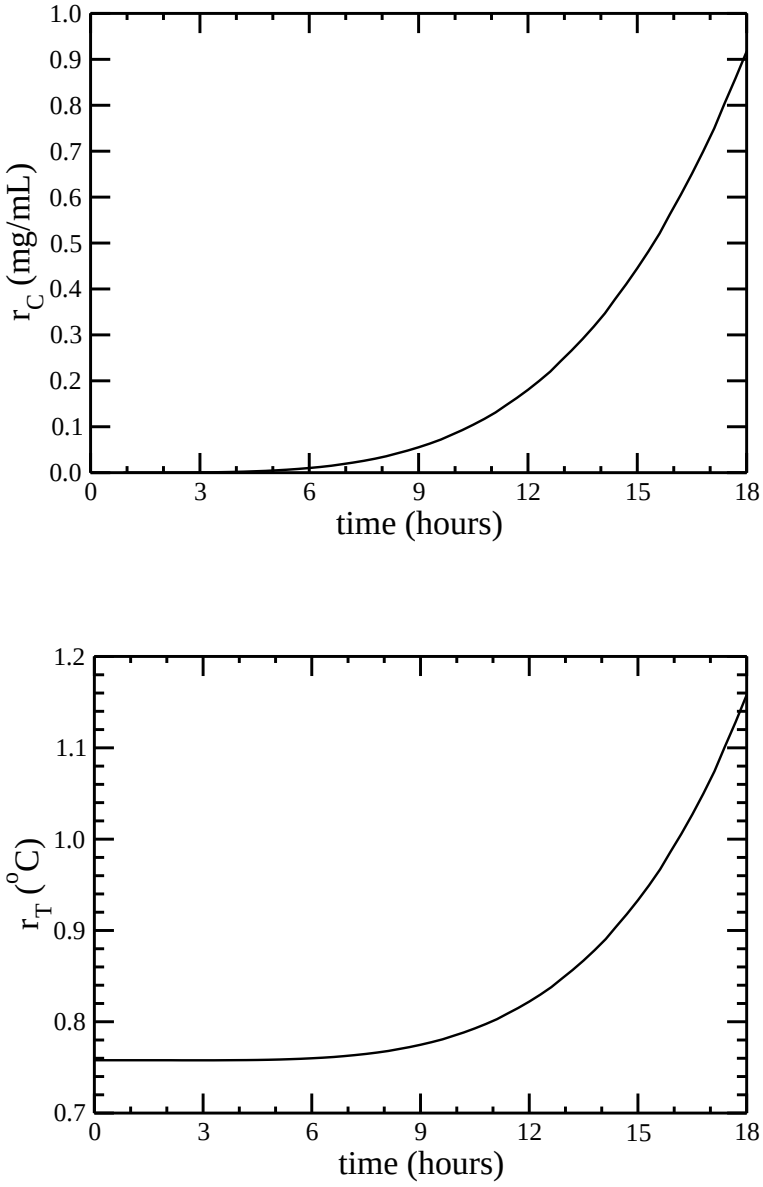

Figure 8.8: Comparison of the residual profiles of the protein solute concentration, r_c, and of the crystallizer temperature, r_T, with time during batch crystallization in response to parametric drifts in the growth rates in the directions of the (110) and (101) faces, Eqs. 8.10 and 8.11, under the PDTC scheme with γ_{110} and γ_{101}, for the growth rate ratio set-point value $\alpha_{\text{set}} = 0.89$.

and Table 8.9, which show that under the PDTC scheme, all residuals stay far below their threshold values. The improvement in performance resulting from the parameter estimation is noticeable when the residuals in Tables 8.8 and 8.9 are compared.

As in the previous case, a comparative study between the PDTC with γ_{110} and γ_{101} and the PDTC with Γ is made and shown in Fig. 8.10 and Table 8.9, where the former control scheme outperforms the latter in handling the effect of the parametric drifts in the G_{110} and G_{101} parameters. This may be because the PDTC with Γ may have degenerate solutions due to its limited access to the crystal product quality. As a result, it is shown in Fig. 8.9 that crystals produced under the PDTC with γ_{110} and γ_{101} are much closer to the desired crystal shape set-point value than those produced under the PDTC with Γ.

Types	$r_{\langle\alpha\rangle}$	r_{M_0}	$r_{\langle h_{110}\rangle}$	$r_{\langle h_{101}\rangle}$
PDTC with γ_{110}, γ_{101}	0.0088	32000	2.21 μm	2.65 μm
PDTC with Γ	0.028	40800	6.28 μm	9.45 μm

Table 8.9: Comparison of the residuals based on the post-batch measurements for the batch crystallization process with a parametric drift in the growth rates in the directions of the (110) and (101) faces under the PDTC scheme with γ_{110} and γ_{101} and the PDTC scheme with Γ at $t = 18$ hours.

Due to the persistent parametric drift and the nature of the batch crystallization process, it is often the case that the original set-point value becomes physically inaccessible though the MPC continues to attempt to regulate the system as closely as possible to the original set-point value. For example, if G_{101} is increased by 15% (i.e., the growth rate curve for

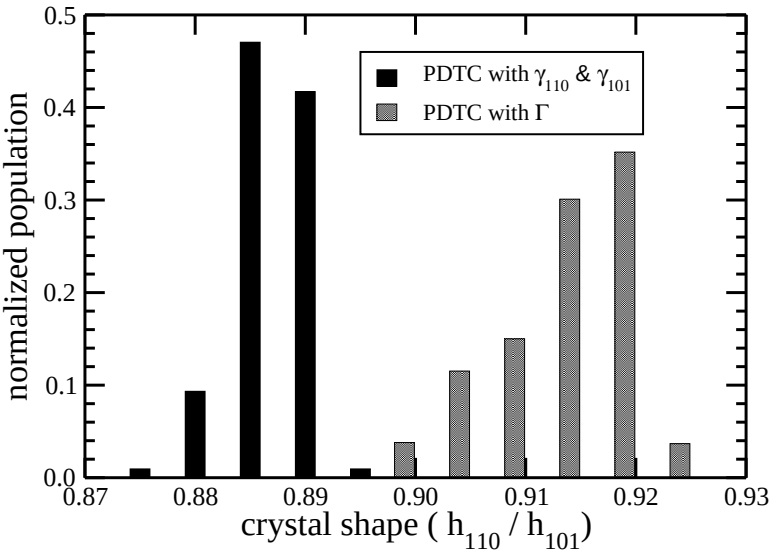

Figure 8.9: The normalized crystal shape distribution obtained from the kMC simulations under the PDTC scheme with γ_{110} and γ_{101} is compared with that of the PDTC scheme with Γ (i.e., $\Gamma = [\gamma_{110},\ \gamma_{101},\ \gamma_T,\ \gamma_C,\ \gamma_{\text{nu}},\ \gamma_s]$) for the batch crystallization process with parametric drifts in the growth rates in the directions of the (110) and (101) faces, Eqs. 8.10 and 8.11. The desired set-point value for the average crystal shape is $\alpha_{\text{set}} = 0.89$.

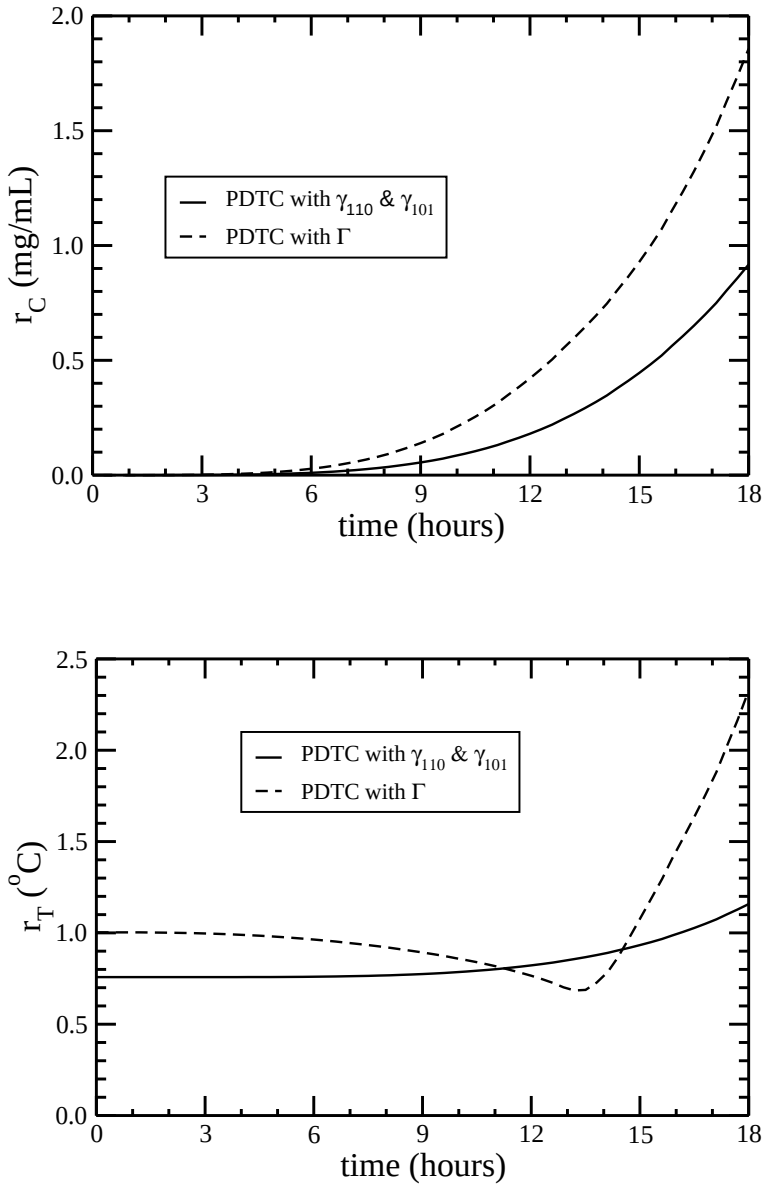

Figure 8.10: Comparison of the residual profiles of the protein solute concentration, r_c, and of the crystallizer temperature, r_T, with time during batch crystallization in response to parametric drifts in the growth rates in the directions of the (110) and (101) faces, Eqs. 8.10 and 8.11, under the PDTC scheme with γ_{110} and γ_{101} and the PDTC scheme with Γ (i.e., $\Gamma = [\gamma_{110},\ \gamma_{101},\ \gamma_T,\ \gamma_C,\ \gamma_{\rm nu},\ \gamma_s]$), for the growth rate ratio set-point value, $\alpha_{\rm set} = 0.89$.

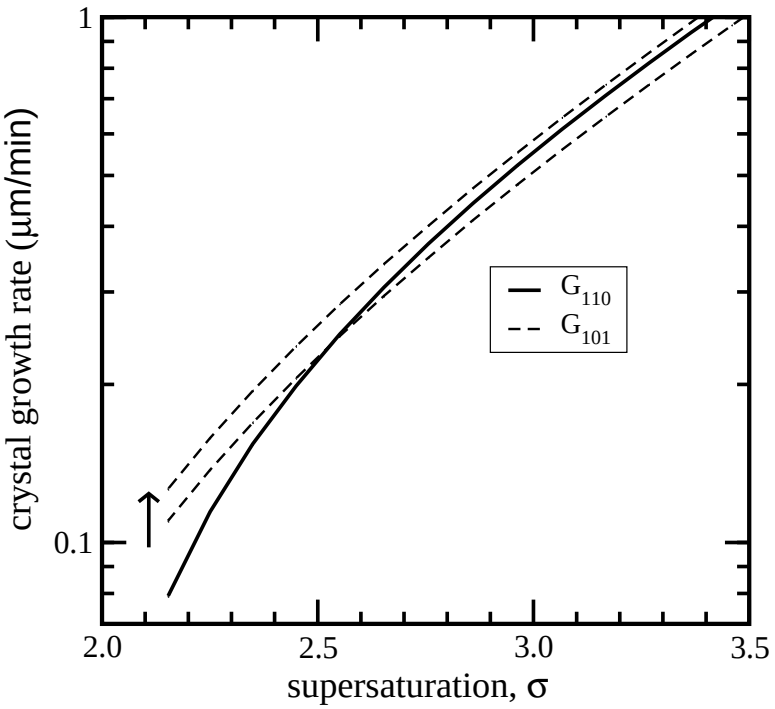

Figure 8.11: The solid and dashed lines show the growth rates obtained from the kMC model in the directions of the (110) and (101) faces, respectively, which are calibrated with the experimental data at 4% NaCl and pH= 4.6 taken from [31]. The arrow indicates the curve for the growth rate in the direction of the (101) face when it is increased by 15%.

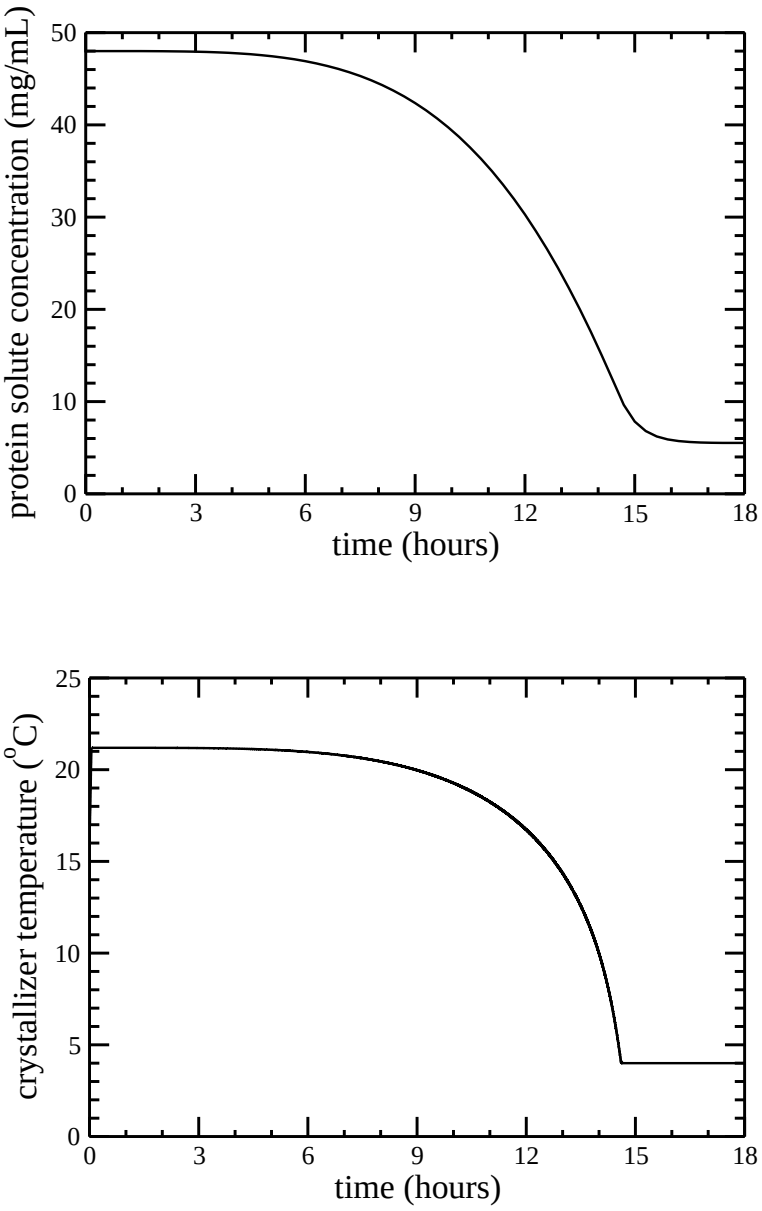

Figure 8.12: Comparison of the profiles of the protein solute concentration and of the crystallizer temperature with time during batch crystallization in response to a parametric drift in the growth rate in the direction of the (101) face, Eq. 8.11, under the PDTC scheme with γ_{101} for the growth rate ratio set-point value $\alpha_{\text{set}} = 0.89$.

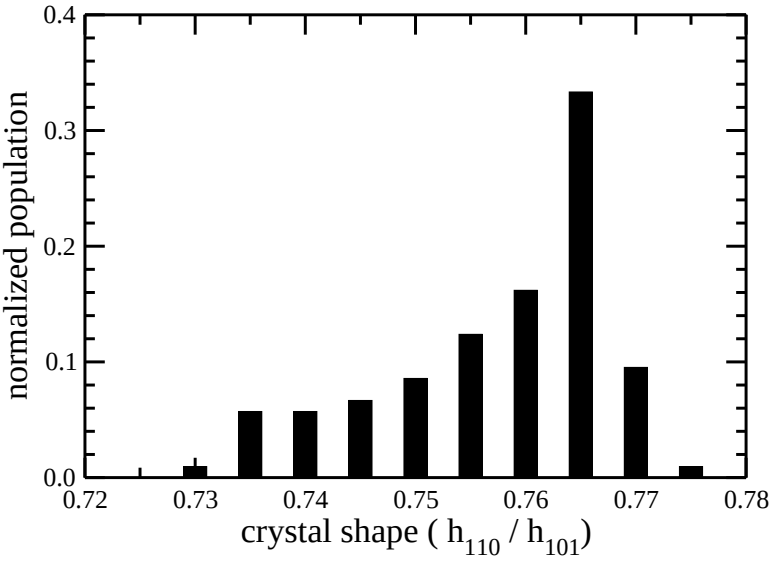

Figure 8.13: The normalized crystal shape distribution obtained from the kMC simulations under the PDTC scheme with γ_{101} for the batch crystallization process with a parametric drift in the growth rate in the direction of the (101) face, Eq. 8.11. The desired set-point value for the average crystal shape is $\alpha_{\text{set}} = 0.89$.

the G_{101} has shifted in the direction of the arrow in Fig. 8.11), the optimal supersaturation level required to achieve the set-point value, $\alpha_{\text{set}} = 0.89$, is also increased, resulting in more rapid crystal growth and as a result more significant depletion in the protein solute concentration. As shown in Fig. 8.12, the concentration may drop to a level which cannot be increased by additionally lowering the jacket temperature because of the constraint on the temperature of the crystallizer (cf. Eq. 8.14c). Therefore, crystals are produced with an undesirably low aspect ratio, as shown in Fig. 8.13.

The proposed PDDI scheme can be applicable to other batch crystallization systems

provided that both in-batch and post-batch measurements are available. More measurements would enhance the performance of the proposed PDDI scheme. Furthermore, in the case in which a first principles model is not available for MPC design, the proposed PDDI scheme can be coupled with a model used in MPC that is derived from process data (i.e., a data-based model) using system identification techniques.

8.5 Conclusions

In this work, a PDDI scheme that consists of a preparatory stage before batch-to-batch operation and a post-batch stage during batch-to-batch operation was proposed for the detection and isolation of batch-to-batch parametric drifts in a batch crystallization process. In the preparatory stage, the threshold values and signatures for each parametric drift were computed without process measurements. Then, during batch-to-batch operation, this scheme computed residuals by evaluating the absolute value of the difference between the process variables obtained from the drift-free simulation with noise from the process variables obtained through post-batch process measurements (e.g., number of crystals, average crystal size and shape) as well as in-batch process measurements (e.g., protein solute concentration, temperature in the crystallizer). The residuals were compared with thresholds and signatures obtained in the preparatory stage for the detection and isolation of a parametric drift. Subsequently, the magnitude of the batch-to-batch parametric drift was estimated by the PDDI system and it was used to update the parameters of the batch process model which was used in the in-batch MPC to compute a set of optimal jacket temperatures for

the production of crystals with a desired shape distribution in the next batch. Using closed-loop simulations, the batch-to-batch process model parameter variations in the solubility and crystal growth rates were properly handled by the proposed PDTC scheme. Furthermore, the performance of the proposed PDTC scheme was evaluated with respect to the number of correction parameters used to estimate various parametric drifts.

Chapter 9

Multiscale, multidomain modeling and parallel computation: application to crystal shape evolution in crystallization

9.1 Introduction

The modeling of multiscale systems has made fundamental understanding and quantitative prediction possible for processes with complex behavior and product characteristics, and it has tremendous potential to significantly contribute to the chemical, pharmaceutical and microelectronics industries [81, 61, 124, 25]. Motivated by the advances in high-performance computing power, an increasing interest in multiscale, multidomain modeling has been triggered. Moreover, chemical engineers, among other scientists and engineers,

have potential to impact the field of multiscale process modeling due to our unique discipline ranging from molecular modeling to large-scale chemical process modeling.

More specifically, kinetic Monte Carlo (kMC) modeling has received growing attention for dynamic simulations of microscopic/mesoscopic process behavior. The basic principle of kMC is that in order to efficiently simulate a dynamical system with a variety of different rates of processes (e.g., adsorption, migration, and desorption of molecules on a surface in crystal growth), at each step in the simulation, the next process is determined based on a probability proportional to the rate for that process, and after an event is executed, the rates for all processes are updated. The time of the next event is determined by the overall rate for the microscopic surface processes and a suitably defined random number. The standard kMC algorithm is a serial algorithm in a sense that one event can occur at each time step. For many problems of practical interest, however, one needs to simulate systems with larger temporal and spatial scales than the ones that can be simulated using a serial algorithm and available computing power. For these problems, motivated by the recent efforts to develop parallel computation frameworks for the simulation of multiscale process models [6, 39, 5, 18, 97, 49, 47, 114, 84, 4], it would be desirable to develop efficient parallel kMC algorithms so that many processors can be used simultaneously in order to accomplish realistic computations over extended temporal and spatial scales.

One of the most frequent uses of parallel architectures is to simply perform independent simulations of a model under different conditions on different processors. Additionally, for very large problems, parallel architectures can be used to improve the speed of the sim-

ulation dramatically by decomposing the system into different components/domains and assigning each component/domain to a different processor. When we design a parallel program, it is important to compare the relative order of magnitudes of the communication time and the computation time. For example, if the size of the individual tasks to be executed is too small, the time used to communicate information between processors may not be small compared to the time needed by each processor for computation. In such a case, the performance may actually worsen as processors are added. On the other hand, for microscopic systems with long range molecular interactions, most of the computational effort goes into the calculation of energy changes, and then the communication overhead is much less of a problem and is minimal relative to the computation time.

Recently, there has been a great deal of work on the development of rigorous asynchronous parallel algorithms for equilibrium MC simulation (eMC) [105, 94, 95, 75]. However, there has been surprisingly little work completed on parallel algorithms for kMC simulation. This is because the interval between successive events in kMC algorithms depends on the surface micro-configuration (for example, in evolution of surface micro-configuration in this film growth and crystal growth), and thus, it requires additional bookkeeping to keep track of the rates (probabilities for each event to be selected). In particular, for systems such as crystallization and thin film deposition, surface processes play a key role, and thus, the possible rates or probabilities for events can vary by several orders of magnitude. Several contributions have been made to the development of multiscale models used to simulate the deposition of thin films for a variety of applications

[74, 50, 99, 106, 102], while the development of efficient parallel algorithms for kMC simulations remains a challenging problem.

Motivated by this, in a previous work [27], we explored a hybrid kMC algorithm originally developed for the growth of silicon films by [121]. To improve computation efficiency, the surface migration was computed separately from the other microscopic processes on the thin film surface. The choice to deal with the surface migration separately is made in an effort to improve computation efficiency. More specifically, due to the high frequency of surface migration events relative to other surface processes, a brute force kMC algorithm would spend more than 99% of computation time on migration alone. The simulation of the surface migration process is decoupled from the standard kMC implementation and separately executed using a one-dimensional lattice random walk process [27]. As a result, significant computation time savings were achieved with a very small compromise of the accuracy of the results.

In this work, we have attempted to directly deal with the problem of reducing computational requirements without compromising the accuracy of established chemical models via a parallelized kMC. We show that choosing an appropriate decomposition strategy is the key to reducing communication among processors and it is ideally suited for parallel implementation without compromising precision. Specifically, the message passing interface (MPI) settings that use the information passing between the cores are selected and are used following a "manager-worker" scheme: there is a processor (i.e., manager) that is responsible for partitioning a problem (e.g., kMC model to simulate batch crystallization

system) into partitions (e.g., crystal growth of a group of crystals) and allocating the partitions to processors (i.e., workers). Workers are responsible for solving assigned partitions, and when a worker completes the simulation of a partition, it notifies the manager. Then, the manager allocates the worker a new task.

9.2 Parallelized computations

9.2.1 Motivation

There are three reasons why one might want to use parallelized computation. Firstly, one may want to speed up simulations by using multiple processors. More specifically, parallelization can reduce the simulation time required for the simulation of a large system that can be done on a single processor. Secondly, one might want to do many simulations at different conditions in order to, for example, find good model parameters by testing parameters over a large range of different parameter values. We can also reduce the noise in a stochastic method such as kMC simulations by running a simulation multiple times. The process of creating a parallel program from a serial one consists of three steps: 1) decomposition of the original serial computation problem into small tasks, 2) assignment of tasks to processors, and 3) orchestration of the communication among processors and synchronization at each time step [28]. Below we discuss these three tasks, as they pertain to parallelized simulation of multiscale models.

9.2.2 Decomposition

Decomposition concerns how to break up or divide a computation problem into a collection of tasks that may be executed concurrently. This does not simply imply a straightforward division of a computation problem into a number of tasks equal to the number of available computers. In some cases, the number of tasks can vary dynamically as the program executes, which is known as an irregular decomposition problem [28]. The main objective in decomposition is to expose enough concurrency to keep all processors busy at all times, yet not decompose so much that the overhead of managing the task's decomposition through communication between processors becomes substantial compared to the computation time. In parallel computations, the theoretical maximum speedup using multiple processors can be computed via Amdahl's Law [28]. More specifically, if P is the fraction of an original serial program that can be parallelized, and $1-P$ is the fraction of a program that cannot be parallelized (thus, remain serial), then the maximum speedup that can be achieved via parallelization using N processors can be computed as follows:

$$S(N) = \frac{1}{(1-P) + \frac{P}{N}} \tag{9.1}$$

where S is the maximum speedup. If some portions of a program's execution do not have as much concurrency as the number of processors used, then some processors will have to be idle for those portions and speedup will be suboptimal.

Initially, the parallel computations may be slower than the serial ones, because of communication and synchronization overheads that are not incurred by the sequential program.

After the parallel program overcomes this overhead, it provides improved performance as the number of processors increases. Eventually, there is a tail-off region where performance does not substantially increase as the number of processors increases. This region occurs because the number of available tasks obtained after the decomposition step can be bounded. Eventually, adding computers does not improve computational performance, because there is not sufficient work to keep all processors busy. Therefore, decomposition should provide a number of tasks considerably greater than the number of processors available.

There are many decomposition techniques. For example, domain decomposition is used to divide up the data of a program and operate on the parts concurrently (e.g., matrix calculations, inner product calculations) while functional decomposition refers to dividing up the function (e.g., computing the integral of a function $f(x)$ on the closed interval $[a,b]$). Furthermore, irregular problem decomposition refers to decomposition in the case that the program structure evolves dynamically as the program executes and cannot be determined a priori (e.g., flow dynamics, particle flow simulations). The size of the tasks in the irregular decomposition problem may vary widely, and thus, a method of load balancing must be employed to keep computers busy. More detailed discussion on the load balancing scheme will be covered in the following section in the context of parallelized computation of a multiscale model of a batch crystallization process.

9.2.3 Assignment

Assignment refers to the mechanism by which tasks will be distributed among processors. The primary goal of the assignment is to balance the workload among processors to reduce communication between processors and the overhead of managing the assignment. Specifically, the workload to be balanced includes computation (i.e., task execution), input/output data access, and communication between processors. The simplest assignment strategy is to divide the total task number by the number of cores available; thus, consecutive partitions are packed into the same processor (i.e., packed allocation). The other widely used strategy is to use a modulus function such as the group number modulus is equal to the number of processors available (i.e., round-robin allocation).

In particular, there are several load balancing strategies to deal with irregular problems where the size of each task changes dynamically. Specifically, bin packing is a technique used in cases where the time required to run a task is proportional to the length of the task where the task size grows with time. The goal is to keep the computation load at each processor balanced.

The manager-worker scheme is a centralized scheme that involves a manager processor and a collection of worker processors. The manager processor is responsible for assigning tasks decomposed from an original problem to worker processors. The worker processors are responsible for processing tasks and are generally independent processors. When a worker processor completes the assigned task, it notifies the manager and the manager allocates it a new task.

Specifically, there are two kinds of manager-worker schemes: synchronous and asynchronous. For the synchronous scheme, before initiating their following task executions, all processors wait until they have received all of the data computed by other processors at the previous task execution step. On the other hand, for the asynchronous scheme, all of the processors perform their computations without waiting for the data computed by other processors (i.e., they do not account for the progression of the other processors). In general, the synchronous manager-worker scheme is suitable for small homogeneous clusters with fast communication whereas the asynchronous manager-worker scheme provides better performance on large-size heterogeneous clusters. Also, when the processors have significantly different performance from each other, the speed of a synchronous manager-worker scheme is limited by the slowest processors. In this case, the asynchronous scheme achieves better performance than the synchronous one.

9.2.4 Orchestration

To execute their assigned tasks, processors need mechanisms to name and access data and to communicate and synchronize with other processors. Orchestration uses available mechanisms to accomplish these goals correctly and efficiently. The major goal in orchestration is to reduce the cost of the communication and synchronization (i.e., the overheads of parallelism management) by preserving locality of data and scheduling tasks so that those on which many other tasks depend on will be located at a position which is easily accessible by many other processors.

The message passing interface (MPI) is one of the most widely used techniques to deal with communication and synchronization between processors in order to solve chemical engineering problems on parallel processors. For example, suppose that a reaction occurs in a batch process, and due to imperfect mixing, the spatial concentration distribution is not uniform throughout the batch system. Next, we can consider that each core runs a kMC code for a time step of a parallel computer to compute the amount of reactant consumed by a reaction in a particular spatial domain of the continuous phase. Then, each core sends these values to the manager core via an MPI data manager, and the manager core adds up these values to compute the total amount of solute depletion over the entire spatial domain in the continuous phase. Lastly, the manager core sends back updated values to each core (i.e., each spatial domain). This sequence is repeated until the specified length of time has been completed. The output files store all the simulation results that belong to the individual kMC.

9.3 Multiscale batch crystallization process model and parallelization

In a crystallization process, there is large disparity of time and length scales of phenomena occurring in the continuous phase and on the crystal surface. For example, the solution density is not constant when the volume containing the medium of the continuous phase keeps shrinking. In this case, it is not valid to assume that the crystal surface is a contin-

uum, and furthermore, it is computationally impossible to model the whole system from a molecular point of view.

Motivated by this, we present an integrated multiscale modeling and parallel computation framework for crystallization processes that elucidates the relationship between molecular-level processes like crystal nucleation, growth, and aggregation and macroscopically-observable process behavior and allows computing optimal design and operation conditions. The multiscale framework encompasses: a) eMC modeling for computing solid-liquid phase diagrams and determining initial crystallization conditions that favor crystal nucleation, b) kMC modeling for simulating crystal growth and aggregation and predicting the evolution of crystal shape distribution, and c) integrated multiscale computation simultaneously linking molecular-level models (e.g., kMC simulation) and continuous-phase macroscopic equations (e.g., mass and energy balance equations), covering the entire batch crystallization system. Specifically, Fig. 9.1 schematically illustrates information is exchanged between models used to describe the molecular, microscopic, and macroscopic levels.

9.3.1 Molecular model

In a previous work, we applied the eMC method for the modeling of crystallization systems at molecular level to calculate suitable phase diagrams. Here we briefly review this approach to demonstrate how the molecular level results are used in the multiscale model of the crystallization process. There are many types of Monte Carlo moves such as particle

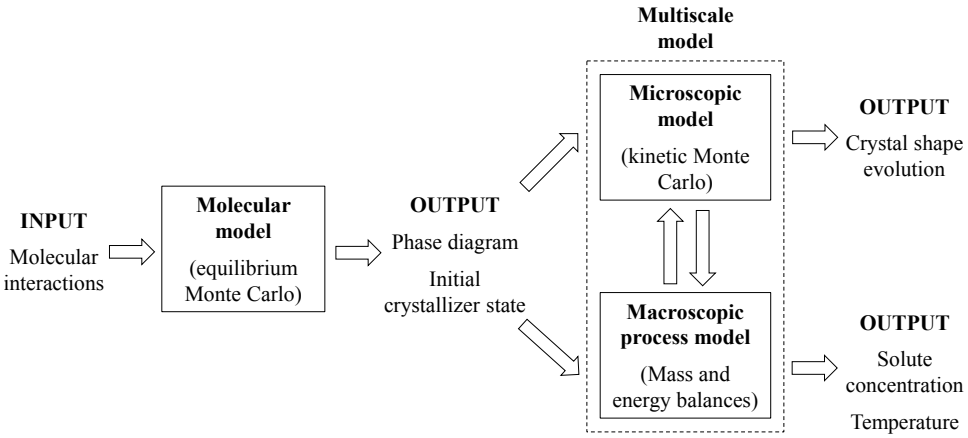

Figure 9.1: Schematic representation of multiscale modeling for batch crystallization process.

displacement, volume changes, and particle switching. Additionally, periodic boundary conditions are used to approximate the infinite dimensional system with a model with a finite number of lattice sites. Then, the probability that the system transitions from a current state m to another state n, $\alpha_{m\to n}$, is computed following the standard Metropolis algorithm as follows:

$$\alpha_{m\to n} = \min\left\{1, \exp\left(-\frac{E_n - E_m}{k_B T}\right)\right\} \tag{9.2}$$

where E_n and E_m are the energies of the system in states n and m, respectively, k_B is the Boltzmann constant, and T is the temperature in Kelvin. To compute the energy of the system, we develop a model to compute the interactions between the particles. A Lennard-Jones type potential is used as follows:

$$U = 4\varepsilon\left[\left(\frac{\sigma}{r}\right)^a - \left(\frac{\sigma}{r}\right)^b\right] \tag{9.3}$$

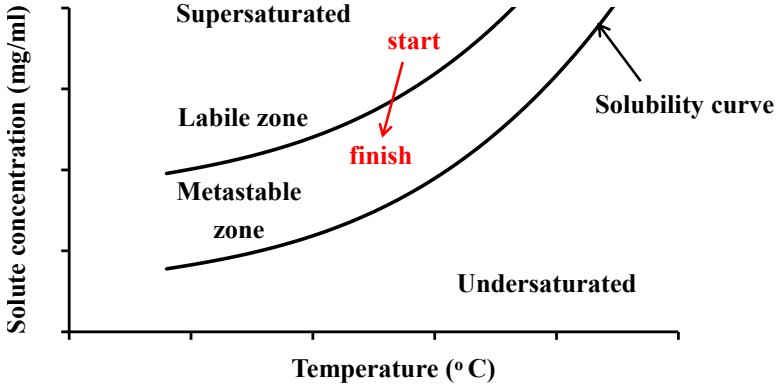

Figure 9.2: Phase diagram. The value of start shows where the initial condition of the batch crystallization system should be to favor nucleation early and the arrow shows how to manipulate the temperature to move into the metastable region to favor growth later in the batch.

where U is the potential energy between two particles, σ is the radius of the particles, r is the distance between the particles, ε is the depth of the potential well, and a and b are model parameters to be determined. Please note that E_n and E_m in Eq. 9.2 are the sum of U in Eq. 9.3 over all possible pairwise combinations of particles. Then, we measure some properties (e.g., solubility) of the material through experiments, where the measurement is available for a small region, and use them to determine the model parameters in Eq. 9.3 that provide a good agreement between simulated and experimental data. We use Eq. 9.3 with the known parameters to calculate the phase diagram (e.g., see Fig. 9.2 which is taken from [96]) to predict the conditions under which a nucleation process is favored and to determine suitable initial nucleation and growth conditions to initialize batch crystallization.

9.3.2 Microscopic model

The solid-on-solid model, which is one of the most widely used techniques to simulate crystal growth accounting for crystal surface microstructure, is employed in this work to model the growth of lysozyme crystals as a specific example. Each event of our kMC simulation is chosen randomly based on the rates of the three surface microscopic phenomena. Please note that the following description of the surface kinetics for the present model follows closely that of [60] which is based on [32]

The adsorption rate is independent of crystal surface micro-configuration and is defined as

$$r_a = K_0^+ \exp\left(\frac{\Delta\mu}{k_B T}\right), \tag{9.4}$$

where K_0^+ is the attachment coefficient, k_B is the Boltzmann constant, T is the temperature in Kelvin, and $\Delta\mu = k_B T \ln(C/s)$, where C is the protein solute concentration and s is its solubility and $\Delta\mu$ is the crystal growth driving force. It is noted that $r_a \propto C$.

The desorption rate of a surface particle depends on its local environment. Thus, the desorption rate of a lattice site with i nearest neighbors is given by

$$r_d(i) = K_0^- \exp\left(-i\frac{E_{pb}}{k_B T}\right) = K_0^+ \exp\left(\frac{\phi}{k_B T} - i\frac{E_{pb}}{k_B T}\right), \tag{9.5}$$

where K_0^- is the desorption coefficient, i is the number of bonds, ϕ is the binding energy per molecule of a fully occupied lattice, and E_{pb} is the average binding energy per bond. The second equality in Eq. 9.5 holds true because of the relationship between K_0^- and K_0^+, which can be found in [66] Specifically, surface particles with less nearest neighbors have

a higher desorption rate. The migration rate is defined similar to the desorption rate in [60] as shown below

$$r_m(i) = K_0^+ \exp\left(\frac{\phi}{k_B T} - i\frac{E_{pb}}{k_B T} + \frac{E_{pb}}{2k_B T}\right). \tag{9.6}$$

The migration rate is the desorption rate multiplied by the extra exponential term $\exp\left(\frac{E_{pb}}{2k_B T}\right)$ to account for the fact that the migration rate is higher than the desorption rate.

In this work, simulations with hundreds of different E_{pb} and ϕ values were performed in parallel until satisfactory agreement was achieved between the growth rate computed by the kMC simulation and the experimental growth rates obtained from the literature [32]. From this, we determined a set of model parameters as follows: $E_{pb}/k_B = 1077.26$ K and $\phi/k_B = 227.10$ K for the (110) crystal face, and $E_{pb}/k_B = 800.66$ K and $\phi/k_B = 241.65$ K for the (101) crystal face, and $K_0^+ = 0.211$ s^{-1}.

9.3.3 Macroscopic model

The following mass and energy balance equations are employed to compute the dynamic evolution of the protein solute concentration and temperature in the batch crystallization process with time:

$$\frac{dC}{dt} = -\frac{\rho_c}{V_{batch}}\frac{dV_{crystal}}{dt}, \qquad C(0) = 48 \text{ mg/mL} \tag{9.7}$$

$$\frac{dT}{dt} = -\frac{\rho_c \Delta H_c}{\rho C_p V_{batch}}\frac{dV_{crystal}}{dt} - \frac{U_j A_j}{\rho C_p V_{batch}}\left(T - T_j\right), \qquad T(0) = 15^\circ\text{C} \tag{9.8}$$

ρ_c	crystal density	1400	mg/cm^3
ΔH_c	enthalpy of crystallization	-4.5	kJ/kg
$\rho(t)$	density of the continuous phase	1000 + C(t)	mg/cm^3
C_p	specific heat capacity	4.13	$kJ/K \cdot kg$
V_{batch}	volume of the crystallizer	1	L
A_j	contact area of the crystallizer wall and jacket	0.25	m^2
U_j	overall heat transfer coefficient	1800	$kJ/m^2 \cdot h \cdot K$

Table 9.1: Parameters for the batch crystallization process model.

where $V_{crystal}$ is the total volume of crystals growing in the crystallizer, and T_j is the jacket temperature (i.e., manipulated input). The process parameter values are shown in Table 9.1.

In the scale-up of a crystallization process, agitation is required in order to maintain the crystal phase in suspension. The resulting shear force induces aggregation processes which have a significant impact on the quality of crystal products as they decrease the total number of crystals and increase the average particle size. Motivated by these considerations, aggregation is taken into consideration in the modeling of large-scale crystallization processes.

More specifically, we assume that the continuous phase is sufficiently dilute that only binary aggregation between two particles is possible. Furthermore, according to the Kolmogorov length analysis [65], shear forces are the major contribution to the aggregation of crystals considered in this work. The corresponding kernel (cf. Eq. 9.9) can be used

to calculate the number of aggregation events taking place during the sampling time Δ in terms of the aggregation kernel $\beta\left(V_i, V_j\right)$, the batch crystallizer volume V_{batch}, the collision efficiency $\alpha\left(V_i, V_j\right)$, and the concentrations of particles of volumes V_i and V_j as follows:

$$N_{ij} = \alpha\left(V_i, V_j\right)\beta\left(V_i, V_j\right) m_i m_j V_{batch}\Delta \qquad 1 \leq i, j \leq C_{total} \tag{9.9}$$

where m_i is the number concentration (i.e., the number of particles of volume V_i per unit volume). The number C_{total} indicates the number of classes, and $\Delta = 0.5$ seconds (i.e., the collision probability is computed every 0.5 seconds). The rate of formation of aggregates of volume V_k from the collision of particles of volumes V_i and V_j is $\frac{1}{2}\sum_{V_i+V_j=V_k} N_{ij}$ where the summation considers all the different combinations of aggregation which result in V_k as follows:

$$V_i + V_j = V_k$$

Within the simulation, it is assumed that the shape of the crystal resulting from aggregation is identical to that of the larger crystal participating in the aggregation event. The reader may refer to [67] for more extensive simulation studies regarding the influence of aggregation on the shape distribution of crystals obtained at the end of the batch process.

9.3.4 Parallel computation of multiscale model

The simulation of the crystal growth process for crystals formed via nucleation is executed in parallel by using MPI through which we are able to divide the crystals between multiple cores by achieving the distribution of the computational cost and memory requirements.

More detailed discussion on the step-by-step parallelization of the crystallization process multiscale model that incorporates nucleation, crystal growth, and aggregation processes will be discussed below.

Decomposition

We can decompose the nucleation and crystal growth processes in a batch crystallization system into collections of tasks where each task is the crystal growth of a nucleated crystal. Furthermore, the time required to run one batch simulation can be further reduced by introducing a new variable N_{rp} to indicate the number of crystals represented by a single crystal that is actually running on a core. If $N_{\text{rp}} = 1000$, a single crystal running in the simulation will now represent 1000 actual crystals. Thus, we are only required to run 10 crystals in the simulation to represent 10000 crystals, and as a result, we compromise the computation time saving with the accuracy of the simulation results.

Assignment

More specifically, as soon as a crystal is nucleated, it will be assigned to one of the available cores, and it will grow to a larger crystal via the kMC simulation. Since crystals are continuously nucleated until the end of the batch process (i.e., at some point in time, the number of crystals growing in the crystallizer will exceed the number of cores), additional crystals need to be assigned to each core throughout the kMC simulation, which makes this an irregular problem where the total size of tasks assigned to each core grows with time.

core	crystal number	crystal number
worker 1	1	$n+1$
worker 2	2	$n+2$
$\vdots$	$\vdots$	$\vdots$
worker n	n	$2n$

Table 9.2: The order that nucleated crystals are assigned to each core, assuming that there are $2n$ crystals.

More specifically, nucleated crystals are assigned following the order described in Table 9.2 (i.e., crystal number modules is equal to the number of cores available). We note that this is a number-based allocation assuming that all cores have identical processor speed and memory.

The probability that an aggregation event takes place between two crystals with volumes V_i and V_j during a time period can be calculated via Eq. 9.9. Next, the aggregation event is executed when a random number generated in the interval $[0,1)$ is less than the collision probability. If an aggregation event occurs, we pick a crystal from each class i and j, respectively, and the smaller crystal between those two crystals will be removed from the kMC simulation while its volume will be added to that of the larger one, making it an aggregate where its volume is equal to the total volume of the two crystals before the aggregation event. This process applies to all possible pairwise combinations of crystal volumes over the course of the entire batch crystallization simulation.

Orchestration

Fig. 9.3 illustrates schematically how the information passing between the cores is managed with the MPI settings in order to link the macroscopic model (i.e., mass and energy balance equations for the continuous phase) to the microscopic model (i.e., kMC model). The coupled simulation follows the "manager-worker" MPI computational scheme: there is a core (i.e., manager) that is responsible for collecting the change in the total volume of crystals assigned to each core (i.e., worker) at each time step required for parallel processing, which corresponds to the amount of solute transported from the continuous phase to the crystal surface. Then, the manager core computes the change in the total volume of the crystals in the crystallizer at each time step and computes the protein solute concentration C and the temperature T for the continuous phase in the crystallizer using mass and energy balance equations. The updated C and T will be sent back to the worker cores, and those values at each core will remain identical until they are updated again after a time step. Then, the crystals assigned to each core will grow with an updated condition via kMC simulations.

In the parallel computation, we only consider synchronous iterations and synchronous communication (SISC). At each time step, all processors wait until they have received all of the data computed by the other processors at the previous task execution step, before beginning their following computations. The design of SISC parallelized code is quite straightforward using the MPI setting. Please note that the SISC penalizes algorithms on systems with a slow and heterogeneous cluster.

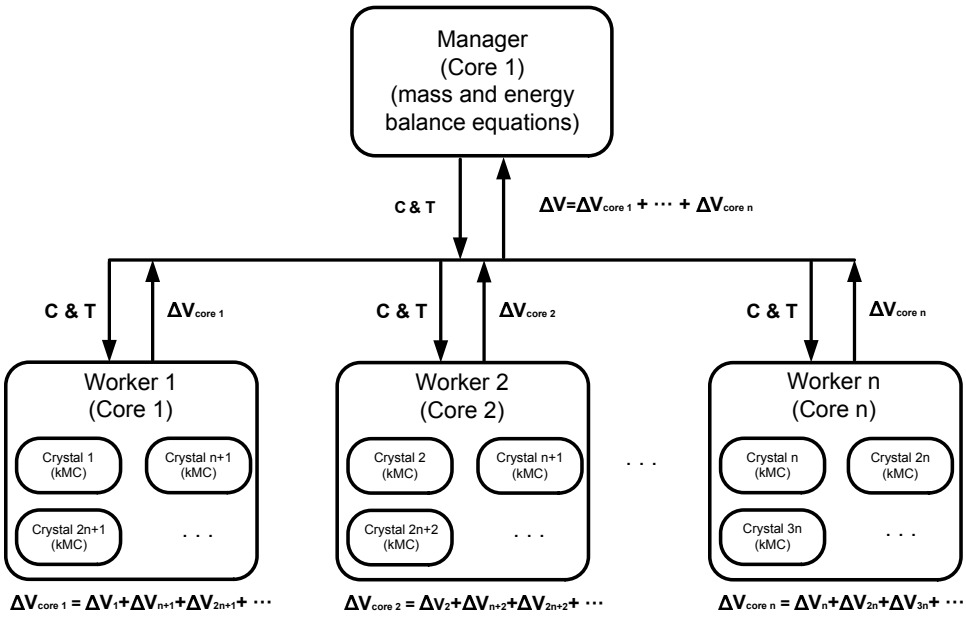

Figure 9.3: Manager-worker parallel computation scheme for multiscale model of batch crystallization process.

Pseudo-code

Algorithm 1 Parallel computation of the multiscale batch crystallization process model

for $i = 1 \rightarrow n$ **do**

if $i == 1$ **then** ▷ Manager core

1. assign nucleated crystals over Δt to each core according to Table 9.2

2. compute $\Delta V_{\text{total}}(t) = \sum_{i=1}^{n} \Delta V_i(t)$

3. update $C(t)$ **and** $T(t)$ **through Eqs. 9.7–9.8**

4. compute the total number of collisions between crystals via Eq. 9.9

else ▷ Worker core

1. have crystals assigned to each core grow via Eqs. 9.4–9.6

2. compute $\Delta V_i(t)$ **and send it to the manager core**

end if

end for

Please note that $\Delta V_{\text{total}}(t)$ is the change in the total volume of crystals in the crystallizer from $t - \Delta t$ to t seconds, and $\Delta V_i(t)$ is the change in the total volume of crystals particularly assigned to the core i from $t - \Delta t$ to t seconds. The readers may refer to [68, 72, 73] for the use of the parallelization scheme in different applications including the plug flow crystallizer and the continuous stirred tank crystallizer with a fines trap and a product classification unit.

9.3.5 Results

In this work, the Hoffman2 cluster, which consists of 1200 nodes with a total of 13,340 cores and over 50 TB of memory, is used along with MPI settings for all of the simulations. The memory on each node varies from 8 to 128 GB, and there are many types of CPUs including Intel and AMD, with 8, 12, 16-core, respectively. Due to the variety of the CPU types, if a small number of cores (e.g., 1, 2, 4, or 8 cores) are requested to the Hoffman2 cluster for the simulation of the multiscale model of the batch crystallization process, it is possible to get one bad CPU that consists of many bad cores, which will result in poor parallelization performance. To circumvent this issue, among the many CPU types in the Hoffman2 cluster, the Intel-E5530 with 8 cores is specifically requested and used for the construction of the plots and tables presented in this section.

It is presented in Table 9.3 that the simulation times required to complete a batch simulation decrease as the number of cores is increased. Also, Fig. 9.4 shows that as the number of cores is doubled, the speedup achieved in comparison to the theoretical maximum speedup (i.e., the theoretical maximum speedup should be n times when n processors are used) decreases, because of overhead costs generated by communication taking place between multiple cores. Overall, it is clear that the batch crystallization process greatly benefits from the use of MPI for the kMC simulations. Furthermore, we have compared the concentration and temperature profiles obtained from the kMC simulations with different numbers of cores, and it is verified in Figs. 9.5 and 9.6 that the concentration and temperature profiles obtained from the kMC simulations with $n_{\text{cores}} = 1$ and $n_{\text{cores}} = 64$ are

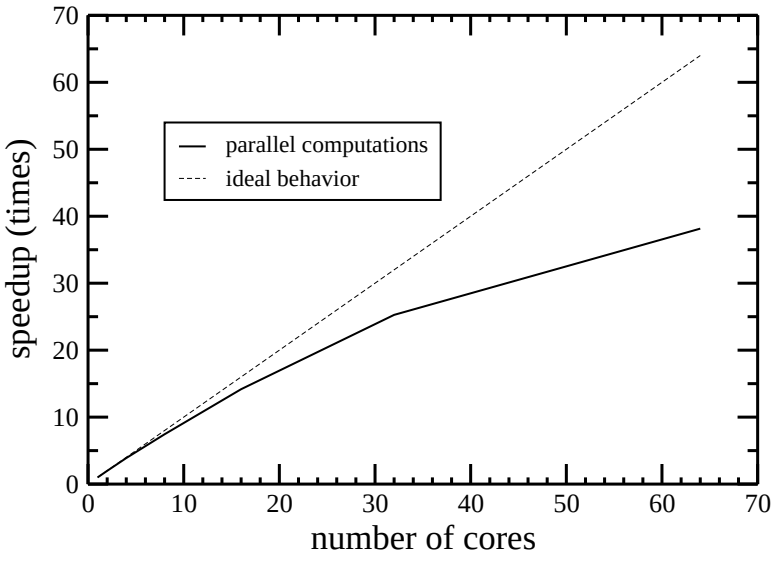

Figure 9.4: The speedup achieved by the parallel computation of the batch crystallization process multiscale model under open-loop operation with the number of cores used for the kMC simulation describing the evolution of the crystal shape distribution. The ideal behavior represents the theoretical maximum speedup.

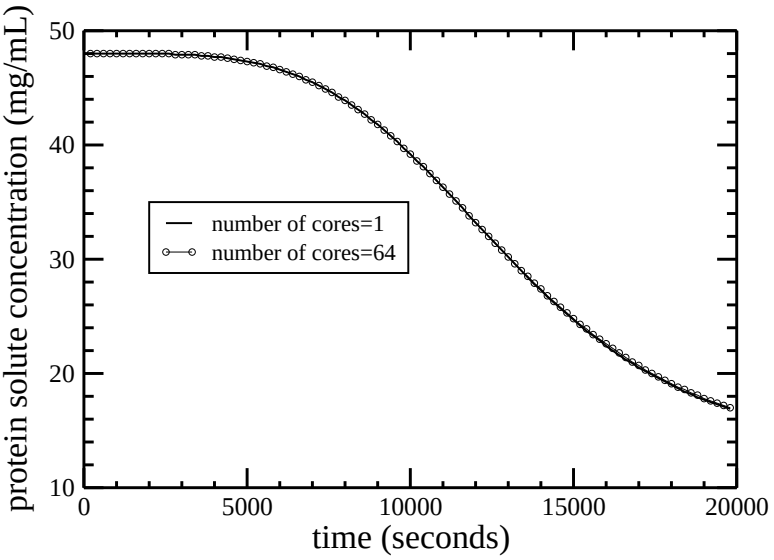

Figure 9.5: Profile of the protein solute concentration with time obtained under the open-loop operation of the batch crystallization process multiscale model for one core and sixty-four cores.

identical. Therefore, we can conclude that the computation time saving is achieved by the parallelized computations while the accuracy of the simulation results is maintained.

In the parallel computations, we might observe a super-linear speedup behavior (i.e., speedup is greater than n times when n processors are used), as is shown in Fig. 9.7. In general, the super-linear speedup in low-level computations is caused by the cache effect due to the different memory hierarchies of a modern computer [28]. More specifically, with the larger accumulated cache size, more simulation tasks can fit into caches, and thus, the memory access time required to reach the higher level (e.g., RAM) for additional memory can be reduced significantly, which results in extra speedup on top of that which is achieved by parallelizing the serial computations.

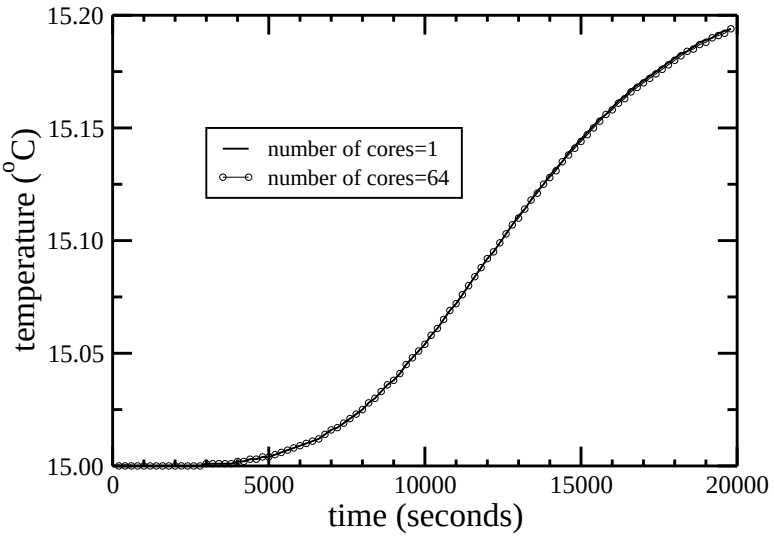

Figure 9.6: Profile of the crystallizer temperature with time obtained under the open-loop operation of the batch crystallization process multiscale model for one core and sixty-four cores.

n_{cores}	time (h)	speedup (times)	theoretical speedup (times)
1	34.97	1.00	1
2	17.63	1.98	2
4	8.98	3.89	4
8	4.71	7.44	8
16	2.47	14.18	16
32	1.38	25.28	32
64	0.92	38.15	64

Table 9.3: The time required to run a batch simulation and the speedup achieved by using different numbers of cores. Please note that n_{cores} is the number of cores and the speedup is defined as $\frac{t_1}{t_n}$, where t_1 is the time the process takes on one core and t_n is the time the process takes on n cores.

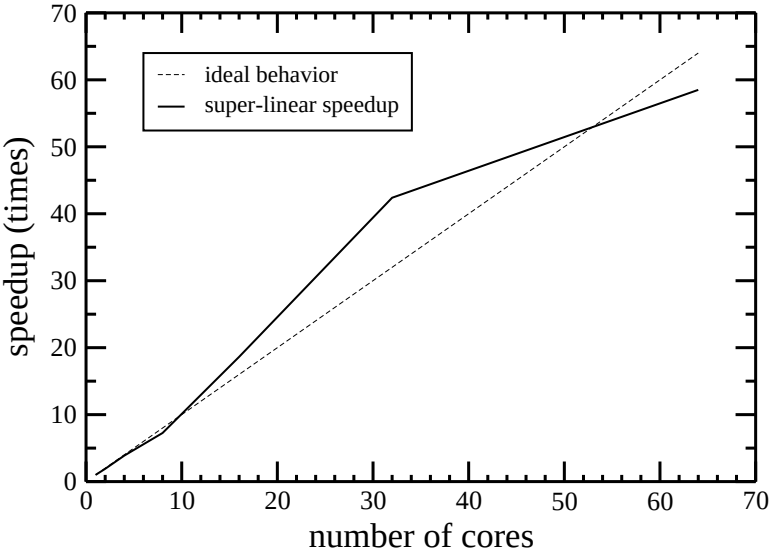

Figure 9.7: The speedup achieved by the parallel computation of the batch crystallization process multiscale model under open-loop operation with the number of cores used for the kMC simulation; super-linear speedup vs. ideal speedup are compared.

In particular, when we do not have access to a sufficient number of identical CPUs, we can still improve the computational efficiency of the parallelized computations by introducing a new variable N_{rp} (please refer to Section 9.3.4 for the definition of N_{rp}). Table 9.4 shows that we can significantly reduce the simulation time required to run one batch simulation by increasing N_{rp}. However, it is shown in Fig. 9.8 that the speedup achieved by increasing n_{cores} decreases as N_{rp} is increased. This is because increasing N_{rp} may unnecessarily simplify the sequential problem such that it is not significantly beneficial to further parallelize the kMC simulation. Furthermore, it is shown in Figs. 9.9 and 9.10 that as N_{rp} is increased (i.e., each crystal represents more crystals; less crystals are used to run the same batch crystallization process, and thus, error may follow), the concentration and the temperature profiles obtained from the parallelized kMC simulation progressively deviate from those profiles obtained from the kMC simulation with $N_{rp} = 1$. By introducing N_{rp}, therefore, we may compromise the accuracy of the simulation results to decrease computation time.

Increasing the stirrer speed induces the aggregation process, which requires transferring crystals from one core to another in parallel computations to model the aggregation of two crystals. Thus, additional overhead costs associated with transferring crystals will be incurred, and as a result, the speedup curve shifts downward as more aggregates are formed, which is shown in Fig. 9.11.

Furthermore, the proposed parallelization scheme has been applied to the simulation of the closed-loop system. Specifically, an in-batch model predictive controller with the

N_{rp}	time (h)
1	34.97
10	4.41
50	1.87
100	0.557
500	0.236

Table 9.4: The time required to finish the batch crystallization process under open-loop operation by varying N_{rp} for $n_{\text{cores}} = 64$.

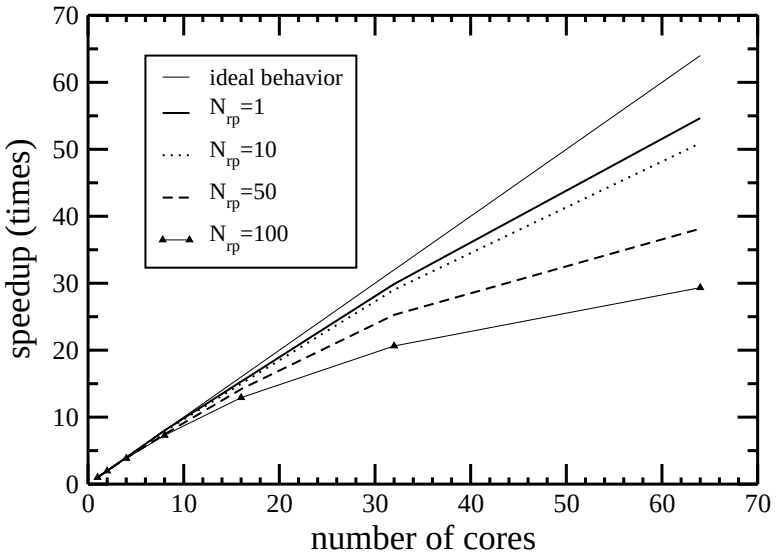

Figure 9.8: The speedup achieved by the parallel computation of the batch crystallization process multiscale model under the open-loop operation with the number of cores used for the kMC simulation for different N_{rp} values.

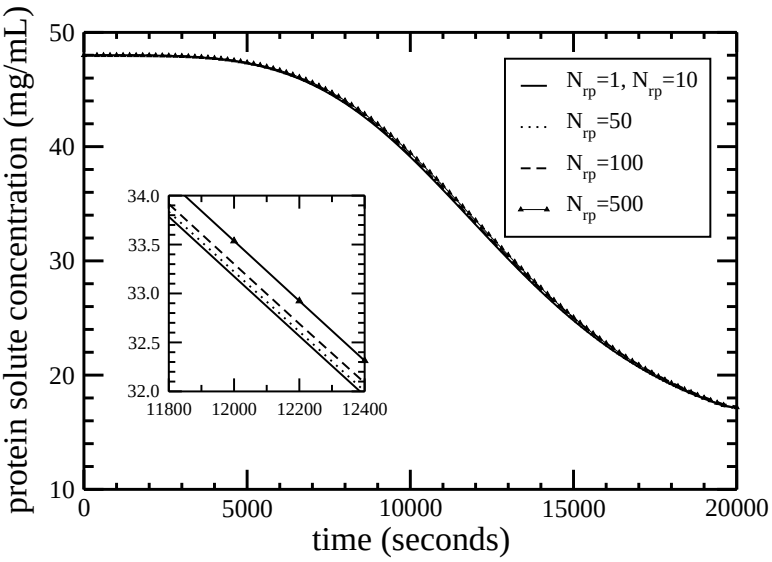

Figure 9.9: Profile of the protein solute concentration with time obtained under the open-loop operation of the batch crystallization process multiscale model for different N_{rp} values. The inset shows the C profile from $t = 11800$ to $t = 12400$ seconds and $C = 32.0$ to $C = 34.0$ mg/mL.

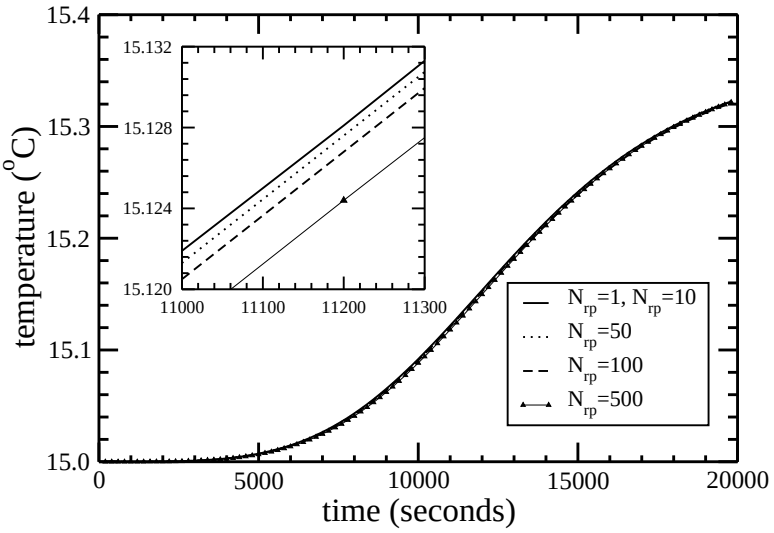

Figure 9.10: Profile of the crystallizer temperature with time obtained under the open-loop operation of the batch crystallization process multiscale model for different N_{rp} values. The inset shows the T profile from $t = 11000$ to $t = 11300$ seconds and $T = 15.120$ to $T = 15.132$ °C.

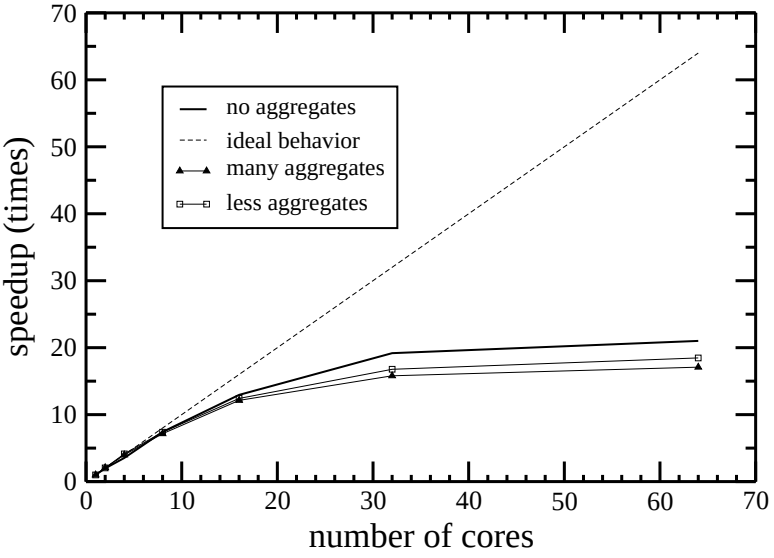

Figure 9.11: The speedup achieved by the parallel computation of the batch crystallization process multiscale model under open-loop operation with the number of cores used for the kMC simulation under conditions where aggregates are formed.

formulation described in [70] is implemented for the batch crystallization process for the production of crystals with a desired crystal shape distribution at the end of the batch process. It is shown in Fig. 9.12 that the computation time can be reduced by the parallel computation of the closed-loop batch crystallization process multiscale model; however, the speedup achieved by the parallel computation depends on the desired set-point value for the crystal shape distribution. For example, the optimal supersaturation level to produce crystals with the higher set-point value, $\alpha_{\text{set}} = 1.05$, favors the nucleation and crystal growth processes, and thus, the computation time is significantly reduced by parallelizing the kMC simulation. On the other hand, for the lower set-point value, $\alpha_{\text{set}} = 0.85$, the optimal supersaturation level is low and the nucleation and crystal growth processes are less favored, in which case the speedup achieved via the parallel computations is not as significant as it is for $\alpha_{\text{set}} = 1.05$.

9.4 Conclusions

In this work, a parallelized multiscale, multidomain modeling scheme was proposed to directly reduce the computation time and memory requirements without compromising the accuracy of the simulation results. The parallelized multiscale modeling strategy that consists of the three steps of decomposition, assignment, and orchestration was applied to a batch crystallization process multiscale model. Firstly, we decomposed the nucleation and crystal growth processes in the batch crystallization system into a collection of tasks where each task represents the crystal growth of a nucleated crystal. Secondly, tasks were assigned

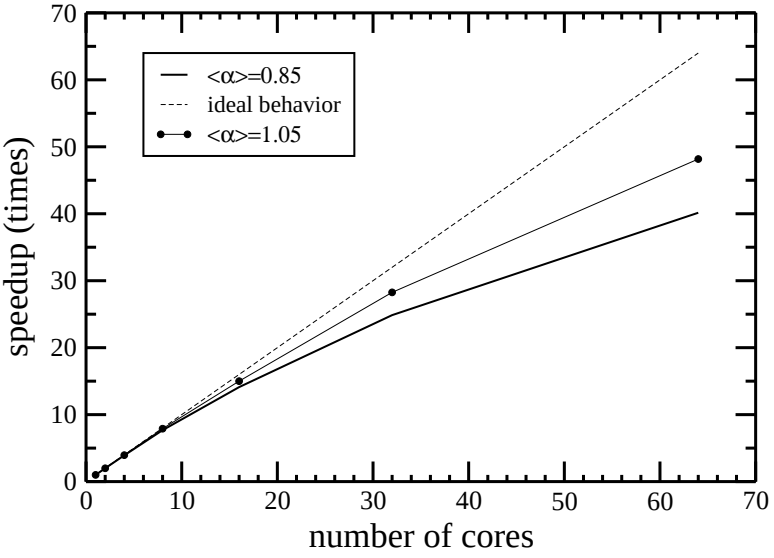

Figure 9.12: The speedup achieved by the parallel computation of the batch crystallization process multiscale model under closed-loop operation with the number of cores used for the kMC simulation under different set-point values: $\alpha_{\text{set}} = 1.05$ and $\alpha_{\text{set}} = 0.85$.

to processors according to a modulus function (i.e., round-robin allocation). Thirdly, a manager-worker MPI computation scheme was used to link the macroscopic model (e.g., mass and energy balance equations for the continuous phase) to the microscopic models (e.g., kinetic Monte Carlo model). Using the proposed parallel computation scheme, a significant decrease in the time required to run the batch crystallization process multiscale model under both open-loop and closed-loop operations was achieved as the number of cores was increased. In particular, the performance of the parallel computation scheme applied to the closed-loop system was dependent on the desired crystal shape. Furthermore, we extended the use of the parallel computation scheme to the crystallization system with a high stirrer speed in which case many crystal aggregates were formed and evaluated the effect of aggregation on the parallelization.

Chapter 10

Conclusions

This dissertation focused on the development of a multiscale modeling and simulation framework for crystallization processes that described the relationship between molecular-level processes like crystal nucleation, growth and aggregation and macroscopically-observable process behavior, and allowed computing optimal design and operation conditions. A practical framework which used multiscale modeling in order to model, simulate, and control crystallization processes was proposed. Furthermore, this dissertation addressed model predictive controller designs that utilized the insight and results from the multiscale modeling work and real-time measurements of solute concentration and temperature to manipulate crystallizer conditions that led to the production of crystals with desired size and shape distributions. In order to deal with batch-to-batch parametric drift, a run-to-run-based model parameter estimation scheme was presented to update the predictive controller model parameters after each batch and led to the consistent production of crystals of desired

shape at the end of each batch.

In Chapter 2, the modeling of a batch crystallization process used to produce tetragonal hen egg white lysozyme crystals via kinetic Monte Carlo (kMC) simulation was presented. The kMC simulation simulated the batch protein crystallization via adsorption, desorption, and migration mechanisms on the (110) and (101) faces. In order to describe the nucleation occurring at different times in the batch simulations, the nucleation rate expression was extracted from experimental results [41]. Mass and energy balances were also used to model the depletion in the protein solute concentration and the drop in the crystallizer temperature by crystallization. Finally, an MPC, which used the mass and energy balances, was designed to produce crystals with a desired morphology by regulating the crystal growth conditions in the crystallizer through the manipulation of the jacket temperature which was in accordance with standard batch crystallization practice.

In Chapter 3, the modeling of aggregation of protein crystals along with crystal nucleation and growth to investigate the influence of stirring on the size and morphology of crystal aggregates was presented. Then, along with nonlinear algebraic equations that described the dependence of crystal growth rates on temperature and protein solute concentration, and the energy and mass balance models that described the changes of the temperature in the crystallizer and the solute concentration in the continuous phase, the moment model was employed to design a model predictive controller (MPC). The proposed model predictive control scheme was used to regulate the average shape of crystal aggregates to a desired set-point value with a low polydispersity.

In Chapter 4, the modeling of the nucleation and crystal growth in a continuous crystallization process with a fines trap through kinetic Monte Carlo (kMC) simulation was presented. The fines trap was modeled through a classification function which used a selection curve for fines dissolution in the continuous crystallizer. In addition to the solute depletion and the temperature change in the continuous phase resulting from crystallization, the interplay of inflow/outflow in the continuous crystallizer was included in the mass and energy balance equations. To deal with a real-time implementation issue of a controller based on PBM, moment models were developed to describe the dominant dynamic behavior of the continuous crystallization along with a fines trap. Subsequently, the three leading moments were used along with the balance equations in order to design a model predictive controller.

In Chapter 5, the modeling and control of a continuous PFC used to produce tetragonal HEW lysozyme crystals was developed. Also, an optimization-based control scheme was proposed to produce crystals with desired size and shape distributions in the presence of feed disturbances. Initially, we modeled a continuous plug flow crystallizer with five segments for the production of lysozyme crystals through kinetic Monte Carlo (kMC) simulation methods following the procedure described in [66] using the rate equations originally developed by [32]. A seeding strategy was used to decouple the nucleation from the crystal growth processes [78, 33, 9, 36]. Specifically, the crystallizer jacket temperatures at each segment and the superficial flow velocity were chosen as the decision variables in the optimization problem. Subsequently, the dynamic model developed in Section 5.2 was

used for the design of an FFC strategy for the production of crystals with desired size and shape distributions that suppressed the undesired effects caused by disturbances [45].

In Chapter 6, a batch process for the crystallization of lysozyme crystals with uncertainties in the crystal growth rates in the directions of the (110) and (101) faces as well as in the solubility was considered. In order to achieve the production of crystals with a desired shape distribution, the optimal jacket temperature profile was computed by a conventional MPC using a nominal reduced-order moment model and was applied to the first batch. After the first run, the post-batch measurements were used to solve a multivariable optimization problem (MOP) off-line for the identification of the process model parameters used in the MPC for the crystal growth rates and solubility. Along with the adapted process model parameters, the exponentially-weighted-moving-average (EWMA) scheme was used to deal with the remaining offset in the crystal shape values and thereby to compute a set of new optimal jacket temperatures. As a result, the production of crystals with a desired shape distribution was achieved by properly suppressing the inherent variation and process drift in the crystal growth rates and solubility.

In Chapter 7, a run-to-run model parameter estimation scheme based on moving horizon estimation concepts was presented in order to model the batch-to-batch dynamics of the process drift and to compute improved estimates of process model parameters, utilizing post-batch measurements from multiple batch runs. The MHE approach was employed because it provided improved parameter estimation and greater robustness to poor guesses for initial states because of its ability to incorporate physical constraints into the optimiza-

tion problem used for parameter estimation. More specifically, the variation of the process model parameters from batch-to-batch was estimated by solving an R2R model parameter estimation scheme incorporating the post-batch measurements from multiple batch runs. Furthermore, the batch-to-batch parametric drift was modeled using a nonlinear function and was used to update the parameters of the model predictive controller (MPC) to suppress the undesired effect of the process drift in the next batch run.

In Chapter 8, an attempt to further refine the approach proposed in Chapter 7 was presented by relaxing the requirement of the in-batch and post-batch process measurements over multiple batch runs and developing a PDDI scheme for the detection and isolation of the parametric drift. Specifically, a PDDI scheme was proposed to detect and isolate parametric drifts introduced to a batch crystallization process. Then, a parametric drift-tolerant control scheme (PDTC) was proposed that used the PDDI scheme to improve the model of the in-batch model predictive controller (MPC) to achieve the production of crystals with a desired shape distribution.

Finally, in Chapter 9, a general parallel computation framework suitable for multiscale models was presented. Then, the proposed parallel computation scheme was applied to a multiscale model, which was used to describe a batch crystallization process, and a series of results that demonstrate the computational efficiency and accuracy of the approach were presented.

Bibliography

[1] N. Aldabaibeh, M. J. Jones, A. S. Myerson, and J. Ulrich. The solubility of orthorhombic lysozyme chloride crystals obtained at high pH. *Crystal Growth & Design*, 9:3313–3317, 2009.

[2] A. Alvarez and A. Myerson. Continuous plug flow crystallization of pharmaceutical compounds. *Crystal Growth & Design*, 10:2219–2228, 2010.

[3] A. Alvarez, A. Singh, and A. S. Myerson. Crystallization of cyclosporine in a multistage continuous MSMPR crystallizer. *Crystal Growth & Design*, 11:4392–4400, 2011.

[4] T. Arbogast and H. Xiao. Two-level mortar domain decomposition preconditioners for heterogeneous elliptic problems. *Comp. Methods in Appl. Mech. and Eng.*, 292:221–242, 2015.

[5] C. Avila, N. Drechse, R. Alcantara, and J. Villa-Freixa. Multiscale molecular dynamics of protein aggregation. *Current Protein & Peptide Science*, 12:221–234, 2011.

[6] G. Ayton, W. Noid, and G. Voth. Multiscale modeling of bimolecular systems: in serial and in parallel. *Current Opinion in Structural Biology*, 17:192–198, 2007.

[7] B. Balakin, A. C. Hoffmann, and P. Kosinski. The collision efficiency in a shear flow. *Chem. Eng. Sci.*, 68:305–312, 2012.

[8] P. Barrett and B. Glennon. Characterizing the metastable zone width and solubility curve using Lasentec FBRM and PVM. *Chem. Eng. Res. Des.*, 80:799–805, 2002.

[9] M. Besenhard, R. Hohl, A. Hodzic, R. Eder, and J. Khinast. Modeling a seeded continuous crystallizer for the production of active pharmaceutical ingredients. *Crystal Research and Technology*, 49:92–108, 2014.

[10] A. B. Bortz, M. H. Kalos, and J. L. Lebowitz. New algorithm for Monte Carlo simulation of Ising spin systems. *J. Comp. Phys.*, 17:10–18, 1975.

[11] S. W. Bulter and J. Stefani. Supervisory run-to-run control of polysilicon gate etch using in situ ellipsometry. *IEEE Trans. Semiconductor Manufacturing*, 7:193–201, 1994.

[12] E. Cacioppo, S. Munson, and M. L. Pusey. Protein solubilities determined by a rapid technique and modification of that technique to a micro-method. *Journal of Crystal Growth*, 110:66–71, 1991.

[13] E. Cacioppo and M. L. Pusey. The solubility of the tetragonal form of hen-egg-white lysozyme from pH 4.0 to 5.4. *Journal of Crystal Growth*, 114:286–292, 1991.

[14] J. Calderon De Anda, X. Z. Wang, X. Lai, and K. J. Roberts. Classifying organic crystals via in-process image analysis and the use of monitoring charts to flow polymorphic and morphological changes. *Journal of Process Control*, 15:785–797, 2005.

[15] J. Calderon De Anda, X. Z. Wang, and K. J. Roberts. Multi-scale segmentation image analysis for the in-process monitoring of a particle shape with batch crystallisers. *Chem. Eng. Sci.*, 60:1053–1065, 2005.

[16] T. R. Camp and P. C. Stein. Velocity gradients and internal work in fluid motion. *J. Boston Soc. Civ. Eng.*, 30:219–237, 1943.

[17] W. Campbell, S. Firth, A. Toprac, and T. F. Edgar. A comparison of run-to-run control algorithms. *Proceedings of the American Control Conference, Anchorage*, AK:2150–2155, 2002.

[18] N. Cheimarios, G. Kokkoris, and A. Boudouvis. An efficient parallel iteration method for multiscale analysis of chemical vapor deposition process. *Appl. Numerical Math.*, 67:78–88, 2013.

[19] A. Chen and Ruey-Shan. Guo. Age-based double EWMA controller and its application to CMP processes. *IEEE Trans. Semiconductor Manufacturing*, 14:11–19, 2001.

[20] J. Chen, B. Sarma, J. M. Evans, and A. S. Myerson. Pharmaceutical crystallization. *Crystal Growth & Design*, 11:887–895, 2011.

[21] J. Cheng, C. Yang, Z. Mao, and C. Zhao. CFD modeling of nucleation, growth, aggregation, and breakage in continuous precipitation of barium sulface in a stirred tank. *Ind. & Eng. Chem. Res.*, 48:6992–7003, 2009.

[22] T. Chiu and P. D. Christofides. Nonlinear control of particulate processes. *AIChE J.*, 45:1279–1297, 1999.

[23] T. Chiu and P. D. Christofides. Robust control of particulate processes using uncertain population balances. *AIChE J.*, 46:266–280, 2000.

[24] P. D. Christofides. *Model-Based Control of Particulate Processes*. Kluwer Academic Publishers, Dordrecht, 2002.

[25] P. D. Christofides, A. Armaou, Y. Lou, and A. Varshney. *Control and Optimization of Multiscale Process Systems*. Birkhäuser, Boston, 2008.

[26] G. Cogoni, D. Widenski, M. Grosso, R. Baratti, and J. Romagnoli. A qualitative comparison between population balances and stochastic models for non-isothermal antisolvent crystallization processes. *Comp. & Chem. Eng.*, 63:82–90, 2014.

[27] M. Crose, J. S. Kwon, M. Nayhouse, D. Ni, and P. D. Christofides. Multiscale modeling and operation of PECVD of thin film solar cells. *Chem. Eng. Sci.*, doi:10.1016/j.ces.2015.02.027 (in press), 2015.

[28] D. Culler, J. Singh, and A. Gupta. *Parallel computer architecture: a hardware/software approach*. Morgan Kaufmann Publishers, Burlington, 1999.

[29] J. Dai, J. M. Kanter, S. S. Kapur, W. D. Seider, and T. Sinno. On-lattice kinetic Monte Carlo simulations of point defect aggregation in entropically influenced crystalline systems. *Phys. Rev. B*, 72:134102, 2005.

[30] J. Dai, W. D. Seider, and T. Sinno. Coarse-grained lattice kinetic Monte Carlo simulation of systems of strongly interacting particles. *J. Chem. Phys.*, 128:194705, 2008.

[31] S. D. Durbin and G. Feher. Crystal growth studies of lysozyme as a model for protein crystallization. *Journal of Crystal Growth*, 76:583–592, 1986.

[32] S. D. Durbin and G. Feher. Simulation of lysozyme crystal growth by the Monte Carlo method. *Journal of Crystal Growth*, 110:41–51, 1991.

[33] R. Eder, E. Schmitt, J. Grill, S. Radl, H. Gruber-Woelfler, and J. Khinast. Seed loading effects on the mean crystal size of acetylsalicylic acid in a continuous-flow crystallization device. *Crystal Research and Technology*, 3:227–237, 2011.

[34] N. El-Farra, T. Chiu, and P. D. Christofides. Analysis and control of particulate processes with input constraints. *AIChE J.*, 47:1849–1865, 2001.

[35] G. Feher and Z. Kam. Nucleation and Growth of Protein Crystals: General Principles and Assays. *Methods in Enzymology*, 114:77–112, 1985.

[36] S. Ferguson, G. Morris, H. Hao, M. Barrett, and B. Glennon. Automated self seeding of batch crystallizations via plug flow seed generation. *Chem. Eng. Res. Des.*, 92:2534–2541, 2014.

[37] K. A. Fichthorn and W. H. Weinberg. Theoretical foundations of dynamical Monte Carlo simulations. *J. Chem. Phys.*, 95:1090–1096, 1991.

[38] E. L. Forsythe, A. Nadarajah, and M. L. Pusey. Growth of (101) faces of tetragonal lysozyme crystals: measured growth-rate trends. *Acta Crystallographica. D*, 55:1005–1011, 1999.

[39] B. Frantzdale, S. Plimpton, and M. Shephard. Software components for parallel multiscale simulation: an example with LAMMPS. *Engineering With Computers*, 26:205–211, 2010.

[40] O. Galkin and P. G. Vekilov. Direct determination of the nucleation rates of protein crystals. *J. Phys. Chem. B*, 103:10965–10971, 1999.

[41] O. Galkin and P. G. Vekilov. Nulceation of protein crystals: critical nuclei, phase behavior, and control pathways. *Journal of Crystal Growth*, 232:63–76, 2001.

[42] D. T. Gillespie. A general method for numerically simulating the stochastic time evolution of coupled chemical reactions. *J. Comp. Phys.*, 22:403–434, 1976.

[43] D. T. Gillespie. Stochastic simulation of chemical kinetics. *Annu. Rev. Phys. Chem.*, 58:35–55, 2007.

[44] G. H. Gilmer and P. Bennema. Simulation of crystal growth with surface diffusion. *J. Appl. Phys.*, 43:1347, 1972.

[45] S. Gnoth, M. Jenzsch, R. Simutis, and A. Luubert. Process analytical technology (PAT): batch-to-batch reproducibility of fermentation processes by robust process operational design and control. *J. Biotechnol.*, 132:180–186, 2007.

[46] M. Graham and J. Rawlings. *Modeling and Analysis Principles for Chemical and Biological Engineers*. Nob Hill Pub, 2013.

[47] M. Griebel and A. Ruttgers. Multiscale simulations of three-dimensional viscoelastic flows in a square-square contraction. *J. of Non-Newtonian Fluid Mech.*, 205:41–63, 2014.

[48] D. W. Griffin, D. A. Mellichamp, and M. F. Doherty. Reducing the mean size of API crystals by continuous manufacturing with product classification and reycle. *Chem. Eng. Sci.*, 65:5770–5780, 2010.

[49] N. Guo and J. Zhao. A coupled FEM/DEM approach for hierachical multiscale modeling of granular media. *Int. J. Numerical Methods in Eng.*, 99:789–818, 2014.

[50] U. Hansen, S. Rodgers, and K. Jensen. Modeling of metal thin film growth: linking angstrom-scale molecular dynamics results to micron-scale film topographies. *Phys. Rev. B*, 62:2869–2878, 2000.

[51] M. L. Hentschel and N. W. Page. Selection of descriptors for particle shape characterization. *Particle & Particle Systems Characterization*, 20:25–38, 2006.

[52] H. Henzler. Particle stress in bioreactors. *Adv. Biochem. Eng. Biotech.*, 67:35–82, 2000.

[53] E. D. Hollander, J. J. Derksen, H. M. J. Kramer, G. M. Van Rosmalen, and H. E. A. Van den Akker. A numerical study on orthokinetic agglomeration in stirred tanks. *Powder Technology*, 130:169–173, 2003.

[54] G. Hou, G. Power, M. Barrett, B. Glennon, G. Morris, and Y. Zhao. Development and characterization of a single stage mixed-suspension mixed-product-removal crystallization process with a novel transfer unit. *Crystal Growth & Design*, 14:1782–1793, 2014.

[55] H. M. Hulburt and S. Katz. Some problems in particle technology. A statistical mechanical formulation. *Chem. Eng. Sci.*, 19:555–574, 1964.

[56] D. Ilievski and I. Livk. An agglomeration efficiency model for gibbsite precipitation in a turbulently stirred vessel. *Chem. Eng. Sci.*, 61:2010–2022, 2006.

[57] A. Ingolfsson and E. Sachs. Stability and sensitivity of an EWMA controller. *J. of Quality Technology*, 25:271–287, 1993.

[58] Q. Jiang and B. E. Logan. Fractal dimensions of aggregates determined from steady-state size distributions. *Environ. Sci. Technol.*, 25:2031–2038, 1991.

[59] A. Kalani and P. D. Christofides. Simulation, estimation and control of size distribution in aerosol processes with simultaneous reaction, nucleation, condensation and coagulation. *Comp. & Chem. Eng.*, 26:1153–1169, 2002.

[60] S. C. Ke, L. J. DeLucas, and J. G. Harrison. Computer simulation of protein crystal growth using aggregates as the growth unit. *J. Phys. D: Appl. Phys.*, 31:1064–1070, 1998.

[61] I. G. Kevrekidis, C. W. Gear, and G. Hummer. Equation-free: the computer-aided analysis of complex multiscale systems. *AIChE J.*, 50:1346–1355, 2004.

[62] Y. C. Kim and A. S. Myerson. Diffusivity of protein in aqueous soutions. *Korean J. of Chem. Eng.*, 13:288–293, 1996.

[63] E. Kougoulos, A.G. Jones, K.H. Jennings, and M.W. Wood-Kaczmar. Use of focused beam reflectance measurement (FBRM) and process video imaging (PVI) in a modified mixed suspension mixed product removal (MSMPR) cooling crystallizer. *Journal of Crystal Growth*, 273:529–534, 2005.

[64] K. Kurihara, S. Miyashita, G. Sazaki, T. Nakada, Y. Suzuki, and H. Komatsu. Interferometric study on the crystal growth of tetragonal lysozyme crystal. *Journal of Crystal Growth*, 166:904–908, 1996.

[65] K. A. Kusters, J. D. Wijers, and D. Thoenes. Aggregation kinetics of small particles in agitated vessels. *Chem. Eng. Sci.*, 52:107–121, 1997.

[66] J. S. Kwon, M. Nayhouse, P. D. Christofides, and G. Orkoulas. Modeling and control of protein crystal shape and size in batch crystallization. *AIChE J.*, 59:2317–2327, 2013.

[67] J. S. Kwon, M. Nayhouse, P. D. Christofides, and G. Orkoulas. Modeling and control of shape distribution of protein crystal aggregates. *Chem. Eng. Sci.*, 104:484–497, 2013.

[68] J. S. Kwon, M. Nayhouse, P. D. Christofides, and G. Orkoulas. Modeling and control of crystal shape in continuous protein crystallization. *Chem. Eng. Sci.*, 107:47–57, 2014.

[69] J. S. Kwon, M. Nayhouse, P. D. Christofides, and G. Orkoulas. Protein cyrstal shape and size control in batch crystallization: Comparing model predictive control with conventional operating policies. *Ind. & Eng. Chem. Res.*, 53:5002–5014, 2014.

[70] J. S. Kwon, M. Nayhouse, Orkoulas G., D. Ni, and P. D. Christofides. A method for handling batch-to-batch parametric drift using moving horizon estimation: application to run-to-run MPC of batch crystallization. *Chem. Eng. Sci*, 127:210–219, 2014.

[71] J. S. Kwon, M. Nayhouse, D. Ni, G. Orkoulas, and P. D. Christofides. Run-to-run based model predictive control of batch crystallization. *Ind. & Eng. Chem. Res.*, dx.doi.org/10.1021/ie502377a, 2014.

[72] J. S. Kwon, M. Nayhouse, G. Orkoulas, and P. D. Christofides. Crystal shape and size control using a plug flow crystallization configuration. *Chem. Eng. Sci.*, 119:30–39, 2014.

[73] J. S. Kwon, M. Nayhouse, G. Orkoulas, and P. D. Christofides. Enhancing crystal production rate and reducing polydispersity in continuous protein crystallization. *Ind. & Eng. Chem. Res.*, 53:15538–15548, 2014.

[74] R. Lam and D. G. Vlachos. Multiscale model for epitaxial growth of films: Growth mode transition. *Phys. Rev. B*, 64:035401, 2001.

[75] D. Landau and K. Binder. *A guide to Monte Carlo simulations in statistical physics*. Cambridge University Press, New York., 2000.

[76] O. Levenspiel. *Chemical Reaction Engineering*. Wiley Eastern, 1998.

[77] M. Liang, F. Jin, R. Liu, Y. Yu, R. Su, L. Wang, W. Qi, and Z. He. Shape evolution and thermal stability of lysozyme crystals: effect of pH and temperature. *Bioprocess & Biosystems Eng.*, 36:91–99, 2013.

[78] J. J. Liu, C. Y. Ma, Y. D. Hu, and X. Z. Wang. Effect of seed loading and cooling rate on crystal size and shape distributions in protein crystallization-a study using morphological population balance simulation. *Comp. & Chem. Eng.*, 34:1945–1952, 2010.

[79] J. J. Liu, C. Y. Ma, Y. D. Hu, and X. Z. Wang. Modelling protein crystallisation using morphological population balance models. *Chem. Eng. Res. Des.*, 88:437–446, 2010.

[80] A. Majumder and Z. Nagy. Fines removal in a continuous plug flow crystallizer by optimal spatial temeprature profiles with controlled dissolution. *AIChE J.*, 59:4582–4594, 2013.

[81] D. Maroudas. Multiscale modeling of hard materials: challenges and opportunities for chemical engineering. *AIChE J.*, 46:878–882, 2000.

[82] C. M*ü*ller and J. Ulrich. A more clear insight of the lysozyme crystal composition. *Cryst. Res. Technol.*, 46:646–650, 2011.

[83] S. M. Miller. *Modelling and Quality Control Strategies for Batch Cooling Crystallizers.* PhD thesis, The University of Texas at Austin, 1993.

[84] M. Mosby, , and K. Matous. Hierarchically parallel coupled finite strain multiscale solver for modeling heterogeneous layers. *Int. J. Numerical Methods in Eng.*, 102:748–765, 2015.

[85] J. Moyne, E. D. Castillo, and A. M. Hurwitz. *Run-to-run control in semiconductor manufacturing*. CRC Press, 2001.

[86] C. Müller, Y. Liu, A. Migge, M. Pietzsch, and J. Ulrich. Recombinant L-asparaginase B and its crystallization - what is the nature of protein crystals?. *Chem. Eng. Technol.*, 34:571–577, 2011.

[87] H. Müller-Krumbhaar and K. Binder. Dynamic properties of the Monte Carlo method in statistical mechanics. *J. Stat. Phys.*, 8:1–24, 1973.

[88] J. Musacchio, S. Rangan, C. Spanos, and K. Poolla. On the utility of run to run control in semiconductor manufacturing. *Semiconductor Manufacturing Conference Proceedings*, San Francisco,CA:D9–D12, 1997.

[89] F. Muth. Optimal properties of exponentially weighted forecasts of time series with permanent and transitory components. *Journal of American Statistical Association*, 55:239–250, 1960.

[90] Aldabaibeh N. *Towards an Improved Understanding of the Variables Controlling Crystal Modification and Phase Transition in Lysozyme Crystals.* PhD thesis, Illinois Institute of Technology, 2010.

[91] S. Nadarajah and J.H. Lee. Repetitive model predictive control applied to a simulated moving bed chromatography system. *Comp. & Chem. Eng.*, 24:1127–1133, 2000.

[92] C. N. Nanev and D. Tsekova. Heterogeneous nucleation of hen-egg-white lysozyme-molecular approach. *Crystal Research and Technology*, 35:189–195, 2000.

[93] M. Nayhouse, J. S. Kwon, P. D. Christofides, and G. Orkoulas. Crystal shape modeling and control in protein crystal growth. *Chem. Eng. Sci.*, 87:216–223, 2013.

[94] C. J. O'Keeffe and G. Orkoulas. Parallel canonical Monte Carlo simulations through sequential updating of particles. *J. Chem. Phys.*, 95:134109, 2009.

[95] C. J. O'Keeffe, R. Ren, and G. Orkoulas. Spatial updating grand canonical Monte Carlo algorithms for fluid simulation: generalization to continuous potentials and parallel implementation. *J. Chem. Phys.*, 127:194103, 2007.

[96] E. Oksanen, M. Blakeley, F. Bonnete, M. Dauvergne, and F. Dauvergne. Large crystal growth by thermal control allows combined x-ray and neutron crystallographic studies to elucidate the protonation states in aspergillus flavus urate oxidase. *J. R. Soc. Interface*, 6:S599–S610, 2009.

[97] L. Pesce, H. Lee, M. Hereld, S. Visser, R. Stevens, A. Wildeman, and W. Van Drongelen. Large-scale modeling of epileptic seizures: scaling properties of two parallel neuronal network simulation algorithms. *Comp. & Math. Methods in Medicine*, 2013:182145, 2013.

[98] P. Pourghahramani and E. Forssberg. Review of applied particle shape descriptors and produced particle shapes in grinding environments. part 1: particle shape descriptors. *Mineral Processing and Extractive Metallurgy Review*, 26:145–166, 2005.

[99] T. Pricer, M. Kushner, and R. Alkire. Monte Carlo simulation of the electrodeposition of copper 1. additive-free acidic sulfate solution. *J. of the Electrochemical Society*, 149:C396–C405, 2002.

[100] M. L. Pusey and A. Nadarajah. A model for tetragonal lysozyme crystal nucleation and growth. *Crystal Growth & Design*, 2:475–483, 2002.

[101] A. Randolph and M. Larson. *Theory of particulate process: analysis and techniques of continuous crystallization*. Academic Press, 1988.

[102] S. Rasoulian and L. Ricardez-Sandoval. Uncertainty analysis and robust optimization of multiscale process systems with application to epitaxial thin film growth. *Chem. Eng. Sci.*, 116:590–600, 2014.

[103] M. Rathinam, L. R. Petzold, Y. Cao, and D. T. Gillespie. Stiffness in stochastic chemically reacting systems: The implicit tau-leaping method. *J. Chem. Phys.*, 119:12784–12794, 2003.

[104] J. S. Reese, S. Raimondeau, and D. G. Vlachos. Monte Carlo Algorithms for Complex Surface Reaction Mechanisms: Efficiency and Accuracy. *J. Comp. Phys.*, 173:302–321, 2001.

[105] R. Ren and G. Orkoulas. Parallel Markov chain Monte Carlo simulations. *J. Chem. Phys.*, 126:211102, 2007.

[106] L. Ricardez-Sandoval. Current challenges in the design and control of multiscale systems. *The Canadian J. of Chem. Eng.*, 9999:1–18, 2011.

[107] E. Sachs, RS. Guo, and A. Ha. On-line process optimization and control using the sequential design of experiments. *Symposium on VLSI Technology*, Honolulu, HI:99–100, 1990.

[108] E. Sachs, A. Hu, and A. Ingolfsson. Run by run process control: combining SPC and feedback control. *IEEE Trans. Semiconductor Manufacturing*, 8:26–43, 1995.

[109] P. G. Saffman and J. S. Turner. On the collision of drops in turbulent clouds. *J. Fluid Mechanics.*, 1:448–462, 1954.

[110] C. Schall, E. Arnold, and J. Wiencek. Enthalpy of crystallization of hen egg-white lysozyme. *Journal of Crystal Growth*, 165:293–298, 1996.

[111] L. D. Schmidt. *The engineering of chemical reactions*. Oxford, 2005.

[112] S. Schmidt, D. Havekost, K. Kaiser, and H. K. Henzler. Crystallization for the downstream processing of proteins. *Eng. Life Sci.*, 5:273–276, 2005.

[113] M. Sen, R. Singh, and R. Ramachandran. Simulation-based design of an efficient control system for the continuous purification and processing of active pharmaceutical ingredients. *J. of Pharm. Innov.*, 9:65–81, 2014.

[114] B. Seny, J. Lambrechts, T. Toulorge, V. Legat, and J. Remacle. An efficient parallel implementation of explicit multirate Runge-Kutta schemes for discontinuous Galergin computations. *J. of Comp. Phys.*, 256:135–160, 2014.

[115] D. Shi, N. H. El-Farra, M. Li, P. Mhaskar, and P. D. Christofides. Predictive control of particle size distribution in particulate processes. *Chem. Eng. Sci.*, 61:268–281, 2006.

[116] D. Shi, P. Mhaskar, N. H. El-Farra, and P. D. Christofides. Predictive control of crystal size distribution in protein crystallization. *Nanotechnology*, 16:S562–S574, 2005.

[117] T. Simith, D. Boning, J. Stefani, and S. Bulter. Run by run advanced process control of metal sputter deposition. *IEEE Trans. Semiconductor Manufacturing*, 11:276–284, 1998.

[118] B. Smejkal, B. Helk, J. Rondeau, S. Anton, A. Wilke, P. Scheyerer, J. Fries, D. Hekmat, and D. Weuster-Botz. Protein crystallization in stirred systems-scale-up via the maximum local energy dissipation. *Biotechnology and Bioengineering*, 110:1956–1963, 2013.

[119] M. A. Snyder, A. Chatterjee, and D. G. Vlachos. Net-event kinetic Monte Carlo for overcoming stiffness in spatially homogeneous and distributed systems. *Comp. & Chem. Eng.*, 29:701–712, 2005.

[120] Y. Suzuki, S. Miyashita, H. Komatsu, K. Sato, and T. Yagi. Crystal growth of hen egg white lysozyme under high pressure. *Japanese Journal of Applied Physics*, 33:1568–1570, 1994.

[121] D. Tsalikis, C. Baig, V. Mavrantzas, E. Amanatides, and D. Mataras. A hybrid kinetic Monte Carlo method for simulating silicon films grown by plasma-enhanced chemical vapor deposition. *J. Chem. Phys.*, 139:204706, 2013.

[122] M. Vanni and G. Baldi. Coagulation efficiency of colloidal particles in shear flow. *Adv. Colloid Interface Sci.*, 97:151–177, 2002.

[123] T. Vetter, C. Burcham, and M. F. Doherty. Regions of attainable particle sizes in continuous and batch crystallization processes. *Chem. Eng. Sci*, 106:167–180, 2014.

[124] D. G. Vlachos. A review of multiscale analysis: examples from systems biology, materials engineering, and other fluid-surface interacting systems. *Advances in Chem. Eng.*, 30:1–61, 2005.

[125] J. Wang, P. He, and J. Qin. Stability analysis and optimal tuning of EWMA controllers - Gain adaptation vs. intercept adaptation. *Journal of Process Control*, 20:134–142, 2010.

[126] L. Wang, M. H. Lee, J. Barton, L. Hughes, and T. W. Odom. Shape-control of protein crystals in patterned microwells. *J. Am. Chem. Soc.*, 130:2142–2143, 2008.

[127] L. Wang, D. L. Marchisio, R. D. Vigil, and R. O. Fox. CFD simulation of aggregation and breakage processes in laminar Taylor-Couette flow. *J. of Colloid & Interface Sci.*, 282:380–396, 2005.

[128] Y. Wang, F. Gao, and F. J. Doyle. Survey on iterative learning control, repetitive control, and run-to-run control. *Journal of Process Control*, 19:1589–1600, 2009.

[129] M. Weber, M. Jones, and J. Ulrich. Crystallization as a purification method for jack bean urease: on the suitability of poly(ethylene), Li2SO4 and NaCl as precipitants. *Crystal Growth & Design*, 8:711–716, 2008.

[130] S.Y. Wong, A. Tatusko, B.L. Trout, and A.S. Myerson. Development of continuous crystallization processes using a single stage msmpr crystallizer with recycle. *Crystal Growth & Design*, 12:5701–5707, 2012.

[131] G. Yang, N. Kubota, Z. Sha, M. Louhi-Kultanen, and J. Wang. Crystal shape control by manipulating supersaturation in batch cooling crystallization. *Crystal Growth & Design*, 6:2799–2803, 2006.